This is to certify that the
dissertation entitled

SOLID-STATE NUCLEAR MAGNETIC RESONANCE STUDIES OF THE STRUCTURE AND MEMBRANE INSERTION OF HIV FUSION PEPTIDES

presented by

Wei Qiang

has been accepted towards fulfillment
of the requirements for the

Ph.D. degree in Department of Chemistry

David P. Weliky
Major Professor's Signature

May 26, 2009
Date

SOLID-STATE NUCLEAR MAGNETIC RESONANCE STUDIES OF THE STRUCTURE AND MEMBRANE INSERTION OF HIV FUSION PEPTIDES

By

Wei Qiang

A DISSERTATION

Submitted to
Michigan State University
In partial fulfillment of the requirements
For the degree of

DOCTOR OF PHILOSOPHY

Chemistry

2009

role

hyd

by i

varia

an e

(HFP

three

mem

nor c

^{13}C ch

and H

memb

the m

(HFPm

membr

ABSTRACT

SOLID-STATE NUCLEAR MAGNETIC RESONANCE STUDIES OF THE STRUCTURE AND MEMBRANE INSERTION OF HIV FUSION PEPTIDES

By

Wei Qiang

Fusion between the viral and target cell membranes plays an important role in the infection of human immunodeficiency virus (HIV). The ~20-residue hydrophobic N-terminal HIV fusion peptide (HFP) catalyzes the membrane fusion by interacting with the cell membranes. In the present studies, a series of the variant peptides of HFP were synthesized. The first part of the results describes an efficient synthetic scheme for HFP oligomers, in particular for HFP trimers (HFPtr). Compared with previous schemes, the present method shows at least three-fold increase in the overall yield as well as a great enhancement in purity.

Solid-state nuclear magnetic resonance (NMR) was applied to the membrane-associated HFP systems because such systems were neither soluble nor crystalline. The residue-specific secondary structure was obtained through ^{13}C chemical shift measurements. For HFP monomer (HFPmn), dimer (HFPdm) and HFPtr, both α-helical and β-strand conformations were observed in the membrane without cholesterol while only β-strand conformation was detected in the membrane with cholesterol. For the V2E mutated HFP monomer (HFPmn_mut), a mixture of α-helix and β-strand were observed in both membranes. These observations indicated the conformation of HFP was

dependent on the membrane composition and in particular the existence of cholesterol; however, there was not an obvious correlation between the secondary structure and the fusion activity of HFPs.

The tertiary structure of HFPmn associated with cholesterol-containing membrane was studied using rotational-echo double resonance (REDOR) method. Two specific anti-parallel β-sheet registries were identified for HFPmn with overlapping of the N-terminal 16 or 17 residues. 50 -60 % of the membrane-associated HFPmn adopted these two registries. The study provided an applicable approach to quantify the registries for the membrane-associated β-sheet HFPs.

A systematic study of the membrane location of specifically-labeled residues in HFPmn_mut, HFPmn and HFPtr was conducted using ^{13}C-^{31}P and ^{13}C-^{19}F REDOR approaches in both cholesterol-containing and non-cholesterol membranes. It was observed that in the cholesterol-containing membranes, the membrane insertion depth followed the trend HFPmn_mut < HFPmn < HFPtr. In the non-cholesterol-containing membranes where the peptides adopted both α-helical and β-strand conformations, both the membrane insertion depth and the deeply-inserted population followed the same trend as in cholesterol-containing membranes regardless of the secondary structures. These results suggested that there is a positive correlation between the fusion activity of a HFP construct and the insertion depth and deeply-inserted population of the construct, which may be independent on the secondary structure of the HFPs.

Dedicated to my beloved wife, Yan Sun

ACKOWNLEDGEMENTS

I would like to at first thank my advisor Dr. David Weliky for his instruction, support and help during the five years. It is his encouragement and patience that help me to become interested in and to decide to stick at the area of biological solid-state Nuclear Magnetic Resonance.

I would like to give my thankfulness to the professors, seniors and colleagues who are always supportive to my research. Especially I would like to thank my committee members Dr. John McCracken, Dr. Michael Feig and Dr. Gavin Reid for their valuable suggestions on the thesis, my former group members Dr. Zhaoxiong Zheng (Norm), Dr. Michelle Bodner and Dr. Rong Yang for their kindness and help when I first joined the group and my current colleagues Scott Schmick, Dr. Kelly Sackett, Dr. Charles Gabrys, Jaime Curtis-Fisk, Matt Nethercott and Erica Schwander for their useful discussions about my projects.

I would also like to thank my family and friends, in particular my parents for their edification and stimulation not only during my graduate studies, but also throughout my entire education.

Finally, I will express my greatest appreciation to my beloved wife, Yan Sun, who is also my lab colleague. It is her support both inside and outside work that makes me successfully complete my graduate study with much less tough experience than what I heard at the beginning.

TABLE OF CONTENTS

List of Tables viii

List of Figures ix

List of Symbols and Abbreviations xviii

Chapter I. Introduction
Background 1
Reference 10

Chapter II. Optimization of the Synthesis of HIV Fusion Peptide Oligomers
Background 16
Materials 17
Results and Discussion
Optimization of Coupling Time 19
Synthesis of HFPdm 20
Synthesis of HFPtr 21
Conclusion 23
Reference 32

Chapter III. Optimization fo Solid-state NMR Experiments
Theoretical Background
Average Hamiltonian Theory (AHT) 33
Theory of REDOR Experiments 39
Double CP (DCP) Experiments 44
Experimental Optimization
^{13}C-^{31}P REDOR Experiment 49
^{13}C-^{19}F REDOR Experiment 52
DCP experiment 53
Reference 56

Chapter IV. Secondary Structures of Membrane-Associated HIV Fusion Peptides
Background 59
Materials and Methods
NMR Sample Preparation 61
Solid-state NMR Experiments 62
Results and Discussion
Residue Specific Chemical Shifts 67

Conc
Refe

Chap
Back
Mate

Resu

Conc
Refe

Chap
Back
Mate

Resu

Concl
Refer

Chapt
Refer

Apper
Apper
Apper
Appen

Cholesterol-dependence of the HFP Conformation 69
Construct-dependence of the HFP conformation 71
Conclusion 76
Reference 77

Chapter V. Tertiary Structure of Membrane-Associated HIV Fusion Peptides
Background 81
Materials and Methods
Peptide 83
NMR Sample Preparation 83
^{13}C-^{15}N REDOR Experiments and Simulations 84
Results and Discussion
Anti-parallel β-sheet Registries for HFPmn 90
Quantitative Anti-parallel β-sheet Registry Models 96
Conclusion 104
Reference 106

Chapter VI. Membrane Insertion of HIV Fusion Peptides
Background 110
Materials and Methods
Peptides 113
Lipid Mixing Induced by HFPs 114
Synthesis of the Precursor of 5-^{19}F-DPPC 118
Solid-state NMR Samples Preparation and Experiments 119
Natural Abundance Correction for $(\Delta S/S_0)^{exp}$ 122
Results and Discussion
Fusion Activities of Different HFP Constructs 126
Membrane Insertion of Triply-labeled HFPs 127
Membrane Insertion of β-strand HFPs 139
Membrane Insertion of α-helical HFPs 159
Conclusion 194
Reference 196

Chapter VII. Summary and Future Work
Reference 208

Appendix 1. NMR Files Checklist 209
Appendix 2. Trouble Shooting for MAS Probes 215
Appendix 3. FMOC Manual Peptide Synthesis 219
Appendix 4. Introduction to NMR 225

Tab
Tab
Tab
PC
PC
HF
Tab
Tab
the
Tab
Tabl
Tabl
Tabl
Tabl
Tabl
Tabl
Tabl

LIST OF TABLES

Table 1 Names and sequences of the HIV fusion peptides. 17

Table 2 Hamiltonians in REDOR S_0 and S_1 spectra. 39

Table 3 ^{13}C chemical shift Assignments for (a) HFPmn in PC:PG, (b) HFPdm in PC:PG, (c) HFPtr in PC:PG, (d) HFPmn in PC:PG:CHOL, (e) HFPdm in PC:PG:CHOL, (f) HFPtr in PC:PG:CHOL, (g) HFPmn_mut in PC:PG and (h) HFPmn_mut in PC:PG:CHOL. 65

Table 4 Peptide sequences and labeling schemes. 80

Table 5 The parameters of (a) $(\Delta S/S_0)^{na}$(HFP) and (b) $(\Delta S/S_0)^{na}$(DPPC) used for the REDOR natural abundance correction. 121

Table 6 Fitting parameters for the lipid mixing kinetics at 35°C. 124

Table 7 ^{13}CO chemical shifts in PC:PG:CHOL membrane. 138

Table 8 Best-fit distances and populations for samples in PC:PG:CHOL. 145

Table 9 13CO chemical shifts in PC:PG membrane. 158

Table 10 ^{13}CO-^{31}P internuclear distances and populations for HFPmn_mut. ...165

Table 11 The best-fit *A* and *B* population for HFPmn and HFPtr in PC:PG. 174

Table 12 Summary of the fitting for ^{13}C-^{31}P and ^{13}C-^{19}F(C16) experiments. 174

Table 13 Fitting results for the ^{13}C-^{19}F(C5) experiments. 182

Fig
to h
por
the

Fig
time
figu
rods
tran
with
(iii)

Figu
AVG
are
reac
reac
depr
Read
used
for T
resid
TFA/
react
with

Figu
MALD
mark
labele

Figure
circles
c wer
(a) fo
hour

LIST OF FIGURES

Figure 1. Model (left) and Electron Microscopy (right) of the HIV virus (a) binding to host cell (b) fusion of viral and host cell membranes (c, d) formation of large pore and infection of host cell. The triangle represents the viral RNA that enters the host cells. 2

Figure 2. (a) Model of HIV infection. "F" indicates the HIV fusion peptide and the time sequence is left to right. (b) Model for HIV/host cell fusion. In the left-most figure, a gp120/gp41 trimer is displayed with the balls representing gp120 and rods representing gp41. "F" represents the fusion peptide and "A" represents the transmembrane anchorage of gp41. Fusion proceeds temporally from left to right with (i) initial state, (ii) receptor binding and fusion peptide membrane insertion, (iii) gp41 conformational change, and (iv) membrane fusion. 3

Figure 3. Synthesis scheme for HFPmn and FP represents the sequence AVGIGALFLGFLGAAGSTMGARS. A black circle represents a resin bead, lines are drawn to clarify chemical functionalities, an arrow signifies a chemical reaction, and two arrows signify multiple sequential chemical reactions. All reactions were carried out at ambient temperature. Reaction **a**: Fmoc deprotection in 3 mL of 20% piperidine/DMF (v/v), 15 minutes/cycle, 2 cycles. Reaction **b:** Peptide synthesis with Fmoc chemistry. 2-hour single couplings were used for each amino acid with the following exceptions: 4-hour single couplings for Trp, Ser and Arg residues; 6-hour single couplings for the Leu-12 to Leu-7 residues. Reaction **c**: Cleavage from the resin using a 4 mL solution containing TFA/thioanisole/ethanedithiol/anisole in 90:5:3:2 volume ratio. After 2.5 hours reaction time, TFA was removed with nitrogen gas and peptide was precipitated with cold methyl t-butyl ether. 23

Figure 4. (a) The HPLC chromatograms for the purification of HFPmn. (b) The MALDI-TOF MS spectrum for the identification of HFPmn. The HPLC fraction marked with asterisk in (a) was analyzed and the corresponding mass was labeled using asterisk in (b). 24

Figure 5. Synthesis schemes for (a) HFPdm and (b) HFPdm(Cys). The black circles, lines and arrows had the same meaning as in Fig. 3. The reactions **a** and **c** were the same as in Fig. 3. In reaction **b**, the synthesis of HFPmn with Cys in (a) followed the coupling time in Fig. 3. For the HFPdm(Cys) synthesis in (b), 4-hour single couplings were used for each amino acid with the following

ex
ac
12
ra
Ly
Hf
Mt

Fig
HF
HF
we
and

Figu
the
in F
ope
solu

Figu
MA
bot
time
aste
aste

Figu
MA
mar
labe

Figu
≈2
mag
by o
shift

Figu
indic

exceptions: 8-hour single couplings for Trp, Ser, and Arg residues; double couplings with 4-hours per coupling for the ^{13}CO labeled residue and for the Leu-12 to Leu-7 residues. Reaction **d**: Coupling using PyAOP and DIPEA (1:2 molar ratio) in 4 mL DMF with 6 hour reaction times for Cys and 2 hour reaction time for Lys. Reaction **e**: Cross-linking in 5 mM DMAP, pH = 8.4, open to the air. 1 μmol HFPmn(Cys) in 400 μL solution overnight. Reaction **f**: Selective deprotection of Mtt in 3 mL of 1% TFA/DCM (v/v), 6 minutes/cycle, 6 cycles. 25

Figure 6. (a) and (c) The HPLC chromatograms for the purification of HFPdm and HFPdm(Cys). (b) and (d) The MALDI-TOF MS spectrum for the identification of HFPdm and HFPdm(Cys). The HPLC fraction marked with asterisk in (a) and (c) were analyzed and the corresponding peaks were labeled using asterisk in (b) and (d) respectively. The mass spectra were discussed in the main text. 26

Figure 7. Synthesis schemes for HFPtr. The black circles, lines and arrows had the same meaning as in Fig. 3. All reaction conditions were the same as shown in Fig. 3 and Fig. 5 except for reaction **e**: Cross-linking in 5 mM DMAP, pH = 8.4, open to the air. 1 μmol HFPmn(Cys) and 1.5 μmol HFPdm(Cys) in 400 μL solution for 2.5 hours. 27

Figure 8 (a) The HPLC chromatograms for the purification of HFPtr. (b) The MALDI-TOF MS spectrum for the identification of HFPtr. The top, middle, and bottom chromatograms in panel a are for syntheses with HFPtr cross-linking times of 0.5, 1.5, and 2.5 hours, respectively. The HPLC fraction marked with asterisk in (a) was analyzed and the corresponding peaks were labeled using asterisk in (b). The mass spectra were discussed in the main text. 28

Figure 9 (a) The HPLC chromatograms for the purification of HFPte. (b) The MALDI-TOF MS spectrum for the identification of HFPte. The HPLC fraction marked with asterisk in (a) was analyzed and the corresponding mass was labeled using asterisk in (b). 29

Figure 10 1D ^{13}C-^{15}N REDOR pulse sequence. The open columns represent the $\pi/2$ and π pulses. CP transfers ^{1}H transverse magnetization to ^{13}C. ^{13}C magnetization is dephased (i.e., reduced) by ^{13}C-^{15}N dipolar coupling mediated by one ^{15}N π pulse per rotor period. The ^{13}C π pulses refocus the ^{13}C chemical shift. 36

Figure 11 Double Cross Polarization (DCP) pulse sequence. CP1 and CP2 indicate the $^{1}H \rightarrow ^{15}N$ and $^{15}N \rightarrow ^{13}C$ cross polarization respectively. There is a

short delay τ between the first and second CP process. TPPM decoupling was applied during the τ, CP2 and acquisition periods. 45

Figure 12 $(\Delta S/S_0)^{exp}$ (error bars) and best-fit $(\Delta S/S_0)^{sim}$ (lines with or without diamonds) vs dephasing time (τ) for (a) the ^{13}C-^{31}P setup and (b) the ^{13}C-^{19}F setup. In panel (a) the experimental data was fit to a two-spin system. In panel (b), the experimental data was fit to either a two-spin system (dash line) or a three-spin system (solid line). 49

Figure 13 (a) ^{13}CO region of *D*-^{13}CO-NAL spectrum acquired using the CP pulse sequence. (b) ^{13}CO region of *D*-^{13}CO-NAL spectrum acquired using the DCP pulse sequence. The vertical scales in (a) and (b) are the same so that the relative intensity reflects the DCP transfer efficiency. Both spectra were processed with 100Hz Gaussian line broadening and baseline correction. (c) A negative control experiments without ^{15}N CP2 amplitude (c.f. Fig. 11). The number of scans used in (a), (b) and (c) was 32. Panel (d) displays the optimization of ^{15}N CP2 amplitude as given in Fig.11. The ^{15}N rf field was scanned from 11.8 kHz to 17.8 kHz with the increment of 0.16 kHz. Panel (e) displays the optimization of ^{15}N CP2 offset frequency. The offset was scanned from -10 kHz to 10 kHz with the increment of 0.5 kHz. 53

Figure 14 The aliphatic region of the 2D ^{13}C-^{13}C correlation spectra for (a) HFPmn in PC:PG, (b) HFPdm in PC:PG, (c) HFPtr in PC:PG, (d) HFPmn in PC:PG:CHOL, (e) HFPdm in PC:PG:CHOL and (f) HFPtr in PC:PG:CHOL. All spectra were processed with 100 Hz Gaussian line broadening in both dimensions. The individual peaks were assigned and given in the spectra. For example, the peak assigned to A6 Cβ/Cα(β) represent the cross peak between Cβ(f_1 dimension) and Cα(f_2 dimension) for Ala-6 in β-strand conformation. The spectra (g) through (l) display the representative 1D slice of the PDSD spectra (a) through (f) respectively. For the spectra (a), (c), (d), (e) and (f), the 1D slice is along ~23 ppm in the f_1 dimension which corresponds to the Cβ of Ala-6 in β-strand conformation. For the spectrum (b), the 1D slice is along ~18 ppm in the f_2 dimension which corresponds to the Cβ of Ala-6 in α-helical conformation. 61

Figure 15 ^{13}CO spectra of (a) Ala1, (b) Ile4, (c) Ala6, (d) Leu9, (e) Leu12 and (f) Ala14 in HFPmn_mut associated with PC:PG and PC:PG:CHOL. For each labeled residue, the spectrum with PC:PG is shown in the left and the spectrum with PC:PG:CHOL is shown in the right. ^{13}CO peaks of Ala15 in (g) HFPmn, (h) HFPdm and (i) HFPtr associated with PC:PG in the top row and PC:PG:CHOL in the bottom row. All spectra are obtained with the ^{13}C-^{31}P REDOR pulse sequence with 2 ms dephasing time, and processed with 200 Hz Gaussian line broadening and baseline correction. All PC:PG spectra are acquired with 3000

scans
dash

Figur
HFP
verti
Cα:C
CO:C
^{13}C-^{3}
left p
stran

Figur
rows
its co
Figur
d) H
obta
32 m
broa
4132
8185

Figu
samp
is: d
The

Figu
cons
and
used
Each
alwa
letter
and
X is
HFP
hydr
dista
= 6.

scans and all PC:PG:CHOL spectra are acquired with 1500 scans. The vertical dashed lines in (g)-(i) indicate the chemical shift of β-strand ^{13}CO. 72

Figure 16 (a) 1D slices along the chemical shift of Cγ of Leu12 for HFPmn, HFPdm and HFPtr in the top, middle and bottom spectrum respectively. The vertical dashed lines labeled 1-3 are assigned to the chemical shifts for CO/Cγ, Cα/Cγ and Cβ/Cγ cross peaks in helical conformation respectively, and 4-6 are CO/Cγ, Cα/Cγ and Cβ/Cγ cross peaks in strand conformation respectively. (b) ^{13}C-^{31}P REDOR S_0 spectra for Ala6 and Ala15 samples. In each spectrum, the left peak corresponds to α-helical structure and the right peak corresponds to β-strand structure. 73

Figure 17 Flow chart of derivation of $(\Delta S/S_0)^{cor}$ for REDOR of HFP-B. The four rows in each box are in sequence: the site description, its relative population, and its contributions to S_0 and S_1. 84
Figure 18 REDOR S_0 and S_1 spectra for membrane-associated (a, b) HFP-A, (c, d) HFP-B, (e, f) HFP-C, (g, h) HFP-D and (i, j) HFP-E. Spectra a, c, e, g, i were obtained with 24 ms dephasing time and spectra b, d, f, h, j were obtained with 32 ms dephasing time. Each spectrum was processed with 200 Hz Gaussian line broadening and baseline correction. Each S_0 or S_1 spectrum was the sum of (a) 41328, (b) 56448, (c) 45920, (d) 81460, (e) 55936, (f) 79744, (g) 30898, (h) 81856, (i) 45920 or (j) 71040 scans. 90

Figure 19 Plots of $(\Delta S/S_0)^{cor}$ vs dephasing time for membrane-associated HFP samples prepared with $[HFP]_{initial}$ of (a) 400 μM or (b) 25 μM. The symbol legend is: diamonds, HFP-B; triangles, HFP-C; circles, HFP-D; and squares, HFP-E. The σ^{cor} were ~0.04. 91

Figure 20 (a) Two antiparallel registries of residues 1-16 of HFP that were consistent with the REDOR data shown in Fig. 20. The registries are denoted *A* and *B* and the ^{13}CO labeled Ala-14 residue is highlighted in blue. (b) Models used to calculate $(\Delta S/S_0)^{sim}$ and spin geometries specific for the HFP-C sample. Each model includes nuclei from three adjacent strands with the Ala-14 ^{13}CO always in the middle strand and ^{15}N in the top and/or bottom strands. The first letter in the labeling of each model refers to the middle strand/top strand registry and the second letter refers to the middle strand/bottom strand registry. Registry *X* is any registry for which the interpeptide ^{13}CO-^{15}N distance was large in the HFP-H, HFP-I, HFP-J, or HFP-K samples so that $d \approx 0$. The Ala-14 ^{13}CO is hydrogen bonded to an amide proton in the top strand. Relevant labeled ^{13}C-^{15}N distances and ^{15}N-^{13}C-^{15}N angles are: r_1 = 4.063 Å; r_1' = 5.890 Å; r_2 = 5.455 Å; r_2' = 6.431 Å; θ_1 = 161.1°; θ_2 = 131.9°; θ_3 = 130.2°; and θ_4= 117.0°. Each

parameter value was the average of 10 specific values taken from the crystal structure of outer membrane protein G. 92

Figure 21 Contour plots of χ^2 vs strand fitting parameters for (a) unconstrained; (b) partially constrained; and (c) fully constrained fittings. The *a*, *b*, a^2, and b^2 parameters refer to probabilities for different adjacent strand arrangements. In plot a, the black, green, blue, red, and white regions respectively correspond to $\chi^2 < 19$, $19 < \chi^2 < 21$, $21 < \chi^2 < 23$, $23 < \chi^2 < 25$, and $\chi^2 > 25$. In plot b, the regions respectively correspond to $\chi^2 < 18$, $18 < \chi^2 < 20$, $20 < \chi^2 < 22$, $22 < \chi^2 < 24$, and $\chi^2 > 24$, and in plot c, the regions respectively correspond to $\chi^2 < 15$, $15 < \chi^2 < 17$, $17 < \chi^2 < 19$, $19 < \chi^2 < 21$, and $\chi^2 > 21$. Best-fit parameters were: **plot a**, $a = 0.22$, $b = 0.31$, $\chi^2 = 16.5$; **plot b**, $a = 0.31$, $b = 0.42$, $\chi^2 = 15.1$; and **plot c**, $a^2 = 0.26$, $b^2 = 0.33$, $\chi^2 = 12.7$. In plot a, the *a* and *b* parameters are the fractional probabilities of adjacent strands having *A* or *B* registries, respectively. In plot c, the a^2 and b^2 parameters are the fractional probabilities of domains of *A* or *B* registries, respectively. 97

Figure 22 Peptide sequences of the basic constructs of HFPmn_mut, HFPmn and HFPtr. The specific labeling sites were described in the main text. 110

Figure 23 Synthetic scheme of 5-F-palmitic acid. 115

Figure 24 (a) Plot of $(\Delta S/S_0)^{exp}$ vs mol fraction of 5-^{19}F-DPPC at $\tau = 16$ ms. All samples contained HFPmn-L9. (b) static ^{31}P spectra for PC:PG and PC:PG:CHOL bilayer with and without 9 mol fraction ^{19}F-DPPC. Each spectrum was acquired with 1024 scans and processed with 300 Hz Gaussian line broadening. The spectra were acquired at 35 °C. 118

Figure 25 Panel a displays stopped-flow monitored changes in lipid fluorescence induced by addition of different HFP constructs to an aqueous solution containing membrane vesicles. Increased fluorescence is a result of mixing of lipids between different vesicles and this mixing is one consequence of vesicle fusion. The lines are color coded: HFPmn (black); HFPdm (red); HFPtr (blue); and HFPte (green). The total lipid concentration was 150 μM and the HFPmn, HFPdm, HFPtr, and HFPte concentrations were 1.50, 0.75, 0.50, and 0.37 μM, respectively, so that peptide strand:lipid = 0.01. The data were collected at 25 °C, the vesicle composition was 4:1 POPC:POPG, and the initial vesicle diameter was ~100 nm. Additional data (not shown) were obtained for HFPdm, HFPtr, and HFPte at 30, 35, and 40 °C. Each data set for each construct was analyzed as the sum of two exponential buildup functions. Panel b displays Arrhenius plots for the rate constants of the fast buildup function with legend: HFPdm (open square);

HFPtr (open circle); and HFPte (open triangle). The best-fit lines are also displayed and result in the respective activation energies 41 ± 3, 26 ± 1, and 20 ± 1 kJ/mol. 122

Figure 26 S_0 spectra for membrane-associated HFP with peptide:lipid ~0.04. The dotted lines are at 175 ppm. All spectra were obtained with τ = 2 ms and were processed with 200 Hz Gaussian line broadening and baseline correction. The membrane composition for samples a-d was PC:PG and the membrane composition for samples e-h was PC:PG:CHOL. The peptides were: a, e, HFPmn-^{5}GAL; b, f, HFPmn-^{8}FLG; c, g, HFPmn-^{11}FLG; and d, h HFPmn-^{14}AAG. The numbers of scans summed to obtain spectra a-h were 4823, 3867, 4823, 8500, 3259, 1001, 4320 and 6992, respectively. 127

Figure 27 ^{13}CO-^{31}P REDOR spectra of membrane-associated HFP with peptide:lipid ~0.04. Each letter corresponds to a single sample which contained (a-d) PC:PG or (e-h) PC:PG:CHOL and (a, e) HFPmn-^{5}GAL, (b, f) HFPmn-^{8}FLG, (c, g) HFPmn-^{11}FLG, or (d, h) HFPmn-^{14}AAG. For each letter/sample, S_0 (left), S_1 (right), τ = 16 ms (top), and τ = 24 ms (bottom) spectra are displayed. The dotted lines are drawn for visual comparison of S_0 and S_1 peak intensities. Each spectrum was processed with 300 Hz Gaussian line broadening and baseline correction. The numbers of S_0 or S_1 scans summed to obtain the top and bottom spectra were respectively: a, 30000, 56000; b, 27509, 29463; c, 20000, 40000; d, 44129, 48296; e, 8448, 52384; f, 5488, 21664; g, 28032, 52384; and h, 22576, 50240. 131

Figure 28 ($\Delta S/S_0$) vs dephasing time for membrane-associated HFP in (a,c) PC:PG or (b,d) PC:PG:CHOL. For panels a and b, the points correspond to $(\Delta S/S_0)^{exp}$ and the symbol legend is: squares, HFP2-^{5}GAL; circles, HFP3-^{8}FLG; triangles, HFP2-^{11}FLG; and diamonds, HFP2-^{14}AAG. The vertical dimensions of each symbol approximately correspond to the ±1 σ uncertainty limits. Lines are drawn between $(\Delta S/S_0)^{exp}$ values with adjacent values of τ. Each $(\Delta S/S_0)^{exp}$ value was determined by integration of 10 ppm regions of the S_0 and S_1 spectra. Panels c and d respectively correspond to the HFPmn-^{14}AAG/PC:PG and the HFPmn-^{14}AAG/PC:PG:CHOL samples and the points correspond to $(\Delta S/S_0)^{lab}$ (vertical lines with error bars) and best-fit $(\Delta S/S_0)^{sim}$ (diamonds). Lines are drawn between points with adjacent τ values. For plot c, the best-fit d = 91 ± 8 Hz with corresponding r = 5.12 ± 0.16 Å, f = 0.45 ± 0.02, and χ^2_{min} = 5.0. For plot d, the best-fit d = 85 ± 6 Hz with corresponding r = 5.24 ± 0.13 Å, f = 0.32 ± 0.02, and χ^2_{min} = 3.8. 132

Figure 29 (a) Partial membrane insertion (PMI) and (b, c) full membrane insertion (FMI) models for antiparallel β strand HFP. The red arrows represent the A1 to

G
S2
dis
dis
dis
kn
are
the
ab
the
res

Fig
dif
32
mo
line
sca
exp

Fig
dis
bot
for

Fig
sam
con
the
(ΔS
±0

Figu
sam
sam
A6,
broa
the
HFp
For
othe
and

G16 residues in strand conformation and the black lines represent the S17 to S23 residues in random coil conformations. For clarity, black lines are not displayed in c. Lipids are represented in blue and grey and cholesterol is not displayed. Three antiparallel strands are displayed in a, b and twelve strands are displayed in c but the actual number of strands in the oligomer/aggregate is not known. The curvature and angle of the strands with respect to the bilayer normal are not known but the models consider that A1-G16 has ~55 Å length and that the transbilayer distance is ~48 Å. The experiments do not provide information about the membrane locations of residues S17 to S23. Relative to FMI model (b), the FMI β barrel variant (c) could have reduced energy because all of the residues in the membrane interior have backbone hydrogen bonds. 134

Figure 30 REDOR ^{13}C S_0 and S_1 NMR spectra for different labeled residues and different HFP constructs. The dephasing time for each ^{13}CO-^{31}P spectrum was 32 ms and for each ^{13}CO-^{19}F spectrum was 24 ms. The membranes contained 9 mol% 16-F-DPPC lipid. Each spectrum was processed with 200 Hz Gaussian line broadening and polynomial baseline correction and was the sum of ~30000 scans for ^{13}CO-^{31}P experiments and ~20000 scans for ^{13}CO-^{19}F experiments. 139

Figure 31 Summary of experimental REDOR dephasing $(\Delta S/S_0)^{exp}$ for the spectra displayed in Fig. 31. The top box in each panel is the ^{13}CO-^{31}P data and the bottom box is the ^{13}CO-^{19}F(C16) data. The $(\Delta S/S_0)^{exp}$ values are shown as bars for different labeled samples and a typical uncertainty is ±0.04. 141

Figure 32 ^{13}CO-^{31}P and ^{13}CO-^{19}F REDOR dephasing curves for different HFP samples labeled at (a, d) Ala1, (b, e) Ala6 or (c, f) Ala14. The membranes contained 9 mol% 16-F-DPPC lipid. The color coding of the constructs is given in the legend of panel b. For 2 ms dephasing time, the typical uncertainty in $(\Delta S/S_0)^{exp}$ is ±0.02 and for the other dephasing times, the typical uncertainty is ±0.04. 146

Figure 33 ^{13}C S_0 and S_1 NMR spectra from ^{13}CO-^{19}F REDOR experiments of samples made with 9 mol% 5-F-DPPC lipid. For panels a, b, c, d, and e the samples respectively contained HFPmn-A1, HFPmn-A6, HFPmn_mut-A6, HFPtr-A6, and HFPmn-L9. Each spectrum was processed with 200 Hz Gaussian line broadening and polynomial baseline correction. Each S_0 and S_1 spectrum was the sum of ~ 20000 scans. ^{13}CO-^{19}F(C5) REDOR dephasing curves for different HFPs are plotted in panel f and the constructs are coded as shown in the legend. For 2 ms dephasing time, the typical uncertainty in $(\Delta S/S_0)^{exp}$ is ±0.02 and for the other dephasing times, the typical uncertainty is ±0.04. In panel g the ^{13}C-^{19}F(C5) and ^{13}C-^{19}F(C16) spectra of HFPmn and HFPtr at 16 or 24 ms dephasing time

were
the r

Figu
Lipid
and
oligo
The
near
pepti
numt
linkin
the H

Figur
S_c ar
^{31}P e
right
respe
and b
3000
scans

Figure
depha
was c
corres
repres
the (1

Figure
differe
for I4,
circles
depha
The ty
uncert

Figure
depha
experi

were shown in the stack form with S_0 spectra on the left side and S_1 spectra on the right side. The dash lines reflect the intensities of the S_0 spectra. 147

Figure 34 Insertion models of β sheet (a) HFPmn_mut, (b) HFPmn, and (c) HFPtr. Lipid headgroups are drawn as blue balls, lipid alkyl chains are drawn in grey, and peptides are drawn in red. In all models, peptides are represented as oligomers with either six (HFPmn and HFPmn_mut) or two (HFPtr) molecules. The strands are in antiparallel β sheet structure with adjacent strand crossing near Phe8 and Leu9. This is the known structure for a large fraction of HFPmn peptides. The number of strands in a sheet is not known but is likely a small number. The lines at the C-terminus of HFPtr represent the chemical cross-linking of the HFPtr construct. For clarity, not all lipid molecules are shown near the HFP. 149

Figure 35 (a) ^{13}C-^{31}P REDOR S_0 spectra with 2 ms dephasing time. (b) REDOR S_0 and S_1 spectra for HFPmn_mut with long dephasing time (τ = 32 ms for ^{13}C-^{31}P experiments and τ = 24 ms for ^{13}C-^{19}F experiments). The left, middle and right columns in (b) are ^{13}C-^{31}P, ^{13}C-^{19}F(C5) and ^{13}C-^{19}F(C16) experiments respectively. All spectra were processed with 200 Hz Gaussian line broadening and baseline correction. In panel (b) each of the ^{13}C-^{31}P spectra was acquired for 30000 scans and each of the ^{13}C-^{19}F spectra was acquired for ~ 20000 scans. 159

Figure 36 Plots of $(\Delta S/S_0)^{exp}$ for HFPmn_mut ^{13}C-^{31}P experiments at 32 ms dephasing time and ^{13}C-^{19}F experiments at 24 ms. The experimental dephasing was obtained by integrating over a 1 ppm interval around the ^{13}CO peaks in the corresponding S_0 and S_1 spectra shown in Fig. 35. For Leu12, the black bar represents the $(\Delta S/S_0)^{exp}$ for α-helical conformation and the red bar represents the $(\Delta S/S_0)^{exp}$ for β-strand conformation. The typical uncertainty is ± 0.02. 160

Figure 37 (a) Plots of ^{13}C-^{31}P $(\Delta S/S_0)^{exp}$ vs. dephasing time for HFPmn_mut with different labeled positions. The symbols are open diamonds for A1, open squares for I4, open triangles for A6, crosses for L9, stars for the α-helical L12 and open circles for A14. (b) Plots of ^{13}C-^{31}P $(\Delta S/S_0)^{lab}$ (open squares) and $(\Delta S/S_0)^{sim}$ vs. dephasing time for different residues (as labeled in the figures) of HFPmn_mut. The typical experimental uncertainties are ±0.02-0.03 and the typical corrected uncertainties are ±0.03-0.04. 163

Figure 38 REDOR S_0 and S_1 spectra for (a) HFPmn and (b) HFPtr at long dephasing time (τ = 32 ms for ^{13}C-^{31}P experiments and τ = 24 ms for ^{13}C-^{19}F experiments). The S_0 and S_1 spectra were shown in black and red respectively.

All sp
correc
spectr

Figure
and (c
strand
the op
of (ΔS
symbo
interva
S. spe

Figure
measu
measu
triangl
distanc
of $^{31}P_{-}$
circle f
region
Leu12
longitu
^{19}F(C5

Figure
the de
and β-
and at
(ΔS/S
^{13}C-^{19}F
region
green
given i

Figure
HFPtr
for ^{13}C
respec
and ba
and th
^{13}C-^{19}F

All spectra were processed with 200 Hz Gaussian line broadening and baseline correction. The ^{13}C-^{31}P spectra were acquired for ~ 30000 scans and the ^{13}C-^{31}P spectra were acquired for ~ 20000 scans. 166

Figure 39 Plots of $(\Delta S/S_0)^{exp}$ vs. dephasing time for the (a) ^{13}C-^{31}P, (b) ^{13}C-^{19}F(C5) and (c) ^{13}C-^{19}F(C16) experiments for HFPmn and HFPtr in the α-helical and β-strand conformations. The residues Ala6, Leu9 and Leu12 are represented with the open squares, open circles and open triangles respectively. The uncertainties of $(\Delta S/S_0)^{exp}$ are typically ±0.02 ~ 0.03 and are approximately the size of the symbols. The $(\Delta S/S_0)^{exp}$ values were determined by integrating over a 1 ppm interval around the α-helical or β-strand ^{13}CO peaks in the corresponding S_0 and S_1 spectra. 168

Figure 40 (a) Geometry Model for the consideration of ^{13}C-^{31}P and ^{13}C-^{19}F measurement limit. The two circles with 11 Å and 14 Å radii indicate the measurement limits of ^{13}C-^{31}P and ^{13}C-^{19}F(C16) REDOR respectively. The yellow triangle shows the geometry of the case where a ^{13}CO has the maximum vertical distance (3.5 Å) relative to the lipid alkyl chain. (b) and (c) Longitudinal positions of ^{31}P, ^{19}F(C5) and ^{19}F(C16) in the membrane bilayer. In panel (b), the dotted circle has the radius of ~ 10 Å and the solid circle has the radius of ~ 14 Å. The region marked in red indicates the possible location of the ^{13}COs of Ala6 and Leu12 in the β-strand HFPmn as described in the main text. In panel (c), the longitudinal distance between ^{31}P and ^{19}F(C5) is 10 Å and the distance between ^{19}F(C5) and ^{19}F(C16) is 12 Å. 173

Figure 41 (a)-(d) Plot of $(\Delta S/S_0)^{lab}$ (open squares) and $(\Delta S/S_0)^{sim}$ (solid lines) vs. the dephasing time for Ala6, Leu9 and Leu12 in HFPmn and HFPtr with α-helical and β-strand conformations. The data with $(\Delta S/S_0)^{lab} < 0.1$ at 32 ms for ^{13}C-^{31}P and at 24 ms for ^{13}C-^{19}F(C16) were not fit and were labeled "N/A". (e) Plots of $(\Delta S/S_0)^{lab}$ (open squares) and $(\Delta S/S_0)^{sim}$ (solid lines) vs. the dephasing time for ^{13}C-^{19}F(C5) experiments. (f) Contour plots for the data fittings shown in (e). The regions with χ^2 values χ^2_{min} +1, χ^2_{min} +2 and χ^2_{min} +3 were shown in red, blue and green respectively, where χ^2_{min} is the best-fit root-mean-squared deviation as given in Table 13 of the main text. 177

Figure 42 REDOR S_0 and S_1 spectra for Ala1, Ile4 and Ala14 in HFPmn and HFPtr at long dephasing time (τ = 32 ms for ^{13}C-^{31}P experiments and τ = 24 ms for ^{13}C-^{19}F experiments). The S_0 and S_1 spectra are shown in black and red respectively. All spectra were processed with 200 Hz Gaussian line broadening and baseline correction. The ^{13}C-^{31}P spectra were acquired for ~ 30000 scans and the ^{13}C-^{31}P spectra were acquired for ~ 20000 scans. The arrows indicate ^{13}C-^{19}F(C5) dephasing for Ile4 and Ala14. 185

Figure 43 F
(open circle
calculated b
S_1 spectra. .

Figure 44 I
secondary s
chains were
were shown
were displa
terminus. ....

Figure 43 Plots of $(\Delta S/S_0)^{exp}$ vs. dephasing time for Ala1(open squares), Ile4 (open circles) and Ala14 (open triangles) labeled samples. The dephasing was calculated by integrating over the entire ^{13}CO peaks in the corresponding S_0 and S_1 spectra. 186

Figure 44 Insertion models for HFPmn_mut, HFPmn and HFPtr and different secondary structures. The lipid headgroups were shown in blue and the alkyl chains were displayed in gray. For the peptides, the residues from Ala6 to Leu12 were shown in red with definitive secondary structures and the other residues were displayed in black. The arrows indicated the direction from N to C terminus. 188

AH

AIE

AL

CD

CH

CH

CP

CS

D:

d:

DC

DIP

DM

DM

DP

1-

DTP

DTP

ESR

FM

Fmo

LIST OF SYMBOLS AND ABBREVIATIONS

AHT: Average Hamiltonian Theory

AIDS: Acquired Immune Deficiency Syndrome

AUC: Analytical Ultracentrifugation

CD: Circular Dichroism

CHOL: cholesterol

CHR: C-terminal heptad repeat

CP: Cross Polarization

CS: Chemical Shift

D: Dipolar Coupling

d: Dipolar coupling frequency

DCP: Double Cross Polarization

DIPEA: *N, N*-diisopropylethylamine

DMAP: dimethylaminopyridine

DMPC: 1, 2-dimyristoyl-*sn*-glycerol-3-phosphocholine

DPC: dodecylphosphocholine

1-^{13}C-DPPC: [1-^{13}C]-1, 2-dipalmitoyl-*sn*-glycero-3-phosphocholine

DTPC: 1, 2-di-*O*-tetradecyl-*sn*-glycerol-3-phosphocholine

DTPG: 1, 2-di-*O*-tetradecyl-*sn*-glycerol-3-[phosphor-*rac*-(1-glycerol)]

ESR: Electron Spin Resonance

FMI: Full Membrane Insertion

Fmoc: 9-fluorenylmethoxycarbonyl

HBTU: O

HEPES:

HFP: HIV

HFPdm: I

HFPmn: I

HFPmn_r

HFPte: HI

HFPtr: HF

HIV: Hum

HOBt: 1-h

HPLC: Hig

IR: Infrare

LUVs: Larg

MALDI: Ma

MAS: Mag

MD: Molec

NAL: N-ac

N-NBD-PE

NHR: N-te

NMR: Nucl

NOE: Nucle

N-Rh-PE: N

OMPG: out

HBTU: *O*-benzotriazole-N,N,N',N'-tetramethyl-uronium-hexafluoro-phosphate

HEPES: *N*-(2-hydroxyethyl)piperazine-*N'*-2-ethanesulfonic acid

HFP: HIV Fusion Peptide

HFPdm: HFP dimer

HFPmn: HFP monomer

HFPmn_mut: HFP monomer with V2E mutation

HFPte: HFP tetramer

HFPtr: HFP trimer

HIV: Human Immunodeficiency Virus

HOBt: 1-hydroxybenzotriazole

HPLC: High-performance liquid cheomotography

IR: Infrared

LUVs: Large Unilamellar Vesicles

MALDI: Matrix-assisted laser desorption/ionization

MAS: Magic Angle Spinning

MD: Molecular Dynamics

NAL: *N*-acetyl-Leucine

N-NBD-PE: *N*-(7-nitro-2,1,3-benzoxadiazol-4-yl)-phosphatiylethanolamine

NHR: N-terminal heptad repeat

NMR: Nuclear Magnetic Resonance

NOE: Nuclear Overhauser Effect

N-Rh-PE: N-(lissamine Rhodamine B sulfonyl)-phosphatiylethanolamine

OMPG: outer membrane protein G

PAS: Principle Axis System

PDB: Protein Data Bank

PyAOP: 7-azabenzotriazol-1-yloxy-tris-(pyrrolidino)-phosphonium Hexafluorophosphate

PMI: partial membrane insertion

PDSD: Proton-driven Spin Diffusion

POPC: 1, 2-dimyristoyl-*sn*-glycerol-3-phosphocholine

POPG: 1, 2-dimyristoyl-*sn*-glycerol-3-[phosphor-*rac*-(1-glycerol)]

REDOR: Rotational-echo Double Resonance

RMSD: root-mean-asquared deviation

r: internuclear distance

rf: radiofrequency

SDS: sodium dodecyl sulfate

SUL: "scatter-uniform" labeling

TFA: trifluoroacetic acid

TOF: time-of-flight

TPPM: Two-pulse phase modulation

CHAPTER I

INTRODUCTION

BACKGROUND

Membrane fusion is an important step in viral infection for widespread and serious diseases such as influenza and acquired immune deficiency syndrome (AIDS).*(1-2)* Understanding of viral fusion is thus important both as a key step in the viral life cycle and as a target for anti-viral therapeutics.*(3-5)* Fusion between two membrane-bound bodies such as cells, viruses or vesicles is a protein-mediated process and is generally separated into three sequential steps: (1) binding of the two bodies; (2) mixing of their membrane lipids; (3) formation of a large fusion pore through which the contents of virus and cell can mix.*(6)* Figure 1 illustrates a series of freeze-fracture electron micrographs that follows the time evolution of human immunodeficiency virus (HIV) infection of a host cell.*(7)*

In AIDS, fusion and infection are initialized by strong interactions of two highly glycosylated viral envelope proteins gp120 and gp41 with the CD4 and chemokine (e.g. CXCR4) receptors of human T and macrophage cells.(*1*) The glycosylation of gp120 is extensive with glycans representing 50% of the molecular mass of the mature protein.(*8*) The glycosylation of gp41 is less abundant relative to gp120, and there are only four or five potential glycosylation sites.(*9-12*) However, these potential sites have been thought to be a requirement for the fusion activity of gp41.(*13*) The proteins gp120 and gp41 are

Figure
to hos
pore a
the hos

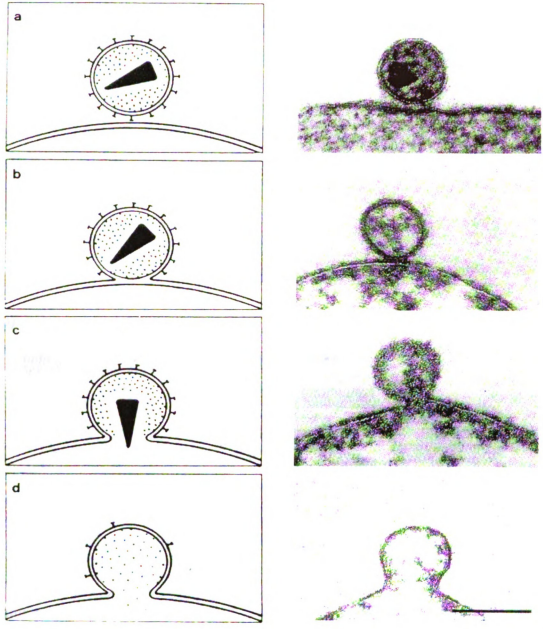

Figure 1 Model (left) and Electron Microscopy (right) of the HIV virus (a) binding to host cell (b) fusion of viral and host cell membranes (c, d) formation of large pore and infection of host cell. The triangle represents the viral RNA that enters the host cells. (Adapted from Reference 7)

(a)

(b)

Figure
from R
gp120
repres
transm
with (i)
(iii) gp
Refere

(a)

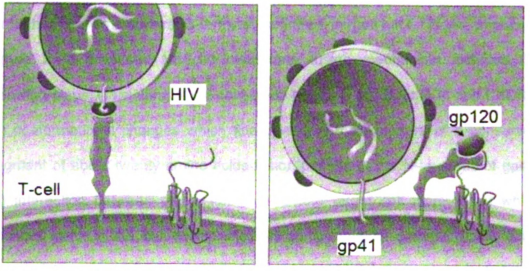

(b)

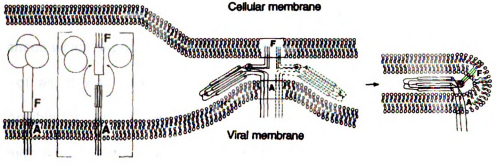

Figure 2 (a) Model of HIV infection. The time sequence is left to right. (Adapted from Reference 16) (b) Model for HIV/host cell fusion. In the left-most figure, a gp120/gp41 trimer is displayed with the balls representing gp120 and rods representing gp41. "F" represents the fusion peptide and "A" represents the transmembrane anchorage of gp41. Fusion proceeds temporally from left to right with (i) initial state, (ii) receptor binding and fusion peptide membrane insertion, (iii) gp41 conformational change, and (iv) membrane fusion. (Adapted from Reference 17)

non-

throu

Figu

follo

(2) c

segn

(3) i

anch

doma

bring

forma

evide

First

respo

althou

not we

gp120

extend

repeat

the ext

associa

fusion

peptide

non-covalently bound to form a complex and the complex is attached to the HIV through a transmembrane C-terminal segment in gp41.*(14,15)* As shown in Figure 2, a proposed HIV/cell membrane fusion mechanism includes the following steps: (1) binding of the conserved region in gp120 to CD4 and CXCR4; (2) conformational changes which finally lead to the exposure of a conserved segment of about twenty amino acids fusion peptide at the N-terminus of gp41; (3) interaction between the fusion peptide and target cell membranes which anchors gp41 in the cell membrane; (4) conformational change of the ecto-domain of gp41 which locates outside of the viral and cell membranes helps to bring the HIV and cell membranes close together; (5) mixing of lipids and formation of large fusion pores.*(16,17)* There were various experimental evidences which supported the different steps of the mechanism proposed above. First of all, it was known that conserved regions in the gp120 subunit are responsible for the binding of the virus to the CD4 and CXCR4.*(14,15)* Second, although the conformational change of gp120 after binding to the receptor was not well understood, the extended conformation of gp41 after the releasing of gp120 was characterized and there have been antibodies which can bond to the extended and exposed N-terminal heptad repeat (NHR) and C-terminal heptad repeat (CHR) segments.*(2,18-23)* In addition, the conformational change from the extended gp41 was supported by the fact that gp41 folded back on itself and associated as very stable six-helical-bundle structure, which was observed at the fusion sites.*(24-26)* However, the interaction between the N-terminal fusion peptide and the cell membranes was not clear at this point.

In our studies, the HIV Fusion peptide (HFP) sequence contains 23 native amino acids: Ala-Val-Gly-Ile-Gly-Ala-Leu-Phe-Leu-Gly-Phe-Leu-Gly-Ala-Ala-Gly-Ser-Thr-Met-Gly-Ala-Arg-Ser. These residues are located at the N-terminus of the HIV gp41. The hydrophobic amino acids such as Val, Phe and Leu are in great abundance in the HFP sequence and are also highly conserved in the analogs of HFP such as the fusion peptides of the glycoproteins in HIV-II and SIV.(*27, 28*) In the following chapters, HFP and its derivatives will serve as model peptides of the gp41 in the investigation of structure and membrane insertion. The HFPs are reasonable substitution for gp41 because (1) in the absence of the rest part of gp41, the HFP itself can cause rapid fusion and/or leakage of lipid vesicles or erythrocytes, and (2) several mutational studies have shown strong correlations between FP-induced fusion and viral/host cell fusion.*(29-32)*

The secondary structure of the micelle-associated HFP has been probed using solution Nuclear Magnetic Resonance (NMR) in both sodium dodecyl sulfate (SDS) or dodecylphosphocholine (DPC) micelles.(*33-38*) The secondary and tertiary structures are obtained from chemical shifts and nuclear Overhauser effect (NOE) crosspeaks.(*39,40*) For HFP:detergent ~0.01, solution NMR results suggested the presence of helical structure from Ile4 to Leu12 in negatively charged SDS or neutral DPC micelles.(*33,36-38*) However, different solution NMR studies suggested there may be additional helical, β-turn or more disordered and dynamic structures in the C-terminus of HFP.*(33-38)* Structure of HFP associated with membranes has been studied using circular dichroism (CD) or infrared (IR) spectroscopy. A previous CD measurement showed that the HFP

adop

nega

signif

vesic

predo

struc

inves

the p

the

differ

lipid c

factor

the lo

solutio

simula

HFP

suppo

HFP-(

fully sh

interfac

HFP-Fg

with ch

adopted a significant helical character in SDS detergent or in an environment of negatively charged vesicles with a 1:200 peptide:lipid molar ratio,*(33,41-43)* but a significant β-strand character in 1:30 peptide:lipid ratio.*(41)* With neutral lipid vesicles at peptide:lipid molar ratios of ~ 1:200, there are two infrared reports of predominantly helical structure,*(43,44)* three reports of predominantly β structure,*(41,45,46)* and one report of mixed helical and β structure.*(47)* Two investigators report that the peptide conformation changes from helical to β as the peptide:lipid ratio is increased from 1:200 to 1:30 while two others report that the β conformation does not change with these ratios.*(41,43-45)* There differences in structure may have to do with differences in peptide sequence, lipid compositions, sample preparation, or hydration level.*(48)*

The membrane location of HFP has been suggested as an important factor to understand the peptide/membrane interaction. Previous studies about the location of HFP in micelles and/or membranes have been performed using solution NMR, fluorescence spectroscopy, electron spin resonance (ESR) and simulation. Unfortunately, there is not yet a consensus for the micelle location of HFP based on the solution NMR results. There are distinct models which supported either predominant micelle surface location or micelle traversal by HFP.(*33, 37*) In one solution NMR study, residues I4 to A15 were found to be fully shielded from solvent and residues G3 and G16 were at the micelle/solvent interface.*(37)* HFP location in membranes has been primarily probed using a HFP-F8W mutant and by variation of the tryptophan fluorescence of this mutant with changes in environment.*(49,50)* Key results have included: (1) fluorescence

was

sal

for

simi

obs

bro

bro

solv

ass

tryp

lipid

phos

loca

away

been

have

alwa

gene

respe

differ

sidec

longit

was higher for membrane-associated HFP-F8W than for HFP-F8W in buffered saline solution; (2) greater fluorescence quenching by acrylamide was observed for a soluble tryptophan analog than for membrane-associated HFP-F8W; and (3) similar fluorescence quenching of membrane-associated HFP-F8W was observed in samples containing either 1-palmitoyl-2-stearoyl-phosphocholine brominated at the 6, 7 carbons of the stearoyl chain or the corresponding lipid brominated at the 11, 12 carbons of the chain. The first two results indicated that solvent exposure of the HFP-F8W tryptophan is reduced with membrane association and the third result indicated that the membrane location of the tryptophan indole group is centered near the carbon 9 position of the brominated lipid stearoyl chain; i.e. ~8.5 Å from the bilayer center and ~11 Å from the lipid phosphorus. In a different set of experiments, ESR spectra showed that a M19 location close to the aqueous interface of the membrane and an A1 location away from this interface.*(43)* Models for HFP location in membranes have also been developed from simulations of a single HFP molecule in membranes and have shown either partial insertion or traversal of the membrane. The HFP always adopted predominant α helical conformation and in one simulation was generally near the membrane surface with the F8 backbone and sidechain nuclei respectively 4 Å and 6 Å deeper than the phosphorus longitude.*(51)* For a different simulation, HFP traversed the membrane and the backbone and sidechain F8 nuclei were at the bilayer center, i.e. ~19 Å from the phosphorus longitude.*(52)*

The current studies mainly utilized solid-state NMR to investigate the structures as well as the membrane location of HFPs. Without the need for crystallization or solvation, solid-state NMR is a useful method to probe membrane associated peptide/protein systems. Measurements of chemical shifts and internuclear dipolar couplings provide information about the secondary structure, tertiary structure, insertion depths and insertion angles of HFPs associated with membranes. Some of the important results obtained previously in our group include: (1) Helical, β strand and random coil structure were observed at specific residues in HFP and the distribution of the conformations at specific residues was shown to depend on the lipid headgroup and cholesterol composition of the membrane.(*53-57*) HFP was also shown to fuse vesicles with different compositions, which suggests that more than one conformation is fusogenic.*(58)* (2) Measurements of dipolar couplings between different HFPs showed that the β strand structure is oligomeric and contains interpeptide hydrogen bonding. There may be approximately equal populations of parallel and antiparallel strand alignment. The adjacent strand in the parallel alignment may be two residues out-of-registry and the adjacent strands in the antiparallel alignment are crossing between F8 and L9.*(59,60)*

The present work will mainly focus on the solid-state NMR studies of the structure and insertion depth of membrane-associated HFP oligomers, which will contribute to understand the question about which characters of HFP may be closely associated with fusion activities. In Chapter II the synthesis of biological relevant HIV fusion peptide constructs will be described. In particular, the

experiment

proposed a

introduce th

HFP syste

(REDOR).

(DCP) exp

Theory (AH

and the set

studies of

especially th

will report t

membrane

sheet for a

with the ove

will describe

constructs:

membranes

disruption of

HFP constru

conclusion is

experimental conditions for the synthesis of HFP trimer (HFPtr), which has been proposed as a HFP construct at the fusion site, will be discussed. Chapter III will introduce the solid-state NMR methods used to study the membrane-associated HFP system, including ^{13}C-^{31}P and ^{13}C-^{19}F rotational-echo double resonance (REDOR), proton-driven spin diffusion (PDSD), and double cross polarization (DCP) experiments. The theoretical approach named Average Hamiltonian Theory (AHT) for understanding these pulse sequences will be briefly introduced and the setup procedure will be described in details. Chapter IV will focus on the studies of the secondary structure of membrane-associated HFP constructs; especially the dependence on lipid compositions and HFP constructs. Chapter V will report the tertiary structure of HFP monomer (HFPmn) in a host-cell-like membrane. The results in this chapter revealed the existence of anti-parallel β-sheet for a membrane-associated HFPmn construct and two preferred registries with the overlapping of most N-terminal hydrophobic residues. Finally, chapter VI will describe the studies about the membrane insertion of three different HFP constructs: V2E mutated HFPmn (HFPmn_mut), HFPmn and HFPtr in membranes both with and without cholesterol. It has been concluded that both disruption of membrane caused by HFP insertion and fusion activities of these HFP constructs followed the trend HFPmn_mut < HFPmn < HFPtr, and the conclusion is independent on the secondary structure of the peptide.

REFERENCE

1. Eckert, D.M.; Kim, P.S., Mechanisms of Viral Membrane Fusion and its Inhibition. *Annu Rev Biochem* **2001**, 70, 777-810.

2. Piel, J., The Science of AIDS. **1998**.

3. Wild, C. T.; Shugars, D. C.; Greenwell, T. K.; McDanal, C. B.; Matthews, T. J., Peptides corresponding to a predictive alpha-helical domain of human immunodeficiency virus type 1 gp41 are potent inhibitors of virus infection. *Proc Natl Acad Sci U S A* **1994,** 91, (21), 9770-4.

4. Kilby, J. M.; Hopkins, S.; Venetta, T. M.; DiMassimo, B.; Cloud, G. A.; Lee, J. Y.; Alldredge, L.; Hunter, E.; Lambert, D.; Bolognesi, D.; Matthews, T.; Johnson, M. R.; Nowak, M. A.; Shaw, G. M.; Saag, M. S., Potent suppression of HIV-1 replication in humans by T-20, a peptide inhibitor of gp41-mediated virus entry. *Nat Med* **1998,** 4, (11), 1302-7.

5. Kilby, J. M., Lalezari, J.P., Eron, J.J., Carlson, M., Cohen, C., Arduino, R.C., Goodgame, J.C., Gallant, J.E., Volberding, P., Murphy, R.L., Valentine, F., Saag, M.S., Nelson, E.L., Sista, P.R., and Dusek, A., The safety, plasma pharmacokinetics, and antiviral activity of subcutaneous enfuvirtide (T-20), a peptide inhibitor of gp41-mediated virus fusion, in HIV-infected adults. *Aids Res. Hum. Retrovir.* **2002,** 18, 685-693.

6. Hernandez, L. D.; Hoffman, L. R.; Wolfsberg, T. G.; White, J. M., Virus-cell and cell-cell fusion. *Annu. Rev. Cell. Dev. Biol.* **1996,** 12, 627-661.

7. Grewe, C.; Beck, A.; Gelderblom, H. R., HIV: early virus-cell interactions. *J Acquir Immune Defic Syndr* **1990,** 3, (10), 965-74.

8. Geyer, H.; Hoischbach, C.; Hunsmann, G.; Schneider, J., Carbohydrates of human immunodeficiency virus. *J. Biol. Chem.* **1988**, 263, 11760-11767.

9. Chakrabarti, L.; Guyader, M; Sonigo, P. Sequence of simian immunodeficiency virus from macaque and its relationship to other human and simian retroviruses. *Nature* **1987**, 328, 543-547.

10. Dedera, D.A.; Gu, R.; Ratner, L. Role of asparagine linked glycosylation in human immunodeficiency virus type I transmembrane envelop function. Virology 1992, 187, 377-382.

11. Fenouillet, E.; Jones, I.M.; Gluckman, J.C., Functional role of the glycan cluster of the human immunodeficiency virus type 1 transmembrane glycoprotein (gp41) ectodomain. *J. Virol.*, **1993**, 67, 150-160.

12.
glyc
179

13.
the
glyc

14.
and
LES

15.
Aren
Loet
ligan
Natu

16.
Atom
426-

17.
Mem
Sequ
Jour

18.
immu
viral

19.
Dilati
pore
Biol.

20.
confo

21.
(6442

22.
immu
of gp

12. Lee, W.R.; Yu, X.F.; Lee, T.H., Mutational analysis of conserved N-linked glycosylation sites of human immunodeficiency type 1 gp41. *J. Virol.* **1992**, 66, 1799-1803.

13. Perrin, C.; Fenouillet, E.; Jones, I. M., Role of gp41 glycosylation sites in the biological activity of Human Immunodeficiency virus type 1 envelope glycoprotein. *Virology* **1998**, 242, 338-345.

14. Bleul, C. C., Farzan, M., Choe, H., parolin, C., ClarkLewis, I., Sodroski, J., and Springer, T.A., The lymphocyte chemoattractant SDF-1 is a ligand for LESTR/fusin and blocks HIV-1 entry. *Nature* **1996,** 382, 829-833.

15. Oberlin, E., Amara, A., Bachelerie, F., Bessia, C., Virelizier, J.L., ArenzanaSeisdedos, F., Schwartz, O., Heard, J.M., ClarkLewis, I., Legler, D.F., Loetscher, M., Baggiolini, M., and Moser, B., The CXC chemokine SDF-1 is the ligand for LESTR/fusin and prevents infection by T-cell-line-adapted HIV-1. *Nature* **1996,** 382, 833-835.

16. Weissenhorn, W.; Dessen, A.; Harrison, S. C.; Skehel, J. J.; Wiley, D. C., Atomic structure of the ectodomain from HIV-1 gp41. *Nature* **1997,** 387, (6631), 426-430.

17. Murata, M.; Sugahara, Y.; Takahashi, S.; Ohnishi, S., Ph-Dependent Membrane-Fusion Activity of a Synthetic 20 Amino-Acid Peptide With the Same Sequence As That of the Hydrophobic Segment of Influenza-Virus Hemagglutinin. *Journal of Biochemistry* **1987,** 102, (4), 957-962.

18. Wild, C., and Oas, T., A synthetic peptide inhibitor of human immunodeficiency virus replication: correlation between solution structure and viral inhibition. *Proc. Natl. Acad. Sci. USA* **1992,** 89, (21), 10537-10541.

19. Munoz-Barroso, I.; Durell, S.; Sakaguchi, K.; Appella, E.; Blumenthal, R., Dilation of the human immunodeficiency virus-1 envelope glycoprotein fusion pore revealed by the inhibitory action of a synthetic peptide from gp41. *J. Cell Biol.* **1998,** 140, (2), 315-323.

20. Furata, R. A., and Wild, C.T., Capture of an early fusion-active conformation of HIV-1 gp41. *Nat. Struct. Biol.* **1998,** 5, (4), 276-279.

21. Jiang, S., and Lin, K., HIV-1 inhibition by a peptide. *Nature* **1993,** 365, (6442), 113.

22. Chen, C. H., and Matthews, T.J., A molecular clasp in the human immunodeficiency virus (HIV) type 1 TM protein determines the anti-HIV activity of gp41 derivatives: implication for viral fusion. *J. Virol.* **1995,** 69, (6), 3771-3777.

23.
fus
27

24.
68

25
Wil
Pro

26.
prot
Bio

27.
fusc
imm

28.
J.M.
pept

29.
stud
mem

30.
Mem
Prot

31.
Biop

32.
fusio

33.
doma
sodiu
the m

34.
Intera
Confo
Biol.

23. Bewley, C. A., and Louis, J.M., Design of a novel peptide inhibitor of HIV fusion that disrupts the internal trimeric coiled-coil of gp41. *J. Biol. Chem.* **2002,** 277, (16), 14238-14245.

24. Chan, D. C., and Kim, P.S., HIV entry and its inhibition. *Cell* **1998,** 93, (5), 681-684.

25. Weissenhorn, W.; Dessen, A.; Calder, L. J.; Harrison, S. C.; Skehel, J. J.; Wiley, D. C., Structural basis for membrane fusion by enveloped viruses [In Process Citation]. *Mol Membr Biol* **1999,** 16, (1), 3-9.

26. Schibli, D. J., and Weissenhorn, W., Class I and Class II viral fusion protein structures reveals similar principles in membrane fusion. *Mol. Membr. Biol.* **2004,** 21, (6), 361-371.

27. Steffy, K.R.; Kraus, G., Looney, D.J., Wong-Staal, F., Role of the fusogenic peptide sequence in syncytium induction and infectivity of human immunodeficiency virus type 2. *J. Virol.* **1992**, 66(7), 4532-4535.

28. Horth, M.; Lambrecht, B.; Khim, M.C.; Bex, F.; Thiriart, C.; Ruysschaert, J.M., Burny, A., Brasseur, R. Theoretical and functional analysis of the SIV fusion peptide. *EMBO J.* **1991**, 10(10), 2747-2755.

29. Durell, S. R.; Martin, I.; Ruysschaert, J. M.; Shai, Y.; Blumenthal, R., What studies of fusion peptides tell us about viral envelope glycoprotein-mediated membrane fusion. *Mol. Membr. Biol.* **1997,** 14, (3), 97-112.

30. Pecheur, E.; Sainte-Marie, J.; Bienvenue, A.; Hoekstra, D., Peptides and Membrane Fusion: Towards an Understanding of the Molecular Mechanism of Protein-Induced Fusion. *J Membr Biol* **1999,** 167, (1), 1-17.

31. Epand, R. M., Fusion peptides and the mechanism of viral fusion. *Biochim. Biophys. Acta-Biomembr.* **2003,** 1614, (1), 116-121.

32. Nieva, J. L.; Agirre, A., Are fusion peptides a good model to study viral cell fusion? *Biochim. Biophys. Acta-Biomembr.* **2003,** 1614, (1), 104-115.

33. Chang, D. K.; Cheng, S. F.; Chien, W. J., The amino-terminal fusion domain peptide of human immunodeficiency virus type 1 gp41 inserts into the sodium dodecyl sulfate micelle primarily as a helix with a conserved glycine at the micelle-water interface. *J. Virol.* **1997,** 71, (9), 6593-6602.

34. Vidal, P.; Chaloin, L.; Heitz, A.; Van Mau, N.; Mery, J.; Divita, G.; Heitz, F., Interactions of primary amphipathic vector peptides with membranes. Conformational consequences and influence on cellular localization. *J. Membr. Biol.* **1998,** 162, (3), 259-264.

35.
inse
type
resi

36.
fusi
spe

37.
Win
imm
161

38.
Stru
Dod

39.
refe

40.
411-

41.
synt
29. (

42.
Fusi
phos
Biol.

43.
Wari
huma
aggre

44.
fusion
extre
298-3

45.
fusion

35. Chang, D. K.; Cheng, S. F., Determination of the equilibrium micelle-inserting position of the fusion peptide of gp41 of human immunodeficiency virus type 1 at amino acid resolution by exchange broadening of amide proton resonances. *J. Biomol. NMR* **1998,** 12, (4), 549-552.

36. Morris, K. F.; Gao, X. F.; Wong, T. C., The interactions of the HIV gp41 fusion peptides with zwitterionic membrane mimics determined by NMR spectroscopy. *Biochim. Biophys. Acta-Biomembr.* **2004,** 1667, (1), 67-81.

37. Jaroniec, C. P.; Kaufman, J. D.; Stahl, S. J.; Viard, M.; Blumenthal, R.; Wingfield, P. T.; Bax, A., Structure and dynamics of micelle-associated human immunodeficiency virus gp41 fusion domain. *Biochemistry* **2005,** 44, (49), 16167-16180.

38. Gabrys, C. M., and Weliky, D.P., Chemical Shift Assignment and Structural Plasticity of a HIV Fusion Peptide Derivative in Dodecylphosphocholine Micelles. *BBA-Biomembranes* **2007,** 1768, 3225-3234.

39. Zhang, H. Y.; Neal, S.; Wishart, D. S., RefDB: A database of uniformly referenced protein chemical shifts. *J. Biomol. NMR* **2003,** 25, (3), 173-195.

40. Overhauser, A.W., Polarization of Nuclei in Metals. *Phys. Rev.* **1953**, 92(2) 411-415.

41. Rafalski, M.; Lear, J. D.; DeGrado, W. F., Phospholipid interactions of synthetic peptides representing the N-terminus of HIV gp41. *Biochemistry* **1990,** 29, (34), 7917-7922.

42. Kliger, Y.; Aharoni, A.; Rapaport, D.; Jones, P.; Blumenthal, R.; Shai, Y., Fusion peptides derived from the HIV type 1 glycoprotein 41 associate within phospholipid membranes and inhibit cell-cell Fusion. Structure- function study. *J. Biol. Chem.* **1997,** 272, (21), 13496-13505.

43. Gordon, L. M.; Curtain, C. C.; Zhong, Y. C.; Kirkpatrick, A.; Mobley, P. W.; Waring, A. J., The amino-terminal peptide of HIV-1 glycoprotein 41 interacts with human erythrocyte membranes: peptide conformation, orientation and aggregation. *Biochim. Biophys. Acta* **1992,** 1139, (4), 257-274.

44. Martin, I.; Schaal, H.; Scheid, A.; Ruysschaert, J. M., Lipid membrane fusion induced by the human immunodeficiency virus type 1 gp41 N-terminal extremity is determined by its orientation in the lipid bilayer. *J. Virol.* **1996,** 70, (1), 298-304.

45. Pereira, F. B.; Goni, F. M.; Muga, A.; Nieva, J. L., Permeabilization and fusion of uncharged lipid vesicles induced by the HIV-1 fusion peptide adopting

an e
197

46.
pola
fusic

47.
R.; F
pept
(1). 1

48.
Schw
deter
micro

49.
J.: Ni
vesic
Biopl

50.
struct
Implic

51.
immu
Biopl

52.
peptic
J. 20(

53.
reson
bcunc

54.
Applic
backb
159. (

55.
structi
monoi

an extended conformation: dose and sequence effects. *Biophys. J.* **1997,** 73, (4), 1977-1986.

46. Peisajovich, S. G.; Epand, R. F.; Pritsker, M.; Shai, Y.; Epand, R. M., The polar region consecutive to the HIV fusion peptide participates in membrane fusion. *Biochemistry* **2000,** 39, (7), 1826-33.

47. Martin, I.; Defrise-Quertain, F.; Decroly, E.; Vandenbranden, M.; Brasseur, R.; Ruysschaert, J. M., Orientation and structure of the NH_2-terminal HIV-1 gp41 peptide in fused and aggregated liposomes. *Biochim. Biophys. Acta* **1993,** 1145, (1), 124-133.

48. Taylor, S. E.; Desbat, B.; Blaudez, D.; Jacobi, S.; Chi, L. F.; Fuchs, H.; Schwarz, G., Structure of a fusion peptide analogue at the air-water interface, determined from surface activity, infrared spectroscopy and scanning force microscopy. *Biophys. Chem.* **2000,** 87, (1), 63-72.

49. Agirre, A.; Flach, C.; Goni, F. M.; Mendelsohn, R.; Valpuesta, J. M.; Wu, F. J.; Nieva, J. L., Interactions of the HIV-1 fusion peptide with large unilamellar vesicles and monolayers. A cryo-TEM and spectroscopic study. *Biochimica Et Biophysica Acta-Biomembranes* **2000,** 1467, (1), 153-164.

50. Haque, M. E.; Koppaka, V.; Axelsen, P. H.; Lentz, B. R., Properties and structures of the influenza and HIV fusion peptides on lipid membranes: Implications for a role in fusion. *Biophys. J.* **2005,** 89, (5), 3183-3194.

51. Kamath, S.; Wong, T. C., Membrane structure of the human immunodeficiency virus gp41 fusion domain by molecular dynamics simulation. *Biophys. J.* **2002,** 83, (1), 135-143.

52. Maddox, M. W.; Longo, M. L., Conformational partitioning of the fusion peptide of HIV-1 gp41 and its structural analogs in bilayer membranes. *Biophys. J.* **2002,** 83, (6), 3088-3096.

53. Yang, J.; Gabrys, C. M.; Weliky, D. P., Solid-state nuclear magnetic resonance evidence for an extended beta strand conformation of the membrane-bound HIV-1 fusion peptide. *Biochemistry* **2001,** 40, (27), 8126-8137.

54. Yang, J.; Parkanzky, P. D.; Bodner, M. L.; Duskin, C. G.; Weliky, D. P., Application of REDOR subtraction for filtered MAS observation of labeled backbone carbons of membrane-bound fusion peptides. *J. Magn. Reson.* **2002,** 159, (2), 101-110.

55. Yang, J.; Prorok, M.; Castellino, F. J.; Weliky, D. P., Oligomeric beta structure of the membrane-bound HIV-1 fusion peptide formed from soluble monomers. *Biophys. J.* **2004,** 87, 1951-1963.

56.
Welik
spect
mem.

57.
state
orient
Phys.

58.
fusion
which
(45),

59.
HIV-1
East L

60.
flexibi
trimer
12975

56. Bodner, M. L.; Gabrys, C. M.; Parkanzky, P. D.; Yang, J.; Duskin, C. A.; Weliky, D. P., Temperature dependence and resonance assignment of ^{13}C NMR spectra of selectively and uniformly labeled fusion peptides associated with membranes. *Magn. Reson. Chem.* **2004,** 42, 187-194.

57. Wasniewski, C. M.; Parkanzky, P. D.; Bodner, M. L.; Weliky, D. P., Solid-state nuclear magnetic resonance studies of HIV and influenza fusion peptide orientations in membrane bilayers using stacked glass plate samples. *Chem. Phys. Lipids* **2004,** 132, (1), 89-100.

58. Yang, R.; Prorok, M.; Castellino, F. J.; Weliky, D. P., A trimeric HIV-1 fusion peptide construct which does not self-associate in aqueous solution and which has 15-fold higher membrane fusion rate. *J. Am. Chem. Soc.* **2004,** 126, (45), 14722-14723.

59. Yang, J. Solid-state nuclear magnetic resonance structural studies of the HIV-1 fusion peptide in the membrane environment. Michigan State University, East Lansing, MI, 2003.

60. Zheng, Z., Yang, R., Bodner, M.L., and Weliky, D.P., Conformational flexibility and strand arrantments of the membrane-associated HIV fusion peptide trimer probed by solid-state NMR spectroscopy. *Biochemistry* **2006,** 45, 12960-12975.

C

BAC

to st

was

relev

cross

HFPr

has

the H

a pep

first

secon

using

growt

was t

5%.(2

was

chain

of the

the o

CHAPTER II

OPTIMIZATION OF THE SYNTHESIS OF FUSION PEPTIDE OLIGOMERS

BACKGROUND

Chemically synthesized HFP has been considered to be a useful model to study the fusion peptide/membrane interaction. However, a practical challenge was the synthesizing of large quantities of pure peptides, especially biological-relevant HFP oligomers such as HFPtr. One synthetic route of HFPtr was the cross-linking between HFPmn with one non-native C-terminal cysteine and HFPmn with two non-native C-terminal cysteines. However, the major product has been proved to be HFP dimer (HFPdm) formed from cross-linking between the HFPmn with one cysteine.*(1)* An alternative approach was initial formation of a peptide scaffold with three lysines and amide bonds between the ε-NH_2 of the first lysine and the COOH of the second lysine and between the ε-NH_2 of the second lysine and the COOH of the third lysine. HFPtr was then synthesized using standard 9-fluorenylmethoxycarbonyl (Fmoc) chemistry and synchronous growth of the peptide chains from the three main chain α-NH_2. This approach was therefore direct synthesis of a ~90-mer and the consequent yield was at best 5%.(*2*) In addition, the final product contained significant impurity HFPtr which was non-separable and which contained one additional lysine in one of the chains.*(2)* This impurity was a consequence of undesired intramolecular removal of the Fmoc protecting group on a Lys α-NH_2 by a free ε-NH_2.*(3)* In this chapter, the optimization of HFP oligomer synthesis will be described. Firstly, the

mo

dis

be

MA

acic

Trp

(Lou

uror

were

(DIP

hexa

Som

Pier

som

Fost

provi

chron

mm

triflu

TFA,

monitoring of coupling time for individual residues in HFP sequence will be discussed, and then, the efficient synthetic schemes for HFPdm and HFPtr will be provided.*(4)*

MATERIALS

The Gly or Ala-preloaded Wang Resins and *N*-Fmoc-protected amino acids Gly, Ala, Ile, Leu, Val, Phe, Ser(*t*Bu), Thr(*t*Bu), Met, Cys(Trt), Arg(Pbf), Trp(Boc), Trp(Mtt) and Lys(Boc) were purchased from Peptides International (Louisville, KY). The coupling reagents *O*-benzotriazole-*N*,*N*,*N'*,*N'*-tetramethyl-uronium-hexafluoro-phosphate (HBTU) and 1-hydroxybenzotriazole (HOBT) were purchased from Novabiochem (San Diego, CA). *N,N*-diisopropylethylamine (DIPEA) and 7-azabenzotriazol-1-yloxy-tris-(pyrrolidino)phosphonium hexafluorophosphate (PyAOP) were obtained from Sigma-Aldrich (St. Louis, MO). Some of the synthesis was done manually in 5 mL polypropylene columns from Pierce (Rockford, IL) and mixing was accomplished with a rotation stage, and some of the synthesis was done on an automated peptide synthesizer (ABI 431A, Foster City, CA). The detailed procedures for the manual peptide synthesis were provided in appendix 3. All peptides were purified using high-performance liquid chromatography (HPLC) (Dionex, Sunnyvale, CA) equipped with a 10 mm * 250 mm C18 column (Vydac, Hesperia, CA). "Buffer A" was water with 0.1% trifluoroacetic acid (TFA), "buffer B" was 90% acetonitrile, 10% water, and 0.1% TFA, and the gradient was 40% to 80% buffer B over 30 minutes. Peptide

mas

fligh

Tabl

H

HFI

H

[a] A line
and the

biospe

4-hydr

280 nn

masses were measured with matrix-assisted laser desorption/ionization-time of flight (MALDI-TOF) mass spectrometry using a Voyager-DE STR

Table 1. Names and sequences of the HIV fusion peptides

Name	Sequence [a]
HFPmn	**AVGIGALFLGFLGAAGSTMGARSWKKKKKKA$^{\beta}$**
HFPmn(Cys)	**AVGIGALFLGFLGAAGSTMGARSWKKKKKCA$^{\beta}$**
HFPmn(Cys/Gly)	**AVGIGALFLGFLGAAGSTMGARSWKKKKKCG**
HFPdm(Cys)	**AVGIGALFLGFLGAAGSTMGARSWKKKKKKA$^{\beta}$** **AVGIGALFLGFLGAAGSTMGARSWKKKKKC**
HFPdm	**AVGIGALFLGFLGAAGSTMGARSWKKKKKCA$^{\beta}$** **AVGIGALFLGFLGAAGSTMGARSWKKKKKCA$^{\beta}$**
HFPtr	**AVGIGALFLGFLGAAGSTMGARSWKKKKKKA$^{\beta}$** **AVGIGALFLGFLGAAGSTMGARSWKKKKKC** **AVGIGALFLGFLGAAGSTMGARSWKKKKKCG**
HFPte	**AVGIGALFLGFLGAAGSTMGARSWKKKKKKA$^{\beta}$** **AVGIGALFLGFLGAAGSTMGARSWKKKKKC** **AVGIGALFLGFLGAAGSTMGARSWKKKKKC** **AVGIGALFLGFLGAAGSTMGARSWKKKKKKA$^{\beta}$**

[a] A line between K and C denotes a peptide bond between the Cys CO and the Lys ε-NH and a line between two Cs denotes a disulfide bond.

biospectrometry workstation (Applied Biosystems, Foster City, CA) and α-cyano-4-hydroxy cinnamic acid matrix. Peptide synthetic yields were quantified using 280 nm absorbance and the extinction coefficients were 5700, 11600 and 17300

cm^{-1} M

monor

were

seque

that (

reactic

RESU

HFPm

for the

of eac

free α

times

single

Ser(tB

12 an

coupli

coupli

purifie

domin

instrur

of sy

cm^{-1} M^{-1} for HFPmn, HFPdm and HFPtr respectively. The sequences of HFP monomers, dimers, trimer and HFP tetramer (HFPte) described in this chapter were summarized in Table 1. The N-terminal 23 residues come from the sequence of gp41. The C-terminal tags contain Lys, Cys and Trp for the reasons that (1) Lys increases the solubility of HFPs, (2) Cys enables the cross-linking reactions and (3) Trp helps to quantify the synthesis.

RESULTS AND DISCUSSION

Optimization of coupling time. A manual synthesis was carried out on HFPmn according to the scheme provided in Figure 3. The detailed procedures for the manual synthesis of HFPmn are provided in the appendix 3. The coupling of each residue was optimized by ninhydrin monitoring every two hours to detect free α-HN_2 groups.*(5)* This information provided the basis for longer coupling times and double couplings at particular residues. It was observed that two-hour single coupling was sufficient for the residues along the sequence except for Ser(*t*Bu), Arg(Pbf), and Trp(Boc) residues as well as the residues between Leu-12 and Leu-7. A complete coupling for these residues were detected for a coupling time 4~6 hours which means either longer coupling times or double coupling should be used. Figure 4 shows the HPLC and mass spectrum for the purified HFPmn using the optimized coupling time. The mass spectrum of the dominant fraction had an intense peak with *m/z* = 3149 which was within the instrumental accuracy of ± 0.1% relative to the expected *m/z* = 3151. The product of synthesis was also subjected to the amino acid analysis by the

Macro

Bioch

showe

1.720

0.795

The d

the gr

proble

difficu

the co

residu

the fu

of HF

Cys c

HFPd

fluore

the bu

sessio

identi

was

fractio

instru

Macromolecular Structure Facility of Michigan State University (Department of Biochemistry and Molecular Biology, Michigan State University). The results showed that the sequence contained 6 Gly, 5.922 Ala, 6.257 Lys, 2.711 Leu, 1.720 Phe, 1.880 Ser, 1.080 Met, 1.003 Trp, 1.298 Arg, 1.115 Thr, 0.700 Val and 0.795 Ile, which were consistent with the sequence of HFPmn given in Table 1. The difficulties for the coupling of Ser(tBu), Arg(Pbf) and Trp(Boc) may be due to the great size of side chains or side chain protection groups which cause steric problem and block the active amino group from the newly added amino acid. The difficulties for the coupling of the residues from Leu7 to Leu12 may come from the continuous increase of hydrophobicity during the coupling of these apolar residues, which will further cause the aggregation of peptide chains and prevent the further coupling.*(6)*

Synthesis of HFPdm. Figure 5 shows the synthetic schemes of two types of HFP dimers: HFPdm and HFPdm(Cys). HFPdm was synthesized using the Cys cross-linking reaction of Cys contained HFPmn (named HFPmn(Cys)) and HFPdm(Cys) was synthesized using the dimeric scaffold with 9-fluorenylmethoxycarbonyl (Fmoc) chemistry.*(7)* HFPdm(Cys) will serve as one of the building blocks in the synthesis of HFPtr which will be described in the next session. Figure 6 displays the HPLC and mass spectra for the purification and identification of HFPdm and HFPdm(Cys). The HPLC retention time of HFPdm was very well-separated from that of unreacted HFPmn(Cys). The HFPdm fraction had a mass spectral peak with *m/z* = 6248 which was within the instrumental accuracy of ± 0.1% relative to the expected *m/z* = 6253, *cf.* Figure

6b. T

HFPr

spect

previ

disulf

increa

fluenc

intens

the o

intern

St. Lo

retent

spect

was v

A pre

impur

Fmoc

subse

scaffo

corres

steps

Figure

6b. There was also a peak at *m/z* = 3124 which corresponded to either the HFPmn(Cys) fragment formed from cleavage of the disulfide bond in the mass spectrometer or to doubly charged HFPdm.(*8*) It has been demonstrated previously that there was prompt fragmentation where the single intermolecularly disulfide-bound peptides can be specifically fragmented at the S-S bond by increasing the laser fluence in MALDI-MS.(*8*) Since we always used high laser fluence in the identification of the HFP oligomers to obtain reasonable signal intensities, it was possible that the interstrand S-S bond was fragmented due to the over-threshold laser fluence. The peak at *m/z* = 5733 corresponded to the internal standard of insulin from bovine pancreas (purchased from Sigma-Aldrich, St. Louis, MO). Figure 6c displays the chromatogram of the synthesis and the retention time of HFPdm(Cys) was very close to that of HFPdm. The mass spectrum of the HFPdm(Cys) fraction had an intense peak with *m/z* = 6190 which was within the ± 0.1% uncertainty relative to the expected *m/z* = 6188, cf. Fig. 6d. A previously published synthesis showed significant higher molecular weight impurities which was the result of: (1) premature removal of the scaffold lysine Fmoc group by nucleophilic attack of the scaffold lysine ε-NH_2; and (2) subsequent coupling of the next amino acid with both the ε- and the α-NH_2 of the scaffold lysine.*(2)* The mass spectrum of HFPdm(Cys) did not show the impurity corresponding to a peptide with an extra Cys. Minimization of the time between steps f and d in Figure 5 was critical to eliminating this impurity.

Synthesis of HFPtr. The synthesis scheme for HFPtr was displayed in Figure 7. HFPtr was formed from cross-linking HFPmn(Cys) and HFPdm(Cys) in

a 1.0:1.

amount

The nor

showed

rapid th

8a shov

chromat

the th

HFPdm/

chromat

respectiv

HFPmn((

spectrum

0.1% un

peak at 4

6194 we

cleavage

5733 cor

the HFP

cross-link

separatio

showed t

12461 an

a 1.0:1.5 mol ratio. The cross-linking reaction was done at *p*H = 8.4 with trace amount of 4-dimethylaminopyridine (DMAP) and with the system open to the air. The non-stoichiometric ratio was based on initial small-scale syntheses which showed that cross-linking of HFPmn(Cys) with itself to form HFPdm was more rapid than cross-linking of HFPmn(Cys) with HFPdm(Cys) to form HFPtr. Figure 8a showed the monitoring of the cross-linking reaction using HPLC. The top chromatogram in Figure 8a was obtained after 0.5 hour cross-linking time and the three prominent peaks from left-to-right were HFPmn(Cys), HFPdm/HFPdm(Cys), and HFPtr, respectively. The middle and bottom chromatograms were obtained with cross-linking times of 1.5 and 2.5 hours, respectively, and showed a relative increase in HFPtr and relative decreases in HFPmn(Cys) and HFPdm(Cys) with longer cross-linking time. The mass spectrum of the HFPtr fraction had a peak with *m/z* = 9307 which was within ± 0.1% uncertainty relative to the expected HFPtr *m/z* = 9312, cf. Figure 8b. The peak at 4653 was assigned to doubly charged HFPtr and the peaks at 3112 and 6194 were assigned to HFPmn(Cys) and HFPdm(Cys) fragments formed from cleavage of the disulfide bond in the mass spectrometer.(*8*) The peak at *m/z* = 5733 corresponded to the internal standard of bovine insulin. One side product in the HFPtr synthesis was the HFP tetramer (HFPte) which was formed by the cross-linking between two HFPdm(Cys) molecules. Figure 9a displayed the separation of HFPte from HFPtr at the retention time ~ 22 minutes and Figure 9b showed the mass spectrum of HFPte. There were broad signals peaked at *m/z* = 12461 and 6235 which were respectively comparable to the expected HFPte *m/z*

= 123

formec

to the

the ex

lower s

a 3-fol

scaffol

been re

followin

reactio

synthes

reactio

cross-li

HPLC p

and HF

synthes

Trp(Boc

protoco

HFPdm

cleavag

This mo

α-NH_2 b

= 12374 and the *m/z* of the doubly charged species or the HFPdm(Cys) fragment formed from cleavage of the disulfide bond in the mass spectrometer.(*8*) Relative to the HFPmn, HFPdm, and HFPtr spectra, there were greater uncertainties of the experimental *m/z* in the HFPte spectra because of both broader signals and a lower signal-to-noise ratio.

The overall yield for the HFPtr synthesis was about 15 % which indicated a 3-fold increase compared with the previous coupling scheme from the trimeric scaffold.(*2*) In addition, the side product with an extra Lys in the C-terminus has been removed. The present study increased the HFPtr yield and purity using the following modifications: (1) HFPtr was formed from a cysteine cross-linking reaction between HFPmn(Cys) and HFPdm(Cys). Because HFPdm(Cys) was synthesized using a dimeric scaffold, a successful synthesis required 1/3 fewer reactions than the earlier HFPtr synthesis. In addition, the purification of the cross-linking reaction was fairly straightforward because of the separation of the HPLC peaks corresponding to HFPmn(Cys), HFPdm and HFPdm(Cys), HFPtr, and HFPte, cf. Figure 8. (2) The monitoring of coupling times in the manual syntheses of HFPmn showed that longer coupling times were required for the Trp(Boc), Ser(tBu), Arg(Pbf), and Leu-7 to Leu-12 residues. The new synthetic protocol used longer coupling times or double coupling at these residues. (3) The HFPdm(Cys) synthetic protocol was modified to minimize the time between the cleavage of the Mtt group of the Lys ε-NH_2 and the subsequent coupling to Cys. This modification reduced undesired deprotection of the Fmoc group of the Lys α-NH_2 by the ε-NH_2.

CON

peptic

hydro

using

residu

betwe

of the

produ

provid

and re

and he

CONCLUSION

This chapter reported efforts on the optimization of the conditions of peptide synthesis, especially HFPtr. It can be concluded that (1) the hydrophobicity of HFP sequence increases the challenge of the synthesis and using either longer coupling times or double coupling for the hydrophobic residues helps to improve the synthesis, (2) it is important to shorten the time between the cleavage of Lys ε-NH_2 side chain protection group and the coupling of the following residue to the unprotected ε-NH_2 in order to eliminate the producing of by products with extra Lysines and (3) the Cys cross-linking strategy provides straightforward HPLC purification for the hydrophobic HFP oligomers and reasonable yield, and should be applicable to the synthesis of other homo and hetero trimeric peptides.

Fmo

Figure 3
AVGIGAL
are draw
reaction.
reactions
deprotect
Reaction
used for
for Trp. S
residues.
TFA/thioa
reaction t
with cold

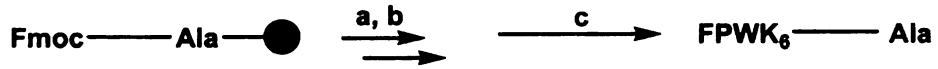

Figure 3 Synthesis scheme for HFPmn and FP represents the sequence AVGIGALFLGFLGAAGSTMGARS. A black circle represents a resin bead, lines are drawn to clarify chemical functionalities, an arrow signifies a chemical reaction, and two arrows signify multiple sequential chemical reactions. All reactions were carried out at ambient temperature. Reaction **a**: Fmoc deprotection in 3 mL of 20% piperidine/DMF (v/v), 15 minutes/cycle, 2 cycles. Reaction **b**: Peptide synthesis with Fmoc chemistry. 2-hour single couplings were used for each amino acid with the following exceptions: 4-hour single couplings for Trp, Ser and Arg residues; 6-hour single couplings for the Leu-12 to Leu-7 residues. Reaction **c**: Cleavage from the resin using a 4 mL solution containing TFA/thioanisole/ethanedithiol/anisole in 90:5:3:2 volume ratio.(*6*) After 2.5 hours reaction time, TFA was removed with nitrogen gas and peptide was precipitated with cold methyl t-butyl ether.

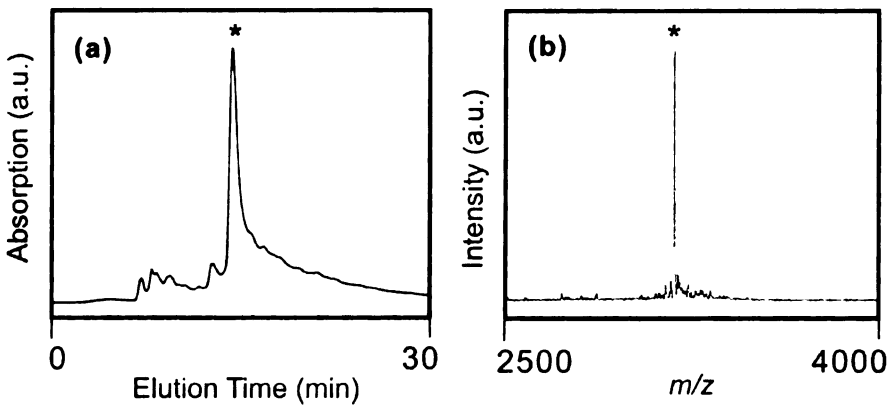

Figure 4 (a) The HPLC chromatograms for the purification of HFPmn. The horizontal axis was the elution time in unit of minute and the vertical axis was the absorption at 214 nm with arbitrary unit. (b) The MALDI-TOF MS spectrum for the identification of HFPmn. The HPLC fraction marked with asterisk in (a) was analyzed and the corresponding mass was labeled using asterisk in (b).

(a)

(b)

Figur
circle
c wer
in (a)
4-hou
excep
doubl
the Le
(1:2 n
reactio
the ai
deprot

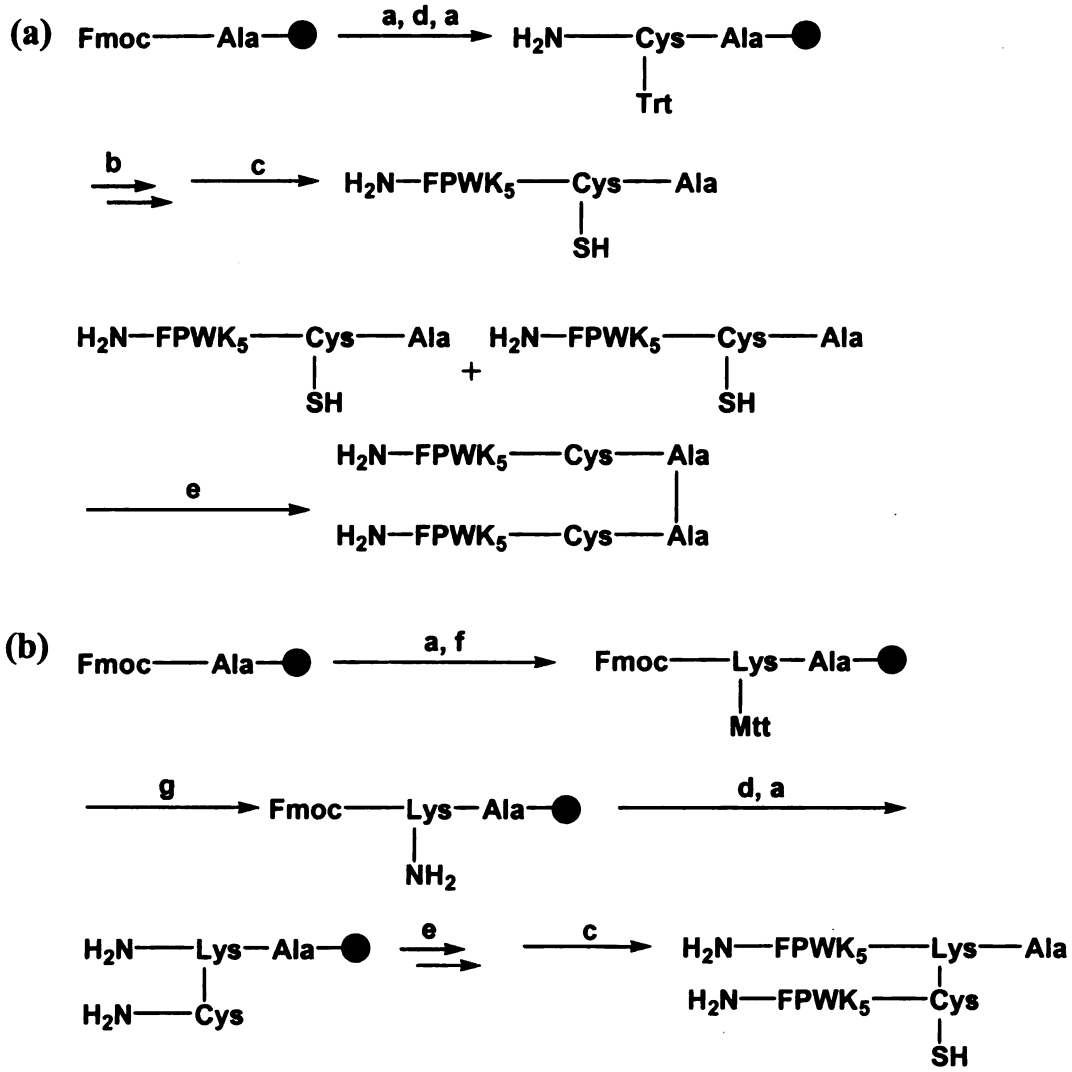

Figure 5 Synthesis schemes for (a) HFPdm and (b) HFPdm(Cys). The black circles, lines and arrows had the same meaning as in Fig. 3. The reactions **a** and **c** were the same as in Fig. 3. In reaction **b**, the synthesis of HFPmn with Cys(Trt) in (a) followed the coupling time in Fig. 3. For the HFPdm(Cys) synthesis in (b), 4-hour single couplings were used for each amino acid with the following exceptions: 8-hour single couplings for Trp(Boc), Ser(*t*Bu), and Arg(Pbf) residues; double couplings with 4-hours per coupling for the ^{13}CO labeled residue and for the Leu-12 to Leu-7 residues. Reaction **d**: Coupling using PyAOP and DIPEA (1:2 molar ratio) in 4 mL DMF with 6 hour reaction times for Cys and 2 hour reaction time for Lys. Reaction **e**: Cross-linking in 5 mM DMAP, pH = 8.4, open to the air. 1 μmol HFPmn(Cys) in 400 μL solution overnight. Reaction **f**: Selective deprotection of Mtt in 3 mL of 1% TFA/DCM (v/v), 6 minutes/cycle, 6 cycles.

Absorption (a.u.)

Absorption (a.u.)

Figure
HFPd
vertica
MALD
HPLC
corres
mass

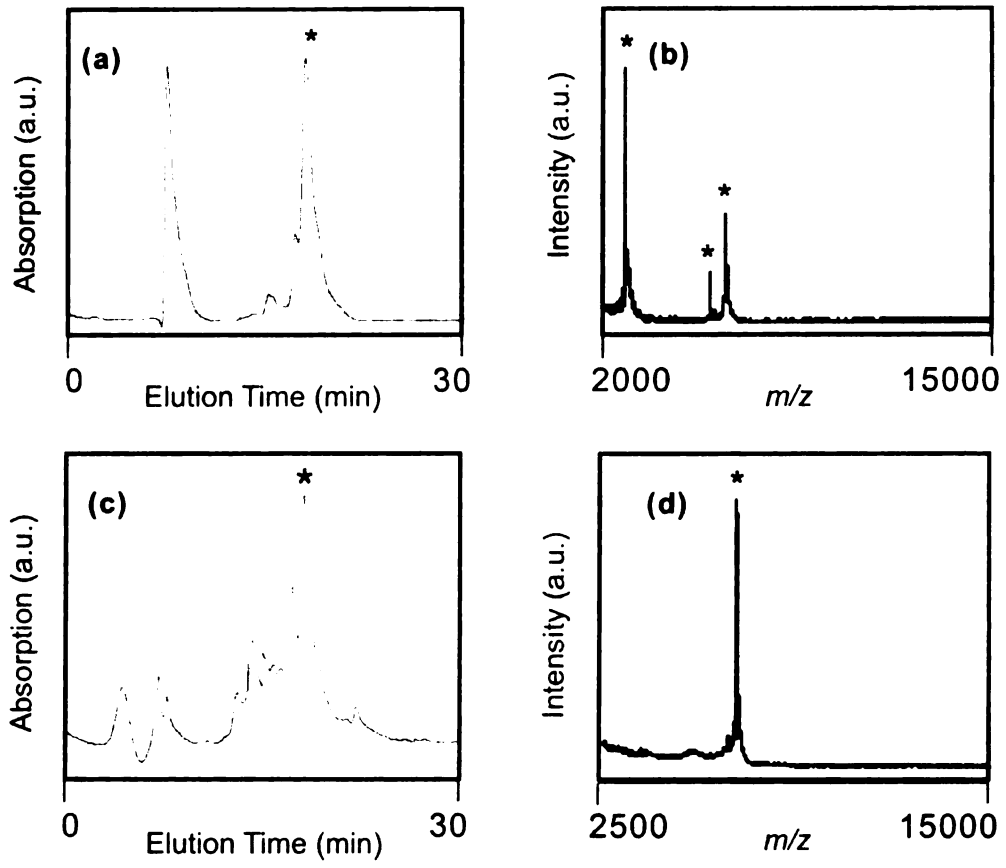

Figure 6 (a) and (c) The HPLC chromatograms for the purification of HFPdm and HFPdm(Cys). The horizontal axes were elution time in unit of minute and the vertical axis were absorption at 214 nm with arbitrary unit. (b) and (d) The MALDI-TOF MS spectrum for the identification of HFPdm and HFPdm(Cys). The HPLC fraction marked with asterisk in (a) and (c) were analyzed and the corresponding peaks were labeled using asterisk in (b) and (d) respectively. The mass spectra were discussed in the main text.

Fm

Fm

e

H_2N

H_2N

Figu
the s
as sh
pH =
µL so

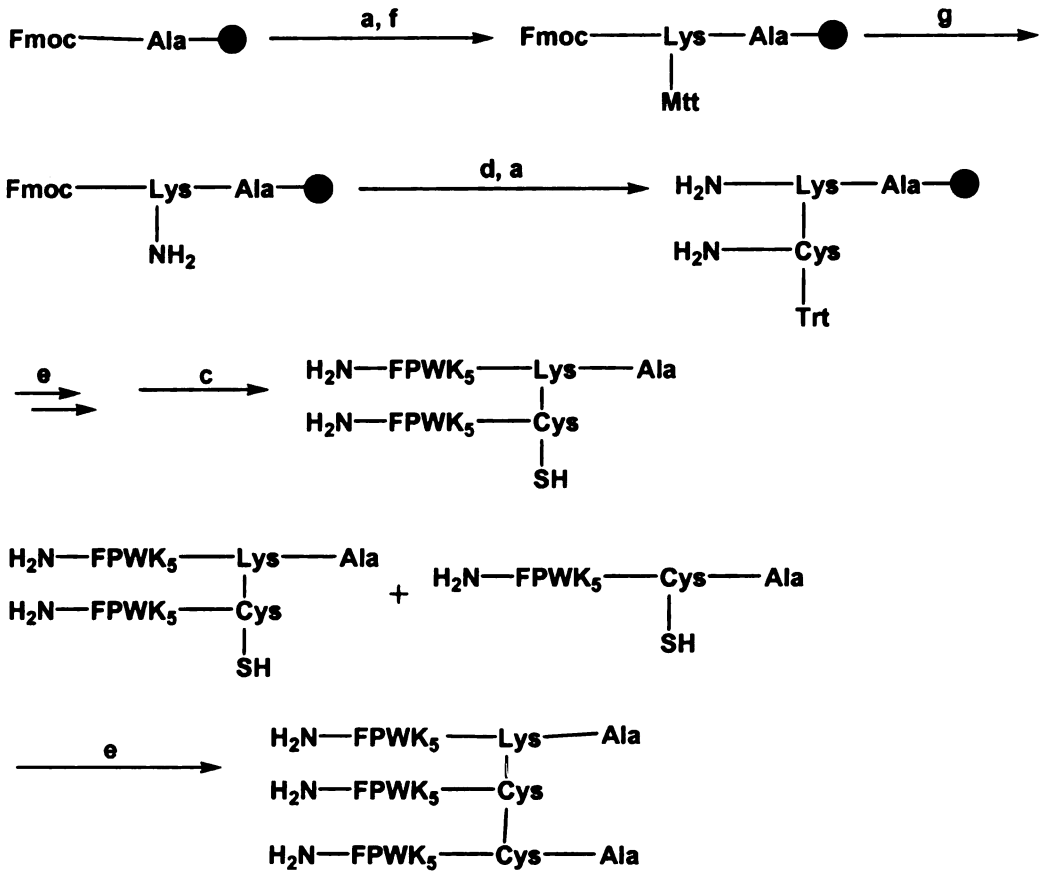

Figure 7 Synthesis schemes for HFPtr. The black circles, lines and arrows had the same meaning as in Fig. 3 and Fig. 5. All reaction conditions were the same as shown in Fig. 3 and Fig. 5 except for reaction **e**: Cross-linking in 5 mM DMAP, pH = 8.4, open to the air. 1 μmol HFPmn(Cys) and 1.5 μmol HFPdm(Cys) in 400 μL solution for 2.5 hours.

(a)

Absorption (a.u.)

Figure
horizont
absorpti
the iden
a are fo
respecti
indicate
right res
and the
spectra

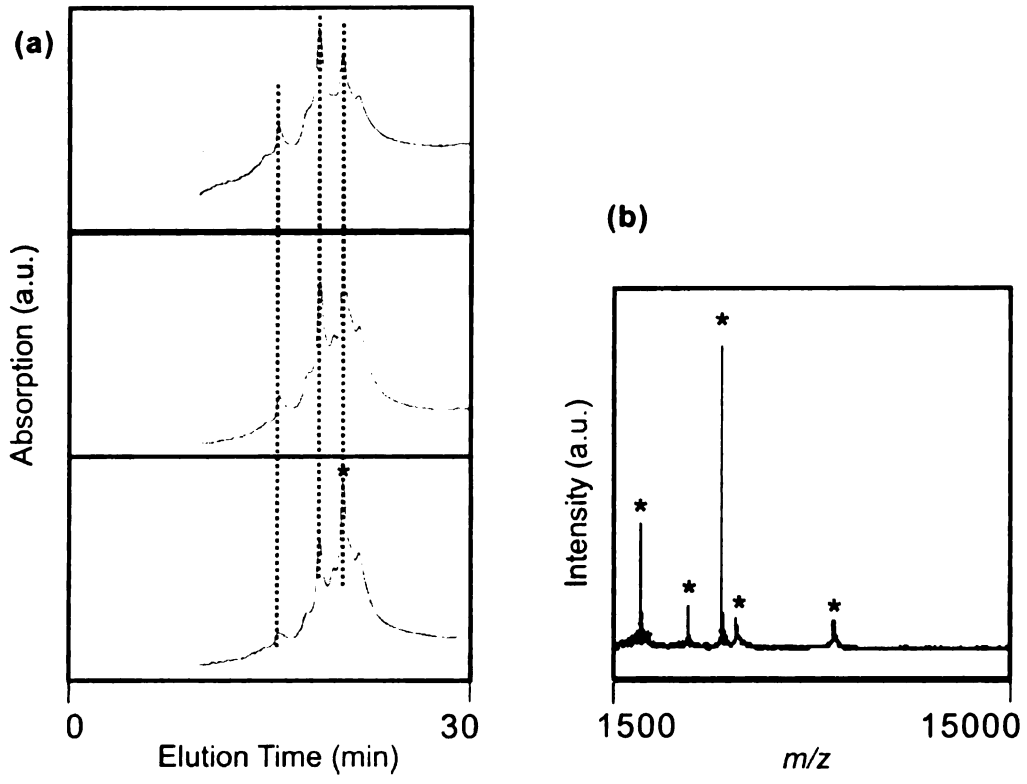

Figure 8 (a) The HPLC chromatograms for the purification of HFPtr. The horizontal axes were elution time in units of minutes and the vertical axes were absorption at 214 nm with arbitrary units. (b) The MALDI-TOF MS spectrum for the identification of HFPtr. The top, middle, and bottom chromatograms in panel a are for syntheses with HFPtr cross-linking times of 0.5, 1.5, and 2.5 hours, respectively. In each chromatogram, the positions of the vertical dotted lines indicated the elution times of monomer, dimer and trimer for the left, middle and right respectively. The HPLC fraction marked with asterisk in (a) was analyzed and the corresponding peaks were labeled using asterisk in (b). The mass spectra were discussed in the main text.

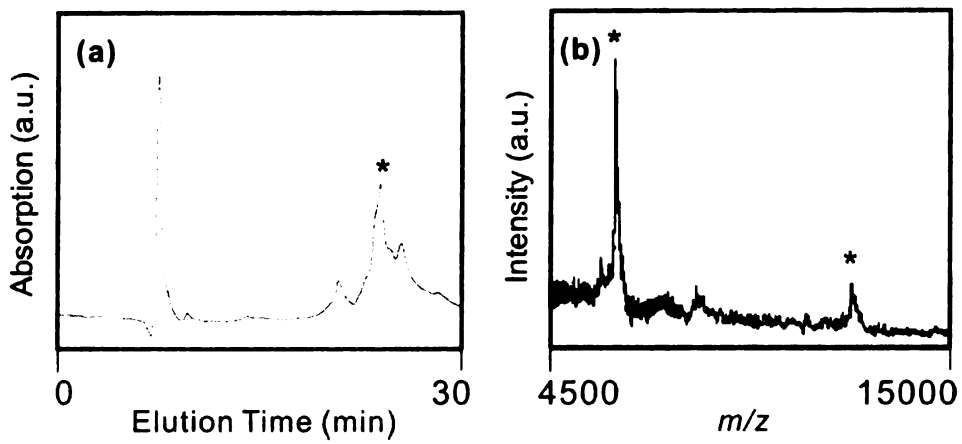

Figure 9 (a) The HPLC chromatograms for the purification of HFPte. The horizontal axis was the elution time and the vertical axis represented the 214 nm absorption in arbitrary unit. (b) The MALDI-TOF MS spectrum for the identification of HFPte. The HPLC fraction marked with asterisk in (a) was analyzed and the corresponding mass was labeled using asterisk in (b).

REF

1.
solid
Bioch

2.
fusio
whic
(45),

3.
Fmoc
Lette

4.
Oligo
Corre
to Lip

5.
detec
Bioch

6.
Pract

7.
2,2,2-
fluore
leavin

8.
during
Chem

REFERENCE

1. Yang, R.; Yang, J.; Weliky, D. P., Synthesis, enhanced fusogenicity, and solid state NMR measurements of cross-linked HIV-1 fusion peptides. *Biochemistry* **2003,** 42, (12), 3527-3535.

2. Yang, R.; Prorok, M.; Castellino, F. J.; Weliky, D. P., A trimeric HIV-1 fusion peptide construct which does not self-associate in aqueous solution and which has 15-fold higher membrane fusion rate. *J. Am. Chem. Soc.* **2004,** 126, (45), 14722-14723.

3. Farrera-Sinfreu, J.; Royo, M.; Albericio, F., Undesired removal of the Fmoc group by the free epsilon-amino function of a lysine residue. *Tetrahedron Letters* **2002,** 43, (43), 7813-7815.

4. Qiang, W., and Weilky, D.P., HIV Fusion Peptide and Its Cross-Linked Oligomers: Efficient Syntheses, Significance of the Trimer in Fusion Activity, Correlation of β Strand Conformation with Membrane Cholesterol, and Proximity to Lipid Headgroups. *Biochemistry* **2009,** 48, (2), 289-301.

5. Kaiser, E., Colescott, R.L., Bossinger, C.D., and Cook, P.I., Color test for detection of free terminal amino groups in solid-phase synthesis of peptides. *Anal. Biochem.* **1970,** 34, 595.

6. Chan, W. C., and White, P.D., *Fmoc Solid Phase Peptide Synthesis: A Practical Approach* **2000**, 94-109.

7. Lapatsanis, L.; Milias, G.; Froussios, K.; Kolovos, M., Synthesis of N-2,2,2-(trichloroethoxycarbonyl)-L-amino acids and N-(9-fluorenylmethoxycarbonyl)-L-amino acids involving succinimidoxy anion as a leaving group in amino-acid protection. *Synthesis-Stuttgart* **1983,** (8), 671-673.

8. Patterson, S.; Katta, V., Prompt fragmentation of disulfide-linked peptides during Matrix-assisted Laser Desorption Ionization Mass Spectrometry. *Anal. Chem.* **1994**, 66, 3727-3732.

THI

info

REI

che

^{13}C

sec

cha

thus

to t

con

spe

inte

the

whi

intr

inclu

cycli

mec

CHAPTER III

OPTIMIZATION OF SOLID-STATE NMR EXPERIMENTS

THERORETICAL BACKGROUND

Solid-state NMR is a useful tool to provide high-resolution structural information for the membrane-associated peptides.*(1-3)* For example, for the REDOR pulse sequence which will be used in the following chapters, the chemical shift of one specifically-labeled ^{13}C or the dipolar coupling between a ^{13}C and a ^{15}N, ^{31}P or ^{19}F provide valuable structural properties such as secondary structure, tertiary structure and internuclear distances.*(4-7)* One characteristics of the solid samples is the absence of free molecular tumbling and thus the co-existence of multiple orientations of chemical shielding tensor relative to the static external magnetic field for a single spin such as a ^{13}C. This will consequently cause the broadening of the resonance and complicate the spectrum. In addition, one always wants to extract a specific intra-system interaction such as isotropic chemical shift or heteronuclear dipolar coupling from the many other intra-system interactions. In this first part of this chapter, a theory which has been widely used to analyze solid-state NMR pulse sequences will be introduced and the analysis of some pulse sequences will be given as examples.

Average Hamiltonian Theory (AHT). Many pulsed NMR techniques, including the methods used in the following work, apply some combination of the cyclic radiofrequency (rf) irradiation (also known as pulses) and the cyclic mechanical manipulation to the nuclear spin systems. This will consequently

make the intra-system interaction Hamiltonians time-dependent, and make the time averaging of such Hamiltonians important to the final spectrum. The Average Hamiltonian Theory (AHT) is helpful to understand the performance of the spin system under such time-dependent interactions. *It states that when a system is subjected to a cyclic external force, and the inspection is restricted to multiple integers of the cycle time, it looks like the system is subjected to a constant Hamiltonian.(8)* Three conditions should be satisfied before the AHT can be applied to analyze a pulse sequence:

(1) The cycle time of *rf* pulses should be a multiple of the cycle time of mechanical manipulation;

(2) The net rotation after the block of *rf* pulses should be zero;

(3) The cycle time of *rf* pulses should be small so that the internal Hamiltonian will not cause significant changes to the spin system during one cycle.

These conditions can be satisfied by carefully choose experimental parameters such as magic angle spinning (MAS) frequency, rf pulse length, time interval between pulses and phase cycling strategy.

The lowest-order approximation of the constant Hamiltonian in AHT can be expressed by Eq. 1

$$\bar{H} = \frac{1}{\tau_C} \int_0^{\tau_C} dt \cdot \tilde{H}^{\text{int}}(t) \quad (1)$$

τ_C represents the cycle time of *rf* pulses and $\tilde{H}^{\text{int}}$ is the interaction Hamiltonian in the toggling frame (or *rf* frame).

$$\tilde{H}^{\text{int}}(t) = U_{rf}^{-1}(t) \cdot H^{\text{int}}(t) \cdot U_{rf}(t) \quad (2)$$

For a

frame

Hami

$U_I(t)$

The c

the p

trunca

$\omega_{ij}(t)$

phase

respe

The e

used

obtair

Hamil

and th

and D

C^{m} co

gener

For all the discussions below, $H^{int}(t)$ has always been expressed in the rotating frame under the condition of MAS and after the truncation of the Zeeman Hamiltonian. The time-dependence of $H^{int}(t)$ is generally introduced through MAS. $U_{rf}(t)$ is a unitary operator defined by the *rf* pulses.

$$U_{rf}(t) = \hat{T}\exp[-i\int_0^t dt' \cdot H^{rf}(t')] \quad (3)$$

The operator $\hat{T}$ is the Dyson time operator which specifies the time ordering of the pulse sequence. $H^{rf}(t)$ is also expressed in the rotating frame and with the truncation of Zeeman Hamiltonian, and has the general form

$$H^{rf}(t) \propto \gamma B_1(t) \cdot [I_x \cos\varphi(t) + I_y \sin\varphi(t)] = \omega_1(t) \cdot [I_x \cos\varphi(t) + I_y \sin\varphi(t)] \quad (4)$$

$\omega_1(t)$ is usually named Rabi frequency and I_x and I_y are spin operators. $\varphi(t)$ is the phase of a rf pulse and generally 0°, 90°, 180° and 270° for x, y, -x, -y pulses respectively.

The expression of $H^{int}(t)$ is dependent on the specific internal interaction. The expressions for chemical shift (CS) and dipolar coupling (D), which will be used in the following chapters, will be introduced here. A general procedure to obtain the expression for any internal Hamiltonian is to initially write the Hamiltonian in the principal axis system (PAS) as H^{int} which is time-independent, and then to convert into the rotating frame. H^{int} has the following form for both CS and D

$$H^{int} = C^{int} \cdot \sum_l \sum_{m=-l}^{l} (-1)^m \cdot R^{int}_{l,-m} \cdot T^{int}_{l,m} \quad (5)$$

C^{int} contains constants which are different for CS or D. The "*R*" and "*T*" terms are generally expressed as the second-rank tensor in spherical coordinates, and

repr

and

In th

CS

The

Eq.

δ_{22}

alwa

rotat

angl

The

angle

frame

integ

the

represent the spatial and spin parts of the Hamiltonian respectively. l = 0, 1 or 2 and m values are integers from $-l$ to l.

$$C^{\text{int}} \equiv \gamma^i (\text{int} \equiv CS) \text{ and } C^{\text{int}} \equiv -2\gamma^i \gamma^j \hbar (\text{int} \equiv D) \quad (6)$$

In the PAS, the "R" terms have their simplest form and the non-zero "R" terms for CS and D are

$$R_{2,0}^{D,ij} = \sqrt{3/2} \cdot r_{ij}^{-3} \quad (7a)$$

$$\begin{aligned} R_{0,0}^{CS,i} &= 1/3 \cdot (\delta_{11} + \delta_{22} + \delta_{33}) \\ R_{2,0}^{CS,i} &= \sqrt{3/2} \cdot [\delta_{33} - 1/3 \cdot (\delta_{11} + \delta_{22} + \delta_{33})] \\ R_{2,\pm 2}^{CS,i} &= 1/2 \cdot (\delta_{22} - \delta_{11}) \end{aligned} \quad (7b)$$

The r_{ij} in Eq. 7a represents the internuclear distance between two spins i and j. In Eq. 7b, δ_{11}, δ_{22} and δ_{33} are three principal values of spin i with the sequence $\delta_{11} < \delta_{22} < \delta_{33}$. In most solid-state NMR techniques with MAS, the Hamiltonians are always expressed in the rotating frame. The "R" terms can be converted into the rotating frame from the PAS with the Euler transformation and two sets of Euler angles.

$$R_{l,-m}^{\text{int}}(rotating\_frame) = \sum_{m'} D_{m',-m}^{l}(\Omega'') \sum_{m''} D_{m'',m'}^{l}(\Omega') R_{l,m''}^{\text{int}}(PAS) \quad (8)$$

The "D" terms are elements in the Wigner rotation matrix. The first set of Euler angles $\Omega' \equiv (\alpha', \beta', \gamma')$ makes a connection between the PAS and some crystal frame axes system and for powder samples; these angles will finally be integrated over a spherical surface. The second set of Euler angle always has the value $\Omega'' \equiv (0, \beta'', \omega_R t)$ under the condition of fast MAS, where $\beta'' = 54.7^\circ$ or

"magic angle" and ω_R is the spinning frequency. The second Euler transformation introduces the time dependence to the "*R*" terms which is related to the MAS rotor cycles.

A full expression of "*R*" terms in the rotating frame will contain 25 terms due to the Wigner expansion. However, the "*T*" terms expressed in the rotating frame are truncated by the Zeeman Hamiltonian which help to simplify the form of the total Hamiltonian.

$$\begin{aligned} T_{l,m}^{\text{int}}(rotating\_frame) &= U_Z^{-1} T_{l,m}^{\text{int}}(lab\_frame) U_Z \\ &= \exp[i\omega t I_z] T_{l,m}^{\text{int}}(lab\_frame) \exp[-i\omega t I_z] \end{aligned} \quad (9)$$

ω is the Larmor frequency and the non-zero "*T*" terms in the rotating frame are:

$$T_{0,0}^{CS,i} = I_z^i B_0 \text{ and } T_{2,0}^{CS,i} = \sqrt{2/3} I_z^i B_0 \quad (10a)$$

$$T_{0,0}^{D,ij} = \vec{I}^i \cdot \vec{I}^j \text{ and } T_{2,0}^{D,ij} = (1/\sqrt{6})[3I_z^i I_z^j - \vec{I}^i \cdot \vec{I}^j] \quad (10b)$$

$$T_{0,0}^{D,ij} = I_z^i S_z^j \text{ and } T_{2,0}^{D,ij} = \sqrt{2/3} I_z^i S_z^j \quad (10c)$$

Eqs. 10a–c give the operators of chemical shift, homonuclear dipolar coupling and heteronuclear dipolar coupling respectively. One typically incorporates Eqs. 6-8 and 10 into Eq. 2 which will further bring time dependence into both "*R*" and "*T*" terms. Many solid-state NMR pulse sequences make use of the combination of these two time dependences to achieve selective averaging when applying Eq. 1. Two pulse sequences used in the following chapters are analyzed with AHT.

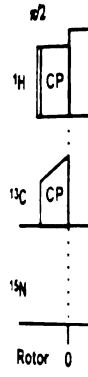

Figure 10
π/2 and
magnetiza
by one ^{15}
shift.

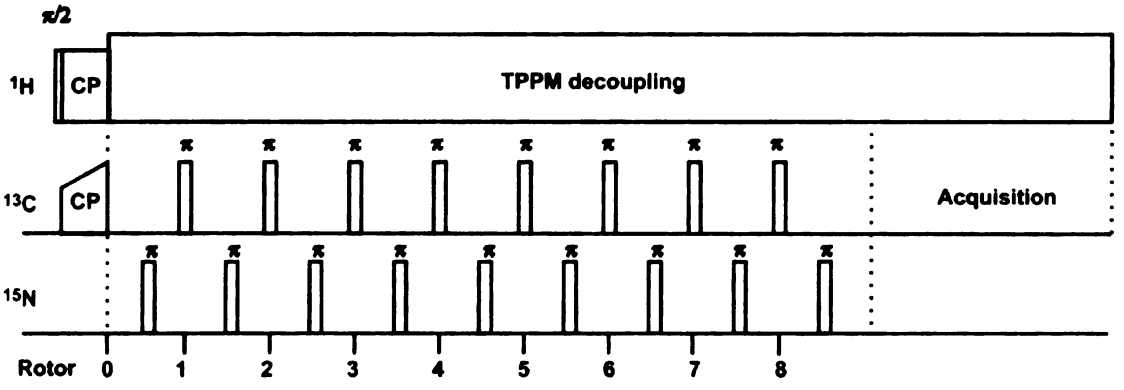

Figure 10 1D ^{13}C-^{15}N REDOR pulse sequence. The open columns represent the $\pi/2$ and π pulses. CP transfers ^{1}H transverse magnetization to ^{13}C. ^{13}C magnetization is dephased (i.e., reduced) by ^{13}C-^{15}N dipolar coupling mediated by one ^{15}N π pulse per rotor period. The ^{13}C π pulses refocus the ^{13}C chemical shift.

MAS

RED

reso

prim

data

Figu

perio

were

colle

but

both

^{15}N

fram

The

dipo

The

deco

sequ

^{13}C

zero

Theory of REDOR experiments. REDOR is one of the most widely used MAS NMR techniques for analysis of molecular structure in the solid-state.*(9-14)* REDOR has found application in detection of formation of chemical bonds and in resonance assignment of small peptides.*(15-17)* The wide use of REDOR is primarily due to the relative simplicity and robustness of its pulse sequence and data analysis. An example of a ^{13}C-^{15}N REDOR pulse sequence is sketched in Figure 10. It contains: (1) ^{1}H to ^{13}C cross polarization (CP), (2) a dephasing period (τ) during which a series of ^{13}C and ^{15}N π pulses and ^{1}H decoupling field were applied and (3) ^{13}C acquisition. For each τ, two separate spectra are collected. The spectrum named "S_0" is π pulses applied only on the ^{13}C channel but not on the ^{15}N channel. The spectrum called "S_1" is the pulses applied on both channels. For a sample with a single ^{13}CO label on one residue and a single ^{15}N label on another residue, the major interaction Hamiltonians in the rotating frame for the labeled ^{13}C are

$$H^{total} = H^{CS} + H^{D}_{CC} + H^{D}_{CN} \quad (11)$$

The terms on the right side of Eq. 11 indicate ^{13}C chemical shift, homonuclear dipolar coupling between ^{13}Cs and heteronuclear coupling between ^{13}C and ^{15}N. The heteronuclear dipolar coupling between ^{13}C and ^{1}H can be removed by ^{1}H decoupling and will not be included in the further discussion. The goal of this sequence is to selectively detect the ^{13}C and ^{15}N dipolar coupling as well as the ^{13}C isotropic chemical shift, while averaging all the other interactions. The non-zero term in the general expression of the dipolar coupling Hamiltonian was

$$H^{D}_{ij} = [A \cdot e^{2i\omega_R t} + B \cdot e^{i\omega_R t} + C \cdot e^{-i\omega_R t} + D \cdot e^{-2i\omega_R t}] \cdot I^{i}_{z} S^{j}_{z} \quad (12a)$$

Eqs.

respe

the E

matri

shift

in wh

set Ω

shift

of MA

one r

$$\int_0^{\pi}$$

$$\propto \{$$

while

$$\int_{\pi}^{2\pi} d$$

$$\propto \{.4[$$

For si

the ar

first a

then s

$$H_{ij}^{D} = [A \cdot e^{2i\omega_R t} + B \cdot e^{i\omega_R t} + C \cdot e^{-i\omega_R t} + D \cdot e^{-2i\omega_R t}] \cdot [3I_z^i I_z^j - \vec{I}^i \cdot \vec{I}^j] \quad (12b)$$

Eqs. 12a and b are for heteronuclear and homonuclear dipolar coupling respectively. The time-independent *A*, *B*, *C* and *D* are functions of C^{int} in Eq. 5, the Euler angle set $\Omega' \equiv (\alpha', \beta', \gamma')$ defined by corresponding Wigner rotation matrix elements and the internuclear distance r_{ij}. The non-zero term for chemical shift was

$$H_i^{CS} = [\sigma_{iso} + (A \cdot e^{2i\omega_R t} + B \cdot e^{i\omega_R t} + C \cdot e^{-i\omega_R t} + D \cdot e^{-2i\omega_R t}) \cdot \delta_{aniso}] \cdot I_z^i B_0 \quad (13)$$

in which the terms *A*, *B*, *C* and *D* are functions of C^{int} in Eq. 5 and the Euler angle set $\Omega' \equiv (\alpha', \beta', \gamma')$. Eq. 13 indicates time-independence for the isotropic chemical shift and time-dependence for the anisotropic chemical shift. Under the condition of MAS and no *rf* pulses, The time integral of H_{ij}^{D} in Eq.12a over the first half of one rotor cycle is

$$\begin{aligned} &\int_0^{\pi} d(\omega_R t) \cdot H_{ij}^{D}(\omega_R t) \\ &\propto \{A[e^{2i\pi} - 1] + B[e^{i\pi} - 1] - C[e^{-i\pi} - 1] - D[e^{-2i\pi} - 1]\} \cdot I_z^i S_z^j = (-B + C) \cdot I_z^i S_z^j \end{aligned} \quad (14a)$$

while over the second half of the cycle is

$$\begin{aligned} &\int_{\pi}^{2\pi} d(\omega_R t) \cdot H_{ij}^{D}(\omega_R t) \\ &\propto \{A[e^{4i\pi} - e^{2i\pi}] + B[e^{2i\pi} - e^{i\pi}] - C[e^{-2i\pi} - e^{-i\pi}] - D[e^{-4i\pi} - e^{-2i\pi}]\} \cdot I_z^i S_z^j = (B - C) \cdot I_z^i S_z^j \end{aligned} \quad (14b)$$

For similar reasons, the homonuclear dipolar coupling Hamiltonian in Eq.12b and the anisotropic part of chemical shift Hamiltonian in Eq.13 will be reversed for the first and second half of one rotor period. According to Eq.1, the spin system is then subjected to a lowest-order averaged Hamiltonian

How

infor

char

Acc

and

and

Tabl

roto

dipo

diffe

Table

hal

c

S_0

S.

$$\bar{H} = \frac{1}{\tau_C}\left(\int_0^{\tau C/2} dt \cdot H^{total}(t) + \int_{\tau C/2}^{\tau C} dt \cdot H^{total}(t)\right) \propto \sigma_{iso} I_z^i B_0 \quad (15)$$

However, the ^{13}C-^{15}N heteronuclear dipolar coupling which includes the distance information has to be recovered with the π pulses applied on ^{13}C and/or ^{15}N channels. The Hamiltonian expressed in Eqs. 12-13 can be generally written as

$$H_{D,hetero} = d(t) \cdot I_z S_z \quad (16a)$$

$$H_{D,homo} = d(t) \cdot [3 I_z^i I_z^j - \vec{I}^i \cdot \vec{I}^j] \quad (16b)$$

$$H_{CS,aniso} = d(t) \cdot I_z \quad (16c)$$

According to Eq. 14, the sign of the integral of $d(t)$ will be flipped during the first and second halves of a rotor cycle. In addition, the sign of the spin operators I_z and S_z will be flipped by the π pulses applied on the corresponding channels. Table 2 summarizes the sign of H_D and $H_{CS,aniso}$ in S_0 and S_1 spectra over eight rotor cycles based on the phase cycling scheme. It is clear that the heteronuclear dipolar coupling has a non-zero time averaging over the entire period, thus the difference spectrum will only reflect the heteronuclear dipolar coupling.

Table 2. Hamiltonians in REDOR S_0 and S_1 spectra

	half rotor cycle	1	2	3	4	5	6	7	8	9	10	11	12	13	14	15	16
	$H_{D,hetero}$	+	-	-	+	+	-	-	+	+	-	-	+	+	-	-	+
S_0	$H_{D,homo}$	+	-	+	-	+	-	+	-	+	-	+	-	+	-	+	-
	$H_{CS,aniso}$	+	-	-	+	+	-	-	+	+	-	-	+	+	-	-	+
	$H_{D,hetero}$	+	+	+	+	+	+	+	+	+	+	+	+	+	+	+	+
S_1	$H_{D,homo}$	+	-	+	-	+	-	+	-	+	-	+	-	+	-	+	-
	$H_{CS,aniso}$	+	-	-	+	+	-	-	+	+	-	-	+	+	-	-	+

com

Tab

cou

ave

ave

The

It is

corr

the

peri

$\rho(0$

whe

Usin

for t

in E

A more detailed analysis of the evolution of initial density operator can be completed using the averaged Hamiltonian over the entire phase cycling period. Table 2 indicates that all the interactions except for the heteronuclear dipolar coupling have been averaged to zero over 16 rotor periods. Thus, the time averaging of the total Hamiltonian H_0 can be expressed by the zero-order time averaging of heteronuclear dipolar coupling over 16 rotor periods.

$$H_0 = \left\langle H_{D,hetero} \right\rangle_0 = d \cdot I_z S_z \quad (17)$$

The term *d* is a function of *B* and *C* according to Eq. 14 and is time-independent. It is related to the heteronuclear dipolar coupling frequency and can be further correlated with the internuclear distance between two spins. According to Fig. 10, the initial direction of the spin operator will be in the transverse plane after the CP period. Assume the initial magnetization is along *x* axis in the rotating frame, i.e. $\rho(0) \propto I_x$. The time evolution of the magnetization can be calculated as

$$\rho(t) = \rho(0) - \frac{it}{1!} \cdot r_1 + \frac{(it)^2}{2!} \cdot r_2 - \frac{(it)^3}{3!} \cdot r_3 + \cdots\cdots \quad (18)$$

where

$$\begin{aligned} r_1 &= [H_0, \rho(0)] \\ r_2 &= [H_0, r_1] = [H_0, [H_0, \rho(0)]] \\ r_3 &= [H_0, r_2] = [H_0, [H_0, [H_0, \rho(0)]]] \end{aligned} \quad (19)$$

Using the expression in Eq. 17 for the averaged Hamiltonian and the assumption for the initial density operator, it can be derived straightforwardly that the *r* terms in Eq. 19 for REDOR pulse sequence are

Thus

comb

ρ

=

The

seco

of th

matri

The

the n

The

23.

$$
\begin{aligned}
r_1 &\propto id \cdot I_y S_z \\
r_2 &\propto d^2 \cdot I_x \qquad (20) \\
r_3 &\propto id^3 \cdot I_y S_z
\end{aligned}
$$

Thus, the time evolution of spin operator for REDOR can be obtained from the combination of Eqs. 18 and 20.

$$
\begin{aligned}
&\rho(t) \propto I_x - \frac{it \cdot id}{1!} \cdot I_y S_z + \frac{(it)^2 \cdot d^2}{2!} \cdot I_x - \frac{(it)^3 \cdot id^3}{3!} \cdot I_y S_z + \cdots\cdots \\
&= I_x \cdot [1 - \frac{(dt)^2}{2!} + \cdots\cdots] + I_y S_z \cdot [(dt) - \frac{(dt)^3}{3!} + \cdots\cdots] = I_x \cos(dt) + I_y S_z \sin(dt)
\end{aligned} \qquad (21)
$$

The first term in the right-most expression of Eq. 21 is detectable while the second term is undetectable. This can be understood with the density matrix form of these spin operators. In two-spin systems such as an I-S spin pair, the density matrix of I_x and $I_y S_z$ can be written as

$$
I_x \propto \begin{bmatrix} 0 & 0 & 1 & 0 \\ 0 & 0 & 0 & 1 \\ 1 & 0 & 0 & 0 \\ 0 & 1 & 0 & 0 \end{bmatrix} \text{ and } I_y S_z \propto \begin{bmatrix} 0 & 0 & -i & 0 \\ 0 & 0 & 0 & i \\ i & 0 & 0 & 0 \\ 0 & -i & 0 & 0 \end{bmatrix} \qquad (22)
$$

The detection operator for a two-spin system can be expressed by I^+, and has the matrix form

$$
I^+ \propto \begin{bmatrix} 0 & 0 & 1 & 0 \\ 0 & 0 & 0 & 1 \\ 0 & 0 & 0 & 0 \\ 0 & 0 & 0 & 0 \end{bmatrix} \qquad (23)
$$

The FID is proportional to the trace of the product of the matrices in Eqs. 22 and 23.

From

of se

signa

frequ

the p

transf

transm

serve

trans

polar

^{15}N c

intra-

Hami

The

aniso

respe

rotati

$$I_x \cdot I^+ \propto \begin{bmatrix} 0 & 0 & 0 & 0 \\ 0 & 0 & 0 & 0 \\ 0 & 0 & 1 & 0 \\ 0 & 0 & 0 & 1 \end{bmatrix} \text{ and } I_y S_z \cdot I^+ \propto \begin{bmatrix} 0 & 0 & 0 & 0 \\ 0 & 0 & 0 & 0 \\ 0 & 0 & i & 0 \\ 0 & 0 & 0 & -i \end{bmatrix} \quad (24)$$

From Eq. 24 one can see that the trace of first product is non-zero while the trace of second product is zero. Consequently, Eq. 21 represents that the detectable signal after the REDOR pulse sequence is related to the I-S dipolar coupling frequency as well as the evolution time.

Double CP (DCP) experiments. In the DCP experiments (*cf.* Figure 11), the polarization transfer follows the route $^1H \rightarrow {}^{15}N \rightarrow {}^{13}C$, and the $^{15}N \rightarrow {}^{13}C$ transfer can be selective for ^{13}CO and $^{13}C\alpha$ by setting the spectrometer transmitter close to the ^{13}CO and $^{13}C\alpha$ frequencies.*(18)* The DCP scheme can serve as building blocks to polarize the labeled ^{13}Cs. The spectra selectivity transfer is achieved by rendering the conventional Hartmann-Hahn cross polarization technique frequency dependent. Typically, the *rf* field applied on the ^{15}N channel is comparable to the ^{15}N spectrometer frequency offset so that the intra-system Hamiltonians can be analyzed in a tilted rotating frame. The major Hamiltonians during the $^{15}N \rightarrow {}^{13}C$ transfer step is

$$H_{total} = H_{CS,iso} + H_{CS,aniso} + H_D \quad (25)$$

The terms on the right side of Eq.25 represent the isotropic chemical shift, the anisotropic chemical shift and the ^{13}C-^{15}N heteronuclear dipolar coupling respectively. These terms have the similar form as shown in Eqs. 12-13 in a rotating frame and could be expressed as

$$H_{CS,iso} = \Omega_I I_z + \Omega_S S_z \quad (26a)$$

$$H_{CS,aniso} = \sigma_I(t) I_z + \sigma_S(t) S_z \quad (26b)$$

$$H_D = d(t) I_z S_z \quad (26c)$$

The *I* and S spins represented ^{13}C and ^{15}N. Here we use a similar strategy to calculate the zero-order average Hamiltonian during the ^{15}N-^{13}C CP step as used previously in the REDOR example. However, since the frequency offset Ω is comparable to the Rabi frequency ω_1, it will be more convenient to apply the AHT in a tilted togging frame by considering both Ω and ω_1. Firstly we can transfer the H_D in Eq. 26c into a tilted rotating frame defined by Ω and ω_1. The z axis in the tilted rotating frame is along the direction of the vector sum of Ω and ω_1. The Euler angle set between the rotating frame and the tilted rotating frame is (0, θ, 0) where $\theta \equiv \theta_I = \arctan(\Omega_I / \omega_{1I})$ or $\theta \equiv \theta_S = \arctan(\Omega_S / \omega_{1S})$ for *I* or *S* and ω_{1I} and ω_{1S} are Rabi frequencies applied on *I* and *S* channels respectively. The dipolar coupling Hamiltonian in Eq. 26c will consequently be expressed in the tilted rotating frame as

$$\begin{aligned} H_D^{tilted} &= \exp[-i\theta_I I_y]\exp[-i\theta_S S_y] H_D \exp[i\theta_S S_y]\exp[i\theta_I I_y] = \\ & d(t)\cos\theta_I \cos\theta_S \cdot 2I_z S_z + d(t)\sin\theta_I \sin\theta_S \cdot (I_+ S_- + I_- S_+)/2 + d(t)\cos\theta_S \sin\theta_S \cdot S_z (I_+ + I_-) \\ & + d(t)\cos\theta_S \sin\theta_I \cdot I_z (S_+ + S_-) + d(t)\sin\theta_I \sin\theta_S \cdot (I_+ S_+ + I_- S_-)/2 \end{aligned} \quad (27)$$

The five terms on the right side of Eq. 27 indicate the Z component, zero-quantum (ZQ), single-quantum in *I* spin space (SQI), single-quantum in *S* spin space (SQS) and double-quantum (DQ) transfer respectively. The time-dependent term $d(t)$ has the same representation as in Eq. 16a. In the tilted

rotat

prop

The

rotat

effec

toggl

Each

$\tilde{H}^{log}_{D,Z}$

$\tilde{H}^{log}_{D,Z}$

$+De^{-}$

$+Ce^{i}$

$\tilde{H}^{log}_{D,S}$

$+[Ce^{-}$

$+i[A$

$+[Ce^{-}$

$\tilde{H}^{log}_{D,S}$

$+[Ce$

$+i[A$

$+[Ce$

rotating frame, the effect of *rf* and chemical shift can be written as a new propagator which is along the z axis.

$$U = \exp[-i(\omega_{1I,eff} I_z + \omega_{1S,eff} S_z)t] \quad (28)$$

The effective Rabi frequency equals the vector sum of chemical shift offset and rotating frame Rabi frequency for individual spins, and the magnitude of the effective Rabi frequency follows $\left|\omega_{1,eff}\right| = \sqrt{\Omega^2 + \omega_1^2}$. Based on Eq. 2, the H_D in the toggling frame can be evaluated by

$$\tilde{H}_D^{toggle} = UH_D^{tilted}U^{-1} \quad (29)$$

Each of the five terms in the right side of Eq.27 can be calculated separately.

$$\tilde{H}_{D,Z}^{toggle} \propto I_z S_z \quad (30a)$$

$$\begin{aligned}\tilde{H}_{D,ZQ}^{toggle} \propto (&Ae^{-i[(\omega_{1I,eff}-\omega_{1S,eff})-2\omega_R]t} + Be^{-i[(\omega_{1I,eff}-\omega_{1S,eff})-\omega_R]t} + Ce^{-i[(\omega_{1I,eff}-\omega_{1S,eff})+\omega_R]t} \\ &+De^{-i[(\omega_{1I,eff}-\omega_{1S,eff})+2\omega_R]t})I_+S_- + (Ae^{i[(\omega_{1I,eff}-\omega_{1S,eff})+2\omega_R]t} + Be^{i[(\omega_{1I,eff}-\omega_{1S,eff})+\omega_R]t} \\ &+Ce^{i[(\omega_{1I,eff}-\omega_{1S,eff})-\omega_R]t} + De^{i[(\omega_{1I,eff}-\omega_{1S,eff})-2\omega_R]t})I_-S_+\end{aligned} \quad (30b)$$

$$\begin{aligned}\tilde{H}_{D,SQI}^{toggle} \propto &\{[Ae^{i(\omega_{1I,eff}-2\omega_R)t} + Ae^{-i(\omega_{1I,eff}+2\omega_R)t}] + [Be^{i(\omega_{1I,eff}-\omega_R)t} + Be^{-i(\omega_{1I,eff}+\omega_R)t}] \\ &+[Ce^{i(\omega_{1I,eff}+\omega_R)t} + Ce^{-i(\omega_{1I,eff}-\omega_R)t}] + [De^{i(\omega_{1I,eff}+2\omega_R)t} + De^{-i(\omega_{1I,eff}-2\omega_R)t}]\}I_xS_z \\ &+\{[Ae^{i(\omega_{1I,eff}-2\omega_R)t} - Ae^{-i(\omega_{1I,eff}+2\omega_R)t}] + [Be^{i(\omega_{1I,eff}-\omega_R)t} - Be^{-i(\omega_{1I,eff}+\omega_R)t}] \\ &+[Ce^{i(\omega_{1I,eff}+\omega_R)t} - Ce^{-i(\omega_{1I,eff}-\omega_R)t}] + [De^{i(\omega_{1I,eff}+2\omega_R)t} - De^{-i(\omega_{1I,eff}-2\omega_R)t}]\}I_yS_z\end{aligned} \quad (30c)$$

$$\begin{aligned}\tilde{H}_{D,SQS}^{toggle} \propto &\{[Ae^{i(\omega_{1S,eff}-2\omega_R)t} + Ae^{-i(\omega_{1S,eff}+2\omega_R)t}] + [Be^{i(\omega_{1S,eff}-\omega_R)t} + Be^{-i(\omega_{1S,eff}+\omega_R)t}] \\ &+[Ce^{i(\omega_{1S,eff}+\omega_R)t} + Ce^{-i(\omega_{1S,eff}-\omega_R)t}] + [De^{i(\omega_{1S,eff}+2\omega_R)t} + De^{-i(\omega_{1S,eff}-2\omega_R)t}]\}I_zS_x \\ &+\{[Ae^{i(\omega_{1S,eff}-2\omega_R)t} - Ae^{-i(\omega_{1S,eff}+2\omega_R)t}] + [Be^{i(\omega_{1S,eff}-\omega_R)t} - Be^{-i(\omega_{1S,eff}+\omega_R)t}] \\ &+[Ce^{i(\omega_{1S,eff}+\omega_R)t} - Ce^{-i(\omega_{1S,eff}-\omega_R)t}] + [De^{i(\omega_{1S,eff}+2\omega_R)t} - De^{-i(\omega_{1S,eff}-2\omega_R)t}]\}I_zS_y\end{aligned} \quad (30d)$$

$$\tilde{H}_{D,DQ}^{toggle} \propto (Ae^{-i[(\omega_{1I,eff}+\omega_{1S,eff})-2\omega_R]t} + Be^{-i[(\omega_{1I,eff}+\omega_{1S,eff})-\omega_R]t} + Ce^{-i[(\omega_{1I,eff}+\omega_{1S,eff})+\omega_R]t}$$
$$+De^{-i[(\omega_{1I,eff}+\omega_{1S,eff})+2\omega_R]t})I_+S_+ + (Ae^{i[(\omega_{1I,eff}+\omega_{1S,eff})+2\omega_R]t} + Be^{i[(\omega_{1I,eff}+\omega_{1S,eff})+\omega_R]t} \quad (30e)$$
$$+Ce^{i[(\omega_{1I,eff}+\omega_{1S,eff})-\omega_R]t} + De^{i[(\omega_{1I,eff}+\omega_{1S,eff})-2\omega_R]t})I\_S\_$$

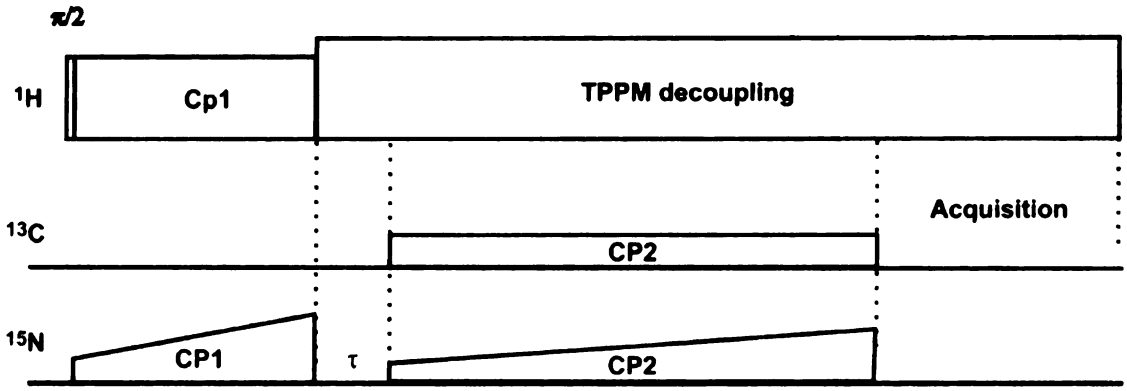

Figure 11 Double Cross Polarization (DCP) pulse sequence. CP1 and CP2 indicate the $^1H \rightarrow ^{15}N$ and $^{15}N \rightarrow ^{13}C$ cross polarization respectively. There is a short delay τ between the first and second CP process. TPPM decoupling was applied during the τ, CP2 and acquisition periods.

The

reco

and

conc

inter

RF

zero

All t

simil

usin

conc

mag

Ham

writt

The

sam

dens

The Eqs. 30 suggests the ZQ, SQI, SQS and DQ components can be selectively recovered when the conditions $\omega_{1I,eff} - \omega_{1S,eff} = n\omega_R$, $\omega_{1I,eff} = n\omega_R$, $\omega_{1S,eff} = n\omega_R$ and $\omega_{1I,eff} + \omega_{1S,eff} = n\omega_R$ (n = 1 or 2) are satisfied respectively. In practice, the conditions $\omega_{1I,eff} = n\omega_R$ and $\omega_{1S,eff} = n\omega_R$ are always avoided because the CSA interaction will also contribute to the zero-order average Hamiltonian under these RF rotational resonance conditions.*(19,20)* Consequently, the general forms of zero-order average Hamiltonian are

$$\left\langle \tilde{H}_D^{toggle} \right\rangle_0 \propto (I_+S_- + I_-S_+) \text{ for } \omega_{1I,eff} - \omega_{1S,eff} = n\omega_R \quad (31a)$$

$$\left\langle \tilde{H}_D^{toggle} \right\rangle_0 \propto (I_+S_+ + I_-S_-) \text{ for } \omega_{1I,eff} + \omega_{1S,eff} = n\omega_R \quad (31b)$$

All the time-oscillated terms will be averaged to zero after one rotor period. A similar derivation of the time evolution of the initial magnetization can be obtained using Eq. 18 with the assumption that the initial condition $\rho(0) \propto S_x$. The initial condition is different from the REDOR sequence because in DCP the ^{1}H magnetization is firstly transferred to ^{15}N instead of ^{13}C. With the averaged Hamiltonian in Eq. 31a, the zero-order averaged Hamiltonian in DCP can be written as

$$H_0 \propto a \cdot I_z S_z + b \cdot (I_+S_- + I_-S_+) \quad (32)$$

The parameters *a* and *b* can be derived from Eqs. 30 and are generally not the same. Based on the zero-order Hamiltonian in Eq. 32, the evolution of initial density matrix should be

$r_0 \propto$

$r_1 =$

$r_2 =$

$= i[($

It ca

mea

mag

EXP

to a

I wi

on t

use

lipic

20

sam

The

vac

with

thro

was

gen

$$r_0 \propto S_x$$
$$r_1 = [H_0, \rho_0] = [aI_zS_z + bI_xS_x + bI_yS_y, S_x] = a[I_zS_z, S_x] + b[I_yS_y, S_x] = ia \cdot I_zS_y - ib \cdot I_yS_z$$
$$r_2 = [H_0, r_1] = [aI_zS_z + bI_xS_x + bI_yS_y, ia \cdot I_zS_y - ib \cdot I_yS_z] = i[aI_zS_z + bI_yS_y, aI_zS_y - bI_yS_z]$$
$$= i[(a^2 + b^2)(S_zS_y - S_yS_z) + ab(I_yI_z - I_zI_y)] = (a^2 + b^2)S_x - abI_x \quad (33)$$

It can be seen from Eq. 33 that the term r_2 includes the spin operator I_x, which means the ^{13}C magnetization can be generated from the coupled ^{15}N magnetization.

EXPERIMENTAL OPTIMIZATION

In the following chapters, multiple solid-state NMR methods will be used to achieve measurements of different characters for the HFP/membrane system. I will give an introduction to the experimental setup in this section and will focus on the results and interpretations of these experiments in the following chapters.

^{13}C-^{31}P REDOR experiment. ^{13}C-^{31}P REDOR experiments are going to be used to measure the distances between ^{13}CO-labeled HFP backbone and the lipid phosphate ^{31}Ps. The sample used for setup contains 0.8 μmol HFPmn and 20 μmol [1-^{13}C]-1,2-dipalmitoyl-*sn*-glycero-3-phosphocholine (1-^{13}C-DPPC). The sample preparation started with dissolution in chloroform of 20 μmol 1-^{13}C-DPPC. The chloroform was removed under a stream of nitrogen followed by overnight vacuum pumping. The lipid film was suspended in 2 mL buffer and homogenized with ten freeze-thaw cycles. Large unilamellar vesicles were formed by extrusion through a 100 nm diameter polycarbonate filter (Avestin, Ottawa, ON). HFPmn was dissolved in 2 mL buffer and the HFPmn and vesicle solutions were then gently vortexed together. The mixture was refrigerated overnight and

ultra

boun

repla

deph

of ea

each

^{13}C-

(ΔS/

the

Dete

whe

with

the

The

τ =

Figu

DPF

a 5,

ultracentrifuged at ~150000g for five hours. The membrane pellet with associated bound HFPmn was transferred to a 4 mm diameter MAS NMR rotor.*(4)*

The REDOR pulse sequence is the same as sketched in Figure 10 by replacing ^{15}N with ^{31}P channel. As described in the previous section, the dephasing period during the "S_1" acquisition contained a ^{13}C π pulse at the end of each rotor cycle except for the last cycle and a ^{31}P π pulse in the middle of each cycle. In principle, the difference spectrum will contain information about the ^{13}C-^{31}P dipolar coupling (d). In practice, the experimental REDOR dephasing $(\Delta S/S_0)^{exp}$ was defined as $(S_0-S_1)/S_0$ where S_0 and S_1 represent the intensities of the interested ^{13}CO resonance in the S_0 and S_1 spectra, respectively. Determination of d was based on fitting $(\Delta S/S_0)^{exp}$ to $(\Delta S/S_0)^{sim}$:

$$\left(\frac{\Delta S}{S_0}\right)^{sim} = 1 - [J_0(\sqrt{2}\lambda)]^2 + \left\{2 \times \sum_{k=1}^{5} \frac{[J_k(\sqrt{2}\lambda)]^2}{16k^2 - 1}\right\} \quad (34)$$

where $\lambda = d\tau$ and J_k is the kth order Bessel function of the first kind.*(21)*

During the setup process, the ^1H and ^{13}C *rf* fields were initially calibrated with adamantane and the ^{13}C cross-polarization field was then adjusted to give the maximum ^{13}CO signal of the sample containing HFPmn and 1-^{13}C-DPPC. The ^{31}P π pulse length was set by minimization of the S_1 signal in this sample for τ = 8 ms and the ^1H TPPM pulse length was set to give the maximum S_0 signal. Figure 12a displays the plot of $(\Delta S/S_0)^{exp}$ and $(\Delta S/S_0)^{sim}$ vs. τ for HFPmn/1-^{13}C-DPPC sample. The best-fit d = 68 Hz according to Eq.34 which corresponded to a 5.6 Å ^{13}C-^{31}P distance (r) based on the relation d (Hz) = 12250 / r^3(Å). The

Figure
diamon
setup.
(b). the
three-s

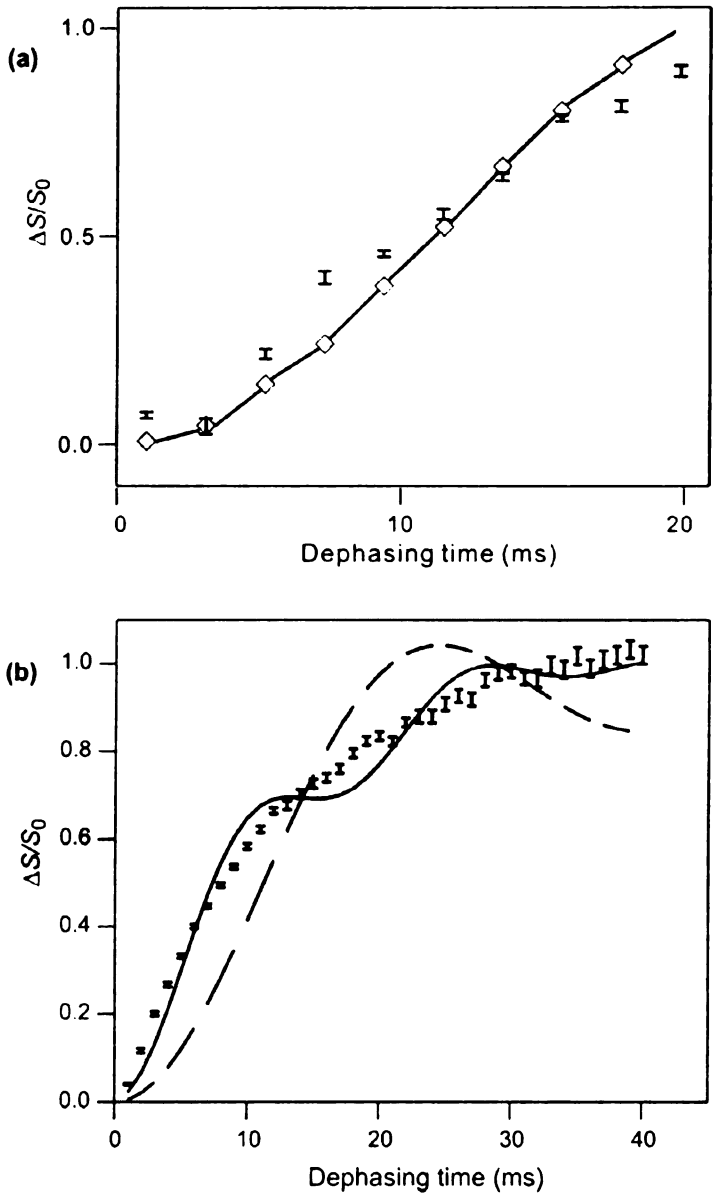

Figure 12 $(\Delta S/S_0)^{exp}$ (error bars) and best-fit $(\Delta S/S_0)^{sim}$ (lines with or without diamonds) vs dephasing time (τ) for (a) the ^{13}C-^{31}P setup and (b) the ^{13}C-^{19}F setup. In panel (a) the experimental data was fit to a two-spin system. In panel (b), the experimental data was fit to either a two-spin system (dash line) or a three-spin system (solid line).

best

crys

phos

glyc

simu

(ΔS

inter

^{13}C

^{13}C

struc

yield

valu

com

inse

with

mod

amir

adja

simu

the

^{19}F-

oligo

best-fit NMR value of *r* is comparable to the 5-6 Å values of *r* observed in the crystal structures of the related lipids, 1,2-dimyristoyl-*sn*-glycero-3-*phosphocholine* (DMPC) and 1,2-dipalmitoyl-*sn*-glycero-[phospho-rac-(1-glycerol)] (DPPC) (which had both been dehydrated) and in molecular dynamics simulations of gel-phase DPPC.*(22-24)* The differences between $(\Delta S/S_0)^{exp}$ and $(\Delta S/S_0)^{sim}$ are likely due to: (1) contributions to $(\Delta S/S_0)^{exp}$ from intra- and intermolecular ^{31}P with comparable values of *r* which contrasts with the single ^{13}CO-^{31}P spin pair model used to calculate $(\Delta S/S_0)^{sim}$; (2) two structurally distinct ^{13}COs in each headgroup with different intra- and intermolecular *r* values; and (3) structural disorder within the headgroups.*(25)* Overall, the 1-^{13}C-DPPC fitting yielded good agreement between the NMR *r* value and the expected range of *r* values in the lipid.

^{13}C-^{19}F REDOR experiment. ^{13}C-^{19}F experiments can provide complementary distance information for ^{13}C-^{31}P experiments in the membrane insertion studies.*(26)* These measurements used the same pulse sequence but with ^{19}F as the third channel. The ^{19}F compound to setup the ^{19}F π pulses was a modified helical peptide F (EQLLKALEFLLKELLEKL) with Phe9 substituted by 2-amino-3-(4-fluorophenyl) propanoic acid (Sigma-Aldrich, St. Louis, MO) and the adjacent Leu10 labeled with ^{13}CO. Figure 12b showed the experimental and simulated dephasing curves for the fluorinated peptide F. It was observed that the experimental data fit better to a "^{19}F-^{13}C-^{19}F" three-spin system than a "^{13}C-^{19}F" two spin system, which may indicate that the helical peptide F could form oligomers and the labeled ^{13}CO could locate close to more than one ^{19}Fs. The

RED

6.8

com

non-

with

bond

→ 1

prev

coup

Here

was

were

inter

labe

Figu

177

resp

the

Fig.

^1H–

tran

and

REDOR-determined ^{13}CO-^{19}F distances for the three spin system were 7.6 Å and 6.8 Å with 162° between the two ^{13}CO-^{19}F vectors. The distances were comparable with the ~ 7.1 Å distance measured in the crystal structure of the non-fluorinated compound.*(27)*

DCP experiments. The DCP building block is expected to be incorporated with other pulse sequences and served to polarize ^{13}C nucleus that are directly bonded to ^{15}N nucleus and not natural abundance ^{13}Cs. The optimization for $^{15}N \rightarrow {}^{13}C$ transfer during the DCP will be described in this section. According to the previous discussion about the theory, both the ZQ and DQ parts of the dipolar coupling Hamiltonian can contribute to the transfer under different conditions. Here the ZQ transfer condition with n = 1 as described in the previous section was chosen and the key parameters such as ω_{1S}, ω_{1I} and Ω_S (I ≡ ^{13}C and S ≡ ^{15}N) were optimized. The ^{13}C transmitter was always set close to the resonance of interest so that $\Omega_I \approx 0$ and the MAS frequency was fixed at 8 kHz. A double ^{13}CO-labeled *N*-acetyl-Leucine (D-^{13}CO-NAL) was used as the setup compound. Figure 13a showed a regular ^{1}H-^{13}C CP spectrum of D-^{13}CO-NAL in which the 177.2 and 175.4 ppm can be assigned to the carboxyl and the acetyl ^{13}COs respectively.*(28)* In Figure 13b where the DCP pulse sequence was applied, only the ^{13}CO peak at 175.4 ppm was observed because it was directly bonded to ^{15}N. Fig. 13c showed that ^{13}C signal came from the $^{15}N \rightarrow {}^{13}C$ transfer instead of $^{1}H \rightarrow {}^{13}C$ transfer by removing the CP2 on ^{15}N channel in Figure 11. The ^{13}C transmitter was set to 160.0 ppm. The optimization of ω_{1S} is shown in Figure 13d and the $^{15}N \rightarrow {}^{13}C$ transfer efficiency was greatly affected by the ^{15}N *rf* field. Figure

13e shows the arrayed spectra for calibrating the ^{15}N frequency offset. The optimized ^{15}N *rf* field was 14.8 kHz and the ^{15}N frequency offset was 5.5 kHz. The center frequency of ^{13}C ramp during the $^{15}N \rightarrow {}^{13}C$ transfer step was 24.0 kHz so that the condition of ZQ n = 1 transfer was satisfied. In addition, ~ 10 % ^{13}C ramp and ~ 8 ms contact time was required for a efficient $^{15}N \rightarrow {}^{13}C$ transfer and the optimized transfer efficiency was 40-50 % compared with direct ^{1}H-^{13}C CP experiment.

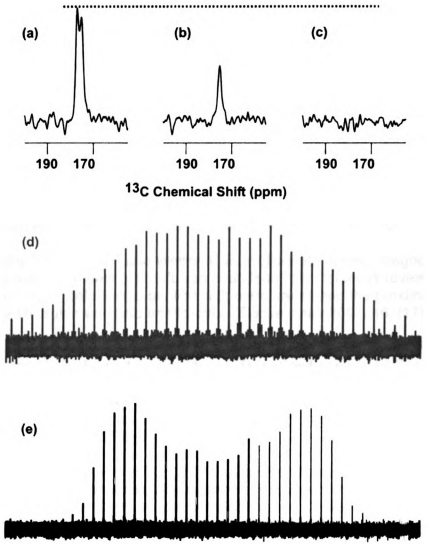

Figure 13 (a) ^{13}CO region of *D*-^{13}CO-NAL spectrum acquired using the CP pulse sequence. (b) ^{13}CO region of *D*-^{13}CO-NAL spectrum acquired using the DCP pulse sequence. The vertical scales in (a) and (b) are the same so that the relative intensity reflects the DCP transfer efficiency. Both spectra were processed with 100Hz Gaussian line broadening and baseline correction. (c) A negative control experiments without ^{15}N CP2 amplitude (*cf.* Figure 11). The number of scans used in (a), (b) and (c) was 32. Panel (d) displays the optimization of ^{15}N CP2 amplitude as given in Fig.11. The ^{15}N *rf* field was scanned from 11.8 kHz to 17.8 kHz with the increment of 0.16 kHz. Panel (e) displays the optimization of ^{15}N CP2 offset frequency. The offset was scanned from -10 kHz to 10 kHz with the increment of 0.5 kHz.

REFERENCE

1. Tycko, R., Biomolecular solid state NMR: Advances in structural methodology and applications to peptide and protein fibrils. *Annual Review of Physical Chemistry* **2001,** 52, 575-606.

2. Drobny, G. P.; Long, J. R.; Karlsson, T.; Shaw, W.; Popham, J.; Oyler, N.; Bower, P.; Stringer, J.; Gregory, D.; Mehta, M.; Stayton, P. S., Structural studies of biomaterials using double-quantum solid-state NMR spectroscopy. *Annual Review of Physical Chemistry* **2003,** 54, 531-571.

3. Hong, M., Oligomeric structure, dynamics, and orientation of membrane proteins from solid-state NMR. *Structure* **2006,** 14, (12), 1731-1740.

4. Qiang, W., Yang, J., and Weliky, D.P., Solid-state nuclear magnetic resonance measurements of HIV fusion peptide to lipid distances reveal the intimate contact of beta strand peptide with membranes and the proximity of the Ala-14-Gly-16 region with lipid headgroups. *Biochemistry* **2007,** 46, (17), 4997-5008.

5. Qiang, W., Bodner, M.L., and Weilky, D.P., Solid-state NMR Spectroscopy of HIV Fusion Peptides Associated with Host-Cell-Like Membranes: 2D Correlation Spectra and Distance Measurements Support a Fully Extended Conformation and Models for Specific Antiparallel Strand Registries. *J. Am. Chem. Soc.* **2008,** 130, 5459-5471.

6. Qiang, W., and Weilky, D.P., HIV Fusion Peptide and Its Cross-Linked Oligomers: Efficient Syntheses, Significance of the Trimer in Fusion Activity, Correlation of β Strand Conformation with Membrane Cholesterol, and Proximity to Lipid Headgroups. *Biochemistry* **2009,** 48, (2), 289-301.

7. Qiang, W., Sun, Y., and Weliky, D.P., A strong correlation between fusogenicity and membrane insertion depth of the HIV fusion peptide. *submitted to Proc. Natl. Acad. Sci. USA.*

8. Haeberlen, U., High Resolution NMR in solids Selective Averaging. **1976.**

9. Gullion, T.; Schaefer, J., Rotational-echo double-resonance NMR. *J. Magn. Reson.* **1989,** 81, (1), 196-200.

10. Hing, A. W.; Tjandra, N.; Cottam, P. F.; Schaefer, J.; Ho, C., An investigation of the ligand-binding site of the glutamine-binding protein of Escherichia coli using rotational-echo double-resonance NMR. *Biochemistry* **1994,** 33, (29), 8651-61.

11. Gullion, T., Introduction to rotational-echo, double-resonance NMR. *Concepts Magn. Reson.* **1998,** 10, (5), 277-289.

12. Middleton, D. A.; Ahmed, Z.; Glaubitz, C.; Watts, A., REDOR NMR on a hydrophobic peptide in oriented membranes. *Journal of Magnetic Resonance* **2000,** 147, (2), 366-370.

13. Jaroniec, C. P.; Tounge, B. A.; Herzfeld, J.; Griffin, R. G., Frequency selective heteronuclear dipolar recoupling in rotating solids: Accurate ^{13}C-^{15}N distance measurements in uniformly ^{13}C, ^{15}N-labeled peptides. *Journal of the American Chemical Society* **2001,** 123, (15), 3507-3519.

14. Murphy, O. J., 3rd; Kovacs, F. A.; Sicard, E. L.; Thompson, L. K., Site-directed solid-state NMR measurement of a ligand-induced conformational change in the serine bacterial chemoreceptor. *Biochemistry* **2001,** 40, (5), 1358-1366.

15. Forrest, T. M.; Wilson, G. E.; Pan, Y.; Schaefer, J., Characterization of Cross-Linking of Cell-Walls of Bacillus- Subtilis By a Combination of Magic-Angle Spinning Nmr and Gas- Chromatography Mass-Spectrometry of Both Intact and Hydrolyzed C-13-Labeled and N-15-Labeled Cell-Wall Peptidoglycan. *Journal of Biological Chemistry* **1991,** 266, (36), 24485-24491.

16. Merritt, M. E.; Christensen, A. M.; Kramer, K. J.; Hopkins, T. L.; Schaefer, J., Detection of intercatechol cross-links in insect cuticle by solid-state carbon-13 and nitrogen-15 NMR. *Journal of the American Chemical Society* **1996,** 118, (45), 11278-11282.

17. Hong, M.; Griffin, R. G., Resonance assignments for solid peptides by dipolar-mediated C- 13/N-15 correlation solid-state NMR. *Journal of the American Chemical Society* **1998,** 120, (28), 7113-7114.

18. Baldus, M.; Petkova, A. T.; Herzfeld, J.; Griffin, R. G., Cross polarization in the tilted frame: assignment and spectral simplification in heteronuclear spin systems. *Molecular Physics* **1998,** 95, (6), 1197-1207.

19. Osa, T. G., Griffin, R.G., and Levitt, M.H., Rotary resonance recoupling of dipolar interactions in solid state nuclear magnetic resonance spectroscopy. *J. Chem. Phys* **1988,** 89, 692-695.

20. Gan, Z. H., and Grant, D.M., Rotational resonance in a spin-locked field for solid-state NMR. *Chem. Phys. Lett.* **1990,** 168, 304-308.

21. Mueller, K. T., Analytical Solutions for the Time Evolution of Dipolar-dephasing NMR Signals. *Journal of Magnetic Resonance Series A* **1995,** 113, (1), 81-93.

22.
simu
surfa

23.
pack
dimy

24.
Natu

25.
Stayt
stath
Cher

26.
struc
RED

27.
nove

28.
influ
State

22. Venable, R. M., Brooks, B.R., and Pastor, R.W., Molecular dynamics simulations of gel ($L\beta_1$) phase lipid bilayers in constant pressure and constant surface area ensembles. *J. Chem. Phys* **2000,** 112, 4822-4832.

23. Pascher, I., Sundell, S., Harlos, K., and Eibl, H., Conformation and packing properties of membrane lipids: The crystal structure of sodium dimyristoylphosphatidylglycerol. *Biochim. Biophys. Acta.* **1987,** 896, 77-88.

24. Pearson, R. H., and Pascher, I., Molecular structure of lecithin dihydrate. *Nature* **1979,** 281, 499-501.

25. Raghunathan, V.; Gibson, J. M.; Goobes, G.; Popham, J. M.; Louie, E. A.; Stayton, P. S.; Drobny, G. P., Homonuclear and heteronuclear NMR studies of a statherin fragment bound to hydroxyapatite crystals. *Journal Of Physical Chemistry B* **2006,** 110, (18), 9324-9332.

26. Toke, O.; Maloy, W. L.; Kim, S. J.; Blazyk, J.; Schaefer, J., Secondary structure and lipid contact of a peptide antibiotic in phospholipid Bilayers by REDOR. *Biophys. J.* **2004,** 87, (1), 662-674.

27. Taylor, K. S., Lou, M.Z., Chin, T.M., Yang, N.C., and Garavito, R.M., A novel, multilayer structure of a helical peptide. *Protein sci.* **1996,** 5, 414-421.

28. Bodner, M. L., *Solid state nuclear magnetic resonance of the HIV-1 and influenza fusion peptides associated with membranes.* Ph. D. thesis, Michigan State University: East Lansing, 2006; p 122.

CHAPTER IV

SECONDARY STRUCTURES OF MEMBRANE-ASSOCIATED HIV FUSION PEPTIDE OLIGOMERS

BACKGROUND

The ~ 20-residue HIV fusion peptide (HFP) (with the sequence AVGIGALFLGFLGAAGSTMGARS) has been considered to be a good model peptide to study the properties of HIV gp41 induced membrane fusion process, at least to the lipid mixing stage. The free HFP causes fusion of liposomes and erythrocytes, and numerous mutational studies have shown strong correlations between fusion peptide-induced liposome fusion and viral/host cell fusion.*(1-4)* A variety of experimental methods have shown that the HFP can assume helical or non-helical structures when associated with micelles or membranes with different components or with different peptide to phospholipids molar ratios.*(5-16)* For HFP associated with negatively charged sodium dodecyl sulfate (SDS) micelles, one liquid-state NMR study showed that there was uninterrupted α-helical conformation from I4 to M19,*(15)* while another study showed a helix from I4 to A14 followed by a β turn.*(11)* For HFP associated with neutral dodecylphosphocholine (DPC) micelles, helical structure was detected from I4 to L12.*(16, 35)* Cholesterol is an important membrane component because the cholesterol:phospholipid molar ratios are ~0.5 and 0.8 for HIV host cell and HIV membranes, respectively.*(17)* Solid-state NMR provided residue-specific conformational information about HFP associated with membranes whose lipid headgroup and cholesterol composition were comparable to that of host cells of

the virus. A β strand conformation was observed for residues A1-G16, while A21 appears to be unstructured.*(18,19)* In addition, recent solid-state NMR studies showed that the secondary structure of the membrane-associated HFP can be affected by the existence of pre-HFP domains, i.e. the hairpin formed by CHR and NHR domains. It has been observed that in the cholesterol-containing membranes with comparable peptide to lipid molar ratio, more fraction of α-helix was presented for the HFP samples with the pre-HFP domain than those without the pre-HFP domain.*(20)*

This chapter will summarize the residue specific chemical shifts obtained with 2D solid-state NMR and compare the experimental ^{13}C chemical shifts with the RefDB database to determine the secondary structures of the labeled residues.(*23*) This database correlates the ^{1}H, ^{13}C and ^{15}N chemical shifts of previously assigned proteins and the secondary structures determined from X-ray coordinate data of these proteins. In the database, the secondary structures of residues were classified as helix, beta strand and coil based on the ϕ and ψ dihedral angles. A residue was defined as helix if $-120 < \phi < -34$ and $-80 < \psi < 6$. A residue was defined as beta strand if $-180 < \phi < -40$ or $160 < \phi < 180$ and $70 < \psi < 180$ or $-180 < \psi < -170$. A residue with dihedral angles in other regions was defined as coil.(*23*) With the information of secondary structure, we will discuss (1) the effect of the existence of cholesterol on the secondary structure, and (2) the effect of HFP constructs on the secondary structure. For the third part, the chemical shift information from four different HFP constructs, HFPmn, HFPdm,

HFI

will

MA

eth

1.2

the

The

pho

gly

sig

ten

"PC

Th

the

1:5

ch

sp

an

rer

lipi

HFPtr and HFPmn_mut, will be summarized and the similaritiesy and differences will be discussed.

MATERIALS AND METHODS

NMR Sample Preparation. Solid-state NMR samples were made with ether-linked lipids 1,2-di-*O*-tetradecyl-*sn*-glycerol-3-phosphocholine (DTPC) and 1,2-di-*O*-tetradecyl-*sn*-glycerol-3-[phosphor-*rac*-(1-glycerol)] (DTPG) because these are commercially available lipids which do not contain carbonyl groups. The typical ester-linked phospholipids such as 1,2-dimyristoyl-*sn*-glycerol-3-phosphocholine (POPC) and 1,2-dimyristoyl-*sn*-glycerol-3-[phosphor-*rac*-(1-glycerol)] (POPG) were not chosen their large natural abundance lipid ^{13}CO signals would overlap with the peptide ^{13}CO signals. For the current chapter, the term "PC:PG" denotes the membrane with 4:1 DTPC:DTPG ratio and the term "PC:PG:CHOL" denotes the membrane with 8:2:5 DTPC:DTPG:cholesterol ratio. These ratios reflect the approximate fraction of phospholipids and cholesterol in the HIV-infected host cell.(*17*) The typical peptide strand:lipid molar ratios are 1:50 for PC:PG and 1:25 for PC:PG:CHOL, and the total amount of lipid and cholesterol are 20 μmol for PC:PG and 30 μmol for PC:PG:CHOL unless specifically mentioned.

Each sample preparation began with dissolution in chloroform of the total amount of lipid and/or cholesterol as described above. The chloroform was removed under a stream of nitrogen followed by overnight vacuum pumping. The lipid film was suspended in 2 mL of buffer and homogenized with 10 freeze-thaw

cyc

dia

HF

eth

wis

pep

PC

ves

PC

ultr

bor

the

an

Le

(Va

lab

ms

the

de

lab

sh

40

cycles. Large unilamellar vesicles were formed by extrusion through a 100 nm diameter polycarbonate filter. For PC:PG samples, the corresponding amount of HFPs were dissolved in 30 mL of *N*-(2-hydroxyethyl)piperazine-*N'*-2-ethanesulfonic acid (HEPES) buffer, and the peptide solution was added drop wise into the vesicle solution with gentle vortex to prevent the aggregation of the peptides and to increase the population of α-helical conformation. For PC:PG:CHOL samples, the HFPs were dissolved in 2 mL HEPES buffer and the vesicle and HFP solutions were mixed together. Both mixtures with PC:PG and PC:PG:CHOL were vortexed at ambient temperature for overnight and ultracentrifuged at ~150000g for 5 hours. The membrane pellet with associated bound HFP was transferred to a 4 mm diameter MAS NMR rotor. The majority of the HFP binds to membranes under these conditions.*(21,22)*

Solid-state NMR Experiments. All HFPmn_muts were singly-^{13}CO labeled and the HFPmn, HFPdm and HFPtr were uniformly-^{13}C-labeled at Ile4, Ala6 and Leu12. All solid-state NMR experiments were conducted on a 9.4T spectrometer (Varian Infinity Plus, Palo Alto, CA). The ^{13}CO chemical shifts for different ^{13}CO-labeled HFPmn_mut were determined from the ^{13}C-^{31}P REDOR S_0 spectra with 2 ms dephasing time and the secondary structures were obtained by comparing the experimental ^{13}CO chemical shifts to the RefDB databases.*(23)* A more detailed assignment was done for HFPmn. HFPdm and HFPtr with uniformly ^{13}C labeled residues using Proton-driven Spin-diffusion (PDSD) methods. All ^{13}C shifts were externally referenced to the methylene resonance of adamantane at 40.5 ppm. The REDOR pulse sequences is similar to the sequence sketched in

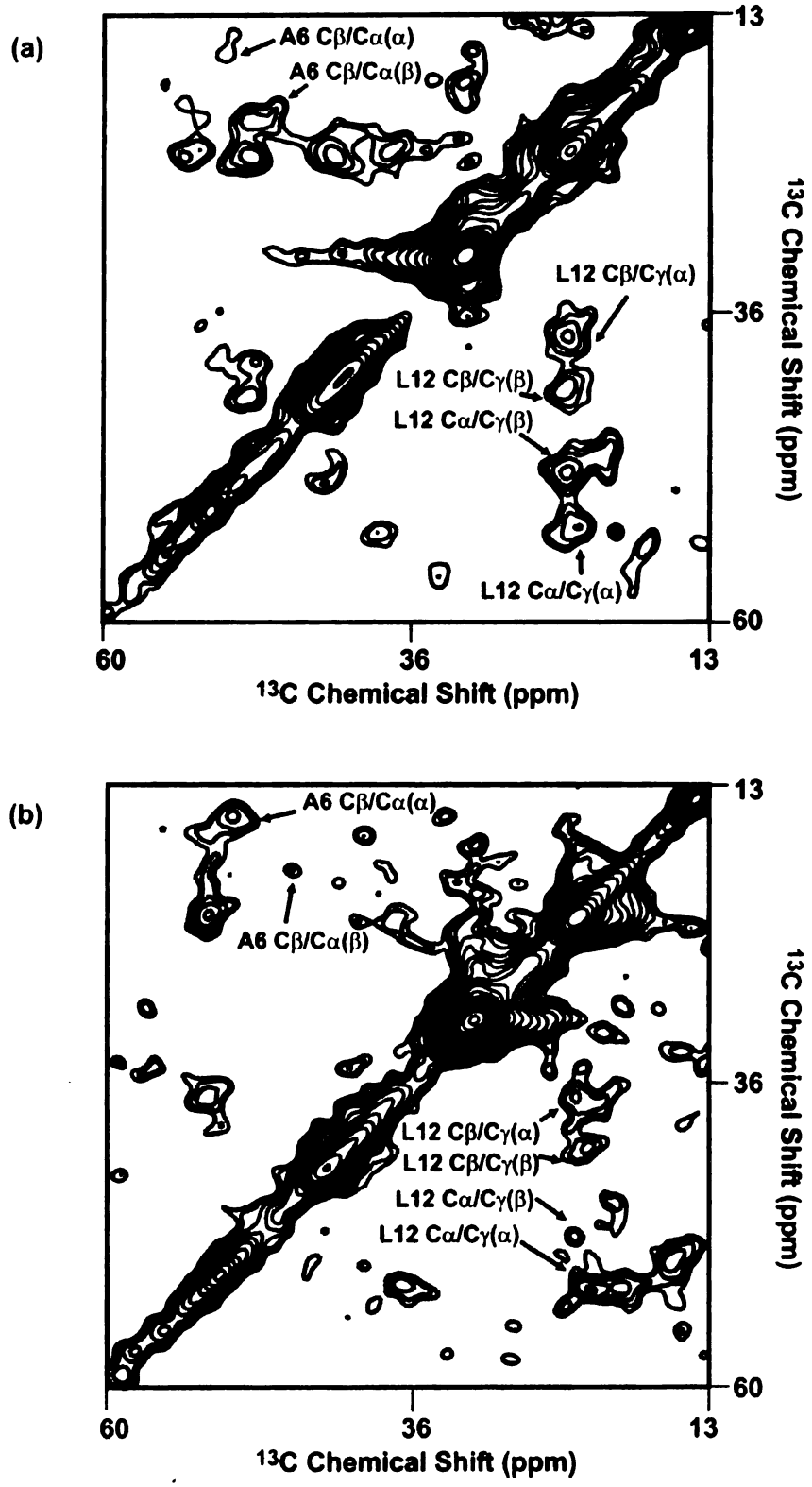

Figure 14 PDSD spectra for (a) HFPmn in PC:PG and (b) HFPdm in PC:PG.

Fig

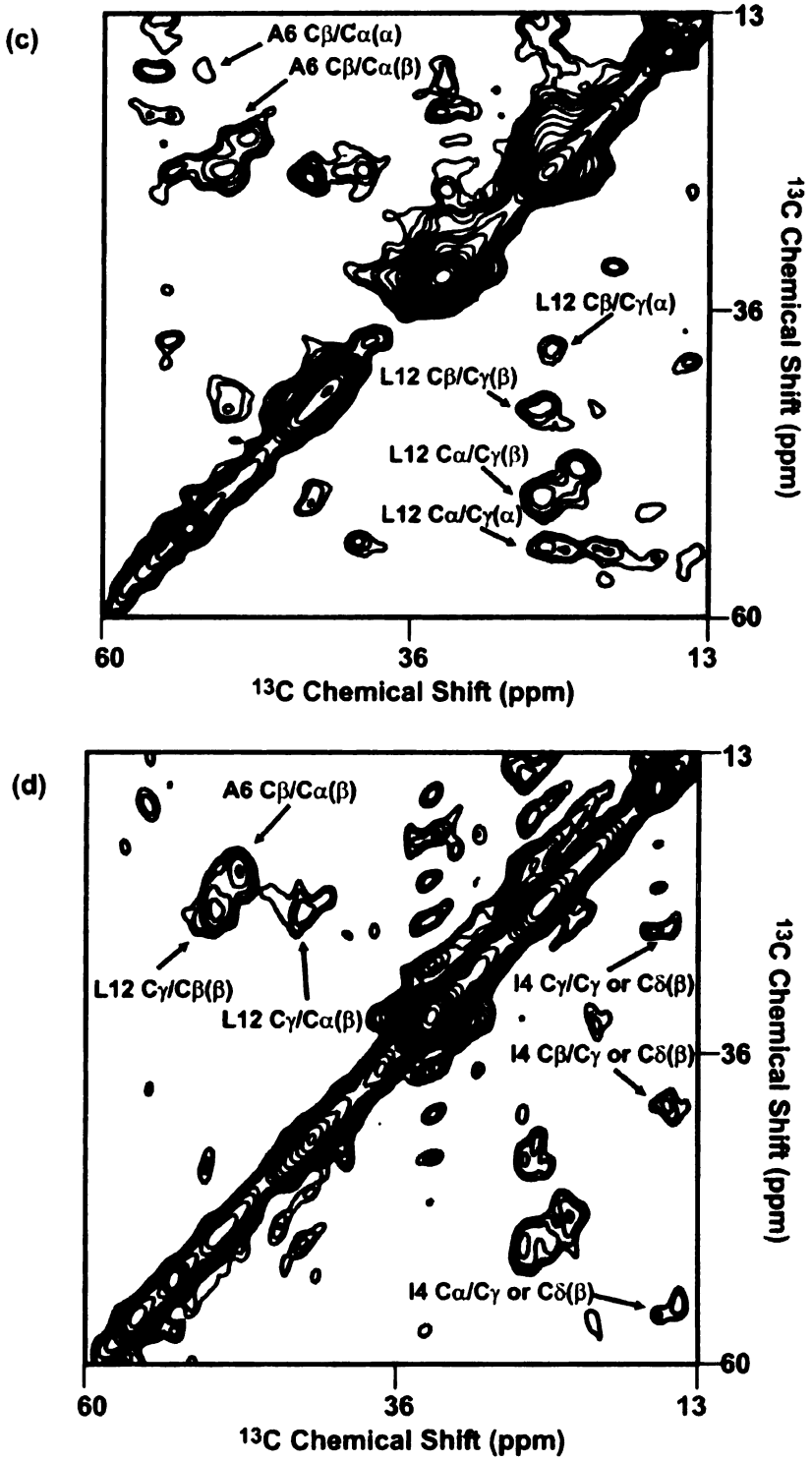

Figure 14 PDSD spectra for (c) HFPtr in PC:PG and (d) HFPmn in PC:PG:CHOL.

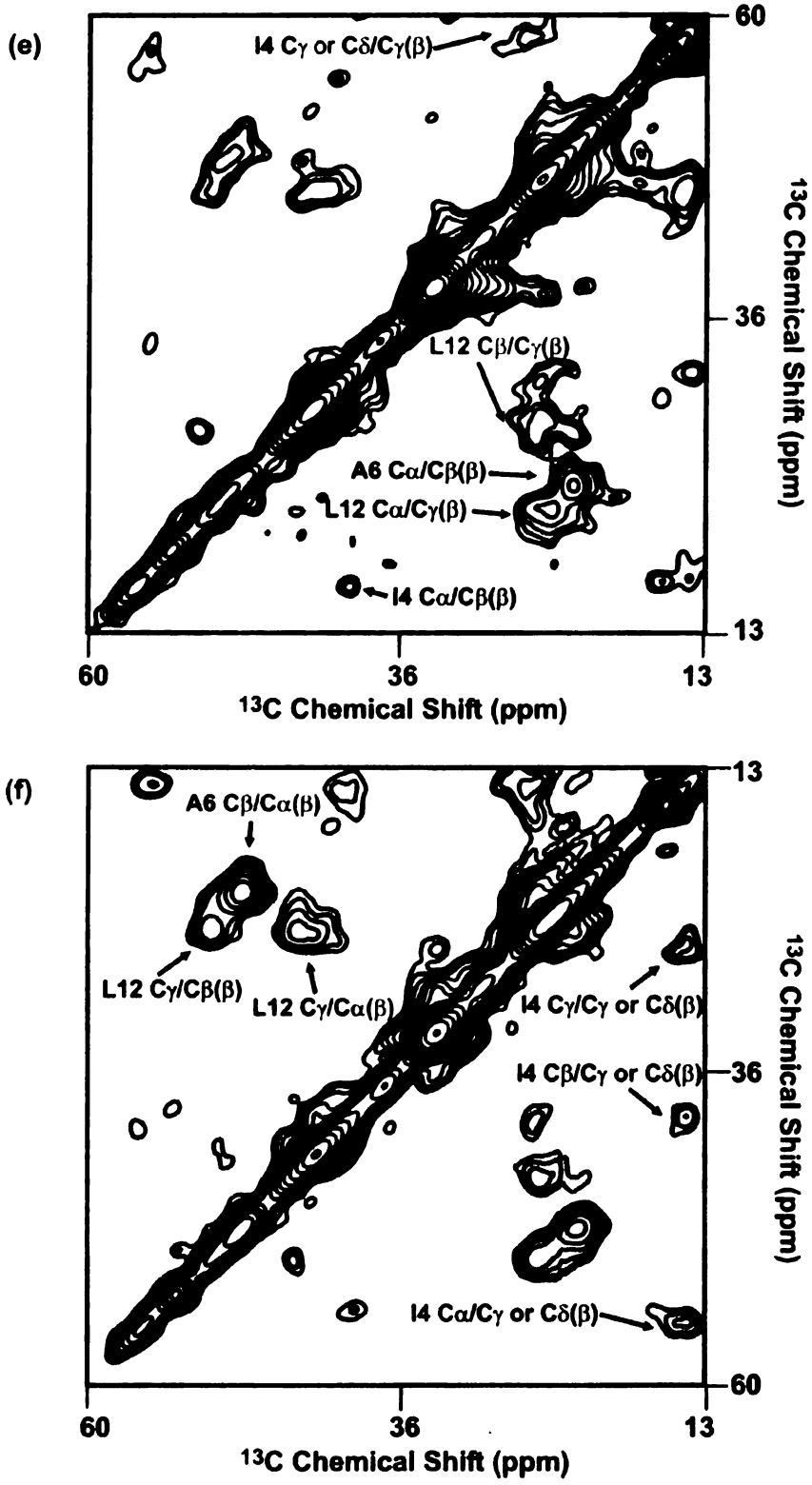

Figure 14 PDSD spectra for (e) HFPdm in PC:PG:CHOL and (f) HFPtr in PC:PG:CHOL.

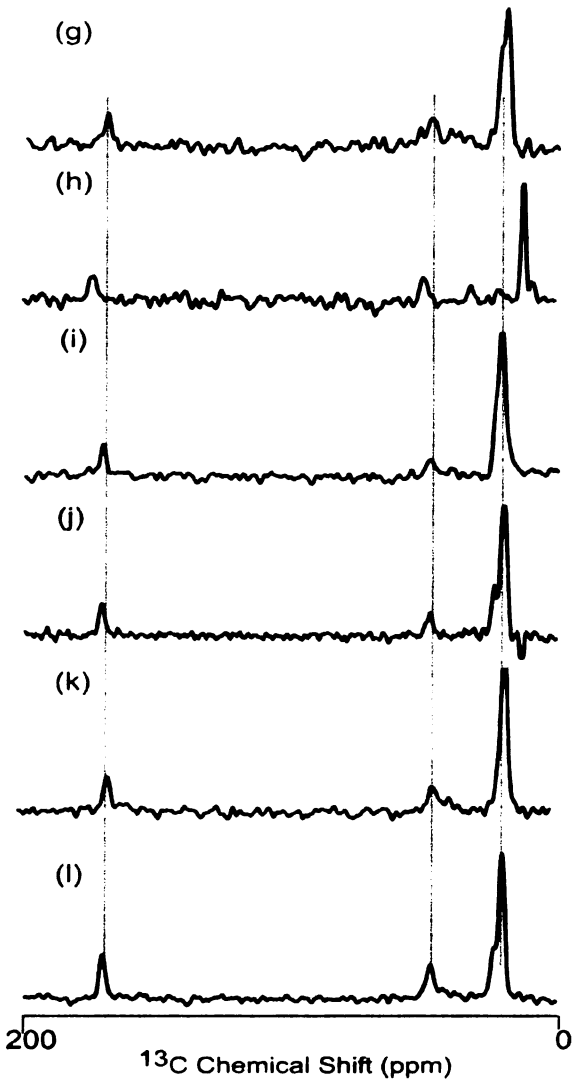

Figure 14 (f) HFPtr in PC:PG:CHOL. All spectra were processed with 100 Hz Gaussian line broadening in both dimensions. The individual peaks were assigned and given in the spectra. For example, the peak assigned to A6 Cβ/Cα(β) represent the cross peak between Cβ(f_1 dimension) and Cα(f_2 dimension) for Ala-6 in β-strand conformation. The spectra (g) through (l) display the representative 1D slice of the PDSD spectra (a) through (f) respectively. For the spectra (a), (c), (d), (e) and (f), the 1D slice is along ~23 ppm in the f_1 dimension which corresponds to the Cβ of Ala-6 in β-strand conformation. For the spectrum (b), the 1D slice is along ~18 ppm in the f_2 dimension which corresponds to the Cβ of Ala-6 in α-helical conformation.

Figure

paran

used

kHz r

50 kH

and

NAL

to en

RES

for

PC:F

For

Ile4

for H

resic

conc

sam

stra

PC:

Ala6

whic

Figure 10 with ^{31}P as the third channel instead of ^{15}N. The experimental parameters for ^{13}C-^{31}P REDOR will be discussed in chapter VI. The parameters used in PDSD experiments (*cf.* Figure 14a) are: 10 kHz MAS frequency; 44-64 kHz ramp on the ^{13}C CP *rf* field; 62.5 kHz ^{1}H CP *rf* field; 2 ms CP contact time; 50 kHz ^{13}C $\pi/2$ pulse *rf* field; 25 μs t_1 dwell time; 200 t_1 values; 20 μs t_2 dwell time; and 1 s recycle delay. The parameters were optimized using uniformly labeled NAL (*cf.* Figure 14b). Both REDOR and PDSD experiments were done at -50 °C to enhance the ^{13}C signal.

RESULTS AND DISCUSSION

Residue Specific Chemical Shifts. Figure 14 displays the PDSD spectra for HFPmn, HFPdm and HFPtr in PC:PG and PC:PG:CHOL.*(24)* For PC:PG:CHOL spectra, the assignments were achieved for Ile4, Ala6 and Leu12. For PC:PG spectra, the assignments were achieved for Ala6 and Leu12, but the Ile4 cross peaks were not clearly identified. Figure 15a-f shows the ^{13}CO peaks for HFPmn_mut in PC:PG and PC:PG:CHOL. The ^{13}C chemical shifts of these residues were summarized in the Table 3a through Table 3h. The following conclusions can be obtained by directly comparing the chemical shifts for these samples: (1) The HFPmn, HFPdm and HFPtr can adopt both α-helical and β-strand structures in PC:PG and adopt only β-strand conformation in PC:PG:CHOL. (2) There are not obvious chemical shift differences for residue Ala6 and Leu12 between the three oligomers in either PC:PG or PC:PG:CHOL, which probably means the oligomerization will not affect the secondary structure

of the region around Ala6 and Leu12. (3) There is a mixture of α-helix and β-strand conformations for the residues Ala6, Leu9 and Leu12 of HFPmn_mut in both PC:PG and PC:PG:CHOL. The fraction of α-helix is higher in PC:PG compared with in PC:PG:CHOL.

Table 3a. Assignments of residues in HFPmn with PC:PG[a]

Residues	Cα	Cβ	Cγ	CO
Ala6	51.0	23.3		175.3
	(55.8)[b]	(18.1)		(180.3)
Leu12	52.8	46.6	26.1	173.7
	(57.7)	(42.4)	(25.9)	(178.8)

[a] All chemical shifts are in unit of ppm.
[b] The chemical shifts shown in parentheses indicate α-helical conformation.

Table 3b. Assignments of residues in HFPdm with PC:PG

Residues	Cα	Cβ	Cγ	CO
Ala6	50.5	23.7		175.1
	(55.8)	(18.3)		(180.2)
Leu12	53.4	46.0	26.2	173.2
	(57.8)	(41.7)	(26.0)	(179.1)

Table 3c. Assignments of residues in HFPtr with PC:PG

Residues	Cα	Cβ	Cγ	CO
Ala6	51.1	23.3		175.4
	(55.8)	(17.8)		(180.3)
Leu12	53.5	45.8	27.0	173.6
	(57.8)	(41.9)	(26.9)	(179.2)

Table 3d. Assignments of residues in HFPmn with PC:PG:CHOL

Residues	Cα	Cβ	Cγ	CO
Ile4	59.2	41.8	27.2	174.2
Ala6	50.6	22.8		175.3
Leu12	53.5	46.5	27.0	173.7

Table 3e. Assignments of residues in HFPdm with PC:PG:CHOL

Residues	Cα	Cβ	Cγ	CO
Ile4	58.9	42.0	27.5	173.9
Ala6	50.3	22.7		175.5
Leu12	53.3	45.8	26.5	173.5

Table 3f. Assignments of residues in HFPtr with PC:PG:CHOL

Residues	Cα	Cβ	Cγ	CO
Ile4	58.2	41.2	27.4	174.2
Ala6	50.4	23.3		175.1
Leu12	52.9	46.3	26.5	174.1

Table 3g. ^{13}CO chemical shift of residues in HFPmn_mut with PC:PG

Residues	Ala1	Ile4	Ala6	Leu9	Leu12	Ala14
^{13}CO chemical shift (ppm)	175.6	176.5	175.8 (180.3)	175.5 (179.3)	175.4 (178.9)	176.8 (179.3)

Table 3h. ^{13}CO chemical shift of residues in HFPmn_mut with PC:PG:CHOL

Residues	Ala1	Ile4	Ala6	Leu9	Leu12	Ala14
^{13}CO chemical shift (ppm)	175.5	174.9	176.1 (179.8)	175.8 (179.2)	175.8 (179.0)	176.9

The results shown above suggested the dependence of global secondary structure of HFP constructs on the lipid membrane composition, especially the presence of cholesterol. These data also indicated there was not obvious HFP constructs-secondary structure correlation for HFPmn_mut, HFPmn, HFPdm and HFPtr, which might suggested that the secondary structure of HFP was not a crucial factor to affect the HFP fusion activities because these HFP constructs were known to have very different fusogenities.*(25-27)* In the following two sections, the effect of cholesterol and constructs on the HFP conformation will be discussed.

Cholesterol-dependence of the HFP Conformation. The presence of cholesterol in membranes is known to increase the lateral molecular packing density and membrane tensile strength, decrease the permeability of water

through the membrane, and promote formation of the "liquid-ordered phase".*(28-33)* This phase is characterized by a rapid lateral molecular translational diffusion coefficient similar to that of the "liquid-disordered" phase at high temperature without cholesterol and high configurational order of the lipid acyl chains similar to that of the "solid-ordered" phase at low temperature without cholesterol.*(33,34)* The chemical shifts in Table 3a through 3f suggested that Ala6 and Leu12 in HFPmn, HFPdm and HFPtr will adopt a mixture of α-helical and β-strand conformation in PC:PG and only β-strand conformation in PC:PG:CHOL. In another set of experiments shown in Figure 15g-i, the ^{13}CO chemical shift of Ala15 in HFPmn, HFPdm and HFPtr were measured when the peptides were associated with PC:PG or PC:PG:CHOL. It was observed that the predominant ^{13}CO chemical shift in PC:PG was ~178 ppm with a shoulder at ~176 ppm, while in PC:PG:CHOL there were single peaks at ~176 ppm. The 178 ppm signal was assigned to helical conformation and the 176 ppm signal was assigned to β-stand conformation for Ala15.*(26)* The combination of these two pieces of information suggested there was partial α-helical conformation formed in PC:PG for the hydrophobic region of HFP constructs, i.e. Ala6 through Ala15. The helical conformation of the residues Ala6 through Ala15 detected in membranes is in general agreement with the observed conformation for this region in micelles in previous solution NMR experiments. There was a general agreement about the formation of an α-helix from residues Ile4 to Leu12 in both SDS and DPC micelles, while some experiments supported the fact that the helix can be extended to Met19.*(11,15)* A recent solution NMR structure for the N-terminal 23

residue HFP also indicated the formation of an α-helix from Ile4 to Ala14 in micelles.*(35)* In addition, a similar correlation between the presence of membrane cholesterol and the preference of β-strand conformation has been observed for the influenza virus fusion peptide so that the correlation may be a general property of fusion peptides.*(36,37)* Although the reasons for the structural effect of membrane cholesterol are poorly understood, it is useful to consider the increased lateral molecular packing density in cholesterol-containing membranes and the possibility to form large β sheet aggregates for the β-strand HFPs.*(31)* Relative to the β aggregates, the small monomeric α-helix might experience a more positive increase in free energy of membrane insertion with higher packing density.

Construct-dependence of the HFP Conformation. Different HFP constructs were known to induce lipid mixing and vesicle fusion with different rates. One previous study concluded that the lipid mixing rate induced by HFPtr was at least 15 times faster compared with that induced by HFPmn, and HFPdm has a fusion activity between HFPmn and HFPtr.*(25)* In addition, there have been studies both *in vivo* and *in vitro* which showed that the V2E mutation has a transdominant effect on the fusion activity of HFP.*(27)* One possible explanation is that there is a required secondary structure for HFP to induced vesicle fusion and different HFP constructs would adopt different fractions of such fusion active conformation. In that case one would expect to observe a continuous increase of a certain secondary structure following the trend HFPmn_mut < HFPmn < HFPdm < HFPtr. In figure 14a-c, the relative intensities of Cα/Cβ cross peaks for

Ala6 in α-helical and β-strand conformations are different for different HFP constructs. For HFPmn and HFPtr, the cross peaks for β-strand conformation is more intense compared with the peaks for α-helix. For HFPdm, on the other hand, the cross peak for helical structure is more intense compared with that for strand structure. Figure 16a displays the 1D slice along the chemical shift of Cγ in f_1 dimension for HFPmn, HFPdm and HFPtr. This position was chosen because the chemical shifts of Cγ of Leu12 in helical and strand conformations were very close according to the Table 3a-c, which would make it convenient to compare the relative intensity of cross peaks for the two conformations directly. Figure 16a indicates that for Leu12, there is more β-strand than α-helix in HFPmn and HFPtr, and more helix than strand in HFPdm. The trend that the relative helical fraction in HFPdm is larger compared with that in HFPmn and HFPtr was also observed in other sets of ^{13}C-^{31}P REDOR experiments for Ala6 and Ala15.(*26*) As shown in Figure 16b, the ^{13}CO intensity for α-helical conformation is greater than that for β-strand conformation in HFPdm, but not in HFPmn or HFPtr. In addition, the ^{13}CO chemical shifts for HFPmn_mut summarized in Table 3h reveals that for a non-fusogenic HFP construct, the residues Ala6, Leu9, Leu12 and Ala14 can adopt both helical and strand structures. The combination of these information suggested (1) the loss of fusion activity does not associate with the disappearance of a particular secondary structure because there are mixed helical and strand conformations in HFPmn_mut, and (2) the increase of fusion activity does not associate with the increase of a particular secondary structure, e.g., from HFPmn to HFPdm, there is an increase in the relative population of α-

helix, while from HFPdm to HFPtr, there is an increase in the relative population of β-strand. This further means (1) both the helical and the β strand conformations are fusion active; or (2) fusion is induced by unstructured HFP. This transient HFP state would not be apparent in the NMR samples which reflect the long-time end-state HFP structure.*(38,39)* Experimental support for the first interpretation is an HFPmn study which showed that the rates of membrane binding and secondary structure formation were faster than the rate of lipid mixing.*(40)*

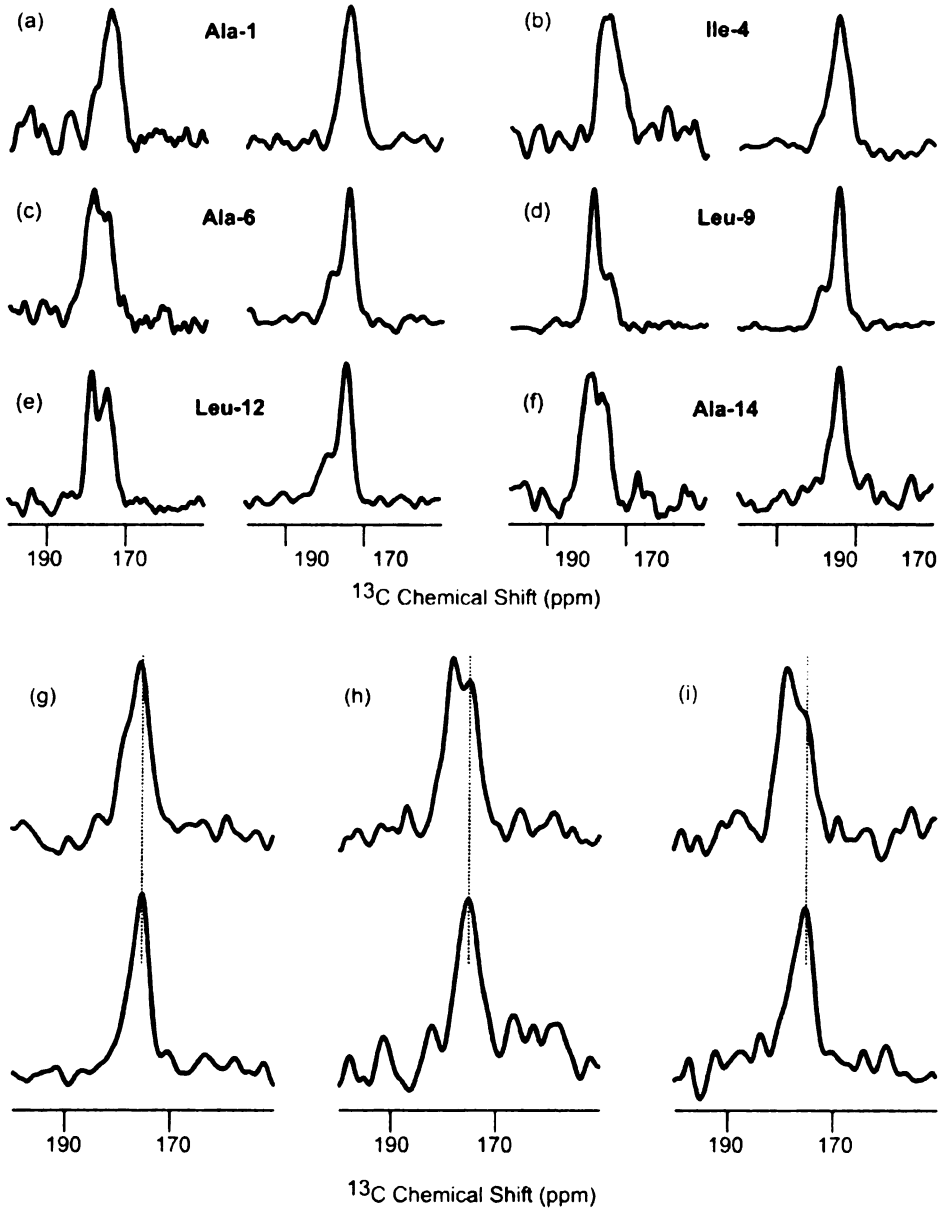

Figure 15 ^{13}CO spectra of (a) Ala1, (b) Ile4, (c) Ala6, (d) Leu9, (e) Leu12 and (f) Ala14 in HFPmn_mut associated with PC:PG and PC:PG:CHOL. For each labeled residue, the spectrum with PC:PG is shown in the left and the spectrum with PC:PG:CHOL is shown in the right. ^{13}CO peaks of Ala15 in (g) HFPmn, (h) HFPdm and (i) HFPtr associated with PC:PG in the top row and PC:PG:CHOL in the bottom row. All spectra are obtained with the ^{13}C-^{31}P REDOR pulse sequence with 2 ms dephasing time, and processed with 200 Hz Gaussian line broadening and baseline correction. All PC:PG spectra are acquired with 3000 scans and all PC:PG:CHOL spectra are acquired with 1500 scans. The vertical dashed lines in (g)-(i) indicate the chemical shift of β-strand ^{13}CO.

(a)

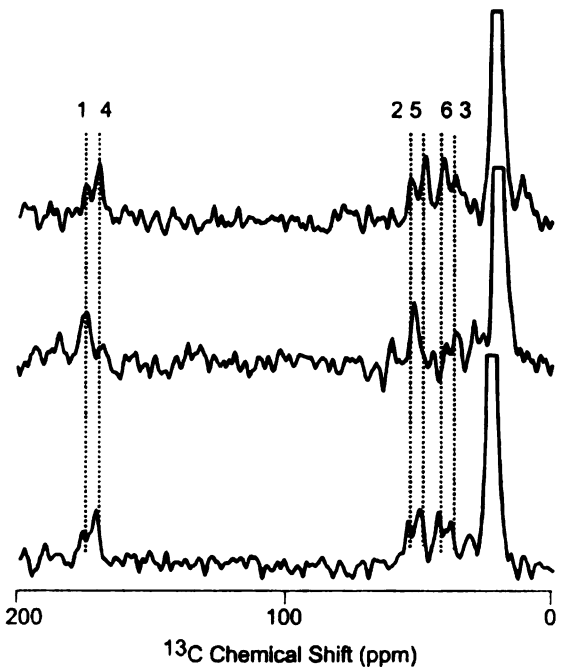

(b)

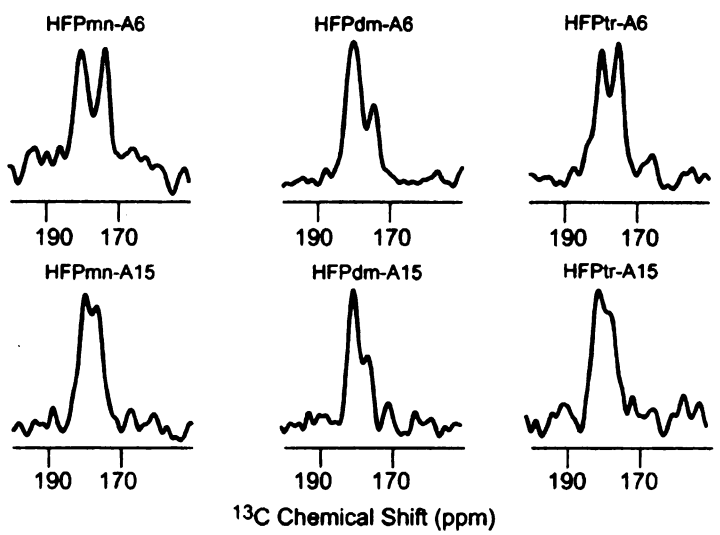

Figure 16 (a) 1D slices along the chemical shift of Cγ of Leu12 for HFPmn, HFPdm and HFPtr in the top, middle and bottom spectrum respectively. The vertical dashed lines labeled 1-3 are assigned to the chemical shifts for CO/Cγ, Cα/Cγ and Cβ/Cγ cross peaks in helical conformation respectively, and 4-6 are CO/Cγ, Cα/Cγ and Cβ/Cγ cross peaks in strand conformation respectively. (b) ^{13}C-^{31}P REDOR S_0 spectra for Ala6 and Ala15 samples. In each spectrum, the left peak corresponds to α-helical structure and the right peak corresponds to β-strand structure.

CONCLUSION

The secondary structure studies on a variety of HFP constructs concluded: (1) In PC:PG:CHOL, there is a predominant β-strand conformation for HFPmn, HFPdm and HFPtr, while HFPmn_mut can adopt partial helical conformation; (2) In membranes without cholesterol, there is a mixture of α-helix and β-strand secondary structures, and the α-helix is located from Ala6 to Ala15; (3) There is not an obvious correlation between the secondary structure and fusion activities for different HFP constructs, which suggested both α-helical and β-strand conformations can be fusion active.

REF

1.
stud
mem

2.
Mem
Prot

3.
Biop

4.
fusic

5.
synt
29.

6.
fusic
extr
298

7.
Fus
pho
Biol

8.
fusi
an e
197

9.
Grig
V.,
inte
199

10.
Wa
hun
agg

REFERENCE

1. Durell, S. R.; Martin, I.; Ruysschaert, J. M.; Shai, Y.; Blumenthal, R., What studies of fusion peptides tell us about viral envelope glycoprotein-mediated membrane fusion. *Mol. Membr. Biol.* **1997,** 14, (3), 97-112.

2. Pecheur, E.; Sainte-Marie, J.; Bienvenue, A.; Hoekstra, D., Peptides and Membrane Fusion: Towards an Understanding of the Molecular Mechanism of Protein-Induced Fusion. *J Membr Biol* **1999,** 167, (1), 1-17.

3. Epand, R. M., Fusion peptides and the mechanism of viral fusion. *Biochim. Biophys. Acta-Biomembr.* **2003,** 1614, (1), 116-121.

4. Nieva, J. L.; Agirre, A., Are fusion peptides a good model to study viral cell fusion? *Biochim. Biophys. Acta-Biomembr.* **2003,** 1614, (1), 104-115.

5. Rafalski, M.; Lear, J. D.; DeGrado, W. F., Phospholipid interactions of synthetic peptides representing the N-terminus of HIV gp41. *Biochemistry* **1990,** 29, (34), 7917-7922.

6. Martin, I.; Schaal, H.; Scheid, A.; Ruysschaert, J. M., Lipid membrane fusion induced by the human immunodeficiency virus type 1 gp41 N-terminal extremity is determined by its orientation in the lipid bilayer. *J. Virol.* **1996,** 70, (1), 298-304.

7. Kliger, Y.; Aharoni, A.; Rapaport, D.; Jones, P.; Blumenthal, R.; Shai, Y., Fusion peptides derived from the HIV type 1 glycoprotein 41 associate within phospholipid membranes and inhibit cell-cell Fusion. Structure- function study. *J. Biol. Chem.* **1997,** 272, (21), 13496-13505.

8. Pereira, F. B.; Goni, F. M.; Muga, A.; Nieva, J. L., Permeabilization and fusion of uncharged lipid vesicles induced by the HIV-1 fusion peptide adopting an extended conformation: dose and sequence effects. *Biophys. J.* **1997,** 73, (4), 1977-1986.

9. Slepushkin, V. A.; Andreev, S. M.; Sidorova, M. V.; Melikyan, G. B.; Grigoriev, V. B.; Chumakov, V. M.; Grinfeldt, A. E.; Manukyan, R. A.; Karamov, E. V., Investigation of human immunodeficiency virus fusion peptides. Analysis of interrelations between their structure and function. *AIDS Res Hum Retroviruses* **1992,** 8, (1), 9-18.

10. Gordon, L. M.; Curtain, C. C.; Zhong, Y. C.; Kirkpatrick, A.; Mobley, P. W.; Waring, A. J., The amino-terminal peptide of HIV-1 glycoprotein 41 interacts with human erythrocyte membranes: peptide conformation, orientation and aggregation. *Biochim. Biophys. Acta* **1992,** 1139, (4), 257-274.

11. Chang, D. K.; Cheng, S. F.; Chien, W. J., The amino-terminal fusion domain peptide of human immunodeficiency virus type 1 gp41 inserts into the sodium dodecyl sulfate micelle primarily as a helix with a conserved glycine at the micelle-water interface. *J. Virol.* **1997,** 71, (9), 6593-6602.

12. Waring, A. J.; Mobley, P. W.; Gordon, L. M., Conformational mapping of a viral fusion peptide in structure-promoting solvents using circular dichroism and electrospray mass spectrometry. *Proteins* **1998,** Suppl, (2), 38-49.

13. Peisajovich, S. G.; Epand, R. F.; Pritsker, M.; Shai, Y.; Epand, R. M., The polar region consecutive to the HIV fusion peptide participates in membrane fusion. *Biochemistry* **2000,** 39, (7), 1826-33.

14. Taylor, S. E.; Desbat, B.; Blaudez, D.; Jacobi, S.; Chi, L. F.; Fuchs, H.; Schwarz, G., Structure of a fusion peptide analogue at the air-water interface, determined from surface activity, infrared spectroscopy and scanning force microscopy. *Biophys. Chem.* **2000,** 87, (1), 63-72.

15. Jaroniec, C. P.; Kaufman, J. D.; Stahl, S. J.; Viard, M.; Blumenthal, R.; Wingfield, P. T.; Bax, A., Structure and dynamics of micelle-associated human immunodeficiency virus gp41 fusion domain. *Biochemistry* **2005,** 44, (49), 16167-16180.

16. Gabrys, C. M., and Weliky, D.P., Chemical Shift Assignment and Structural Plasticity of a HIV Fusion Peptide Derivative in Dodecylphosphocholine Micelles. *BBA-Biomembranes* **2007,** 1768, 3225-3234.

17. Aloia, R. C.; Tian, H.; Jensen, F. C., Lipid composition and fluidity of the human immunodeficiency virus envelope and host cell plasma membranes. *Proc. Natl. Acad. Sci. U.S.A.* **1993,** 90, (11), 5181-5185.

18. Bodner, M. L., *Solid state nuclear magnetic resonance of the HIV-1 and influenza fusion peptides associated with membranes*. Ph. D. thesis, Michigan State University: East Lansing, 2006; p 122.

19. Qiang, W., Bodner, M.L., and Weilky, D.P., Solid-state NMR Spectroscopy of HIV Fusion Peptides Associated with Host-Cell-Like Membranes: 2D Correlation Spectra and Distance Measurements Support a Fully Extended Conformation and Models for Specific Antiparallel Strand Registries. *J. Am. Chem. Soc.* **2008,** 130, 5459-5471.

20. Sackett, K., and Weliky, D.P., Unpublished experiments.

21. Yang, J.; Gabrys, C. M.; Weliky, D. P., Solid-state nuclear magnetic resonance evidence for an extended beta strand conformation of the membrane-bound HIV-1 fusion peptide. *Biochemistry* **2001,** 40, (27), 8126-8137.

22.
for p
HIV-

23.
refe

24.

25.
fusic
whic
(45)

26.
Olig
Corr
to Li

27.
A m
glyc
Aca

28.
lipid
199

29.
Pho
elas

30.
Cho
sphi

31.
mod

32.
mem

33.
Ann

22. Yang, J.; Weliky, D. P., Solid state nuclear magnetic resonance evidence for parallel and antiparallel strand arrangements in the membrane-associated HIV-1 fusion peptide. *Biochemistry* **2003,** 42, 11879-11890.

23. Zhang, H. Y.; Neal, S.; Wishart, D. S., RefDB: A database of uniformly referenced protein chemical shifts. *J. Biomol. NMR* **2003,** 25, (3), 173-195.

24. Qiang, W., and Weilky, D.P., unpublished experiments.

25. Yang, R.; Prorok, M.; Castellino, F. J.; Weliky, D. P., A trimeric HIV-1 fusion peptide construct which does not self-associate in aqueous solution and which has 15-fold higher membrane fusion rate. *J. Am. Chem. Soc.* **2004,** 126, (45), 14722-14723.

26. Qiang, W., and Weilky, D.P., HIV Fusion Peptide and Its Cross-Linked Oligomers: Efficient Syntheses, Significance of the Trimer in Fusion Activity, Correlation of β Strand Conformation with Membrane Cholesterol, and Proximity to Lipid Headgroups. *Biochemistry* **2009,** 48, (2), 289-301.

27. Freed, E. O.; Delwart, E. L.; Buchschacher, G. L., Jr.; Panganiban, A. T., A mutation in the human immunodeficiency virus type 1 transmembrane glycoprotein gp41 dominantly interferes with fusion and infectivity. *Proc. Natl. Acad. Sci. U.S.A.* **1992,** 89, (1), 70-74.

28. Bloom, M.; Evans, E.; Mouritsen, O. G., Physical properties of the fluid lipid-bilayer component of cell membranes: a perspective. *Quat. Rev. Biophys.* **1991,** 24, (3), 293-397.

29. Smaby, J. M.; Momsen, M. M.; Brockman, H. L.; Brown, R. E., Phosphatidylcholine acyl unsaturation modulates the decrease in interfacial elasticity induced by cholesterol. *Biophys. J.* **1997,** 73, (3), 1492-1505.

30. Li, X. M.; Momsen, M. M.; Smaby, J. M.; Brockman, H. L.; Brown, R. E., Cholesterol decreases the interfacial elasticity and detergent solubility of sphingomyelins. *Biochemistry* **2001,** 40, (20), 5954-5963.

31. Silvius, J. R., Role of cholesterol in lipid raft formation: lessons from lipid model systems. *Biochim. Biophys. Acta-Biomembr.* **2003,** 1610, (2), 174-183.

32. Binder, W. H.; Barragan, V.; Menger, F. M., Domains and rafts in lipid membranes. *Ange. Chem.-Int. Ed. Engl.* **2003,** 42, (47), 5802-5827.

33. Simons, K.; Vaz, W. L. C., Model systems, lipid rafts, and cell membranes. *Ann. Rev. Biophys. Biomol. Struct.* **2004,** 33, 269-295.

34.
pho
biol

35.
Imr
Bio

36.
C. I
con
Gra

37.
stat
orie
Phy

38.
Hul
des
fusi

39.
A.S
pep
200

40.
gp4
stru

34. McMullen, T. P. W.; Lewis, R.; McElhaney, R. N., Cholesterol-phospholipid interactions, the liquid-ordered phase and lipid rafts in model and biological membranes. *Curr. Opin. Colloid Interface Sci.* **2004,** 8, (6), 459-468.

35. Li, Y. L., AND Tamm, L.K., Structure and Plasticity of the Human Immunodeficiency Virus gp41 Fusion Domain in Lipid Micelles and Bilayers. *Biophys. J.* **2007,** 93, (3), 876-885.

36. Yang, J.; Parkanzky, P. D.; Khunte, B. A.; Canlas, C. G.; Yang, R.; Gabrys, C. M.; Weliky, D. P., Solid state NMR measurements of conformation and conformational distributions in the membrane-bound HIV-1 fusion peptide. *J. Mol. Graph. Model.* **2001,** 19, (1), 129-135.

37. Wasniewski, C. M.; Parkanzky, P. D.; Bodner, M. L.; Weliky, D. P., Solid-state nuclear magnetic resonance studies of HIV and influenza fusion peptide orientations in membrane bilayers using stacked glass plate samples. *Chem. Phys. Lipids* **2004,** 132, (1), 89-100.

38. Hofmann, M. W.; Weise, K.; Ollesch, J.; Agrawal, P.; Stalz, H.; Stelzer, W.; Hulsbergen, F.; de Groot, H.; Gerwert, K.; Reed, J.; Langosch, D., De novo design of conformationally flexible transmembrane peptides driving membrane fusion. *Proc. Natl. Acad. Sci. U.S.A.* **2004,** 101, (41), 14776-14781.

39. Reichert, J., Grasnick, D., Afonin, S., Buerck, J., Wadhwani, P., and Ulrich, A.S., A critical evaluation of the conformational requirements of fusogenic peptides in membranes. *European Biophysics Journal with Biophysics Letters* **2007,** 36, (4-5), 405-413.

40. Buzon, V.; Padros, E.; Cladera, J., Interaction of fusion peptides from HIV gp41 with membranes: A time-resolved membrane binding, lipid mixing, and structural study. *Biochemistry* **2005,** 44, (40), 13354-13364.

CHAPTER V

TERTIARY STRUCTURES OF MEMBRANE-ASSOCIATED HIV FUSION PEPTIDE

BACKGROUND

Previous studies on V2E HIV mutants suggest that HFP oligomerization is a structural requirement for fusion. Such oligomers could be formed in the β strand HFP conformation through inter-peptide hydrogen bonding.*(1)* Solid-state NMR REDOR experiments were performed on HFPmn associated with cholesterol-containing membranes samples in which half of the peptides contained specific ^{13}C carbonyl backbone labels and the other half of the peptides contained specific ^{15}N backbone labels. Strong evidence for oligomeric β structures was provided by observation of a significant reduction of the ^{13}C signals by the ^{15}N nuclei.*(2)* Previous analytical ultracentrifugation (AUC) studies concluded that HFPmn, which contained a number of non-nature charged residues in the C-terminus, was monomeric in solution and was converted to oligomers as a result of membrane association.*(3)* In addition, samples prepared by different methods had very similar NMR spectra, which indicated that the oligomeric β structure was an equilibrium rather than a kinetically trapped structure.*(4)* Since both the host cell and virus membranes contain a large fraction of cholesterol,*(5)* the formation of oligomeric β structures may be biologically relevant when the HIV fusion peptide interacts with the membranes.

The possible biological significance of fusion peptide oligomerization is also suggested by the following evidence: (1) The atomic-resolution structures of

the soluble ectodomain of gp41 showed stable gp41 trimers.*(6)* These structures ended ~ 10 residues C-terminal of the fusion peptide domain, and their three N-termini were close together at the ends of an in-register helical coiled-coil.*(7)* Thus, it appears that at least three fusion peptides are in close proximity when they interact with the target membrane. (2) Experiments and modeling studies further suggested that the fusion site contained multiple envelope protein trimers.*(8,9)* (3) The functionally disruptive Val-2 to Glu-2 mutation in the gp41 fusion peptide is *trans*-dominant, i.e., cells expressing 10% mutant proteins and 90% wild-type protein exhibit only 40% of the fusion activity of cells with 100% wild-type protein. One interpretation of the mutation study was that the mutant peptide disrupts the correction assembly of a functionally important fusion peptide oligomer.*(1)*

The combination of previous works suggested the importance to study the tertiary structure of the membrane-associated β strand HFP. The specific aims include: (1) is there a predominant parallel or anti-parallel β-sheet structure; and (2) is there a preferred or several preferred registries for the β-sheet arrangement? In the results and discussion part of this chapter, the evidence for the existence of anti-parallel β-sheet structure will be provided, and the indirect evidence will be described for the predominance of anti-parallel structure versus parallel structure by comparing the present result with previous studies.*(2,10)* In addition, two anti-parallel β-sheet registries have been observed with the overlap of the N-terminal 16 or 17 residues. Finally, a procedure to quantify the percentage of certain anti-parallel β-sheet registries will be provided, and the

resu

HFF

MA

with

cyst

judg

HFF

Inte

cha

MAL

Tabl

Nar

HFF

HFF

HFF

HFF

HFF

[a] The
the b

proc

assc

results showed that ~ 25 % of HFPmn has a 16-residue overlap and ~ 30 % of HFPmn has a 17-residue overlap.*(10)*

MATERIALS AND METHODS

Peptide. All peptides used in this chapter were summarized in Table 4 with their sequences and ^{13}CO and ^{15}N labeled residues. Although there was a cysteine in the C-terminus, the peptides were predominantly non-cross-linked as judged by monomeric molecular weight in AUC data. *(3,11)* The synthesis of HFP monomers was completed using a 15 mL manual reaction vessel (Peptides International, Louisville, KY) and followed the same procedure as described in chapter II for HFPmn and in appendix 3 with FMOC chemistry.*(12)* HPLC and MALDI-TOF-MS were used to purify and identify the peptides.

Table 4 peptide sequences and labeling schemes.[a]

Name	Sequence
HFP-A	AVGIGALFLGFLGAAGSTMGARSWKKKKKKA$^{\beta}$
HFP-B	AVGIGALFLGFLGAAGSTMGARSWKKKKKKA$^{\beta}$
HFP-C	AVGIGALFLGFLGAAGSTMGARSWKKKKKKA$^{\beta}$
HFP-D	AVGIGALFLGFLGAAGSTMGARSWKKKKKKA$^{\beta}$
HFP-E	AVGIGALFLGFLGAAGSTMGARSWKKKKKKA$^{\beta}$

[a] The red symbol indicates the ^{15}N-labeled amino acids and the blue color indicates the ^{13}CO-labeled amino acids.

NMR Sample Preparation. The sample preparation followed the procedure provided in chapter IV and all peptides described in Table 4 were associated with PC:PG:CHOL.

^{13}C-^{15}N REDOR Experiments and Simulations. The triple resonance MAS probe was used and tuned to ^{13}C, ^{1}H, and ^{15}N frequencies of 100.8 MHz, 400.8 MHz, and 40.6 MHz, respectively and the ^{13}C transmitter was at 152.4 ppm. The REDOR sequence was shown in Fig. 10 and the following parameters were used in the present set of experiments: (1) a 44 kHz ^{1}H $\pi/2$ pulse; (2) 2.2 ms cross-polarization with 63 kHz ^{1}H field and 76-84 kHz ramped ^{13}C field; and (3) a dephasing period of duration τ for which the "S_0" and "S_1" acquisitions contained 62 kHz ^{13}C π pulses at the end of each rotor cycle except the last cycle and for which the S_1 acquisition contained 27 kHz ^{15}N π pulses in the middle of rotor cycles; and (4) ^{13}C detection.*(2,13-16)* XY-8 phase cycling was applied to the ^{13}C and ^{15}N pulses during the dephasing period, TPPM ^{1}H decoupling of ~95 kHz was applied during the dephasing and detection periods, the recycle delay was 1 s, and the MAS frequency was 8000 ± 2 Hz. REDOR experiments were calibrated using a lyophilized "I4" peptide with sequence AcAEAAAKEAAAKEAAAKA-NH_2 and a ^{13}CO label at Ala-9 and a ^{15}N label at Ala-13. For the predominant α helical conformation of I4, the labeled ^{13}CO-^{15}N distance is ~4.1 Å.*(13,17)*

The S_0 REDOR spectrum contained all ^{13}C signals while the S_1 spectrum had reduced signals from ^{13}C with proximal ^{15}N and therefore appreciable ^{13}C-^{15}N dipolar coupling (d). The equation $d = 3100/r^3$ expresses the relation between d in Hz and ^{13}C-^{15}N distance (r) in Å. The data analysis focused on integrated S_0 and S_1 intensities in the labeled ^{13}CO region that were denoted as "S_0" and "S_1", respectively, and an experimental fractional dephasing $(\Delta S/S_0)^{exp} = (S_0^{exp} -$

$S_1^{exp})/S_0^{exp}$ was calculated for each τ. The $(\Delta S/S_0)^{exp}$ provided the experimental basis for determination of d and r. The σ^{exp} uncertainty in $(\Delta S/S_0)^{exp}$ was calculated by

$$\sigma^{exp} = \frac{\sqrt{\left(S_0^2 \times \sigma_{S_1}^2\right) + \left(S_1^2 \times \sigma_{S_0}^2\right)}}{S_0^2} \quad (35)$$

where σ_{S_0} and σ_{S_1} are the experimental root-mean-squared noise of the S_0 and S_1 spectra, respectively.*(18)*

Calculations of $(\Delta S/S_0)$ as a function of spin geometry were denoted $(\Delta S/S_0)^{sim}$ and were made using the SIMPSON program.*(19)* The calculations were based on two or three spins where one of the spins was the Ala-14 ^{13}CO in a central β strand and the other one or two spins were labeled ^{15}N on adjacent strands. In order to make meaningful comparison between the $(\Delta S/S_0)^{sim}$ which were based only on labeled nuclei and $(\Delta S/S_0)^{exp}$ which included contributions from both labeled and natural abundance nuclei, $(\Delta S/S_0)^{cor}$ were calculated from the $(\Delta S/S_0)^{exp}$ and reflected removal of the natural abundance contribution.

The following parameters/approximations are used:

A1. There is 99% labeling of the Ala-14 ^{13}CO and Val-2, Gly-3, Ile-4 or Gly-5 ^{15}N sites. $S_1 = S_0$ for a labeled Ala-9 ^{13}CO in a molecule with a Val-2, Gly-3, Ile-4 or Gly-5 ^{14}N.

A2. Effects of natural abundance ^{15}N on ^{13}CO S_1 signals are evaluated using the following criteria: (1) $S_1 = 0$ for a labeled Ala-14 ^{13}CO separated by one or two bonds from a natural abundance ^{15}N at Ala-15 and Ala-14. Ala-14 S_1 is not

affected by other natural abundance ^{15}N. (2) $S_1 = 0$ for natural abundance backbone ^{13}COs at Ala-1 and Val-2, Val-2 and Gly-3, Gly-3 and Ile-4, or Ile-4 and Gly-5 which are separated by one or two bonds from the labeled Val-2, Gly-3, Ile-4 or Gly-5 ^{15}N, respectively. $S_1 = S_0$ for other natural abundance backbone ^{13}CO sites. Criteria (1) and (2) are based on the close distance (≤ 2.5 Å) and consequent strong (≥ 200 Hz) dipolar coupling of ^{13}CO and ^{15}N nuclei separated by one or two bonds.

Figure 17 displays a flow chart for the determination of $(\Delta S/S_0)^{cor}$ for HFP-B with ^{13}CO labeled Ala-14 and ^{15}N labeled Val-2. $(\Delta S/S_0)^{cor}$ for the other HFP samples were derived based on the same flow chart but only with different ^{15}N labeling.

A complete derivation of $(\Delta S/S_0)^{cor}$ follows:

$$\left(\frac{\Delta S}{S_0}\right)^{exp} = \frac{S_0^{exp} - S_1^{exp}}{S_0^{exp}} \quad (36)$$

S_0^{exp} is expressed as the sum of contributions from labeled ^{13}CO nuclei (S_0^{lab}) and from natural abundance ^{13}CO nuclei ($S_0^{n.a.}$):

$$S_0^{exp} = S_0^{lab} + S_0^{n.a.} = 1 - U_C + n A_C \quad (37)$$

where $1 - U_C$ is the fractional Ala-14 ^{13}CO labeling, A_C is the fractional ^{13}C natural abundance, and n is the total number of unlabeled peptide backbone CO sites in an HFP molecule. S_1^{exp} is also expressed as the sum of contributions from labeled ^{13}CO nuclei (S_1^{lab}) and from natural abundance ^{13}CO nuclei ($S_1^{n.a.}$):

$$S_1^{exp} = S_1^{lab} + S_1^{n.a.} \quad (38)$$

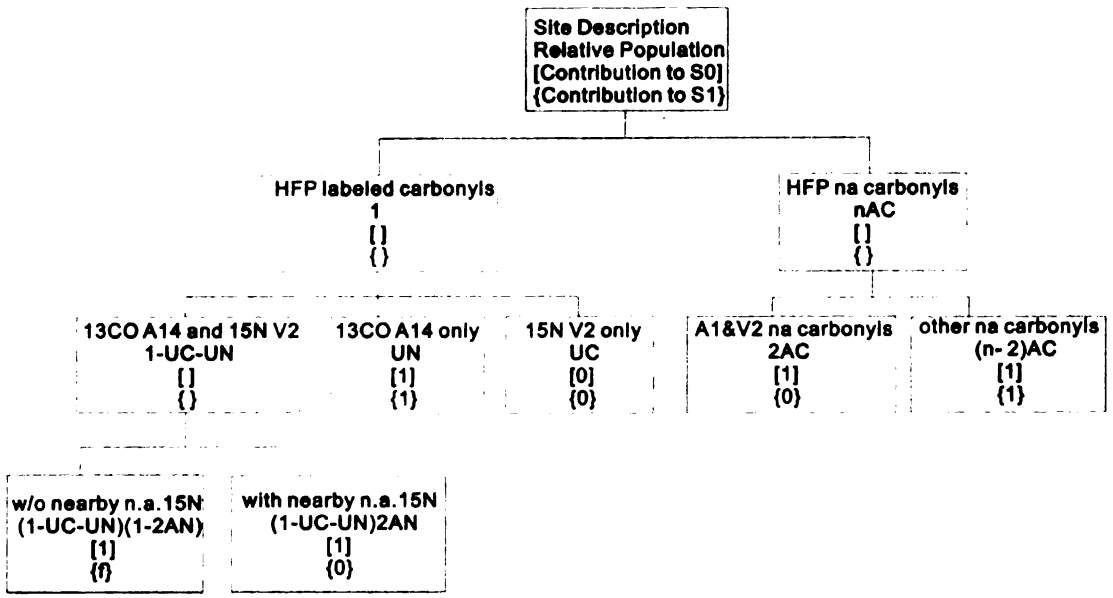

Figure 17 Flow chart of derivation of $(\Delta S/S_0)^{cor}$ for REDOR of HFP-B. The four rows in each box are in sequence: the site description, its relative population, and its contributions to S_0 and S_1.

with:

$$S_1^{lab} = (1 - U_C - U_N)(1 - 2A_N)f + U_N \quad (39)$$

and:

$$S_1^{n.a.} = (n-2)A_C \quad (40)$$

where $1 - U_N$ is the fractional ^{15}N labeling of the Val-2, Gly-3, Ile-4 or Gly-5 residue for HFP-H, HFP-I, HFP-J and HFP-K respectively, A_N is the fractional ^{15}N natural abundance and the parameter f:

$$f = \frac{S_1^{cor}}{S_0^{cor}} = 1 - \frac{S_0^{cor} - S_1^{cor}}{S_0^{cor}} = 1 - \left(\frac{\Delta S}{S_0}\right)^{cor} \quad (41)$$

Incorporate Eq. 41 into Eq. 39:

$$\begin{aligned} S_1^{lab} &= (1 - U_C - U_N)(1 - 2A_N)\left[1 - \left(\frac{\Delta S}{S_0}\right)^{cor}\right] + U_N \\ &= (1 - U_C - U_N)(1 - 2A_N) - (1 - U_C - U_N)(1 - 2A_N)\left(\frac{\Delta S}{S_0}\right)^{cor} + U_N \end{aligned} \quad (42)$$

U_C, U_N, and $2A_N$ are much less than 1 so that:

$$(1 - U_C - U_N)(1 - 2A_N) \cong 1 - U_C - U_N - 2A_N \quad (43)$$

and:

$$S_1^{lab} \cong 1 - U_C - 2A_N - (1 - U_C - U_N - 2A_N)\left(\frac{\Delta S}{S_0}\right)^{cor} \quad (44)$$

Incorporate Eqs. 40 and 44 in Eq. 38:

$$S_1^{exp} = 1 - U_C - 2A_N - (1 - U_C - U_N - 2A_N)\left(\frac{\Delta S}{S_0}\right)^{cor} + (n-2)A_C \quad (45)$$

Combine Eqs. 37, 38, 39, and 45:

$$S_0^{exp} - S_1^{exp} = [1 - U_C + n A_C] - \left[1 - U_C - 2A_N - (1 - U_C - U_N - 2A_N)\left(\frac{\Delta S}{S_0}\right)^{cor} + (n-2) A_C\right]$$

(46)

and simplify:

$$S_0^{exp} - S_1^{exp} = 2A_C + 2A_N + (1 - U_C - U_N - 2A_N)\left(\frac{\Delta S}{S_0}\right)^{cor} \quad (47)$$

Combine Eqs. 37 and 47:

$$\left(\frac{\Delta S}{S_0}\right)^{exp} = \frac{2A_C + 2A_N + (1 - U_C - U_N - 2A_N)\left(\frac{\Delta S}{S_0}\right)^{cor}}{1 - U_C + n A_C} \quad (48)$$

and rewrite:

$$\left(\frac{\Delta S}{S_0}\right)^{cor} = \frac{1 - U_C + n A_C}{(1 - U_C - U_N - 2A_N)}\left(\frac{\Delta S}{S_0}\right)^{exp} - \frac{2A_C + 2A_N}{(1 - U_C - U_N - 2A_N)} \quad (49)$$

Expressions in Eq. 49 were numerically evaluated using A_C = 0.011, A_N = 0.0037, n = 29, and U_C = U_N = 0.01 which were based on 0.99 fractional labeling of the Ala-14 ^{13}CO sites and 0.99 fractional labeling of the Val-2, Gly-3, Ile-4 or Gly-5 ^{15}N sites:

$$\left(\frac{\Delta S}{S_0}\right)^{cor} = 1.360\left(\frac{\Delta S}{S_0}\right)^{exp} - 0.030 \quad (50)$$

Eq. 50 resulted in:

$$\sigma^{cor} = 1.360\,\sigma^{exp} \quad (51)$$

Input parameters to the SIMPSON program included the ^{13}CO-^{15}N dipolar couplings, the Ala-14 ^{13}CO chemical shift and CSA principal values, and sets of

Euler angles which reflected the orientations of ^{13}CO-^{15}N dipolar coupling and ^{13}CO CSA PASs in the fixed crystal frame. The ^{13}CO chemical shift was 175 ppm and CSA principal values were set to 241, 179, and 93 ppm, respectively.*(20)* Determination of Euler angles was based on atomic coordinates of the labeled nuclei and these coordinates were taken from crystal structure coordinates of outer membrane protein G (OMPG) (PDB file 2IWW).*(21,22)* OMPG was chosen because the REDOR experiments probed anti-parallel β strand structure in HFP and this was the predominant OMPG structural motif. After the ^{13}CO coordinates were obtained from a specific residue in OMPG, ^{15}N coordinates were obtained from nearby residues in the two adjacent strands. The Results section includes more detail about the specific choices of these nearby residues. For the two-spin simulations, the (α, β, γ) Euler angles of the dipolar coupling PAS were (0, 0, 0) and for the three-spin simulations, the angles for one dipolar PAS was (0, 0, 0) and for the other PAS were (0, θ,0) where θ was the angle between two ^{13}CO-^{15}N vectors. The Euler angles for the ^{13}CO CSA PAS were calculated using the known orientation of the PAS relative to the ^{13}CO chemical bonds and the OMPG-derived orientation of these chemical bonds relative to the crystal frame.*(23)*

RESULTS AND DISCUSSION

Anti-parallel β-sheet Registries for HFPmn. ^{13}C-^{15}N REDOR experiments were first carried out for HFP-A in Table 4 which contained ^{13}CO labeling at Ala14, Ala15 and Gly16 and ^{15}N labeling at Ala1, Val2 and Gly3. This labeling

scheme was chosen because: (1) if there were adjacent strand crossing between Phe-8 and Leu-9, the ^{13}CO-labeled residues on one strand would be hydrogen bonded to the ^{15}N labeled residues on an adjacent strand with concomitant ^{13}C-^{15}N dipolar couplings of ~ 45 Hz; and (2) intramolecular ^{13}CO-^{15}N couplings are negligible. Representative spectra are displayed in Fig. 18a, b and the respective $(\Delta S/S_0)^{exp}$ were ~ 0.41 and ~ 0.50 for REDOR dephasing time τ = 24 and 32 ms. These values suggested that there was a large population of HFP with the putative anti-parallel strand registry.*(10)* Unambiguous analysis of these data was challenging because there were contributions of three distinct ^{13}COs and because different combinations of anti-parallel strand registries could fit the data.

Ambiguity was reduced by studying samples for which HFPmn had only a single ^{13}CO and a single ^{15}N label. Four HFPs were prepared and all had a ^{13}CO label at Ala-14. This residue had been ^{13}CO labeled in HFP-A and had been previously observed to give a fairly sharp signal.*(24)* The ^{15}N label was at Val-2 (HFP-B), Gly-3 (HFP-C), Ile-4 (HFP-D), or Gly-5 (HFP-E). The variation of the REDOR data among the different HFPs was striking (cf. Figure 18c-j and Figure 19a). For τ = 32 ms, the $(\Delta S/S_0)^{exp}$ were ~0.3 for the HFP-C and HFP-D samples and ~0 for the HFP-B and HFP-E samples. These data suggested that there were two anti-parallel registries which could be classified: (1) Ala-14 on one strand opposite Gly-3 on the adjacent strand; and (2) Ala-14 on one strand opposite Ile-4 on the adjacent strand. These two registries were denoted *A* and *B* and are displayed in Fig. 20a.

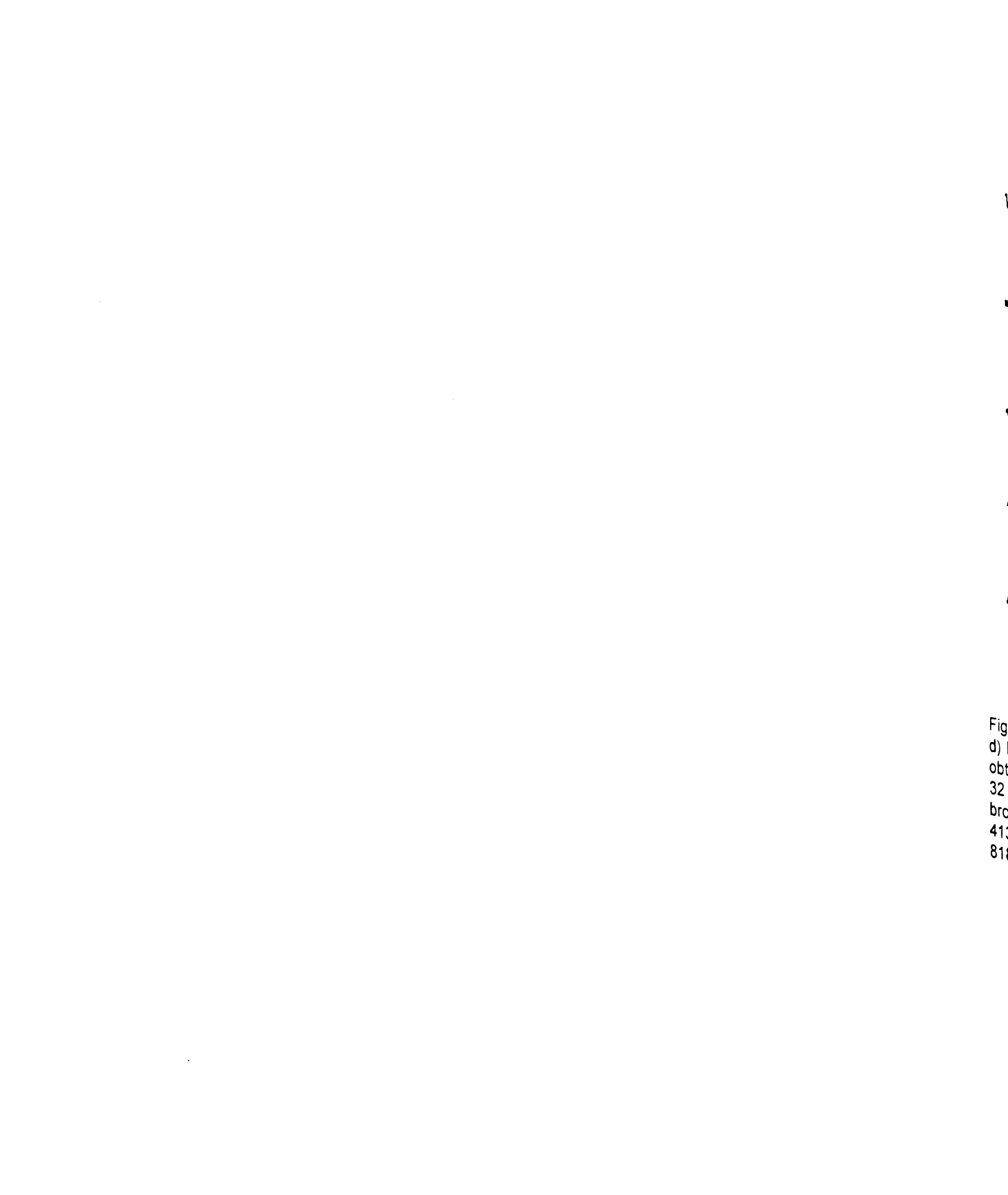

Fig
d)
obt
32
bro
41
81

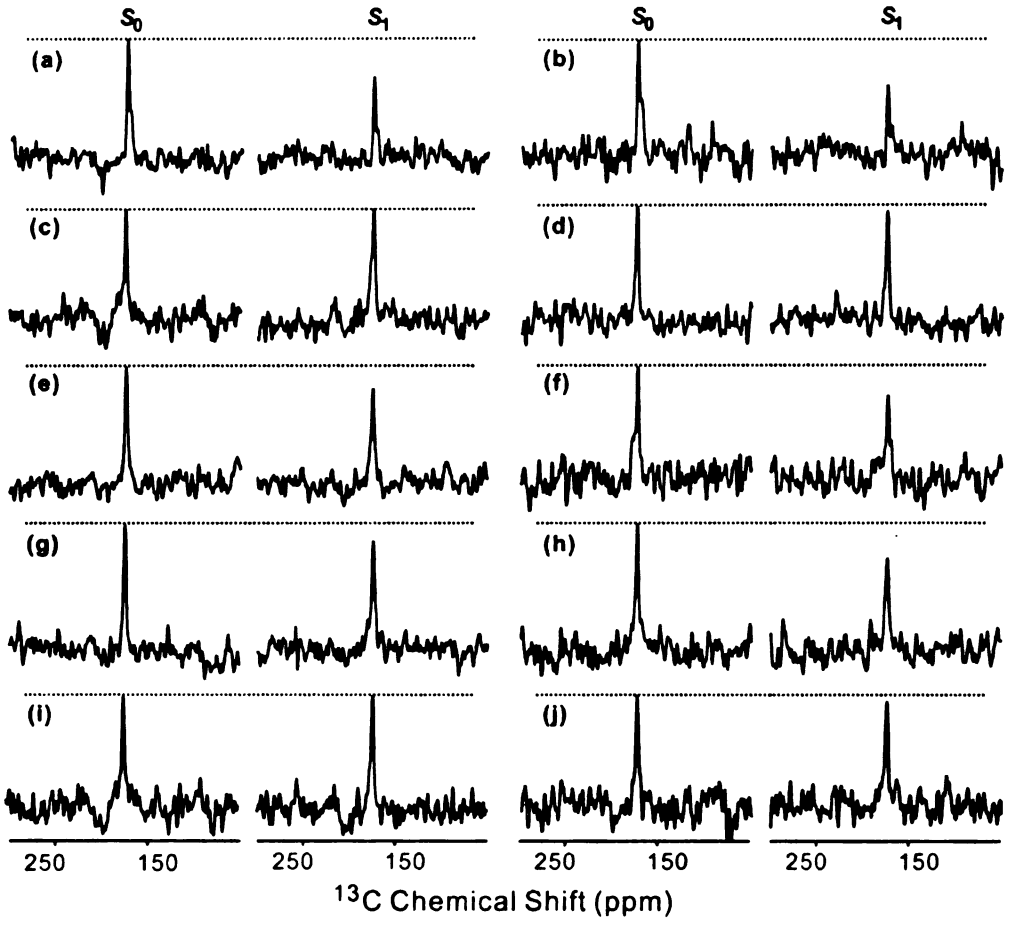

Figure 18 REDOR S_0 and S_1 spectra for membrane-associated (a, b) HFP-A, (c, d) HFP-B, (e, f) HFP-C, (g, h) HFP-D and (i, j) HFP-E. Spectra a, c, e, g, i were obtained with 24 ms dephasing time and spectra b, d, f, h, j were obtained with 32 ms dephasing time. Each spectrum was processed with 200 Hz Gaussian line broadening and baseline correction. Each S_0 or S_1 spectrum was the sum of (a) 41328, (b) 56448, (c) 45920, (d) 81460, (e) 55936, (f) 79744, (g) 30898, (h) 81856, (i) 45920 or (j) 71040 scans.

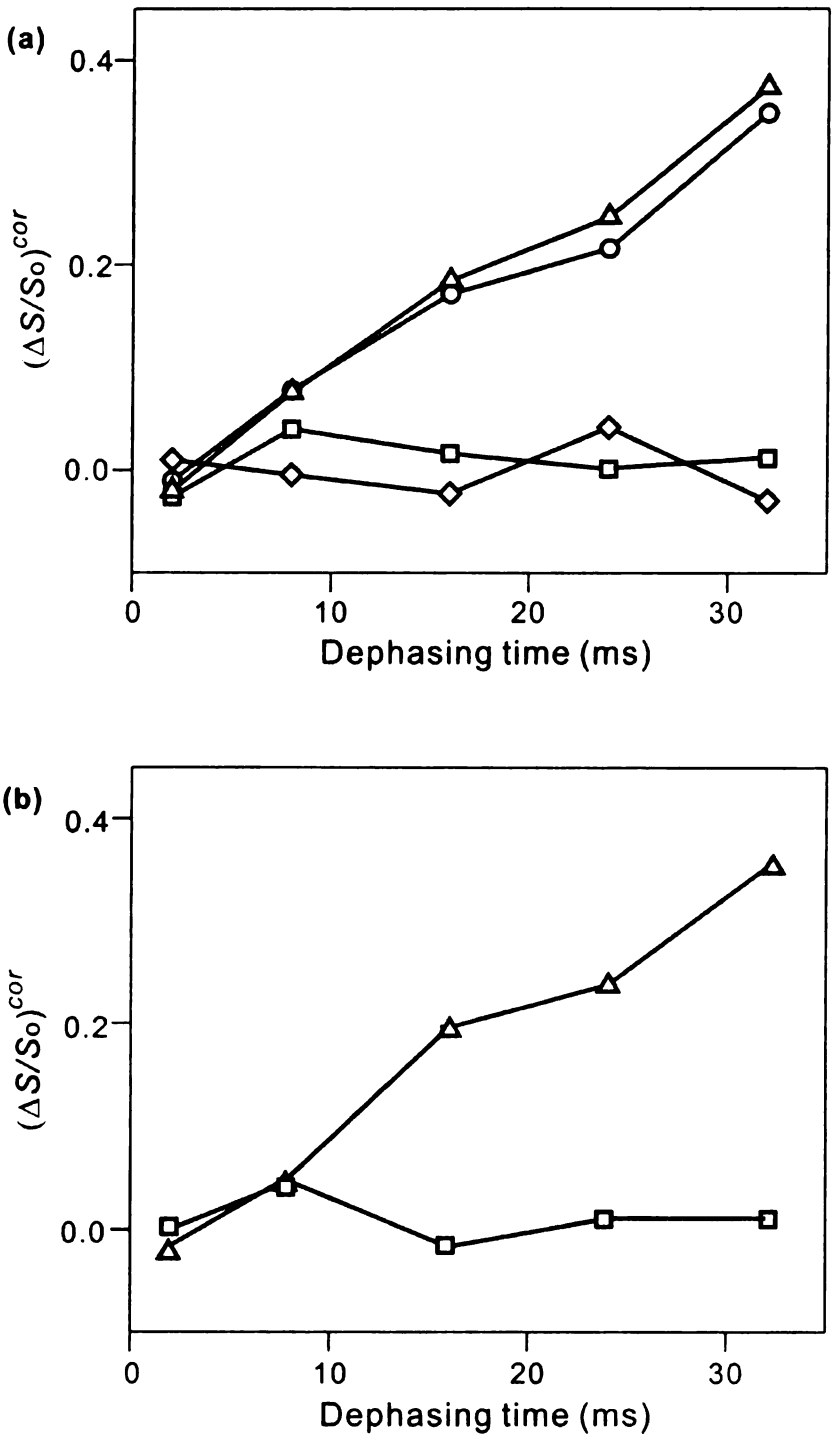

Figure 19 Plots of $(\Delta S/S_0)^{cor}$ vs dephasing time for membrane-associated HFP samples prepared with $[HFP]_{initial}$ of (a) 400 μM or (b) 25 μM. The symbol legend is: diamonds, HFP-B; triangles, HFP-C; circles, HFP-D; and squares, HFP-E. The σ^{cor} were ~0.04.

(a)

(b)

θ_1

Fig
co
an
us
Ea
alv
let
an
X
HF
hy
dis
=
pa
str

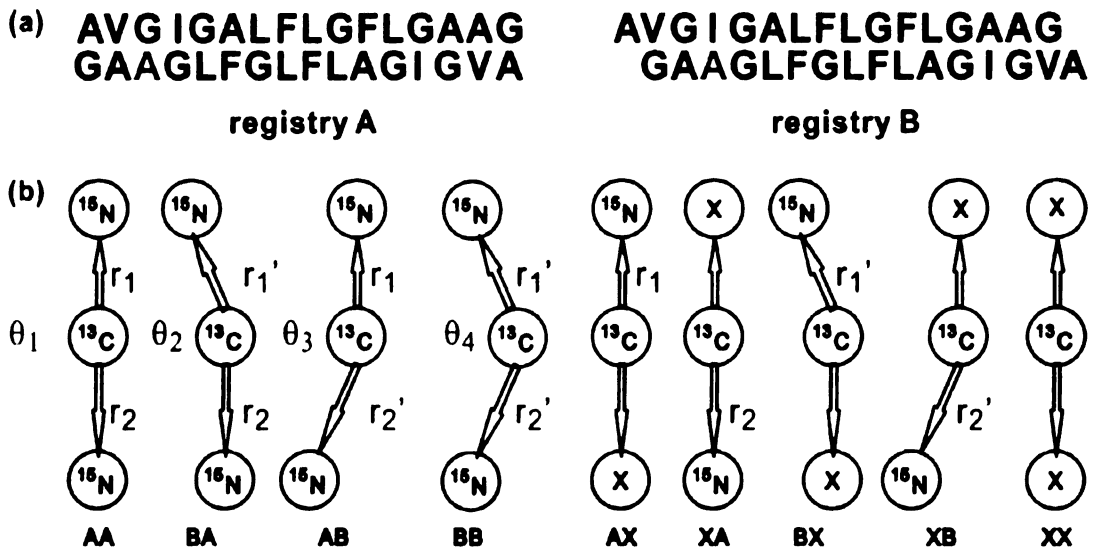

Figure 20 (a) Two antiparallel registries of residues 1-16 of HFP that were consistent with the REDOR data shown in Fig. 20. The registries are denoted *A* and *B* and the ^{13}CO labeled Ala-14 residue is highlighted in blue. (b) Models used to calculate $(\Delta S/S_0)^{sim}$ and spin geometries specific for the HFP-C sample. Each model includes nuclei from three adjacent strands with the Ala-14 ^{13}CO always in the middle strand and ^{15}N in the top and/or bottom strands. The first letter in the labeling of each model refers to the middle strand/top strand registry and the second letter refers to the middle strand/bottom strand registry. Registry *X* is any registry for which the interpeptide ^{13}CO-^{15}N distance was large in the HFP-H, HFP-I, HFP-J, or HFP-K samples so that $d \approx 0$. The Ala-14 ^{13}CO is hydrogen bonded to an amide proton in the top strand. Relevant labeled ^{13}C-^{15}N distances and ^{15}N-^{13}C-^{15}N angles are: r_1 = 4.063 Å; r_1' = 5.890 Å; r_2 = 5.455 Å; r_2' = 6.431 Å; θ_1 = 161.1°; θ_2 = 131.9°; θ_3 = 130.2°; and θ_4= 117.0°. Each parameter value was the average of 10 specific values taken from the crystal structure of outer membrane protein G.

The

[HF

ass

and

con

Figu

of

mer

of I

stu

Ile4

dep

HF

^{15}N

(A1

cor

at 2

the

alig

stu

lab

The samples used to obtain data for Figures 18 and 19a were made with $[HFPmn]_{initial} \approx 400$ μM. In order to check for possible effects of HFP self-association in aqueous solution prior to membrane binding, two additional HFP-C and HFP-E samples were made with $[HFPmn]_{initial} \approx 25$ μM which is a concentration for which HFP is known to be monomeric in the HEPES buffer.*(4)* Figures 19a,b illustrates that very similar $(\Delta S/S_0)^{cor}$ were obtained for both values of $[HFPmn]_{initial}$ and the apparent strand registries appear to be due to membrane-association.

The registries proposed in Figure 20a were consistent with a previous set of PDSD experiments in which "scatter-uniform" labeled (SUL) HFPmn were studied and crosspeaks were observed between Ala6 and Gly10 and between Ile4 and Ala13.*(25)* In addition, it was worthwhile comparing the REDOR dephasing obtained at τ = 24 ms for HFP-A to a previous set of triply-labeled HFP monomer samples where 50 % triply ^{13}CO-labeled peptide and 50 % triply ^{15}N-labeled peptide had been used. In those cases the combination HFPmn-$(A14A15G16)_C$/HFPmn-$(A14A15G16)_N$ provided ~ 4 % dephasing and the combination HFPmn-$(A14A15G16)_C$/HFPmn-$(G5A6L7)_N$ gave ~ 16 % dephasing at 24 ms, while Figure 18a showed the HFP-A sample gave ~ 55 % dephasing at the same dephasing period.*(2)* Although the probability for a ^{13}C-labeled HFP aligned with a ^{15}N-labeled HFP was only half of this probability in the present study, there was still a clear trend that the dephasing will increase when the labeling pattern satisfy an anti-parallel instead of a parallel β-sheet arrangement.

Quantitative Anti-parallel β-sheet Registry Models. More quantitative analysis of the $(\Delta S/S_0)^{cor}$ of the samples was done using calculations of $(\Delta S/S_0)^{sim}$ based on different models for registries of three adjacent strands with the overall goal of quantization of the populations of the different registries. The strands were denoted, "top", "middle", and "bottom". Figure 20b displays the models as well as spin geometries specific to the HFP-C sample. The models were focused on registries at the middle strand Ala14 whose ^{13}CO group was hydrogen bonded to an amide proton in the top strand. Each model was labeled by two letters which were either *A*, *B*, or *X*. The first letter described the registry relating the middle strand and the top strand and the second letter described the registry relating the middle strand and the bottom strand. For registry *A*, Ala14 in the middle strand was across from Gly3 in the adjacent strand and for registry *B*, Ala14 in the middle strand was across from Ile4 in the adjacent strand (*cf.* Figure 20a). Registry *X* was defined as any registry for which the inter-peptide ^{13}CO-^{15}N distance was large in the HFP-B, HFP-C, HFP-D, and HFP-E samples so that $d \approx 0$. Registry *X* could include the in-register parallel strand arrangement. Such registry has been proposed for membrane-associated gp41 constructs which contain the HFP.*(26)*

Model *XX* had $(\Delta S/S_0)^{sim} = 0$ for all dephasing times while models *AX*, *XA*, *BX*, and *XB* resulted in two-spin systems for which $(\Delta S/S_0)^{sim}$ were primarily dependent on the ^{13}CO-^{15}N distance. Models *AA*, *BA*, *AB*, and *BB* were three-spin systems for which $(\Delta S/S_0)^{sim}$ depended both on the two ^{13}CO-^{15}N distances and on the angle between the two ^{13}CO-^{15}N vectors.*(27)* For all samples and all

models, $(\Delta S/S_0)^{sim}$ were calculated for each of the five experimental dephasing times.

The fractional populations of each of the models were calculated with fitting of the $(\Delta S/S_0)^{sim}$ and the $(\Delta S/S_0)^{cor}$. The fitting was primarily based on the data from the HFP-C and HFP-D samples because many of the $(\Delta S/S_0)^{cor}$ for these samples were appreciably positive. Fitting was accomplished with the equations:

$$\chi^2 = \sum_{j=1}^{2}\sum_{k=1}^{5} \frac{\left\{\left(\Delta S/S_0\right)_{j,k}^{calc} - \left(\Delta S/S_0\right)_{j,k}^{cor}\right\}^2}{\left(\sigma_{j,k}^{cor}\right)^2} \quad (52)$$

$$\left(\Delta S/S_0\right)_{j,k}^{calc} = \sum_{l=1}^{9} f_l \times \left(\Delta S/S_0\right)_{j,k}^{sim} \quad (53)$$

for which j was the index of the sample, k was the index of the dephasing time, l was the index of the model, and f_l was the fractional population of model l.

Three types of fitting were done and differed in the choice of which f_l were fitted and which were set to zero. For all fittings, $\Sigma f_l = 1$. For "unconstrained" fitting, there was no correlation between the registry of the middle and top strands and the registry of the middle and bottom strands. All f were therefore fitted and each f was a function of "a" and "b" which were defined as the fractional probabilities of two adjacent strands having A or B registries, respectively. The fractional probability of the X registries was then $1 - a - b$. Each f was the product of the fractional probabilities of the middle strand/top strand registries and middle strand/bottom strand registries with resulting $f_{AA} = a^2$,

$f_{BA} = ab$, $f_{AB} = ab$, $f_{BB} = b^2$, $f_{AX} = a(1 - a - b)$, $f_{XA} = a(1 - a - b)$, $f_{BX} = b(1 - a - b)$, $f_{XB} = b(1 - a - b)$, and $f_{XX} = (1 - a - b)^2$. "Partially constrained" fitting was done based on the idea that there were domains of antiparallel strand registry and domains of *X* registry so that $f_{AA} = a^2$, $f_{BA} = ab$, $f_{AB} = ab$, $f_{BB} = b^2$, $f_{AX} = 0$, $f_{XA} = 0$, $f_{BX} = 0$, $f_{XB} = 0$, and $f_{XX} = 1 - (a + b)^2$. For partially constrained fitting, physically meaningful expressions of *a* and *b* included: (1) *a*/*b* which was the ratio of probability that two adjacent strands had *A* registry to the probability that they had *B* registry; and (2) $(a + b)^2/[(1 - (a + b)]^2$ which was the ratio of the total population of the *A* and *B* antiparallel structures to the population of the *X* structures. For "fully constrained" fitting, it was assumed that β strand domains would form with only *A* or only *B* or only *X* registries so that $f_{AA} = a^2$, $f_{BA} = 0$, $f_{AB} = 0$, $f_{BB} = b^2$, $f_{AX} = 0$, $f_{XA} = 0$, $f_{BX} = 0$, $f_{XB} = 0$, and $f_{XX} = 1 - a^2 - b^2$. In this fitting, the fractional populations of the *A*, *B*, and *X* strand arrangements were a^2, b^2, and $1 - a^2 - b^2$, respectively.

The results of unconstrained fitting are displayed in Figure 21a as a 2D contour plot of χ^2 vs *a* and *b*. The best-fit $a = 0.22$ and $b = 0.31$ with $\chi^2_{min} = 16.5$ and good-fit *a* and *b* represented in the black region.*(18,20)* The good-fit regions of the plot showed negative correlation between *a* and *b* as might be expected from the positive correlation between $(\Delta S/S_0)^{calc}$ and either *a* or *b* for both the HFP-I and HFP-J samples. The $(\Delta S/S_0)^{calc}$ were also computed for the HFP-H and HFP-K samples using the best-fit *a* and *b*. At $\tau = 32$ ms, maximum $(\Delta S/S_0)^{calc}$ of 0.08 and 0.09 were obtained for the HFP-H and HFP-K samples, respectively, and can be compared to the maximum $(\Delta S/S_0)^{cor} = 0.05 \pm 0.04$ for these samples.

Figure 21b displays the 2D contour plot of partially constrained fitting with best-fit $a = 0.31$ and $b = 0.42$ with $\chi^2_{min} = 15.1$. At $\tau = 32$ ms, these a and b values led to $(\Delta S/S_0)^{calc} = 0.11$ and 0.13 for the HFP-H and HFP-K samples, respectively. Figure 21c displays the 2D contour plot of fully constrained fitting with best-fit $a^2 = 0.26$ and $b^2 = 0.33$ with $\chi^2_{min} = 12.7$ and $(\Delta S/S_0)^{calc} = 0.09$ and 0.12 at $\tau = 32$ ms for the HFP-H and HFP-K samples, respectively. For all three fittings, the χ^2_{min} are reasonable, as evidenced by being within a factor of 2 of 8, the number of degree of freedom of the fitting. This suggests that each model is plausible. The limits of the good-fit black regions have been generously set and include all parameter space with χ^2 2-3 units higher than χ^2_{min}.

The best-fit f of the three fittings were used to calculate P_A, P_B, and P_X which were fractional populations of the A, B, and X registries, respectively: $P_A = f_{AA} + (f_{BA} + f_{AB} + f_{AX} + f_{XA})/2$; $P_B = f_{BB} + (f_{BA} + f_{AB} + f_{BX} + f_{XB})/2$; and $P_X = f_{XX} + (f_{AX} + f_{XA} + f_{BX} + f_{XB})/2$ with $P_A + P_B + P_X = 1$. The resulting fractional populations were: (1) unconstrained fitting, $P_A = 0.22$, $P_B = 0.31$, and $P_X = 0.47$; (2) partially constrained fitting, $P_A = 0.23$, $P_B = 0.31$, and $P_X = 0.46$; and (3) fully constrained fitting, $P_A = 0.26$, $P_B = 0.33$, and $P_X = 0.41$. An overall result of the three fittings was therefore $P_A \approx 0.25$, $P_B \approx 0.30$, and $P_X \approx 0.45$. In addition, examination of the values in the black regions of the three plots showed that the approximate range of reasonable values for the sum $P_A + P_B$ was 0.5-0.6 and the corresponding range of P_X was 0.4-0.5.

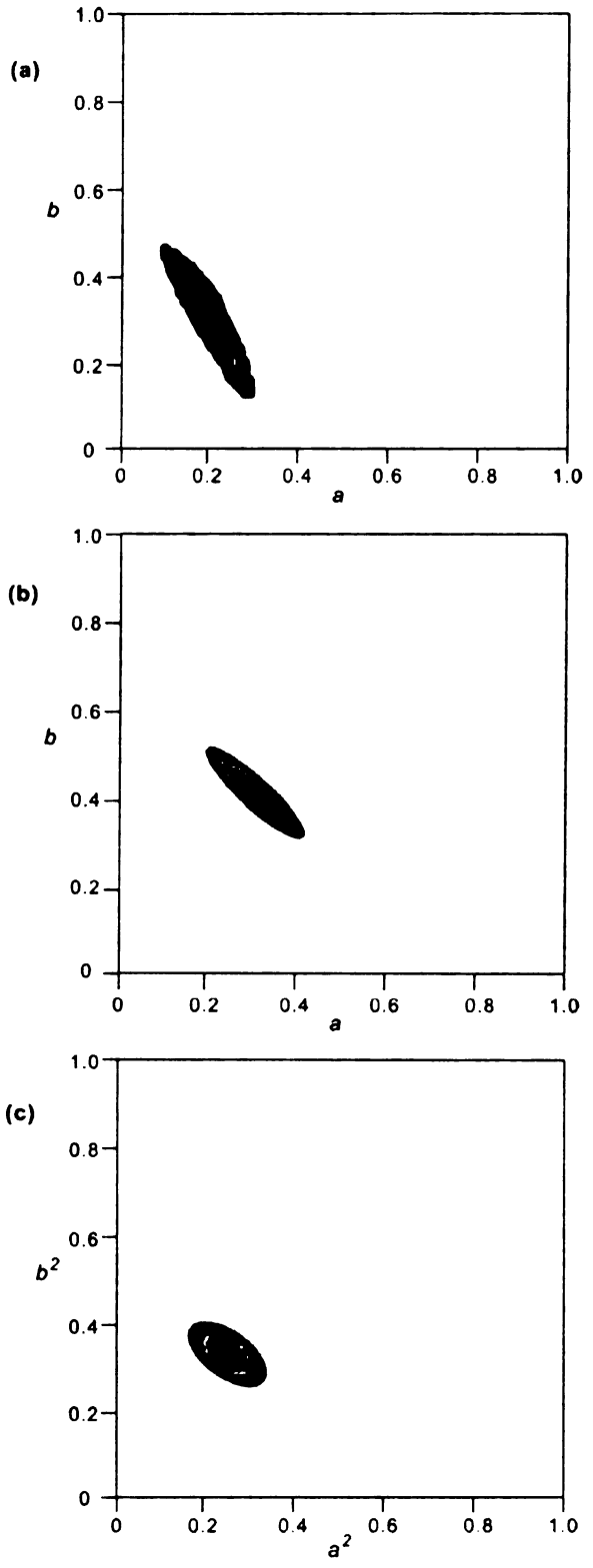

Figure 21 Contour plots of χ^2 vs strand fitting parameters for (a) unconstrained; (b) partially constrained; and (c) fully constrained fittings. The a, b, a^2, and b^2 parameters refer to probabilities for different adjacent strand arrangements. In plot a, the black, green, blue, red, and white regions respectively correspond to $\chi^2 < 19$, $19 < \chi^2 < 21$, $21 < \chi^2 < 23$, $23 < \chi^2 < 25$, and $\chi^2 > 25$. In plot b, the regions respectively correspond to $\chi^2 < 18$, $18 < \chi^2 < 20$, $20 < \chi^2 < 22$, $22 < \chi^2 < 24$, and $\chi^2 > 24$, and in plot c, the regions respectively correspond to $\chi^2 < 15$, $15 < \chi^2 < 17$, $17 < \chi^2 < 19$, $19 < \chi^2 < 21$, and $\chi^2 > 21$. Best-fit parameters were: **plot a**, $a = 0.22$, $b = 0.31$, $\chi^2 = 16.5$; **plot b**, $a = 0.31$, $b = 0.42$, $\chi^2 = 15.1$; and **plot c**, $a^2 = 0.26$, $b^2 = 0.33$, $\chi^2 = 12.7$. In plot a, the a and b parameters are the fractional probabilities of adjacent strands having *A* or *B* registries, respectively. In plot c, the a^2 and b^2 parameters are the fractional probabilities of domains of *A* or *B* registries, respectively.

Previous studies in our group using 2D PDSD methods detected inter-peptide or inter-residue crosspeaks with long mixing times between Ala6 and Gly10, and between Ile4 and Gly13.*(25)* These observations were consistent with the A and B registries. Compared with the previous SUL samples, the REDOR data were more quantitatively analyzed and also significant based on our knowledge because it provided the first residue-specific structural model for the β-strand HFPs. There would be complete (registry A) or nearly complete (registry B) inter-peptide hydrogen bonding for residues Ala1 to Gly16 which form the apolar region of the HFP. These hydrogen bonding patterns would be favored if this region were predominantly located in the membrane interior. The existence of multiple β-strand structures is also consistent with a recent ^{13}C and ^{15}N assignment of a membrane-associated HFP with SUL at Phe8, Leu9 and Gly10. *(28)* There were two crosspeaks with comparable intensity for the Leu9 ^{13}CO/Gly10 ^{15}N correlation and two crosspeaks with comparable intensity for the Gly10 ^{13}CO/Gly10 ^{15}N correlation. For a given pair, the two ^{13}C shifts differed by ~0.5 ppm and were both consistent with β-strand conformation whereas the Gly10 ^{15}N shifts were 107 and 111 ppm. The two crosspeaks may correlate with the multiple β-strand structures inferred from analysis of the REDOR data in the present study. It was also interesting to compare the current REDOR work with one anti-parallel registry suggested by a previous REDOR work where samples contained an equimolar mixture of a HFP with three sequential ^{13}CO labels and a HFP with three sequential ^{15}N labels were used.*(2)* Data were only acquired for a single dephasing time (τ = 24 ms) and the best-guess anti-parallel registry had

Ala14 hydrogen bonded with Leu7 which is different than the registries A and B in the present study. The Ala14/Leu7 could be one of the X registries but it is noted that there was significant uncertainty in the determination of this registry because of the multiple ^{13}CO and ^{15}N labels. Because of the single site ^{13}CO and ^{15}N labeling in the present study, there was definitive determination of the A and B registries and these registries are biologically reasonable.

The model peptide-membrane system was used to mimic the environment of membrane-associated gp41 protein so it would be worthwhile considering the registries A and B in the context of the full gp41 proteins. The gp41 ectodomain structures to-date show a symmetric trimer with an in-register parallel coiled-coil extending over residues 30-80.*(7)* The residues N-terminal of Ala30 are disordered and the soluble ectodomain construct also lacked the N-terminal HFP. Although there is no evidence that the oligomeric state of the membrane-associated HFP of the present study is a trimer, it is interesting to consider the anti-parallel β-sheet structure in the context of a putative trimeric state of intact gp41. It is difficult to understand this structure in the context of a single gp41 trimer, but this structure could be understood considering two trimers denoted "C" and "D" with respective HFP strands C_1, C_2 and C_3 and D_1, D_2 and D_3. A $C_1D_3C_2D_2C_3D_1$ anti-parallel β-sheet structure could be formed with the C_1, C_2 and C_3 strands parallel to one another, and the D_1, D_2 and D_3 strand parallel to one another, and the C and D strands anti-parallel to one another with D_3 hydrogen bonded to C_1 and C_2, C_2 hydrogen bonded with D_3 and D_2, etc. There is some support for this model from internuclear distance measurements on a HFP trimer

construct composed of three HFP strands chemically cross-linked at their C-termini. The ^{13}C-^{13}C and ^{13}C-^{15}N distances determined for this membrane-associated trimer were consistent with the A anti-parallel registry deduced from the present study.*(13)* The existence of multiple registries for a membrane-associated HFP could be biological relevant. One factor favoring the formation of A registry is inter-peptide hydrogen bonding for all the residues between Ala1 and Gly16. This hydrogen bonding would reduce the unfavorable Born energy of CO and NH dipoles in the low electric environment of the membrane interior. For the B registry, Ala1 is not part of the hydrogen bonding β-sheet registry and if the HFP N-terminus is charged, better charge solvation might be achieved relative to the A registry. Ala1 could adopt a broader range of conformation in the B registry which might facilitate the location of the charged N-terminus in a solvated environment. A greater distribution of the conformations for Ala1 is supported by linewidths which were broader than those of residues in the central region of HFP.*(29)* Although the ionization state(s) of membrane-associated β-strand HFP have not yet been experimentally determined, there is evidence for a charged amino terminus in the related influenza fusion peptide in its helical conformation.*(30)* The β-sheet registries may also relate to the fusion activities of membrane-associated HFPs. Either HIV or HFP with the Val2 → Glu2 point mutation is known to be nonfusogenic.*(1,31,32)* In the context of our results, this lack of fusion activity may be related to a change in the strand registries arising from the charged Glu2 side chain. The V2E mutation is trans-dominant, that is, mixtures of wild-type and mutant proteins correlated with fusion activities which

were reduced by much more than would be expected from the fraction of mutant proteins. This effect could be explained by registry changes for several strands near the mutant HFP which might affect HFP oligomerization and/or membrane locations.*(32)*

Finally, the data in our study restrict the X registry to structures other than the Ala14/Val2, Gly3, Ile4 or Gly5 anti-parallel registries. There are therefore many possibilities for the X structures and one of these possibilities, Ala14/Leu7 anti-parallel registry, has been discussed previously. Another reasonable possibility is parallel β-strand structure either in-register or close to in-register. This structural model is appealing because therefore most of the residues in the Ala1 to Gly16 region could have inter-peptide hydrogen bonds and this region could be located in the membrane interior. Previous solid-state NMR ^{13}C-^{15}N distance measurements were consistent with some population of in-register parallel strand structure over residues Gly5 to Gly13 in addition to anti-parallel population over residue Gly5 to Gly16.*(2,33)* In addition, infrared studies on constructs containing the first 34 or first 70 residues of gp41 were consistent with predominant in-register parallel β-sheet structure from residue Ala1 to Gly16.*(26)* The interpretation of the infrared data was based on shifts in peak wavenumbers of ^{13}C labeled relative to natural abundance peptides.

CONCLUSION

In the present work, different β-sheet registry models were tested with REDOR ^{13}CO-^{15}N distance measurements on a few selectively labeled samples.

Two
regi
hyd
bon
loca
dev
bec
whi
act
str

Two of the registries were shown to have significant population and both registries were consistent with complete or nearly complete inter-peptide hydrogen bonding for the apolar N-terminal domain of the HFP. This hydrogen bonding scheme would be favored if a significant part of this domain were located in the membrane interior where there is low water content. The development of a detailed structural model for β-strand HFP is significant because this is the observed conformation in cholesterol-containing membranes which reflect the composition of membranes of the host cells of HIV. HFP fusion activity is also observed for vesicles with this membrane composition and the β-strand conformation may therefore be a physiologically relevant HFP structure.

REFERENCE

1. Freed, E. O.; Delwart, E. L.; Buchschacher, G. L., Jr.; Panganiban, A. T., A mutation in the human immunodeficiency virus type 1 transmembrane glycoprotein gp41 dominantly interferes with fusion and infectivity. *Proc. Natl. Acad. Sci. U.S.A.* **1992,** 89, (1), 70-74.

2. Yang, J.; Weliky, D. P., Solid state nuclear magnetic resonance evidence for parallel and antiparallel strand arrangements in the membrane-associated HIV-1 fusion peptide. *Biochemistry* **2003,** 42, 11879-11890.

3. Yang, R.; Prorok, M.; Castellino, F. J.; Weliky, D. P., A trimeric HIV-1 fusion peptide construct which does not self-associate in aqueous solution and which has 15-fold higher membrane fusion rate. *J. Am. Chem. Soc.* **2004,** 126, (45), 14722-14723.

4. Yang, J.; Prorok, M.; Castellino, F. J.; Weliky, D. P., Oligomeric beta structure of the membrane-bound HIV-1 fusion peptide formed from soluble monomers. *Biophys. J.* **2004,** 87, 1951-1963.

5. Aloia, R. C.; Tian, H.; Jensen, F. C., Lipid composition and fluidity of the human immunodeficiency virus envelope and host cell plasma membranes. *Proc. Natl. Acad. Sci. U.S.A.* **1993,** 90, (11), 5181-5185.

6. Lu, M.; Blacklow, S. C.; Kim, P. S., A trimeric structural domain of the HIV-1 transmembrane glycoprotein. *Nat Struct Biol* **1995,** 2, (12), 1075-82.

7. Caffrey, M.; Cai, M.; Kaufman, J.; Stahl, S. J.; Wingfield, P. T.; Covell, D. G.; Gronenborn, A. M.; Clore, G. M., Three-dimensional solution structure of the 44 kDa ectodomain of SIV gp41. *EMBO J.* **1998,** 17, (16), 4572-4584.

8. Munoz-Barroso, I.; Durell, S.; Sakaguchi, K.; Appella, E.; Blumenthal, R., Dilation of the human immunodeficiency virus-1 envelope glycoprotein fusion pore revealed by the inhibitory action of a synthetic peptide from gp41. *J. Cell Biol.* **1998,** 140, (2), 315-323.

9. Bentz, J., Minimal aggregate size and minimal fusion unit for the first fusion pore of influenza hemagglutinin-mediated membrane fusion. *Biophys J* **2000,** 78, (1), 227-45.

10. Qiang, W., Bodner, M.L., and Weilky, D.P., Solid-state NMR Spectroscopy of HIV Fusion Peptides Associated with Host-Cell-Like Membranes: 2D Correlation Spectra and Distance Measurements Support a Fully Extended Conformation and Models for Specific Antiparallel Strand Registries. *J. Am. Chem. Soc.* **2008,** 130, 5459-5471.

11.
soli
Bio
12.
Pra

13.
flexi
trim
129

14.
trypt
Bioc

15.
Web
doub
1995

16.
Conc

17.
solid-
Cher

18.
the P

19.
simul
147,

20.
mem
rotor-
49-68

21.
of the
confo

22.
ed.; S

11. Yang, R.; Yang, J.; Weliky, D. P., Synthesis, enhanced fusogenicity, and solid state NMR measurements of cross-linked HIV-1 fusion peptides. *Biochemistry* **2003,** 42, (12), 3527-3535.
12. Chan, W. C., and White, P.D., *Fmoc Solid Phase Peptide Synthesis: A Practical Approach* **2000**, 94-109.

13. Zheng, Z., Yang, R., Bodner, M.L., and Weliky, D.P., Conformational flexibility and strand arrantments of the membrane-associated HIV fusion peptide trimer probed by solid-state NMR spectroscopy. *Biochemistry* **2006,** 45, 12960-12975.

14. McDowell, L. M.; Holl, S. M.; Qian, S. J.; Li, E.; Schaefer, J., Inter-tryptophan distances in rat cellular retinol-binding Protein Ii by solid-state NMR. *Biochemistry* **1993,** 32, (17), 4560-4563.

15. Anderson, R. C.; Gullion, T.; Joers, J. M.; Shapiro, M.; Villhauer, E. B.; Weber, H. P., Conformation of [1-^{13}C,^{15}N]acetyl-L-carnitine - rotational- echo, double-resonance nuclear-magnetic-resonance spectroscopy. *J. Am. Chem. Soc.* **1995,** 117, (42), 10546-10550.

16. Gullion, T., Introduction to rotational-echo, double-resonance NMR. *Concepts Magn. Reson.* **1998,** 10, (5), 277-289.

17. Long, H. W.; Tycko, R., Biopolymer conformational distributions from solid-state NMR: alpha-helix and 3(10)-helix contents of a helical peptide. *J. Am. Chem. Soc.* **1998,** 120, (28), 7039-7048.

18. Bevington, P. R.; Robinson, D. K., *Data Reduction and Error Analysis for the Physical Sciences*. 2nd ed.; McGraw-Hill: Boston, 1992; p 38-52.

19. Bak, M.; Rasmussen, J. T.; Nielsen, N. C., SIMPSON: A general simulation program for solid-state NMR spectroscopy. *J. Magn. Reson.* **2000,** 147, (2), 296-330.

20. Gabrys, C. M.; Yang, J.; Weliky, D. P., Analysis of local conformation of membrane-bound and polycrystalline peptides by two-dimensional slow-spinning rotor-synchronized MAS exchange spectroscopy. *J. Biomol. NMR* **2003,** 26, (1), 49-68.

21. Yildiz, O., Vinothkumar, K.R., Goswami, P., and Kuhlbrandt, W., Structure of the monomeric outer-membrane porin OmpG in the open and closed conformation. *EMBO Journal* **2006,** 25, (15), 3702-3713.

22. Mehring, M., *Principles of high-resolution NMR in solids*. 2nd, rev. and enl. ed.; Springer-Verlag: Berlin; New York, 1983.

23. Oas, T. G.; Hartzell, C. J.; McMahon, T. J.; Drobny, G. P.; Dahlquist, F. W., The carbonyl ^{13}C chemical-shift tensors of 5 peptides determined from ^{15}N dipole-coupled chemical shift powder patterns. *J. Am. Chem. Soc.* **1987,** 109, (20), 5956-5962.

24. Qiang, W., Yang, J., and Weliky, D.P., Solid-state nuclear magnetic resonance measurements of HIV fusion peptide to lipid distances reveal the intimate contact of beta strand peptide with membranes and the proximity of the Ala-14-Gly-16 region with lipid headgroups. *Biochemistry* **2007,** 46, (17), 4997-5008.

25. Bodner, M. L., *Solid state nuclear magnetic resonance of the HIV-1 and influenza fusion peptides associated with membranes.* Ph. D. thesis, Michigan State University: East Lansing, 2006; p 122.

26. Sackett, K.; Shai, Y., The HIV fusion peptide adopts intermolecular parallel β-sheet structure in membranes when stabilized by the adjacent N-terminal heptad repeat: A ^{13}C FTIR study. *J. Mol. Biol.* **2005,** 350, (4), 790-805.

27. Vogt, F. G., Gibson, J.M., Mattingly, S.M., and Mueller, K.T., Determination of molecular geometry in solid-state NMR: Rotational-echo double resonance of three-spin systems. *J. Phys. Chem. B* **2003,** 107, (5), 1272-1283.

28. Bodner, M. L., Gabrys, C.M., Struppe, J.O., and Weliky, D.P., C-13-C-13 and N-15-C-13 correlation spectroscopy of membrane-associated and uniformly labeled human immunodeficiency virus and influenza fusion peptides: Amino acid-type assignments and evidence for multiple conformations. *J. Chem. Phys* **2008,** 128, 052319.

29. Yang, J.; Gabrys, C. M.; Weliky, D. P., Solid-state nuclear magnetic resonance evidence for an extended beta strand conformation of the membrane-bound HIV-1 fusion peptide. *Biochemistry* **2001,** 40, (27), 8126-8137.

30. Zhou, Z.; Macosko, J. C.; Hughes, D. W.; Sayer, B. G.; Hawes, J.; Epand, R. M., N-15 NMR study of the ionization properties of the influenza virus fusion peptide in zwitterionic phospholipid dispersions. *Biophysical Journal* **2000,** 78, (5), 2418-2425.

31. Pereira, F. B.; Goni, F. M.; Muga, A.; Nieva, J. L., Permeabilization and fusion of uncharged lipid vesicles induced by the HIV-1 fusion peptide adopting an extended conformation: dose and sequence effects. *Biophys. J.* **1997,** 73, (4), 1977-1986.

32. Kliger, Y.; Aharoni, A.; Rapaport, D.; Jones, P.; Blumenthal, R.; Shai, Y., Fusion peptides derived from the HIV type 1 glycoprotein 41 associate within

phospholipid membranes and inhibit cell-cell Fusion. Structure- function study. *J. Biol. Chem.* **1997,** 272, (21), 13496-13505.

33. Zheng, Z., Qiang, W., and Weliky, D.P., Investigation of finite-pulse radiofrequency-driven recoupling methods for measurement of intercarbonyl distances in polycrystalline and membrane-associated HIV fusion peptide samples. *Magn. Reson. Chem.* **2007,** 245, S247-S260.

BA

pep

bee

cata

mai

ach

moc

fluor

fluor

in bu

obse

F8W

was

phosp

corre

result

with

locatio

the br

CHAPTER VI

MEMBRANE INSERTION OF HIV FUSION PEPTIDES

BACKGROUND

Current models of HIV/host cell infection include interaction of the fusion peptide with the host cell membrane.*(1,2)* The membrane location of HFP has been hypothesized to be significant structural factors for understanding the catalysis of fusion by HFP. Previous studies about the micelle location of HFP mainly utilized solution NMR methods where high resolution results had been achieved.*(3-7)* However, there is not yet a consensus and there were distinct models of both micelle surface location and micelle traversal.

HFP location in membranes has been primarily probed with tryptophan fluorescence of a HFP-F8W mutant.*(8-9)* Key results have included: (1) fluorescence was higher for membrane-associated HFP-F8W than for HFP-F8W in buffered saline solution; (2) greater fluorescence quenching by acrylamide was observed for a soluble tryptophan analog than for membrane-associated HFP-F8W; and (3) similar fluorescence quenching of membrane-associated HFP-F8W was observed in samples containing either 1-palmitoyl-2-stearoyl-phosphocholine brominated at the 6, 7 carbons of the stearoyl chain or the corresponding lipid brominated at the 11, 12 carbons of the chain. The first two results indicated that solvent exposure of the HFP-F8W tryptophan is reduced with membrane association and the third result indicated that the membrane location of the tryptophan indole group is centered near the carbon 9 position of the brominated lipid stearoyl chain; i.e. ~8.5 Å from the bilayer center and ~10 Å

from the lipid phosphorus. Infrared and solid-state NMR spectra of membrane-associated HFP suggested that the HFP-F8W had predominant β strand conformation under the conditions of the fluorescence experiments. In a different set of experiments, electron spin resonance spectra showed that chromium oxalate in the aqueous phase quenched the signal of membrane-associated HFP which was spin-labeled at M19 but did not quench HFP spin-labeled at A1.*(10)* These data indicated a M19 location close to the aqueous interface of the membrane and an A1 location away from this interface. Models for the membrane location of helical HFPs have also been developed by simulations and there have been distinct models supporting either partial insertion or traversal of the membrane. In one simulation the peptide was generally near the membrane surface with the F8 backbone and sidechain nuclei respectively 4 Å and 6 Å deeper than the phosphorus longitude.*(11)* In a different simulation, HFP traversed the membrane and the backbone and sidechain F8 nuclei were at the bilayer center, i.e. ~19 Å from the phosphorus longitude.*(12)*

The present work has been focused on the study of membrane location of the HFP in a host-cell-like environment. The goal of the research was to build up a high resolution insertion model which would correlate with HFP membrane fusion activities. To achieve the goal, different HFP constructs with very different fusion activities were considered as model peptides based on the previous and present studies using fluorescence spectroscopy.*(13-15)* The HFPmn induces fusion with moderate rate whereas very little fusion is observed for HFPmn_mut. The high-resolution structures of the soluble ectodomain of gp41 which lack the HFP are

Figure 22 Peptide sequences of the basic constructs of HFPmn_mut, HFPmn and HFPtr. The specific labeling sites were described in the main text.

trimeric and suggest that HFP may interact with the target cell membrane in a trimer unit.*(16)* The putative functional significance of trimers is supported by the 15-40 fold higher vesicle fusion rates of the chemically cross-linked HFPtr relative to HFPmn.*(14)* Thus, the fusion rates are ordered HFPmn_mut < HFPmn < HFPtr and the present study examines the structures and membrane locations of these constructs with correlation to their very different fusion activities. Solid-state NMR is suitable and more advantageous compared with other biophysical methods because with an appropriate isotope labeling scheme, it can provide residue-specific membrane insertion depth information with minimum perturbation to the membrane system. In this chapter, the ^{13}C-^{31}P and ^{13}C-^{19}F REDOR experiments which were used to probe the membrane location of different HFP residues will be described, initially with triply ^{13}CO-labeled HFPmn to get a qualitative sense,*(17)* and finally with singly ^{13}CO-labeled HFPmn_mut, HFPmn, and HFPtr to achieve systematic, semi-quantitative insertion models.*(18,19)*

MATERIALS AND METHODS

Peptides. The sequences of HFPmn_mut, HFPmn and HFPtr were summarized in Figure 22. The triply-labeled peptides followed the nomenclature of HFPmn-^{8}FLG, HFPmn-^{5}GAL, etc, and the singly-labeled peptides followed the nomenclature of HFPmn_mut-^{1}A, HFPtr-^{1}A, etc. In general, terms before the dash express HFP sequences with specific C-terminal tags and terms after the dash indicate the ^{13}CO labeling positions. All peptides were synthesized using

the strategies described in chapter II for HFPmn and HFPtr and all syntheses were completed either automatically on peptide synthesizer (Applied Biosystems 431A, Foster City, CA) or manually with a 15mL reaction vessel (Peptides International, Louisville, KY).*(20)* The C-terminal Lys(Boc), Trp(Boc) and Cys(Trt) were introduced to increase the solubility, add an A_{280} chromophore and achieve the synthesis of higher order HFP oligomer with cross-linking, respectively.*(14,15,21)* All peptides were purified using HPLC with a water-acetonitrile gradient, and identified using MALDI-TOF mass spectrometer.

Lipid mixing induced by HFPs. Mixing of lipids between membrane vesicles was monitored by a fluorescence assay to show that different HFP oligomers have very different lipid-mixing activities.*(22)* Together with the previous results which indicated the non-fusogenicity of HFPmn_mut, this work provide the rationale of choosing HFPmn_mut, HFPmn and HFPtr as model peptides to study the membrane location-fusion activity correlation.*(13)* Two types of large unilamellar vesicles (LUVs) were prepared. The "unlabeled LUVs" contained POPC and POPG in a 4:1 mol ratio. This composition approximately reflected the ratio of neutral to negatively charged lipids in membranes of host cells of HIV and correlated with the lipid composition used in previous structural studies of viral fusion peptides.*(23,24)* The "labeled LUVs" contained 77 mol% POPC, 19 mol% POPG, 2 mol% of the fluorescent lipid *N*-(7-nitro-2,1,3-benzoxadiazol-4-yl)-phosphatiylethanolamine (*N*-NBD-PE), and 2 mol% of the quenching lipid *N*-(lissamine Rhodamine B sulfonyl)-phosphatidylethanolamine (*N*-Rh-PE). HFP-induced fusion was examined in a solution with an

unlabeled:labeled vesicle ratio of 1:9 so that a labeled vesicle would likely fuse with an unlabeled vesicle. The resultant lipid mixing would yield a larger average distance between fluorescent and quenching lipids and increased fluorescence.

LUV preparation began with dissolution of lipid in chloroform followed by removal of the chloroform with nitrogen gas and overnight vacuum pumping. The lipid film was suspended in 5 mM HEPES buffer and the lipid dispersion was homogenized with ten freeze-thaw cycles. LUVs were formed by extrusion through a filter with 100 nm diameter pores (Avestin, Ottawa, ON).

Fluorescence was recorded on a stopped-flow fluorimeter (Applied Photophysics SX.18MV-R, Surrey, UK) using excitation and emission wavelengths of 465 and 530 nm, respectively. For a single run, one syringe in the fluorimeter contained HFPmn, HFPdm, HFPtr, or HFPte dissolved at a concentration of 3.00, 1.50, 1.00, or 0.75 μM in HEPES buffer. A second syringe contained labeled and unlabeled LUVs at 300 μM total lipid concentration. At time zero, equal volumes of the two solutions were mixed and fluorescence was recorded every second for 200 s. The HFP concentrations were chosen so that the HFP strand:lipid ratio was always 0.010.

Most reports of fluorescence based lipid mixing have focused on $\Delta F_{fusogen}$, the net change in fluorescence after the fusogen is added to the vesicles. $\Delta F_{fusogen}$ is typically compared to $\Delta F_{detergent}$, the change caused by addition of a detergent which completely solubilizes the vesicles. Because of the very large average distance between fluorescent and quenching lipids in the solubilized vesicles, $\Delta F_{detergent}$ is the maximum observable fluorescence change. The

"percent lipid mixing" is typically defined as $\Delta F_{fusogen}/\Delta F_{detergent} \times 100$. In order to provide some comparison between our stopped-flow fluorescence data and the lipid mixing literature, the raw data at each time point, $F_{raw}(t)$ were converted to normalized $F(t)$:

$$F(t) = \left\{ \left[F_{raw}(t) - F_{initial} \right] / \Delta F_{max} \right\} \times 100 \quad (54)$$

$F_{initial}$ was a typical value of fluorescence at t = 0 and ΔF_{max} was chosen to provide semi-quantitative comparison between $F(t)$ and earlier studies of percent lipid mixing induced by HFPs.*(21)* A single value of $F_{initial}$ and a single value of ΔF_{max} were used for all of the data.

At the end of the 200 s collection time, the fluorescence from HFPmn-induced lipid mixing was still appreciably increasing and it was therefore difficult to fit these data to a buildup function. The fluorescence of the HFPdm, HFPtr, and HFPte constructs had leveled off and these data fitted much better to the sum of two exponential buildup functions than to a single buildup function:

$$F(t) = F_0 + F_1(1 - e^{-k_1 t}) + F_2(1 - e^{-k_2 t}) \quad (55)$$

where F_0, k_1, F_1, k_2, and F_2 were fitting parameters. The best-fit value of F_0 was close to 0 because of the way $F(t)$ was calculated in Eq. 54. A convention was chosen that $k_1 > k_2$ so that k_1 and F_1 were respectively the rate constant and overall fluorescence change of the faster lipid mixing process and k_2 and F_2 were the rate constant and overall fluorescence change of the slow process.

Data were collected for each construct at 25, 30, 35 and 40 °C and each HFPdm, HFPtr, and HFPte data set was fitted with Eq. 55. For each construct,

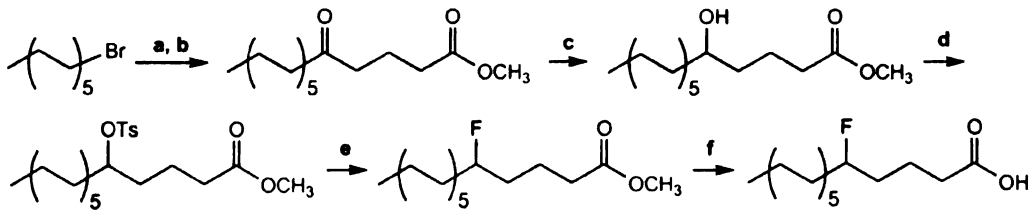

Figure 23 Synthetic scheme of 5-F-palmitic acid.

the temperature dependence of k_1 was fitted to the Arrhenius Equation $ln\ k_1 = ln\ A - E_a/RT$ where R was the ideal gas constant, T was the absolute temperature, and A and E_a were the pre-exponential factor and activation energy, respectively. Three independent runs were done for each construct and temperature.

Synthesis of the precursor of 5-^{19}F-DPPC. In general, the experiments described in this chapter measured the internuclear distances between the selectively labeled ^{13}CO in the HFP strands and the ^{31}P or ^{19}F in the lipid bilayer. Besides the ^{31}P nucleus in the phosphate group, two types of fluorinated lipids were used in order to cover the entire depth of lipid bilayer. The 1-palmitoyl-2-(16-fluoropalmitoyl)-*sn*-glycero-3-phosphocholine (16-^{19}F-DPPC) was purchased from the Avanti Polar Lipids and the precursor of 1-palmitoyl-2-(5-fluoropalmitoyl)-*sn*-glycero-3-phosphocholine (5-^{19}F-DPPC), named 5-F-palmitic acid, was synthesized in our lab. The ^{19}F nuclei were located 8.5 Å and 20.7 Å away from the layer of ^{31}P for the 5-^{19}F-DPPC and 16-^{19}F-DPPC, respectively.*(25)* The synthetic scheme for 5-F-palmitic acid is described in Figure 23. The overall yield of 5-^{19}F-palmitic acid was ~40% and each step was monitored using thin layer chromatography with iodine and phosphomolybdic acid as visualization reagents. The intermediate products were purified using silica gel column chromatography with a mixture of pentane and ethyl acetate as developing solutions.*(26-30)* The 5-^{19}F-DPPC was synthesized by Avanti Polar Lipids using the 5-F-palmitic acid as a precursor.

Reaction conditions in Figure 23 included: (a) 68.2 g undecyl bromide (Sigma-Aldrich, St. Louis, MO) in 350 mL dry diethyl ether was added to 6.94 g Mg in 100 mL dry diethyl ether. Reflux at 34 °C for 2 hours. (b) The diethyl ether was removed and 28.0 g methyl 4-(chloro-formyl) butyrate (Sigma-Aldrich, St. Louis, MO) in 100 mL dry benzene was added to the Grignard solution from step a and 27.5 g $CdCl_2$ in 350 mL dry benzene. Reflux at 78 °C for 1 hour. (c) $NaBH_4$, NaH_2PO_4 and 5-keto-methyl palmitate each at 1 M concentration were dissolved in dry methanol. The mixture was stirred at 0 °C for 15 minutes and at ambient temperature for 1 hour. (d) 5-hydroxy-methyl palmitate and 0.5 M tosyl chloride (Sigma-Aldrich, St. Louis, MO) each at 0.5 M concentration were dissolved in dry CH_2Cl_2 with 0.025 M 4-(dimethylamino)pyridine. The mixture was cooled and held at 0 °C, dry pyridine was added dropwise over 40 minutes to reach a final concentration 0.5 M, and then the mixture was stirred at 0 °C for 2 hours. (e) 0.05 M 5-O-tosyl-methyl palmitate and 0.1 M tetrabutylammonium fluoride (Sigma-Aldrich, St. Louis, MO) in dry CH_3CN were stirred at ambient temperature for 96 hours. (f) 5-F-methyl palmitate and KOH powder were each added into dry methanol at 0 °C to reach a final concentration of 0.1 M of each reagent. The mixture was stirred at 0 °C for 2 hours.

Solid-state NMR Sample Preparation and Experiments. The lipid bilayer samples were prepared using the same procedure as in chapter IV, however, with different lipid compositions. "PC:PG" in this chapter denotes a lipid bilayer with DTPC:DTPG in 4:1 molar ratio for triply-^{13}CO-labeled HFPs and

(a)

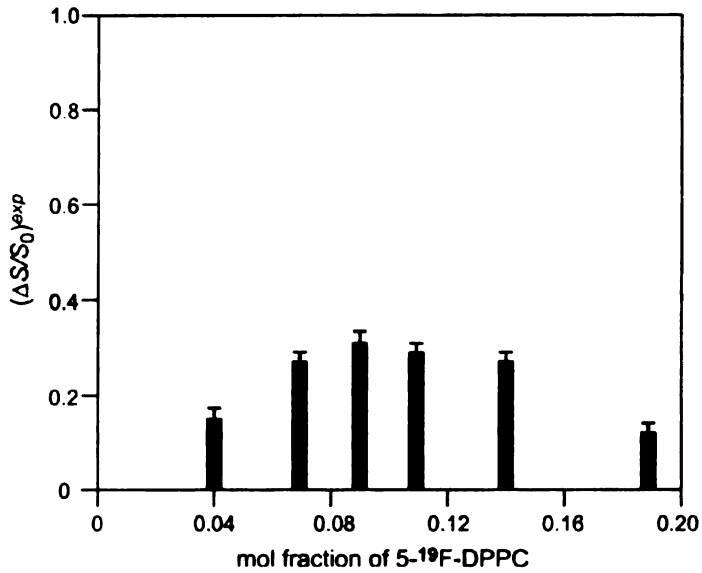

(b)

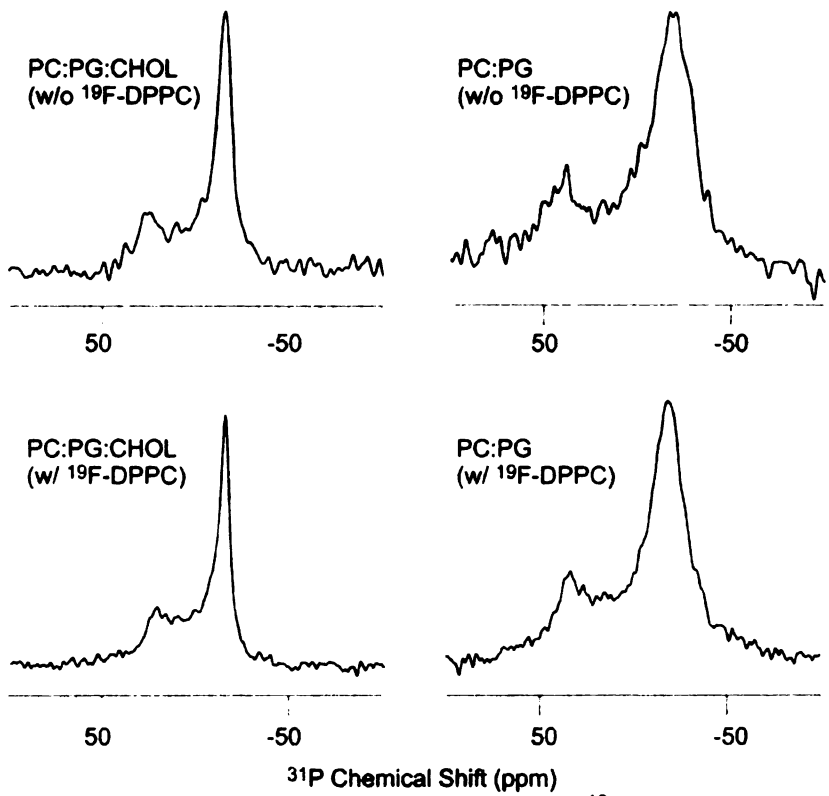

Figure 24 (a) Plot of $(\Delta S/S_0)^{exp}$ vs mol fraction of 5-^{19}F-DPPC at τ = 16 ms. All samples contained HFPmn-L9. (b) Static ^{31}P spectra for PC:PG and PC:PG:CHOL bilayer with and without 9 mol fraction ^{19}F-DPPC. Each spectrum was acquired with 1024 scans and processed with 300 Hz Gaussian line broadening. The spectra were acquired at 35 °C.

DTPC:DTPG:^{19}F-DPPC in molar ratio 8:2:1 for singly-^{13}CO-labeled samples. "PC:PG:CHOL" denotes a lipid bilayer with DTPC:DTPG:cholesterol in 8:2:5 molar ratio for triply-^{13}CO-labeled samples and DTPC:DTPG:cholesterol:^{19}F-DPPC in molar ratio 8:2:5:1 for singly-^{13}CO-labeled samples. The molar ratio for peptide strand to DTPC+DTPG was 1:50 for PC:PG samples and 1:25 for PC:PG:CHOL samples, respectively. Samples containing 100% ^{19}F-DPPC form non-bilayer structures.*(31)* In order to maintain bilayer structure in the NMR samples, 0.09 lipid mol fraction of ^{19}F-DPPC was initially determined with measurements on a series of samples which differed in their mol fraction of 5-^{19}F-DPPC, cf. Figure 24a. The choice of 0.09 mol fraction ^{19}F-DPPC for subsequent samples was based on: (1) maximum $(\Delta S/S_0)^{exp}$; and (2) relatively constant $(\Delta S/S_0)^{exp}$ over the 0.07-0.14 mol fraction range. Static ^{31}P NMR spectra were consistent with overall bilayer structure in samples containing 0.09 mol ^{19}F-DPPC (*cf.* Figure 24b).

The ^{13}C-^{31}P REDOR experiments were conducted on a triple-resonance MAS probe and the ^{13}C-^{19}F REDOR experiments were conducted on a quadruple-resonance MAS probe. The ^{1}H, ^{13}C and ^{31}P channels were tuned at 400.8 MHz, 100.8 MHz and 162.2 MHz respectively for ^{13}C-^{31}P experiments and the ^{1}H, ^{13}C and ^{19}F channels were tuned to 398.7 MHz, 100.2 MHz and 375.1 MHz respectively for ^{13}C-^{19}F experiments. The following parameters were used in both ^{13}C-^{31}P and ^{13}C-^{19}F experiments: 50 kHz ^{1}H $\pi/2$ pulse, 1 ms CP between ^{1}H and ^{13}C channels, 50 kHz constant ^{1}H field and 55-66 kHz ramped ^{13}C field during CP and 50 kHz ^{13}C π pulse in the REDOR dephasing period. A 95 kHz ^{1}H

decoupling field during dephasing and acquisition periods was used for ^{13}C-^{31}P experiments and a 75 kHz ^{1}H decoupling field was used for ^{13}C-^{19}F experiments. The π pulses alternatively applied either on the ^{31}P (50 kHz) or ^{19}F (33 kHz) channel were calibrated by maximizing $(\Delta S/S_0)^{exp}$ in standard samples as described in the experimental setup in chapter III.

Natural Abundance Correction for $(\Delta S/S_0)^{exp}$. The natural abundance correction was required for quantitatively analyzing the REDOR experimental data. The triply and singly-labeled samples followed different natural abundance correction procedures.

For the triply-labeled samples which were associated with ether-linked phospholipids, the natural abundance correction started from considering that both S_0 and S_1 came from the labeled ^{13}CO and the natural abundance of unlabeled residues.

$$\left(\frac{\Delta S}{S_0}\right)^{exp} = \frac{S_0^{lab} + S_0^{na} - S_1^{lab} - S_1^{na}}{S_0^{lab} + S_0^{na}} = 1 - \frac{S_1^{lab}}{S_0^{lab} + S_0^{na}} - \frac{S_1^{na}}{S_0^{lab} + S_0^{na}} \quad (56)$$

A few algebraic manipulations led to the relation between $(\Delta S/S_0)^{lab}$, which was the contribution to REDOR dephasing from the labeled ^{13}CO, and $(\Delta S/S_0)^{exp}$.

$$\left(\frac{\Delta S}{S_0}\right)^{lab} = \left[\left(1 + \frac{S_0^{na}}{S_0^{lab}}\right) \times \left(\frac{\Delta S}{S_0}\right)^{exp}\right] - \left[\left(\frac{S_0^{na}}{S_0^{lab}}\right) \times \left(\frac{\Delta S}{S_0}\right)^{na}\right] \quad (57)$$

The term S_0^{na}/S_0^{lab} was related to the number of unlabeled residues *vs.* labeled residues in the sequence. The term $(\Delta S/S_0)^{na}$ considered the contribution to REDOR dephasing from all the unlabeled residues and was approximately calculated as the average of all available $(\Delta S/S_0)^{exp}$. Although the latter

calculation is an approximation, uncertainties in $(\Delta S/S_0)^{na}$ have a relatively small impact on the value of $(\Delta S/S_0)^{lab}$. For example, consider the spectra for the HFP2-^{14}AAG in PC:PG samples at τ = 24 ms. The values of (S_0^{na}/S_0^{lab}), $(\Delta S/S_0)^{exp}$, and $(\Delta S/S_0)^{na}$ are 0.084, 0.419 ± 0.014, and 0.134, respectively, and result in $(\Delta S/S_0)^{lab}$ = 0.443 ± 0.015. If $(\Delta S/S_0)^{na}$ were 0.0 or 0.25, $(\Delta S/S_0)^{lab}$ would be 0.454 or 0.433, and are within the experimental uncertainty of the reported $(\Delta S/S_0)^{lab}$.

For the singly-labeled samples, 0.09 mol fraction ^{19}F-DPPC with natural abundance ^{13}COs were incorporated into the lipid bilayer. The comparable formulas to Eq. 56 and Eq. 57 were

$$\left(\frac{\Delta S}{S}\right)^{\exp} = \frac{S_0^{lab} + S_0^{na}(HFP) + S_0^{na}(DPPC) - S_1^{lab} - S_1^{na}(HFP) - S_1^{na}(DPPC)}{S_0^{lab} + S_0^{na}(HFP) + S_0^{na}(DPPC)} \quad (58)$$

and

$$\left(\frac{\Delta S}{S_0}\right)^{lab} = (1 + \frac{S_0^{na}(HFP) + S_0^{na}(DPPC)}{S_0^{lab}}) \cdot \left(\frac{\Delta S}{S_0}\right)^{exp} - \frac{S_0^{na}(HFP)}{S_0^{lab}} \cdot \left(\frac{\Delta S}{S_0}\right)^{na}(HFP) - \frac{S_0^{na}(DPPC)}{S_0^{lab}} \cdot \left(\frac{\Delta S}{S_0}\right)^{na}(DPPC) \quad (59)$$

The terms $(\Delta S/S_0)^{lab}$, $(\Delta S/S_0)^{na}$ (HFP) and $(\Delta S/S_0)^{na}$ (DPPC) represented the contribution to REDOR dephasing from the labeled ^{13}CO, the natural abundance of unlabeled residues and the natural abundance ^{13}CO from ^{16}F-DPPC, respectively. The S_0 terms in Eq. 59 had the numerical values

$$\begin{aligned} S_0^{lab} &= 1 \\ S_0^{na}(HFP) &= 29 \times 0.011 = 0.319 \\ S_0^{na}(DPPC) &= 2.5 \times 2 \times 0.011 = 0.055 \end{aligned} \quad (60)$$

The values of $(\Delta S/S_0)^{na}$ (HFP) were calculated from the experimentally available $(\Delta S/S_0)^{exp}$ for a specific HFP construct and the values $(\Delta S/S_0)^{na}$ (DPPC) were

Table 5a. The $(\Delta S/S_0)^{na}$ *(HFP)*

		^{13}CO-^{31}P [a]			^{13}CO-(16-^{19}F) [a b]	^{13}CO-(5-^{19}F) [a b]
Peptide		HFPmn_mut	HFPmn	HFPtr	HFPtr	HFPmn
	2	0.007	0.023	0.010	0.018	0.002
	8	0.118	0.133	0.099	0.004	0.016
τ(ms)	16	0.319	0.260	0.188	0.028	0.032
	24	0.465	0.353	0.294	0.135	0.158
	32	0.444	0.380	0.308	---	---

[a] The ^{13}CO-^{31}P values were based on the $(S_1/S_0)^{exp}$ of samples labeled at Ala1, Ile4, Ala6, Leu9, Leu12, or Ala14, and for HFPmn_mut and HFPmn, Ala21. The ^{13}CO-^{19}F(C16) values were based on samples labeled at Ala1, Ile4, Ala6, Leu9, Leu12, or Ala14 and the ^{13}CO-^{19}F(C5) values were based on samples labeled at Ala1, Ala6, or Leu9.
[b] The maximum τ for ^{13}CO-^{19}F experiments was 24 ms.

Table 5b. The $(\Delta S/S_0)^{na}$ *(DPPC)*

		^{13}CO-^{31}P	^{13}CO-(16-^{19}F) [a]	^{13}CO-(5-^{19}F) [a]
	2	0.025	0.000	0.011
	8	0.318	0.000	0.118
τ(ms)	16	0.695	0.000	0.567
	24	0.811	0.000	0.896
	32	0.907	---	---

[a] The maximum τ for ^{13}CO-^{19}F experiments was 24 ms.

calculated using a ^{13}C-^{31}P or ^{13}C-^{19}F two-spin system with internuclear distance of the setup model compound. Table 5 provides the numerical values.

RESULTS AND DISCUSSION

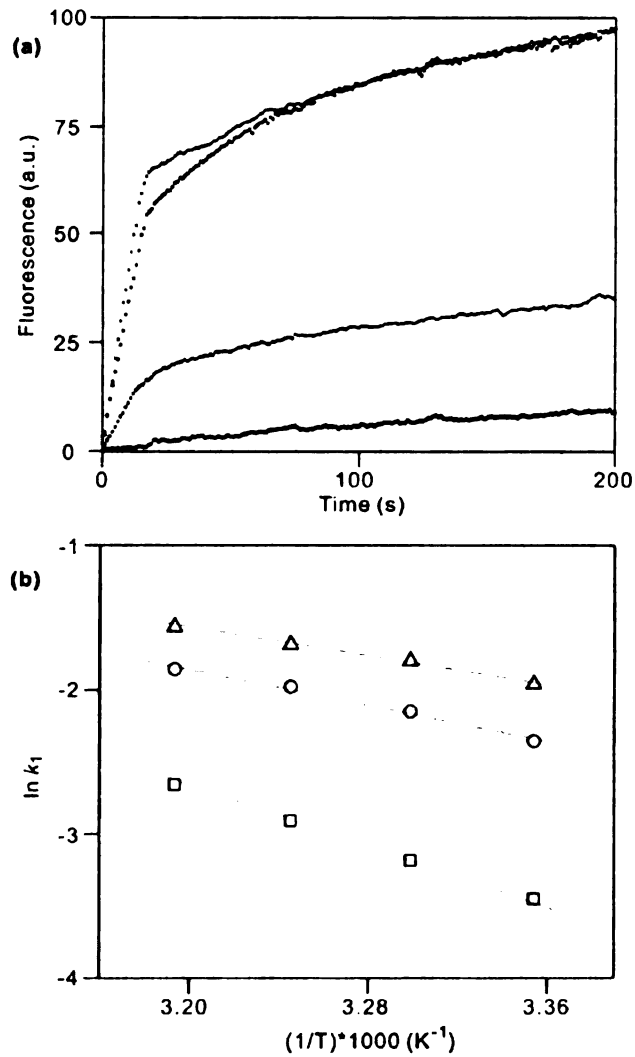

Figure 25 Panel a displays stopped-flow monitored changes in lipid fluorescence induced by addition of different HFP constructs to an aqueous solution containing membrane vesicles. Increased fluorescence is a result of mixing of lipids between different vesicles and this mixing is one consequence of vesicle fusion. The lines are color coded: HFPmn (black); HFPdm (red); HFPtr (blue); and HFPte (green). The total lipid concentration was 150 μM and the HFPmn, HFPdm, HFPtr, and HFPte concentrations were 1.50, 0.75, 0.50, and 0.37 μM, respectively, so that peptide strand:lipid = 0.01. The data were collected at 25 °C, the vesicle composition was 4:1 POPC:POPG, and the initial vesicle diameter was ~100 nm. Additional data (not shown) were obtained for HFPdm, HFPtr, and HFPte at 30, 35, and 40 °C. Each data set for each construct was analyzed as the sum of two exponential buildup functions. Panel b displays Arrhenius plots for the rate constants of the fast buildup function with legend: HFPdm (open square); HFPtr (open circle); and HFPte (open triangle). The best-fit lines are also displayed and result in the respective activation energies 41 ± 3, 26 ± 1, and 20 ± 1 kJ/mol.

Fusion Activities of Different HFP Constructs. The lipid-mixing assay provided the rationale for choosing different HFP constructs to study the membrane location-fusion activity correlation. Previous study in our group suggested the fusion activities for HFPmn, HFPdm and HFPtr followed the trend HFPmn < HFPdm < HFPtr. The present study introduces a higher order HFPte and suggests that HFPtr may have the highest catalytic efficiency among all the four HFP constructs. Figure 25a shows stopped-flow fluorescence data which track lipid mixing induced by HFPs and suggests that the long-time lipid mixing rates are ordered HFPmn < HFPdm < HFPtr ≈ HFPte. Both HFPtr and HFPte induced similar rapid lipid mixing while HFPdm induced slower mixing and HFPmn induced little mixing. For each construct, data were acquired at 25, 30, 35, and 40 °C and the HFPdm, HFPtr, and HFPte data could be fit well to a biexponential buildup function, cf. Eq. 55. The best-fit parameters of the 35 °C data are listed in Table 6 as an example of data fitting. For each of the three constructs, $k_2 \approx 0.1\ k_1$ and $F_1 \approx F_2$. In addition, $k_1^{tr}/k_1^{dm} \approx 2.5$ and $k_1^{te}/k_1^{tr} \approx 1.3$. Figure 25b displays Arrhenius plots for the k_1 rate constants and the best-fit E_as and *ln A*s are listed in Table 6. The values of E_a and *ln A* for HFPdm and HFPtr are comparable to those reported in a previous study.*(14)* The data show that $E_a^{dm} > E_a^{tr} > E_a^{te}$ and $ln\ A_{dm} > ln\ A_{tr} > ln\ A_{te}$. An increased number of strands in the oligomer is therefore correlated with decreased *ln A* and E_a with concomitant opposite effects on k_1. The activation entropies were calculated using the transition state theory equation $\Delta S^{\ddagger} = R \times [ln(Ah/k_BT) - 2]$ where R is the ideal gas constant, h is Planck's constant, k_B is Boltzmann's constant, and T is the

absolute temperature.(*14*) The resultant $\Delta S^{\ddagger}$ were all negative with $\Delta S^{\ddagger}_{dm} > \Delta S^{\ddagger}_{tr} > \Delta S^{\ddagger}_{te}$ but we do not understand the sign or trends of the $\Delta S^{\ddagger}$ values. These data indicate: (1) cross-linking increases the rate and extent of HFP-induced lipid mixing and decreases activation energy; and (2) the increase in lipid-mixing-per-strand and decrease in activation energy with cross-linking levels off at HFPtr. It might be expected that oligomer folding would be more difficult with an increasing number of monomer units so the putative trimeric oligomerization state of gp41 and other class I viral fusion proteins may be the optimal balance between higher catalytic efficiency and more difficult folding.

Table 6. Fitting parameters for the lipid mixing kinetics at 35°C [a,b]

Construct	k_1 (10^{-3} s^{-1})	k_2 (10^{-3} s^{-1})	F_0 (a.u.)	F_1 (a.u.)	F_2 (a.u.)	E_a [c] (kJ/mol)	*ln A*	$\Delta S^{\ddagger}$ [d] (J/mol-K)
HFPdm	54.9 (0.3)	4.9 (0.2)	0.5 (0.1)	19.6 (0.3)	19.8 (0.1)	40.6 (3.4)	13.2 (1.2)	-152
HFPtr	139 (3)	17.3 (0.3)	0.9 (0.2)	50.1 (0.2)	50.0 (0.2)	25.8 (1.2)	8.0 (0.8)	-195
HFPte	185 (7)	20.7 (0.3)	0.9 (0.3)	49.8 (0.3)	50.1 (0.2)	20.1 (0.7)	6.2 (0.5)	-210

[a] Fitting uncertainties are given in parentheses. The variation of a parameter value from fitting data of different runs was less than the fitting uncertainty of a single run.

[b] The k_1, k_2, F_0, F_1 and F_2 were obtained using Eq. 2 in the main text.

[c] E_a and ln A were calculated using $ln\, k_1 = ln\, A - E_a/RT$ and k_1 values from temperatures between 25 and 40 °C.

[d] $\Delta S^{\ddagger}$ was calculated using $\Delta S^{\ddagger} = R \times [ln\,(Ah/k_BT) - 2]$.

Membrane Insertion of triply-labeled HFPs detected by ^{13}C-^{31}P REDOR methods. The long-term goal of the membrane insertion study is a detailed structure of the membrane location of the HFP in helical and β strand

conformations. There was relatively little information about the membrane location of HFP. It was also likely that a large number of ^{13}CO sites had ^{13}CO-^{31}P distances beyond the REDOR detection limit. In addition, HFP ^{13}C linewidths are fairly broad which leads to overlap of ^{13}CO resonances from different residues and the need for specific ^{13}CO labeling. In an effort to reduce the numbers of specifically labeled peptides needed to develop a membrane location model, samples were first made with four peptides each of which had ^{13}CO labels at three sequential residues between G5 and G16. The G5-G16 region was therefore rapidly scanned for ^{13}CO-^{31}P proximity. Although the $(\Delta S/S_0)^{exp}$ data for each of the samples had contributions from three distinct ^{13}CO sites, the individual $(\Delta S/S_0)$ would only be appreciably greater than zero for ^{13}CO-^{31}P distances $\leq$ 8 Å. The regions of HFP proximate to ^{31}P were defined from the REDOR data on the triply labeled samples and these regions provided a basis for choosing sites for single ^{13}CO labeled peptides which will be described later in this chapter.

The secondary structure information that can be obtained with the triply-labeled samples was limited by the overlapping of multiple ^{13}CO labelings, nonetheless, the local peptide conformation was examined by analysis of the ^{13}CO chemical shift distributions in S_0 spectra of HFPs obtained with τ = 2 ms, cf. Figure 26. The data supported the following models: (1) the major fraction of peptides in PC:PG and PC:PG:CHOL adopted a β strand conformation from G5 to G16; and (2) there is a minor fraction of peptides in PC:PG with helical

conformation. The detailed experimental support for the models is based on the

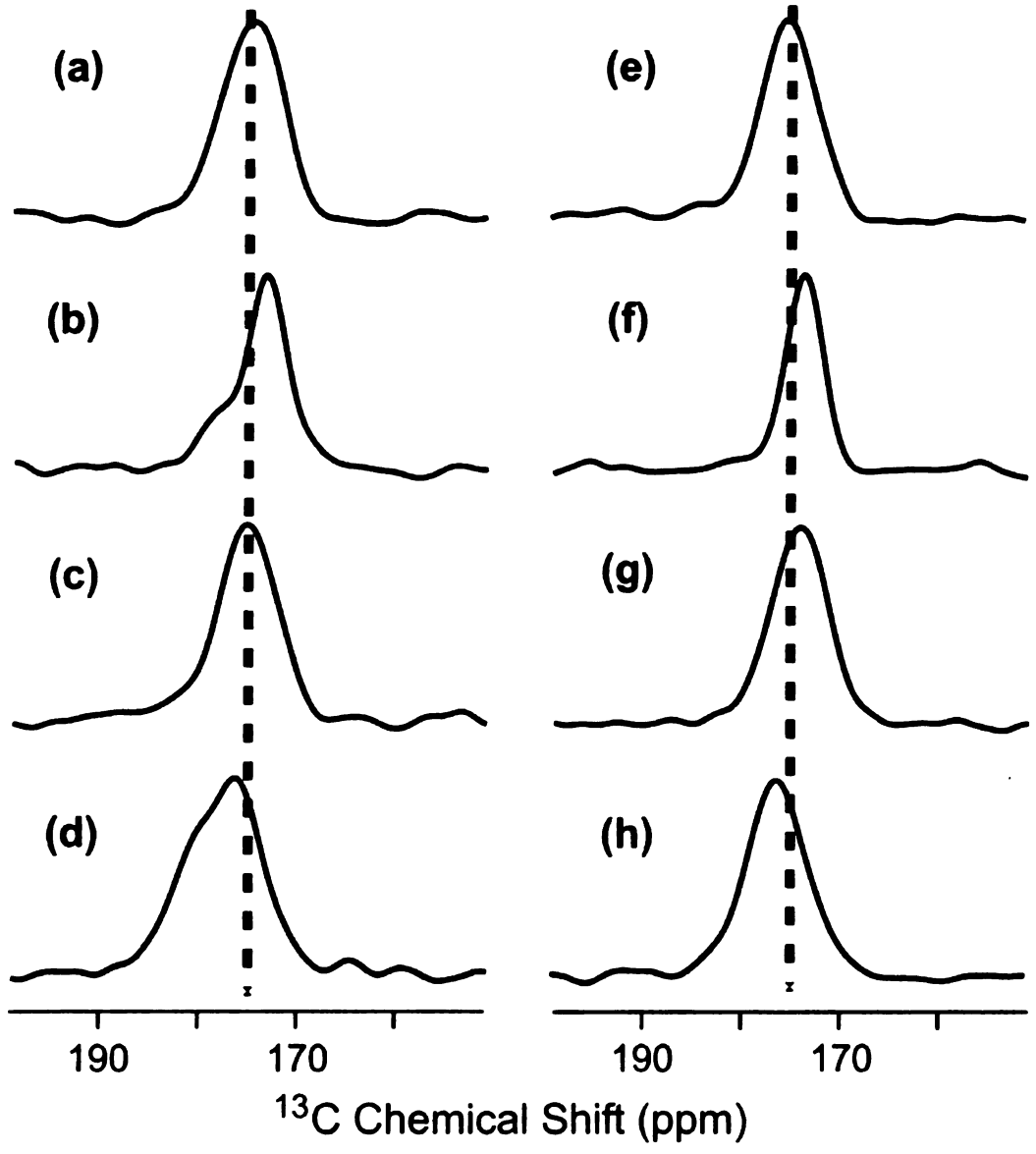

Figure 26 S_0 spectra for membrane-associated HFP with peptide:lipid ~0.04. The dotted lines are at 175 ppm. All spectra were obtained with τ = 2 ms and were processed with 200 Hz Gaussian line broadening and baseline correction. The membrane composition for samples a-d was PC:PG and the membrane composition for samples e-h was PC:PG:CHOL. The peptides were: a, e, HFPmn-^{5}GAL; b, f, HFPmn-^{8}FLG; c, g, HFPmn-^{11}FLG; and d, h HFPmn-^{14}AAG. The numbers of scans summed to obtain spectra a-h were 4823, 3867, 4823, 8500, 3259, 1001, 4320 and 6992, respectively.

known correlation between larger ^{13}CO chemical shifts and local helical conformation and smaller ^{13}CO chemical shifts and local β strand conformation. *(33)* For example, average database values in ppm units of ^{13}CO chemical shifts of helix (strand) conformations are: Gly, 175.5 (172.6); Ala, 179.4 (176.1); Leu, 178.5 (175.7); and Phe, 177.1 (174.2). For the ^{5}GAL, ^{8}FLG, ^{11}FLG, and ^{14}AAG samples, the peak chemical shifts were ~175, 174, 175, and 176 ppm, respectively, and correlated with β strand conformation for the Ala, Leu, and Phe residues. For the ^{8}FLG and ^{14}AAG samples associated with PC:PG, there were shoulders at ~178 and 179 ppm, respectively, which correlated with helical conformation of Ala, Leu, and Phe residues. These results were consistent with previous studies of the conformation of membrane-associated HFP with peptide:lipid ~ 0.04 and with previous observations of greater preference for β strand conformation in cholesterol-containing membranes.*(34-41)*

The values of $(\Delta S/S_0)^{exp}$ were extracted from integrating the ^{13}CO signals of the corresponding S_0 and S_1 spectra. The experimental values were used to obtain $(\Delta S/S_0)^{lab}$ and the corrected dephasing was fit to $(\Delta S/S_0)^{sim}$ from Eq. 34 to achieve the minimum root-mean-squared deviation (RMSD).

$$\chi^2(d) = \sum_{i=1}^{T} \frac{\left\{\left(\frac{\Delta S}{S_0}\right)_i^{lab} - f\left[\frac{\Delta S}{S_0}(d)\right]_i^{sim}\right\}^2}{(\sigma_i^{lab})^2} \quad (61)$$

The fitting parameter *d* represented the dipolar coupling frequency which could be converted into the internuclear distance *r* and *f* was the fraction of ^{13}CO that was close enough to the lipid ^{31}P to provide non-zero dephasing. This fraction

parameter was considered because at large τ values, $(\Delta S/S_0)^{lab}$ reached plateau values of ~1. The corrected uncertainty $\sigma^{lab} = (1 + S_0^{na}/S_0^{lab}) \times \sigma^{exp}$ while the experimental uncertainty was calculated using Eq. 35.*(42)*

Figure 27 displays the τ = 16 and 24 ms REDOR spectra of triply-labeled membrane-associated HFP samples and Figure 28a,b displays comparative plots of $(\Delta S/S_0)^{exp}$ for the different samples. The data demonstrated that samples containing HFPmn-^{14}AAG have qualitatively larger $(\Delta S/S_0)^{exp}$ than do samples containing HFP labeled at other residues. Using the conformational results from Figure 26, it appears: (1) a significant fraction of β strand HFP are in close contact with membranes; and (2) the ^{14}AAG (A14 to G16) region is closer to the lipid ^{31}P than is the ^{5}GALFLGFLG (G5 to G13) region. Figure 28c,d displays plots of $(\Delta S/S_0)^{lab}$ and best-fit $(\Delta S/S_0)^{sim}$ for HFPmn-^{14}AAG in PC:PG and PC:PG:CHOL. The best-fit *r* was ~5.2 Å in both membrane compositions and the best-fit *f* in PC:PG and PC:PG:CHOL were 0.45 and 0.32, respectively. It was not possible to fit the HFPmn-^{14}AAG data well without inclusion of the *f* parameter. Although the $(\Delta S/S_0)^{lab}$ had contributions from three ^{13}CO sites which would each have a distinct *r*, the number of data points and signal-to-noise dictated fitting to a single *r* value. The best-fit *r* should therefore be considered as both approximate and as likely representing the population of ^{13}CO sites with greatest *d* and smallest *r*. Fitting was not done for data from the other samples because of the small $(\Delta S/S_0)^{exp}$ and because the $(\Delta S/S_0)^{exp}$ do not always reach asymptotic values at large τ.

As a control experiment, spectra were also obtained for samples made with HFPmn labeled at ^{8}FLG that did not contain C-terminal lysines (named HFPmn1-^{8}FLG). For τ = 2, 8, 16, and 24 ms, $(\Delta S/S_0)^{exp}$ = -0.02, 0.06, 0.11, and 0.08 for the HFPmn1-^{8}FLG/PC:PG sample and 0.01, 0.03, 0.01, and –0.01 for the HFPmn1-^{8}FLG/PC:PG:CHOL sample. These values correlated with the $(\Delta S/S_0)^{exp}$ of the respective HFPmn-^{8}FLG/PC:PG and HFPmn-^{8}FLG/PC:PG:CHOL samples (circles in Figure 28) and suggested that the additional C-terminal lysines do not greatly affect the REDOR results.

The position of the HFP in the membrane has been postulated to be a significant structural factor in its fusion activity and to our knowledge; this study is the first example of direct distance measurements between the HFP and the lipid headgroups. Values of r ~ 5-6 Å were detected between the ^{13}COs of residues from A14 to G16 and the lipid ^{31}Ps. These r values support intimate association of the HFP and membranes containing either only phospholipids or phospholipids and cholesterol. The average r for ^{5}GALFLGFLG ^{13}COs was likely greater than 8 Å ($d \leq 25$ Hz) as evidenced by the significantly smaller $(\Delta S/S_0)^{exp}$, *cf.* Figure 28. Thus, relative to the ^{5}GALFLGFLG residues, the ^{14}AAG residues are much closer to the lipid ^{31}P. The G5 to G16 ^{13}CO chemical shift distributions of this study were consistent with a major population of HFP with β strand conformation for these residues. This result correlated with previous studies which supported the following structural features: (1) β strand HFP was fully extended between A1 and G16;*(35,43)* (2) β strand HFP formed hydrogen bonded oligomers or aggregates;*(39,44)* and (3) a

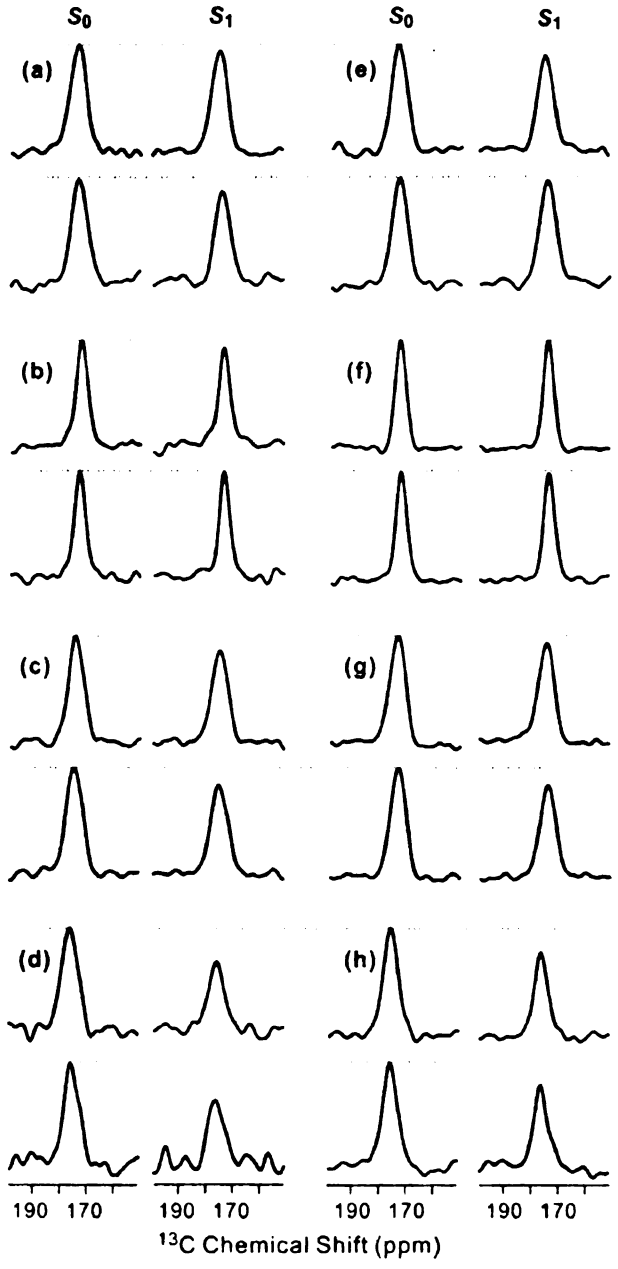

Figure 27 ^{13}CO-^{31}P REDOR spectra of membrane-associated HFP with peptide:lipid ~0.04. Each letter corresponds to a single sample which contained (a-d) PC:PG or (e-h) PC:PG:CHOL and (a, e) HFPmn-^{5}GAL, (b, f) HFPmn-^{8}FLG, (c, g) HFPmn-^{11}FLG, or (d, h) HFPmn-^{14}AAG. For each letter/sample, S_0 (left), S_1 (right), τ = 16 ms (top), and τ = 24 ms (bottom) spectra are displayed. The dotted lines are drawn for visual comparison of S_0 and S_1 peak intensities. Each spectrum was processed with 300 Hz Gaussian line broadening and baseline correction. The numbers of S_0 or S_1 scans summed to obtain the top and bottom spectra were respectively: a, 30000, 56000; b, 27509, 29463; c, 20000, 40000; d, 44129, 48296; e, 8448, 52384; f, 5488, 21664; g, 28032, 52384; and h, 22576, 50240.

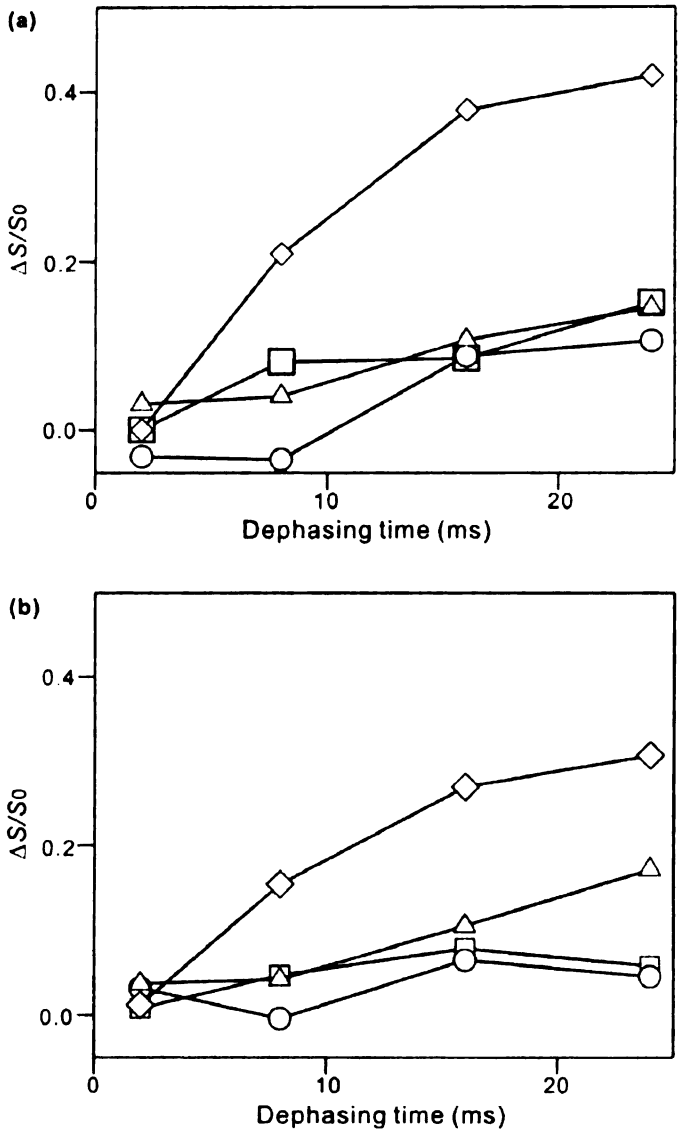

Figure 28 ($\Delta S/S_0$) vs dephasing time for membrane-associated HFP in (a,c) PC:PG or (b,d) PC:PG:CHOL. For panels a and b, the points correspond to $(\Delta S/S_0)^{exp}$ and the symbol legend is: squares, HFP2-^{5}GAL ; circles, HFP3-^{8}FLG; triangles, HFP2-^{11}FLG; and diamonds, HFP2-^{14}AAG. The vertical dimensions of each symbol approximately correspond to the ±1 σ uncertainty limits. Lines are drawn between $(\Delta S/S_0)^{exp}$ values with adjacent values of τ. Each $(\Delta S/S_0)^{exp}$ value was determined by integration of 10 ppm regions of the S_0 and S_1 spectra. Panels c and d respectively correspond to the HFPmn-^{14}AAG/PC:PG and the HFPmn-^{14}AAG/PC:PG:CHOL samples and the points correspond to $(\Delta S/S_0)^{lab}$ (vertical lines with error bars) and best-fit $(\Delta S/S_0)^{sim}$ (diamonds). Lines are drawn between points with adjacent τ values. For plot c, the best-fit d = 91 ± 8 Hz with corresponding r = 5.12 ± 0.16 Å, f = 0.45 ± 0.02, and χ^2_{min} = 5.0. For plot d, the best-fit d = 85 ± 6 Hz with corresponding r = 5.24 ± 0.13 Å, f = 0.32 ± 0.02, and χ^2_{min} = 3.8.

significant fraction of the oligomers have an antiparallel arrangement with adjacent strand crossing between F8 and L9.*(9,36,45,46)* Some of these studies also supported conformational disorder at A21.*(34,35)* Although there are some data supporting a population of parallel strand arrangement,*(47)* "partial membrane insertion (PMI)" and "full membrane insertion (FMI)" models are only presented for the antiparallel arrangement, *cf.* Figure 29. There have been high-resolution structures for the ~130-residue "soluble ectodomain" region of gp41 which begins about ten residues C-terminal of the HFP and ends about twenty residues N-terminal of the gp41 transmembrane domain.*(2,16,48-50)* These structures showed trimeric gp41 with the residues closest to the HFPs in a parallel in-register coiled-coil. Antiparallel HFP strand arrangement in the context of gp41 would then require at least two gp41 trimers. As demonstrated in chapter V, Strands from trimer C (C_1, C_2, C_3) would be parallel to one another and strands from trimer D (D_1, D_2, D_3) would be parallel to one another and an antiparallel interleaved strand arrangement could be formed as $C_1D_3C_2D_2C_3D_1$. There is solid-state NMR evidence for the antiparallel arrangement of membrane-associated HFPs which were cross-linked at their C-termini. *(36)*

For antiparallel strands between A1 and G16, the ^{14}AAG residues in both the PMI and FMI models are at the ends of the hydrogen-bonded oligomer and are closer to the lipid headgroups than residues ^{5}GALFLGFLG. The F8 and L9 residues are at the center of the hydrogen-bonded oligomer and are most deeply membrane-inserted in all models. This result is consistent with the smallest $(\Delta S/S_0)^{exp}$ values observed for the ^{8}FLG samples and with the large number of

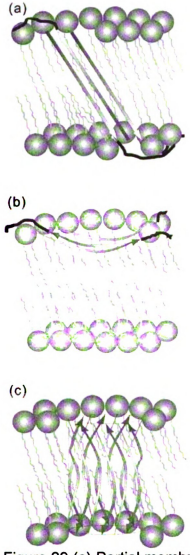

Figure 29 (a) Partial membrane insertion (PMI) and (b, c) full membrane insertion (FMI) models for antiparallel β strand HFP. The red arrows represent the A1 to G16 residues in strand conformation and the black lines represent the S17 to S23 residues in random coil conformations. For clarity, black lines are not displayed in c. Lipids are represented in blue and grey and cholesterol is not displayed. Three antiparallel strands are displayed in a, b and twelve strands are displayed in c but the actual number of strands in the oligomer/aggregate is not known. The curvature and angle of the strands with respect to the bilayer normal are not known but the models consider that A1-G16 has ~55 Å length and that the transbilayer distance is ~48 Å. The experiments do not provide information about the membrane locations of residues S17 to S23. Relative to FMI model (b), the FMI β barrel variant (c) could have reduced energy because all of the residues in the membrane interior have backbone hydrogen bonds.

apolar sidechains in the central ^{7}LFLGFL (L7 to L12) region. Relative to the ^{8}FLG samples, the models also predict smaller *r* and larger $(\Delta S/S_0)^{exp}$ for the ^{5}GAL and ^{11}FLG samples which generally correlates with the experimental data, cf. Figure 28a-b. The models suggest small *r* and significant $(\Delta S/S_0)^{exp}$ for HFPs labeled at the N-terminal residues and future studies could examine samples labeled in this manner.

The PMI model in Figure 29a would likely perturb the membrane and has some similarity with: (1) the PMI of extended conformation internal fusion peptides postulated from structures of dengue, Semliki forest, herpes, and vesicular stomatitis viral fusion proteins; (2) the PMI of helical influenza fusion peptide determined from electron spin resonance experiments; and (3) a PMI model based on the HFP-F8W fluorescence measurements.*(9,51-56)* However, the locations of lipids in the perturbed leaflet in the PMI model are not clear. For the FMI model of Figure 29b, the positions of the lipids are clearer but there are non-hydrogen bonded CO and NH groups at the sheet edges with large Born energies. These energies would be reduced for a FMI β barrel structure, Figure 29c. There is correlation between the FMI model and the deep insertion of the Trp sidechain suggested from fluorescence studies of the HFP-F8W mutant.*(8,9)* In the context of gp41, individual HFP trimers would be on the same side of the membrane in the PMI model but would be on different sides of the membrane in the FMI model. It is not clear how this FMI trimer topology would relate to the positions of the viral membrane-anchored gp41 trimers and the host cell membranes. The free energy difference between the A1 to G16 FMI state and a

non-inserted state is ~3.9 kJ/mol as calculated from the sum of individual residue free energy values derived from transmembrane helices.*(57)* The calculated difference for the I4 to G13 sequence is –2.3 kJ/mol and leads to the general conclusion that the free energy calculations do not strongly distinguish between the PMI and FMI models. Future studies could discriminate between the PMI and FMI models using REDOR distance measurements between peptide nuclei and lipid acyl chain nuclei.*(58)*

There are similarities between these PMI and FMI models of oligomeric β strand HFP and PMI and FMI models which have been developed for a single HFP in a helical conformation.*(11,12,59)* Much of the experimental data for helical HFP insertion has been based on detergent rather than membrane samples and there has been support for both surface location and micelle traversal by HFP.*(3-5,60,61)* Our results on oligomeric β strand HFP were consistent with the previous observations that the A15 and G16 residues of monomeric helical HFP were close to the water-micelle interface and that the F8 to G10 were furthest from this interface. Thus, there may be common features shared by helical and β strand HFP micelle and membrane location.

In summary, ^{13}CO-^{31}P distance measurements suggested that the ^{14}AAG residues have close proximity to the lipid ^{31}P while the $^{5}GALFLGFLG$ residues are relatively farther away from the phosphate groups. The 2D ^{13}C chemical shifts measurements described in chapter IV supported the conclusion that there may not be a particular secondary structure required for HFP inducing the fusion. Given the residue-dependence of the proximity to membrane headgroups, it is

possible that the membrane location of HFP affects the fusion activities of different HFP constructs. In the following sections, the membrane location of HFPs with α-helical and β-strand secondary structures will be discussed with singly-labeled HFP samples. The single ^{13}CO labeling was used to avoid the signal overlapping and to achieve an analysis of the individual conformations. The selection of secondary structures was also helped by using PC:PG:CHOL or PC:PG lipid bilayers. Most of the hydrophobic residues in HFPs adopted β-strand conformation in PC:PG:CHOL while some N-terminal residues adopted a mixture of α-helical and β-strand conformations in PC:PG.

Membrane Insertion of β-strand HFPs. In this part of the membrane insertion studies, a systematic investigation on the membrane location of β-strand HFPmn_mut, HFPmn and HFPtr using ^{13}C-^{31}P and ^{13}C-^{19}F REDOR experiments will be reported. For all the samples described in this section, PC:PG:CHOL membranes were used to make most of the N-terminal residues in β conformation. The reasons to study the β-strand HFPs are: (1) The previous triply-labeled HFP studies demonstrated that β-strand HFP is in intimate contact with membranes and merits serious consideration as a fusogenic conformation;*(17)* (2) The membranes of host cells of HIV have a cholesterol:lipid ratio of ~0.45, and the membranes of HIV have a cholesterol:lipid ratio of ~0.8.*(23)* The chemical shifts derived from previous triply-labeled experiments suggested a predominant population of HFP with β-strand conformation which further indicated that β-strand could potentially be a biological relevant structure. In addition, the current membrane location study was also trying to buildup a

correlation between the membrane position of HFP and the fusion activities of different HFP constructs. Thus HFPmn_mut, HFPmn and HFPtr were chosen as model constructs because of the very different fusion activities of these constructs. In order to achieve a systematic membrane location study which could cover the entire range of lipid bilayer, two types of ^{19}F-DPPCs, 16-^{19}F-DPPC and 5-^{19}F-DPPC, were used and the REDOR experiments were denoted as ^{13}CO-^{31}P, ^{13}CO-^{19}F(C16) and ^{13}CO-^{19}F(C5).

Initially, the ^{13}CO-^{31}P and ^{13}CO-^{19}F(C16) REDOR reveal different membrane locations for different HFP constructs. HFP samples were prepared with single ^{13}CO labels at Ala1, Ile4, Ala6, Leu9, Leu12, Ala14, or Ala21. The labeled constructs are referred to as HFPmn_mut-^{1}A, HFPmn-^{1}A, HFPtr-^{1}A, etc in order to be consistent with the nomenclature used in this chapter. Residues 1-16 are in the apolar region of the HFP sequence while Ala21 is in the more polar C-terminal region. Figure 30 displays ^{13}C-^{31}P and ^{13}C-^{19}F(C16) REDOR spectra for samples containing 9 mol% fraction 16-^{19}F-DPPC lipid. The τ value was 32 or 24 ms for the ^{13}C-^{31}P or ^{13}C-^{19}F spectra, respectively. Table 7 summarizes the peak chemical ^{13}CO chemical shift for each sample as well as characteristic ^{13}CO shifts for helical or β strand conformation.*(33)* All of the peak shifts agree better with β strand than with helical conformation. There may be a ~30% population of helical HFPmn_mut as evidenced by a shoulder at ~180 ppm for samples labeled at Ala6, Leu9, or Leu12. The typical linewidth for samples labeled between Ala1 and Ala14 was 3-5 ppm while the linewidth for samples labeled at Ala21 was ~ 8 ppm (not shown in Figure 30). The chemical shift and linewidth data support

predominant β strand conformation for the N-terminal apolar regions of all three constructs and more disordered structure in the C-terminal polar regions. The chemical shifts were consistent with previous triply-labeled HFP experiments as well as the 2D uniformly-labeled PDSD results in Chapter IV.

Table 7. ^{13}CO chemical shifts in PC:PG:CHOL membrane [a]

	Ala1	Ile4	Ala6	Leu9	Leu12	Ala14
HFPmn_mut	176.5	175.2	175.3	172.7	174.3	176.3
HFPmn	174.3	174.5	175.3	173.0	173.7	176.5
HFPtr	174.7	174.6	175.2	173.5	174.2	176.5
α-helix [b]	179.4	177.7	179.4	178.5	178.5	179.4
β-strand [b]	176.1	174.9	176.1	175.6	175.6	176.1

[a] All chemical shifts are given in unit of ppm.
[b] The typical error for a standard conformation is ± 1.5 ppm.

For each S_0 and S_1 spectrum, a 1 ppm interval around the peak was integrated to calculate the $(\Delta S/S_0)^{exp}$. For each pair of S_0 and S_1 spectra shown in Figure 30, and $(\Delta S/S_0)^{exp}$ is graphically displayed in Figure 31. Subsequent sections of this section describe quantitative distance and population analysis of the $(\Delta S/S_0)^{exp}$ vs τ data of all of the constructs while in this paragraph, a qualitative analysis is provided based on Figure 31. For example, all constructs labeled at Ala1 have ^{13}CO-^{31}P $(\Delta S/S_0)^{exp} \approx 0.8$ which is interpreted to mean that a major fraction of Ala1 ^{13}COs are 5 – 6 Å from a ^{31}P. In some contrast, the HFPmn-^{9}L and HFPtr-^{9}L samples displayed ^{13}CO-^{31}P $(\Delta S/S_0)^{exp} \approx 0$ which is interpreted to mean that most of these Leu9 ^{13}COs are >8 Å from a ^{31}P. Membrane location analysis based on this general approach assumes that all of the constructs have the known HFPmn structure in which the Ala1 to Gly16 region is fully extended and HFPs assemble into an antiparallel β sheet structure

with adjacent strand crossing near Phe8 and Leu9, and this anti-parallel structure was supported by ^{13}C-^{15}N REDOR experiments described in Chapter V.*(43)*

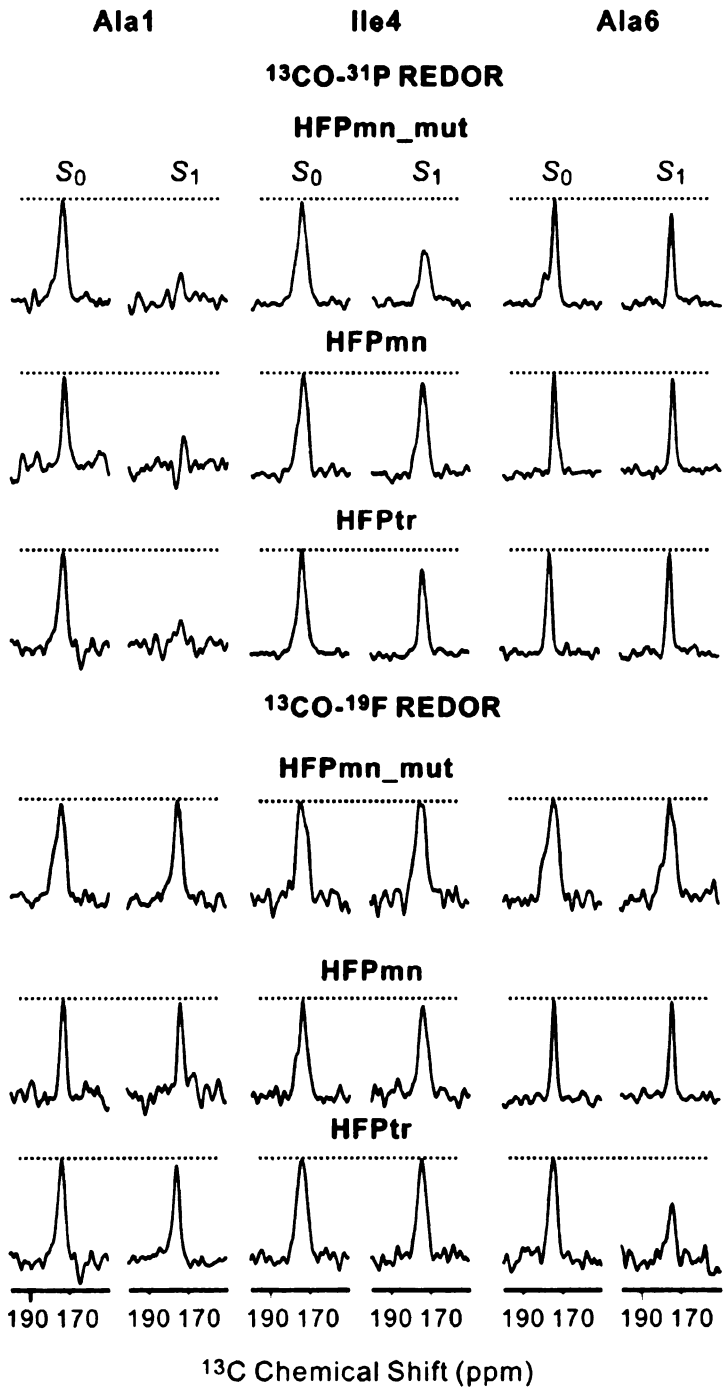

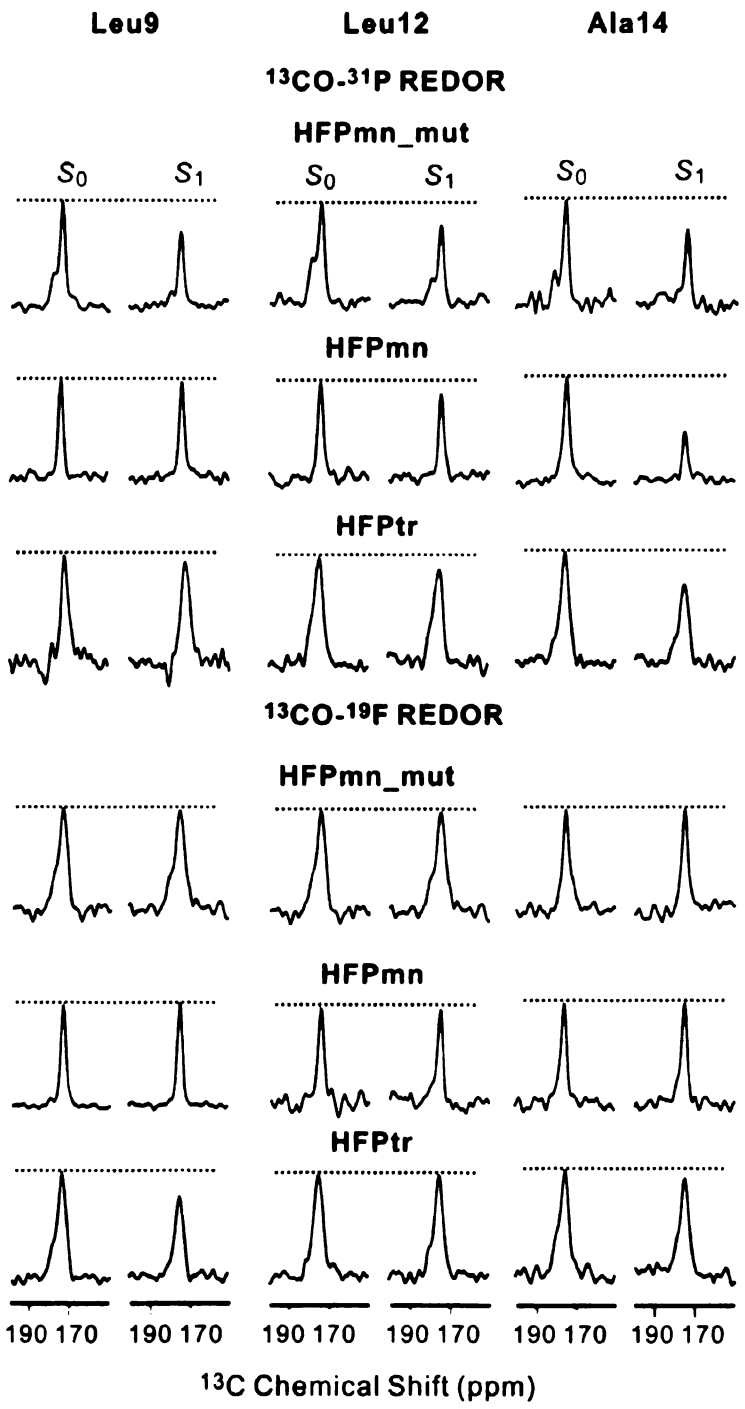

Figure 30 REDOR ^{13}C S_0 and S_1 NMR spectra for different labeled residues and different HFP constructs. The dephasing time for each ^{13}CO-^{31}P spectrum was 32 ms and for each ^{13}CO-^{19}F spectrum was 24 ms. The membranes contained 9 mol% 16-F-DPPC lipid. Each spectrum was processed with 200 Hz Gaussian line broadening and polynomial baseline correction and was the sum of ~30000 scans for ^{13}CO-^{31}P experiments and ~20000 scans for ^{13}CO-^{19}F experiments.

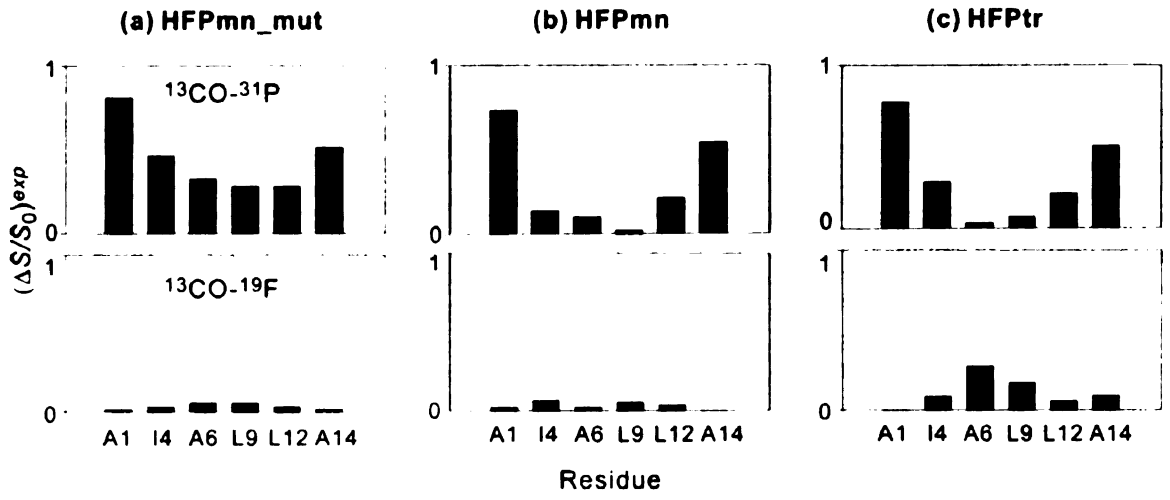

Figure 31 Summary of experimental REDOR dephasing $(\Delta S/S_0)^{exp}$ for the spectra displayed in Fig. 31. The top box in each panel is the ^{13}CO-^{31}P data and the bottom box is the ^{13}CO-^{19}F(C16) data. The $(\Delta S/S_0)^{exp}$ values are shown as bars for different labeled samples and a typical uncertainty is ±0.04.

The results of the analysis analysis include: (1) All HFPmn_mut samples have ^{13}CO-^{31}P $(\Delta S/S_0)^{exp} > 0.3$ and ^{13}CO-$^{19}F(C16)$ $(\Delta S/S_0)^{exp} \approx 0$ which indicates that HFPmn_mut lies on the membrane surface near the phosphate headgroups and is far from the bilayer center. (2) The HFPmn and HFPtr samples with Ala1 or Ala14 labeling show ^{13}CO-^{31}P $(\Delta S/S_0)^{exp} > 0.5$ and ^{13}CO-$^{19}F(C16)$ $(\Delta S/S_0)^{exp} \approx 0$. These residues are near the ends of the β sheet structure which must therefore be close to the phosphate headgroups. (3) The HFPtr-A6 and HFPtr-L9 samples have ^{13}CO-^{31}P $(\Delta S/S_0)^{exp} \approx 0$ and ^{13}CO-$^{19}F(C16)$ $(\Delta S/S_0)^{exp}$ significantly greater than 0. This suggests that the interior residues of the HFPtr β sheet are close to the bilayer center; i.e. a significant fraction of HFPtr is deeply inserted in the membrane. (4) HFPmn samples labeled at Ile4, Ala-6, or Leu-9 have ^{13}CO-^{31}P $(\Delta S/S_0)^{exp}$ and ^{13}CO-$^{19}F(C16)$ $(\Delta S/S_0)^{exp} \approx 0$ which suggests that these interior β sheet residues are neither close to the headgroups or the bilayer center and are instead located midway between these two regions.

Figure 32 displays plots of $(\Delta S/S_0)^{exp}$ vs τ for samples labeled at Ala1, Ala6 or Ala14. These residues were selected to represent the N-terminal, middle and C-terminal parts of the apolar region of the HFP sequence. These data support the qualitative discussion of membrane location of the previous paragraph. The samples labeled at Ala1, *cf.* Figure 32a, d, have ^{13}CO-^{31}P $(\Delta S/S_0)^{exp}$ that increase rapidly with τ while the ^{13}CO-$^{19}F(C16)$ $(\Delta S/S_0)^{exp} \approx 0$ for all τ. After removal of natural abundance ^{13}C contributions from the ^{13}CO-^{31}P $(\Delta S/S_0)^{exp}$ based on the procedure described in the "materials and methods" section, the remaining $(\Delta S/S_0)^{lab}$ reach ~1 at large τ. The $(\Delta S/S_0)^{lab}$ represent

only the Ala1 ^{13}CO signals and the value of ~1 indicates that the N-termini of all constructs are close to the phosphate headgroups. These N-termini are likely positively charged and are therefore attracted to the negatively charged phosphates. Samples labeled at Ala14, cf. Figure 32c, f, show similar large ^{13}CO-^{31}P $(\Delta S/S_0)^{exp}$ and ^{13}CO-$^{19}F(C16)$ $(\Delta S/S_0)^{exp} \approx 0$ indicating proximity to the phosphate headgroups. However, at large τ, $(\Delta S/S_0)^{lab} \approx 0.65$ which might be explained by two populations of Ala14 ^{13}COs in a HFP β sheet structure: (1) ^{13}COs in strands near the edge of the sheet with close contact to lipid ^{31}Ps; and (2) ^{13}COs in interior strands which are far from any lipid molecule. REDOR $(\Delta S/S_0)^{exp}$ for samples labeled at Ala6, cf, Figure 32b, e, depends on HFP construct. HFPmn_mut was the only construct with ^{13}C-^{31}P $(\Delta S/S_0)^{exp}$ significantly greater than zero and HFPtr was the only one with ^{13}C-$^{19}F(C16)$ REDOR $(\Delta S/S_0)^{exp}$ significantly greater than zero. These results revealed that the middle regions of different HFP constructs had different membrane locations. HFPtr had the deepest insertion and induced the most rapid vesicle fusion while HFPmn_mut was located on the membrane surface and was the least fusogenic construct.

The previous ^{13}C-^{31}P and ^{13}C-$^{19}F(C16)$ results suggested that the interior β sheet region of HFPmn was located midway between the headgroups and the bilayer center and more direct evidence was provided by experiments on samples containing 9 mol fraction 5-^{19}F DPPC lipid. The position of the C5 carbon along the bilayer longitude of gel phase DPPC bilayers is ~10 Å from ^{31}P and ~12 Å from the bilayer center.*(25)* Although the cholesterol-rich membranes

Table 8. Best-fit distance and population parameters for samples in PC:PG:CHOL. [a b c]

		^{13}CO-^{31}P					
		Ala1	Ile4	Ala6	Leu9	Leu12	Ala14
HFPmn_mut	*r* (Å)	5.2 (2)	5.5 (2)	5.0 (2)	5.2 (2)	5.7 (2)	6.3 (3)
	f	0.86 (4)	0.45 (3)	0.36 (2)	0.33 (2)	0.39 (2)	0.75 (3)
HFPmn	*r* (Å)	4.8 (2)	n.d.	n.d.	n.d.	8.6 (2)	5.7 (2)
	f	0.87 (3)				0.70 (3)	0.77 (3)
HFPtr	*r* (Å)	5.1 (2)	7.9 (2)	n.d.	n.d.	9.4 (1)	5.9 (2)
	f	0.83 (3)	0.66 (3)			0.63 (3)	0.72 (3)

		^{13}CO-(16-^{19}F)					
		Ala1	Ile4	Ala6	Leu9	Leu12	Ala14
HFPmn_mut	*r* (Å)	n.d.	n.d.	n.d.	n.d.	n.d.	n.d.
	f						
HFPmn	*r* (Å)	n.d.	n.d.	n.d.	n.d.	n.d.	n.d.
	f						
HFPtr	*r* (Å)	n.d.	n.d.	8.1 (3)	6.9 (2)	n.d.	n.d.
	f			0.35 (2)	0.39 (2)		

		^{13}CO-(5-^{19}F)					
		Ala1	Ile4	Ala6	Leu9	Leu12	Ala14
HFPmn_mut	*r* (Å)	n.d.	---	n.d.	---	---	---
	f						
HFPmn	*r* (Å)	n.d.	---	7.0 (2)	7.3 (2)	---	---
	f			0.37 (2)	0.34 (2)		
HFPtr	*r* (Å)	n.d.	---	n.d.	---	---	---
	f						

[a] The best-fit *r* and *f* are given with uncertainties in parentheses. The typical $\chi^2_{min} < 5$ and the uncertainties of *d* and *f* were determined from the region encompassed by $\chi^2 = \chi^2_{min} + 1$.

[b] n.d. means "not determined". Fitting was not done for samples with $(\Delta S/S_0)^{exp} < 0.1$ at $\tau = 32$ ms (^{13}CO-^{31}P) or at $\tau = 24$ ms (^{13}CO-^{19}F), or for samples with no clear buildup curve.

[c] A dashed line means the experiment was not done.

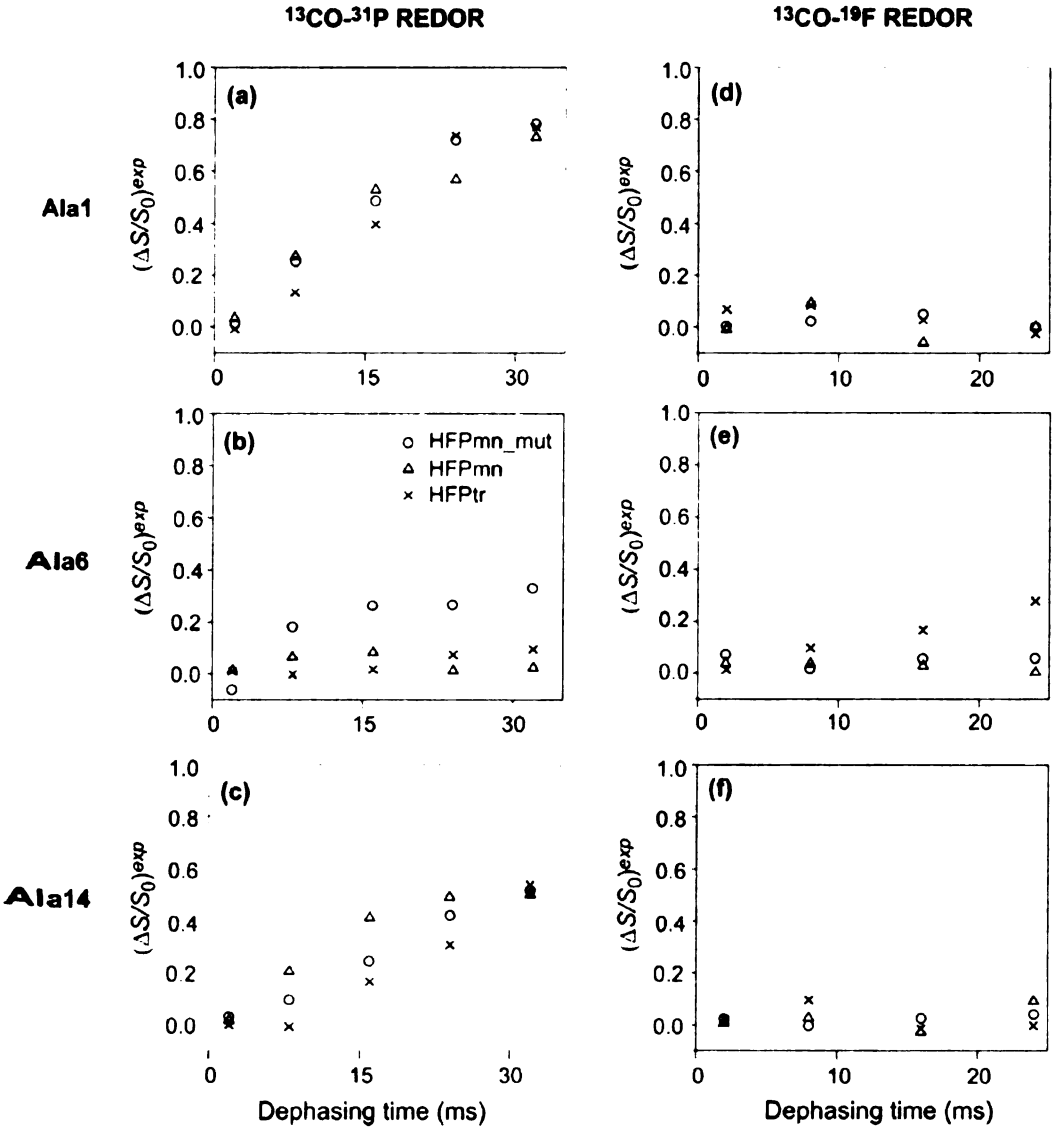

Figure 32 ^{13}CO-^{31}P and ^{13}CO-^{19}F REDOR dephasing curves for different HFP samples labeled at (a, d) Ala1, (b, e) Ala6 or (c, f) Ala14. The membranes contained 9 mol% 16-F-DPPC lipid. The color coding of the constructs is given in the legend of panel b. For 2 ms dephasing time, the typical uncertainty in $(\Delta S/S_0)^{exp}$ is ±0.02 and for the other dephasing times, the typical uncertainty is ±0.04.

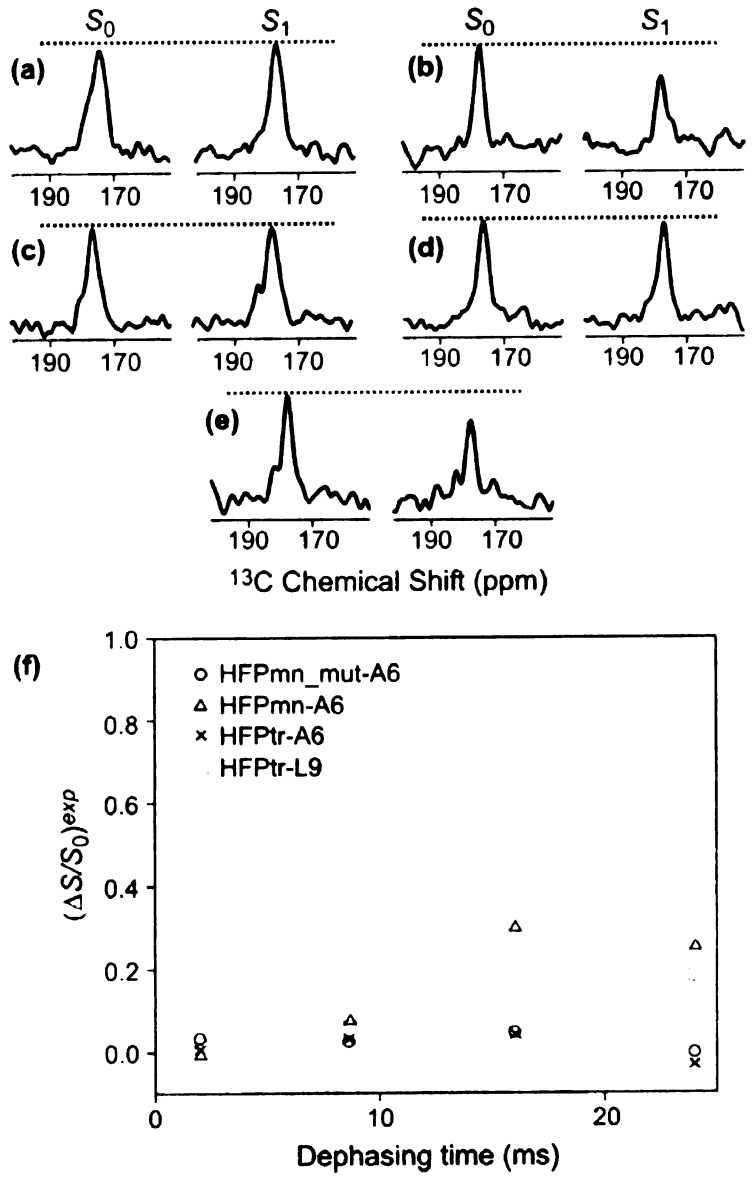

Figure 33 ^{13}C S_0 and S_1 NMR spectra from ^{13}CO-^{19}F REDOR experiments of samples made with 9 mol% 5-F-DPPC lipid. For panels a, b, c, d, and e the samples respectively contained HFPmn-A1, HFPmn-A6, HFPmn_mut-A6, HFPtr-A6, and HFPmn-L9.

(g)

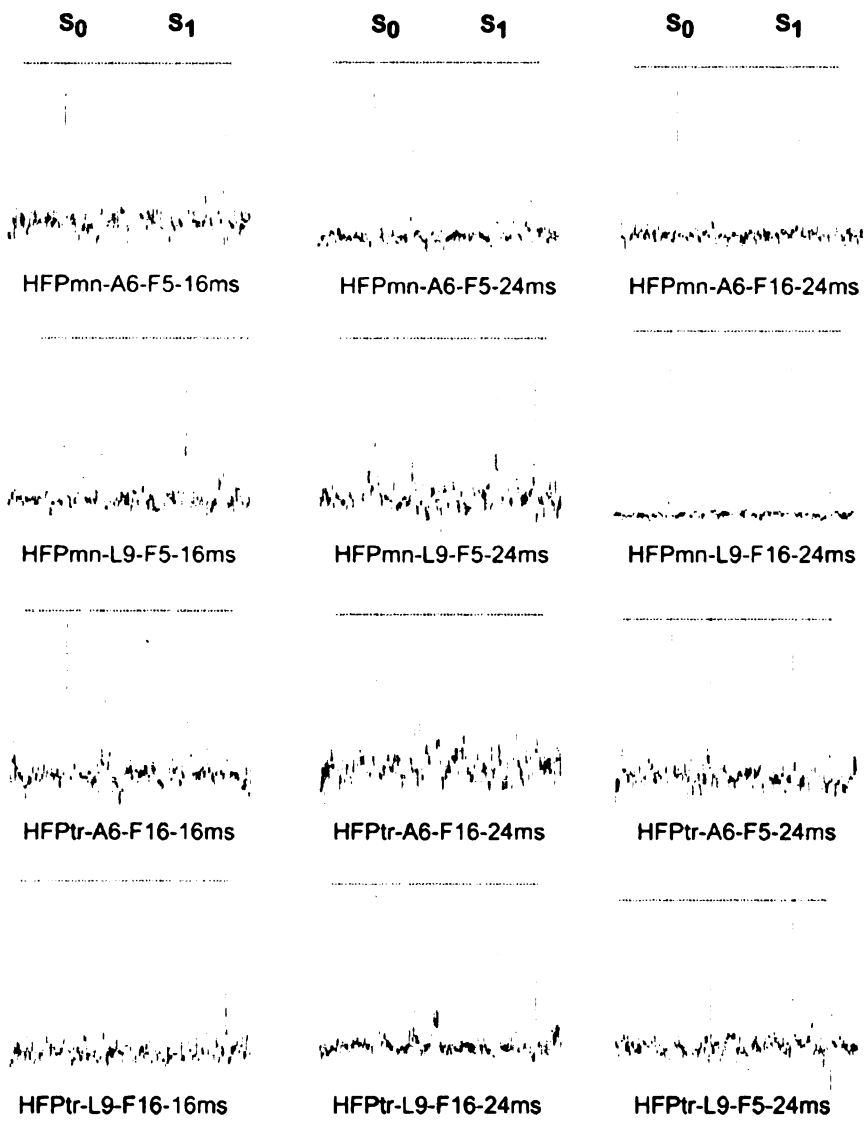

Figure 33 ^{13}C S_0 and S_1 NMR spectra from ^{13}CO-^{19}F REDOR experiments of samples made with 9 mol% 5-F-DPPC lipid. For panels a, b, c, d, and e the samples respectively contained HFPmn-A1, HFPmn-A6, HFPmn_mut-A6, HFPtr-A6, and HFPmn-L9. Each spectrum was processed with 200 Hz Gaussian line broadening and polynomial baseline correction. Each S_0 and S_1 spectrum was the sum of ~ 20000 scans. ^{13}CO-^{19}F(C5) REDOR dephasing curves for different HFPs are plotted in panel f and the constructs are coded as shown in the legend. For 2 ms dephasing time, the typical uncertainty in $(\Delta S/S_0)^{exp}$ is ±0.02 and for the other dephasing times, the typical uncertainty is ±0.04. In panel g the ^{13}C-^{19}F(C5) and ^{13}C-^{19}F(C16) spectra of HFPmn and HFPtr at 16 or 24 ms dephasing time were shown in the stack form with S_0 spectra on the left side and S_1 spectra on the right side. The dash lines reflect the intensities of the S_0 spectra.

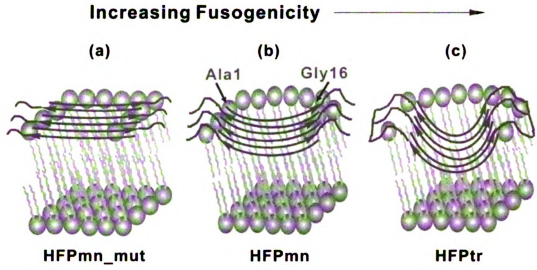

Figure 34 Insertion models of β sheet (a) HFPmn_mut, (b) HFPmn, and (c) HFPtr. Lipid headgroups are drawn as blue balls, lipid alkyl chains are drawn in grey, and peptides are drawn in red. In all models, peptides are represented as oligomers with either six (HFPmn and HFPmn_mut) or two (HFPtr) molecules. The strands are in antiparallel β sheet structure with adjacent strand crossing near Phe8 and Leu9. This is the known structure for a large fraction of HFPmn peptides. The number of strands in a sheet is not known but is likely a small number. The lines at the C-terminus of HFPtr represent the chemical cross-linking of the HFPtr construct. For clarity, not all lipid molecules are shown near the HFP.

of the present study form a liquid-ordered rather a gel phase bilayer, the acyl chain conformation is ordered in both phases with the C5 carbon approximately midway between the ^{31}P and the bilayer center.*(62)* Figure 33 shows the REDOR spectra at τ = 24 ms for samples labeled at Ala1 and Ala6 as well as plots of $(\Delta S/S_0)^{exp}$ vs τ for Ala6 samples. As a negative control, HFPmn-^{1}A, cf. Figure 33a, had $(\Delta S/S_0)^{exp} \approx 0$ which was consistent with the proximity of Ala1 and the lipid phosphate groups deduced from the ^{13}CO-^{31}P REDOR data. Figure 33f shows that among constructs labeled at Ala6, HFPmn-^{6}A was the only one with non-zero $(\Delta S/S_0)^{exp}$. Similar results were obtained for HFPmn-^{9}L as shown in Figure 33e for the τ = 24 ms spectra and in Figure 33f for the dephasing curve. These data along with $(\Delta S/S_0)^{exp} \approx 0$ for the ^{13}CO-^{31}P and ^{13}CO-^{19}F(C16) experiments support a membrane location for the HFPmn interior which is midway between the phosphate headgroups, and the bilayer center, i.e. intermediate between HFPmn_mut and HFPtr. This location correlates with the intermediate fusion rate of HFPmn. The more clearly supplementary experiments shown in Figure 33g proved that the HFPmn-^{6}A and HFPmn-^{9}L have dephasing in the ^{13}C-^{19}F(C5) REDOR, but not in the ^{13}C-^{19}F(C16) REDOR, while the HFPtr-^{6}A and HFPtr-^{9}L have dephasing in the ^{13}C-^{19}F(C16) but not the ^{13}C-^{19}F(C5) REDOR.

Figure 34 shows experimentally-based membrane insertion models for HFPmn_mut, HFPmn and HFPtr in antiparallel β sheet structure. The β strand conformation was supported by the ^{13}CO peak chemical shifts for the labeled residues, cf. Table 7, and the antiparallel β sheet structures for HFPmn and HFPtr were based on previous experiments. *(36,43)* The depths of insertion

follow the trend that HFPmn_mut < HFPmn < HFPtr. Quantitative analysis of the REDOR data was done by first removing the natural abundance ^{13}CO contributions and then fitting the remaining $(\Delta S/S_0)^{lab}$ which represent the signals of only the labeled ^{13}COs. The fitting model was two populations of spin pairs (eg. two ^{13}CO-^{31}P or two ^{13}CO-^{19}F pairs) with one pair having fractional population f and magnitude of dipolar coupling $d > 0$ and the other pair having fractional population $1 - f$ and $d = 0$. For a single spin pair, d is quantitatively related to the internuclear distance r by a r^{-3} dependence. The existence of the $1 - f$, $d = 0$ population was ascribed to ^{13}CO nuclei in the β sheet interior that were far from any region of the membrane and for the ^{13}CO-^{19}F data, the dilute ^{19}F spin density because of the 0.09 mol fraction of fluorinated lipid. Because each data set only contained 4 or 5 points, it was not reasonable to fit the data to more sophisticated structural models, eg. multiple ^{31}P nuclei. The two spin pair model was at least reasonable as evidenced by typical best-fit $\chi^2 < 5$.

Table 8 summarizes the spin pair populations and best-fit internuclear distances for the f fractional populations. A summary of the quantitative data analysis includes: (1) For all HFPmn_mut samples, the best-fit ^{13}CO-^{31}P distances are in the 5.0 – 6.3 Å range. These data and reasonable values of van der Waals radii are consistent with close contact of the β sheet region of HFPmn_mut with the phosphate headgroups. (2) For HFPmn and HFPtr samples labeled at Ala1 or Ala14, the best-fit ^{13}CO-^{31}P distances are in the 4.8 – 5.9 Å range with best-fit $f > 0.7$. For more interior β sheet residues, the $(\Delta S/S_0)^{lab}$ are small, eg. Ala6 or Leu9, and could not be reliably fitted or the fitted distances are

in the 8 – 10 Å range, eg. Ile4 or Leu12. These data suggest membrane insertion of the Ile4 to Leu12 region of HFPmn and HFPtr with the termini of the β sheet, eg. Ala1 and Ala14, in contact with the lipid headgroups, *cf.* Figure 34. (3) For all HFPmn_mut samples and most HFPmn and HFPtr samples, the ^{13}CO-^{19}F $(\Delta S/S_0)^{lab}$ are small and could not be reliably fitted. The exceptions are the samples containing 5-^{19}F lipid and HFPmn labeled at Ala6 or Leu9 and the samples containing 16-^{19}F lipid and HFPtr labeled at Ala6 or Leu9. The best-fit ^{13}CO-^{19}F distances in these samples are in the 7 – 8 Å range and the best-fit *f* are in the 0.34 – 0.39 range. These analyses are consistent with partial membrane insertion of the interior β sheet residues of HFPmn and deeper insertion of HFPtr.

The membrane location of the HFP provides useful information to understand the perturbation of membranes and the catalysis of membrane fusion. The present study provides residue-specific membrane locations based on solid-state NMR experiments for three different HFP constructs with very different fusogenicities. Insertion models for different β strand HFPs will be discussed in the context of previous and present work. The previous study on triply-labeled HFPmn showed that relative to the Gly5 to Gly13 ^{13}COs, the Ala1 to Gly3 and Ala14 to Gly16 ^{13}COs were closer to the lipid ^{31}Ps.*(15,17)* Two insertion models were proposed with either insertion into a single leaflet or membrane traversal of both leaflets. Another study focused on the secondary and tertiary structure of HFPmn in membranes with physiologically relevant cholesterol content and supported the formation of small oligomers in an antiparallel β sheet structure

with adjacent strand crossing near Phe8 and Leu9.*(36)* Therefore, Ala1 to Gly3 and Ala14 to Gly16 were close to one another in adjacent strands of the sheet and were at the termini of the sheet. It was therefore reasonable that both regions could be close to the phosphate groups. All of these results are consistent with the results of the present study and with the HFPmn insertion model present in Figure 34. Furthermore, the proximity of interior β sheet residues to 5-^{19}F but not 16-^{19}F lipid nuclei supports membrane insertion into a single leaflet rather than membrane traversal by HFPmn. This partial insertion model is also consistent with an earlier fluorescence study showing proximity of residue 8 of HFPmn to the middle region of a single leaflet.*(8,9)*

In Figure 34, HFPmn_mut and HFPtr are also represented by antiparallel β sheet structure. Evidence for this structure includes: (1) earlier ^{13}CO-^{15}N REDOR measurements on HFPtr; and (2) peak ^{13}CO chemical shifts in HFPmn_mut and HFPtr which are typically within 0.5 ppm of the corresponding shift of HFPmn, cf. Table 7; and (3) the trend of best-fit ^{13}CO-^{31}P *f*s for HFPmn_mut are consistent with a β sheet structure where relative to the interior residues, eg. Ala6. A greater fraction of the terminal residues, eg. Ala1, have contact with the lipid molecules. The surface location of β sheet HFPmn_mut is also strongly supported by small ^{13}CO-^{19}F $(\Delta S/S_0)^{exp}$ in all HFPmn_mut samples. It is very interesting that the charged Glu2 residue near the terminus of the β sheet appears to induce a significant change in HFP membrane location. The HFPtr antiparallel β sheet is most reasonably described with a minimal unit of two HFPtr molecules "C" and "D" and adjacent antiparallel β strands arranged in an

CDCDCD structure. Because of the close contact of HFPtr Ala6 and Leu9 ^{13}COs with the 16-^{19}F lipid nuclei, it is not possible to discount membrane traversal by HFPtr, ie. molecules C and D on opposite sides of the membrane. However, the displayed model in Figure 34c is more consistent with viral fusion in which multiple gp41 trimers would initially bind to the same outer leaflet of the target cell membrane. The Figure 34c model also correlates with the definitive membrane locations of HFPmn and HFPmn_mut. It is also definitive that relative to HFPmn, HFPtr is more deeply inserted in the membrane. The present study does not provide data to explain the reason for this deeper insertion but it may be related to formation of larger and more hydrophobic oligomers by HFPtr relative to HFPmn.

The present study focuses on membranes with biologically relevant cholesterol content in which all of the constructs have predominant β strand conformation. For HFPmn and HFPtr associated with membranes without cholesterol, significant populations of molecules with helical conformation are detected.*(15)* Helical conformation is also observed for HFPmn in detergent micelles at low HFP:detergent where each micelle contains at most one HFPmn.*(3,4,6)* There is reasonable correlation between the membrane locations of β sheet HFPs and the current data on the micelle and membrane locations of helical HFPs. One point of agreement between all of the data is that in either helical or β strand conformations, Ala14 and Ala15 residues are near the membrane or micelle surface. These residues are on the border between the apolar and polar regions of the HFP sequence which approximately matches the

polarity change at the membrane or micelle surface. The location of these residues appears to be an intrinsic property of the HFP sequence that is independent of conformation. For one model of helical HFPmn in a micelle, the Ile4 to Ala15 region traverses the micelle interior.*(3)* This correlates with the similar membrane location of this region in β sheet HFPmn in the present study, cf. Figure 34b. Molecular dynamics simulations on a single molecule of HFPmn_mut or HFPmn in a membrane show a surface location or shallow insertion, respectively, which correlates with the β sheet HFPs of the present study, cf. Figure 34a, b.*(11)*

It has been proposed that two requirements of virus-cell fusion are assembly of multiple fusion peptides and destabilization of the target cell membrane.*(63)* The present study provides insight into these requirements including a possible link between them. There is a clear positive correlation between the depth of HFP membrane insertion and fusogenicity. The correlation can be understood by a second correlation between depth of membrane insertion and membrane destabilization. For insertion into a single leaflet, there will be perturbation in the packing of lipids near HFP which will likely destabilize this region of the leaflet and reduce the activation energy needed to form membrane fusion intermediate states such as stalks and fusion pores.*(64)* It is reasonable that deeper insertion into a single leaflet will cause greater destabilization and therefore faster fusion rate which correlates with experimental observations for HFPmn_mut, HFPmn, and HFPtr.

For these three constructs, there may also be a positive correlation between number of molecules in the β sheet assembly and depth of membrane insertion. A larger assembly would likely be more hydrophobic and therefore more stable in the membrane interior. Evidence to support this hypothesis includes: (1) HFPtr has the deepest insertion and is pre-organized into trimers; (2) HFPmn_mut has the shallowest insertion and relative to HFPmn and HFPtr, HFPmn_mut has the greatest helical population which is likely helical monomers. Inhibition of HFP oligomeric assembly in HFPmn_mut is reasonable because of charge repulsion between Glu2 sidechains from different molecules. The HFP assembly/fusion correlation is also supported by virus-cell and cell-cell fusion studies with the gp41 V2E mutant. Viruses or cells expressing 91% wild-type gp41 and 9% gp41 V2E mutant had only ~40% of the fusion activity of the corresponding system expressing 100% wild-type gp41.*(65)* Assembly of multiple HFPs for efficient fusion has been inferred from this "trans-dominant" effect.

In this section, the membrane locations have been determined for three different HFP constructs in membranes with biologically relevant cholesterol content. All three constructs adopt predominant β strand conformation for the N-terminal region and are less structured in the C-terminal region. HFPmn_mut is the least fusogenic construct and is located on the membrane surface. HFPmn has intermediate fusion rate and its Ile4 to Leu12 region is inserted into one leaflet of the bilayer. HFPtr has the putative trimeric HFP state of gp41 and is the most fusogenic construct with the deepest membrane insertion that extends to the bilayer center. This study therefore correlates membrane insertion depth into

a single leaflet and fusion rate and this correlation is reasonably understood in terms of destabilization of the lipid packing. In addition, the present work including use of 5-^{19}F-DPPC lipid describes a general approach to study the membrane locations of specifically labeled peptides and proteins, and may also be applicable to more uniformly labeled systems with appropriately modified REDOR pulse sequences.*(66)*

Membrane Insertion of α-helical HFPs. In this section, we will report the studies on the membrane location of HFP which was associated with PC:PG, in particular the membrane location of the residues in HFP which formed α-helical conformation. The motivations to study the helical HFPs include: (1) There is not yet a consensus that β-strand is the only secondary structure which has fusion activity even though it has been shown that HFP adopted a predominant β-strand conformation in a biologically relevant cholesterol-containing membrane.*(6,14,67,68)* In fact, a previous lipid-mixing assay suggested that the α-helical and β-strand HFPs may have comparable fusion activities.*(14)* (2) The helical conformation may also be a biologically relevant structure for HFP present in the entire gp41. There has been experimental evidence which supported the formation of partial α-helical structure for HFP in PC:PG:CHOL membranes when the HFP was combined with the NHR and CHR parts of gp41.*(69)* (3) The results of membrane location of helical HFPs can be directly compared with the HFP location in micelles studied by solution NMR, and also with the simulation studies in which only α-helix structure was considered. (4) It will be interesting to compare the membrane location results from the helical HFPs with those

obtained for the β-strand HFPs, and to learn whether the membrane location of HFPs could be correlated to the fusion activity of different HFP constructs in a conformation-independent manner.

There have been residue-specific conformation studies for the HFP associated with micelles where the HFP adopted helical conformation. It has been generally accepted that the helical conformation extends from Ile4 to Leu12, however, one study reported that the helix extended to Met19 while another study claimed that there was a turn at Ala15 and Gly16.*(3,4,6,7)* The residue-specific secondary structure of HFPs associated with PC:PG membranes have been studied using solid-state NMR. Previously we showed that Ala6 and Ala15 of HFP in PC:PG membranes can adopt both α-helical and β-strand conformations.*(15)* In the present set of experiments, we put a single ^{13}CO-label on either Ala1, Ile4, Ala6, Leu9, Leu12 or Ala14 which covers the entire helical region. The HFPmn_mut, HFPmn and HFPtr were chosen as the model constructs to study the membrane insertion/fusion activity correlation as was done for the cholesterol-containing membranes.

Table 9 summarizes the ^{13}CO chemical shifts for the labeled residues in different HFP constructs. The information was extracted from the corresponding ^{13}CO-^{31}P REDOR S_0 spectra with τ = 2 ms as shown in Figure 35a. The difference in chemical shifts between different τ and different REDOR experiments for a singly labeled residue was always less than 0.3 ppm. The ^{13}CO chemical shift is correlated to the local conformations of proteins. The empirical correlation database RefDB has been established by liquid-state NMR

assignment of proteins. The ^{13}CO chemical shift ranges for Ala, Ile and Leu to be considered in α-helical conformation are 178.1-180.7, 176.4-179.0 and 177.2-179.8 ppm and the range for these residues to be β-strand are 174.5-177.5, 173.4-176.1 and 174.2-177.0 ppm respectively.*(33)*

Table 9. ^{13}CO chemical shifts in PC:PG membranes [a]

	Ala1	Ile4	Ala6	Leu9	Leu12	Ala14
HFPmn_mut	175.6	176.5	177.8[b]	180.0	179.9	180.3
				175.8	175.8	176.9
HFPmn	174.4	178.8	179.8	180.0	179.8	179.8
			174.8	175.5	175.7	176.0
HFPtr	175.4	178.3	179.8	180.1	180.0	180.0
			174.8	175.3	175.6	176.1

[a] All chemical shifts are given in unit of ppm.
[b] The Ala6 ^{13}CO peak for HFPmn_mut is broad and is not correlated with a single secondary structure (c.f. Fig. 35)

The following conclusions can be obtained by comparing the experimental results with the database values: (1) Ala1 is not helical for any of the three constructs. (2) For all three constructs, there is always some fraction of HFPs which adopt helical conformation. (3) Table 9 showed that the variation in the chemical shifts for Ile4 between different constructs in α-helical conformation is larger than those for Ala6, Leu9 and Leu12. Figure 35a showed that Ile4 has broad single peaks in all three constructs while Ala6, Leu9 and Leu12 have either a predominantly single peak or two separated peaks. These results suggested that Ile4 has a more flexible secondary structure compared with Ala6, Leu9 and Leu12, which probably mean that Ile4 is the N-terminus of a helix.*(6)*

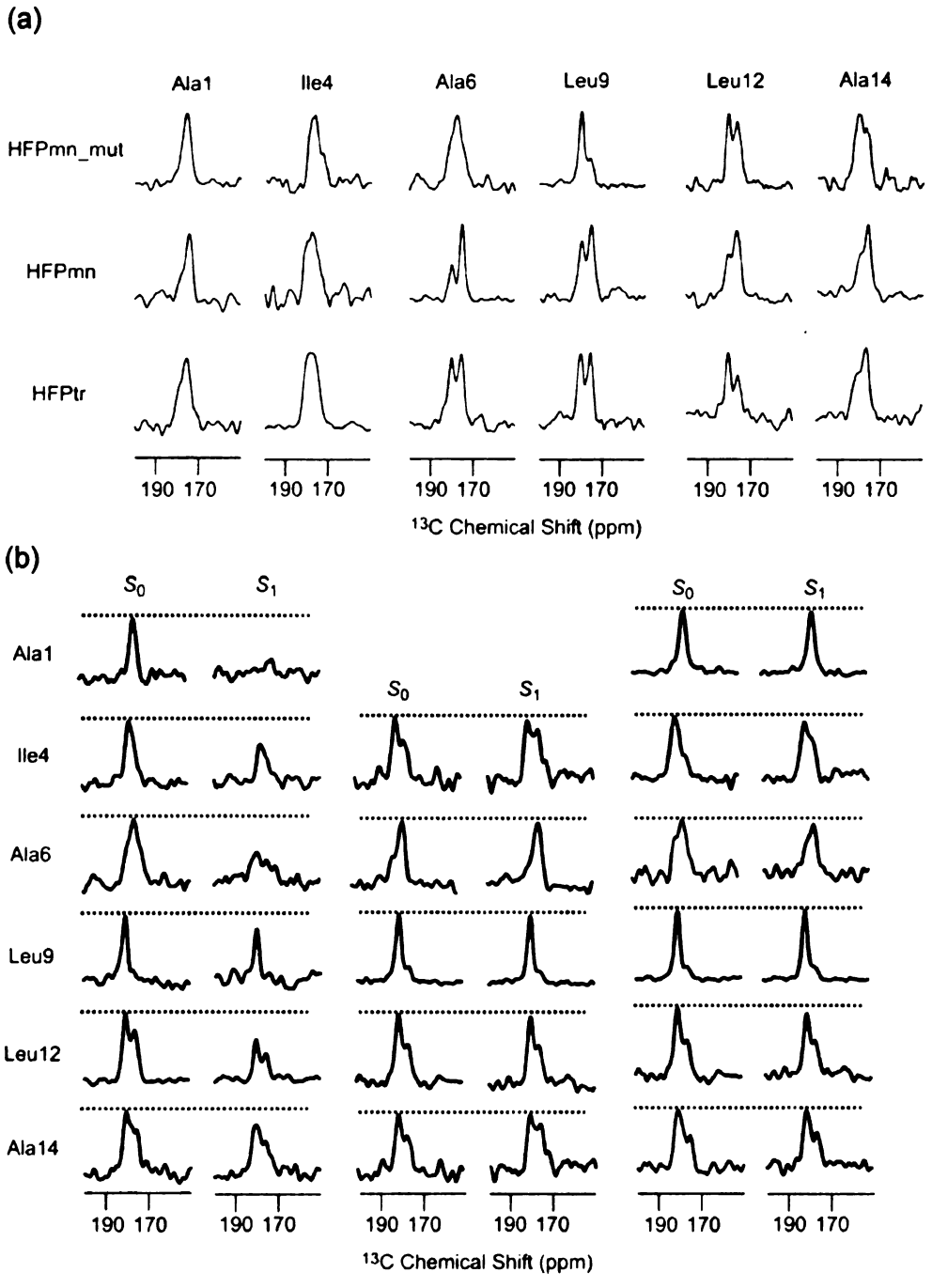

Figure 35 (a) ^{13}C-^{31}P REDOR S_0 spectra with 2 ms dephasing time. (b) REDOR S_0 and S_1 spectra for HFPmn_mut with long dephasing time (τ = 32 ms for ^{13}C-^{31}P experiments and τ = 24 ms for ^{13}C-^{19}F experiments). The left, middle and right columns in (b) are ^{13}C-^{31}P, ^{13}C-^{19}F(C5) and ^{13}C-^{19}F(C16) experiments respectively. All spectra were processed with 200 Hz Gaussian line broadening and baseline correction. In panel (b) each of the ^{13}C-^{31}P spectra was acquired for 30000 scans and each of the ^{13}C-^{19}F spectra was acquired for ~ 20000 scans.

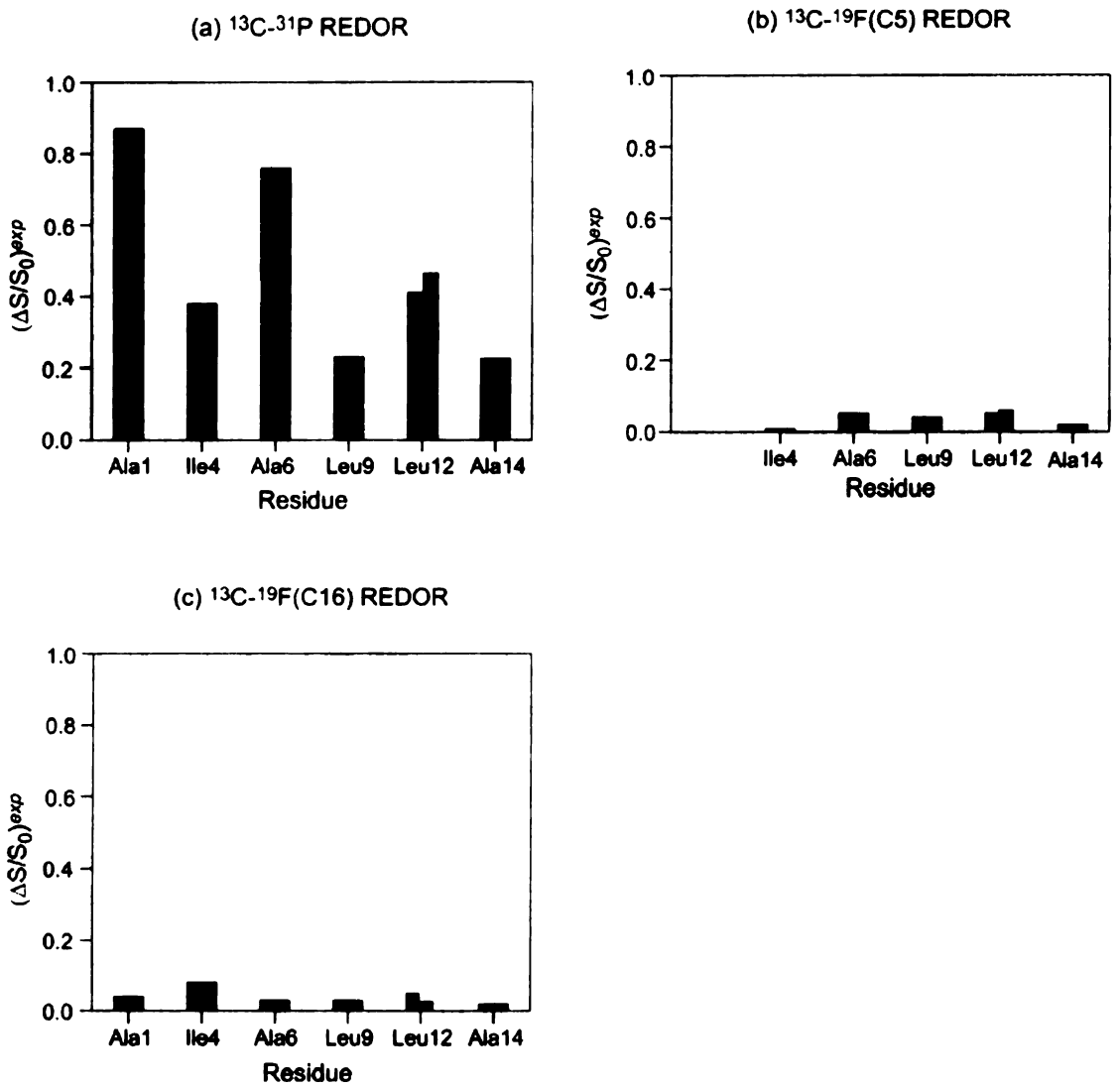

Figure 36 Plots of $(\Delta S/S_0)^{exp}$ for HFPmn_mut ^{13}C-^{31}P experiments at 32 ms dephasing time and ^{13}C-^{19}F experiments at 24 ms. The experimental dephasing was obtained by integrating over a 1 ppm interval around the ^{13}CO peaks in the corresponding S_0 and S_1 spectra shown in Fig. 35. For Leu12, the black bar represents the $(\Delta S/S_0)^{exp}$ for α-helical conformation and the red bar represents the $(\Delta S/S_0)^{exp}$ for β-strand conformation. The typical uncertainty is ± 0.02.

Figure 35b displays the long time REDOR S_0 and S_1 spectra (τ = 32 ms for ^{13}C-^{31}P REDOR and τ = 24 ms for ^{13}C-^{19}F REDOR) for HFPmn_mut and figure 36 summarizes the corresponding experimental dephasing. In figure 36, the residue Leu12 has two $(\Delta S/S_0)^{exp}$ in each plot which correspond to α-helical and β-strand conformations. The values were obtained by integrating over a 1 ppm interval around the corresponding peaks in Figure 35b. For the other residues, only one experimental dephasing was shown either because there is only one major secondary structure (Ala1 and Leu9, c.f. Figure 35b), or because the peaks corresponding to distinct conformations are not clearly separated (Ile4, Ala6 and Ala14, c.f. Figure 35b). The general conclusion for HFPmn_mut is that there are large experimental dephasings for all the residues in ^{13}C-^{31}P REDOR, e.g. $(\Delta S/S_0)^{exp} > 0.2$, and there is almost zero dephasing in both ^{13}C-^{19}F(C5) and ^{13}C-^{19}F(C16) experiments. The results indicate the peptide backbone of HFPmn_mut from Ala1 to Ala14 of HFPmn_mut has close contact with the lipid phosphate groups and little contact with the lipid alkyl chains. Figure 37a shows the experimental ^{13}C-^{31}P REDOR dephasing curves, and the dephasing curves for the ^{13}C-^{19}F experiments are basically flat lines with $(\Delta S/S_0)^{exp} < 0.1$ for the longest dephasing time. A more quantitative analysis can be completed by first calculating the $(\Delta S/S_0)^{lab}$ from the $(\Delta S/S_0)^{exp}$ using Eq. 59, and then fitting the dipolar coupling frequency (d) and a fraction parameter (A) of $(\Delta S/S_0)^{lab}$ by comparison with the $(\Delta S/S_0)^{sim}$ which were calculated using Eq. 34. The best-fit ^{13}C-^{31}P dipolar coupling frequency can be correlated to the ^{13}CO-^{31}P internuclear distance through $r = (12250/d)^{1/3}$ with r in units of Å and d in units of Hz. The

population parameter *A* indicates the fraction of ^{13}COs that are close to a ^{31}P and provide non-zero $(\Delta S/S_0)^{exp}$. The data fitting for the ^{13}C-^{31}P experiments are

(a)

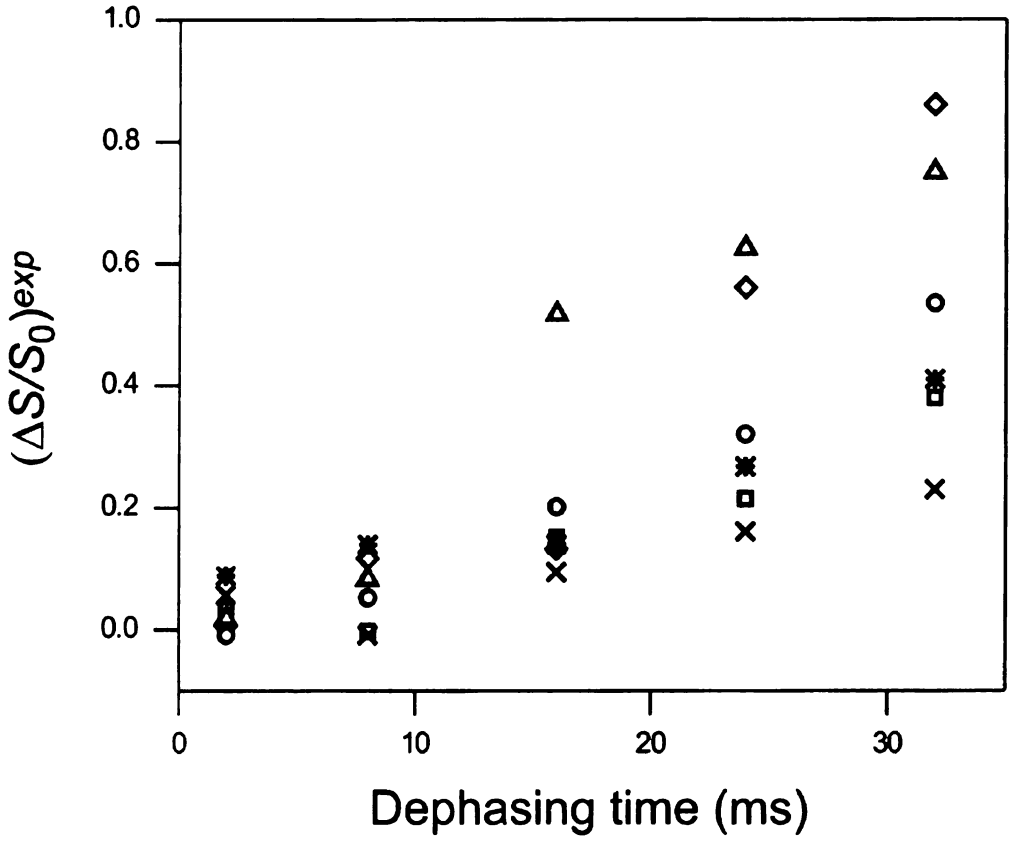

Figure 37 (a) Plots of ^{13}C-^{31}P $(\Delta S/S_0)^{exp}$ vs. dephasing time for HFPmn_mut with different labeled positions. The symbols are open diamonds for A1, open squares for I4, open triangles for A6, crosses for L9, stars for the α-helical L12 and open circles for A14.

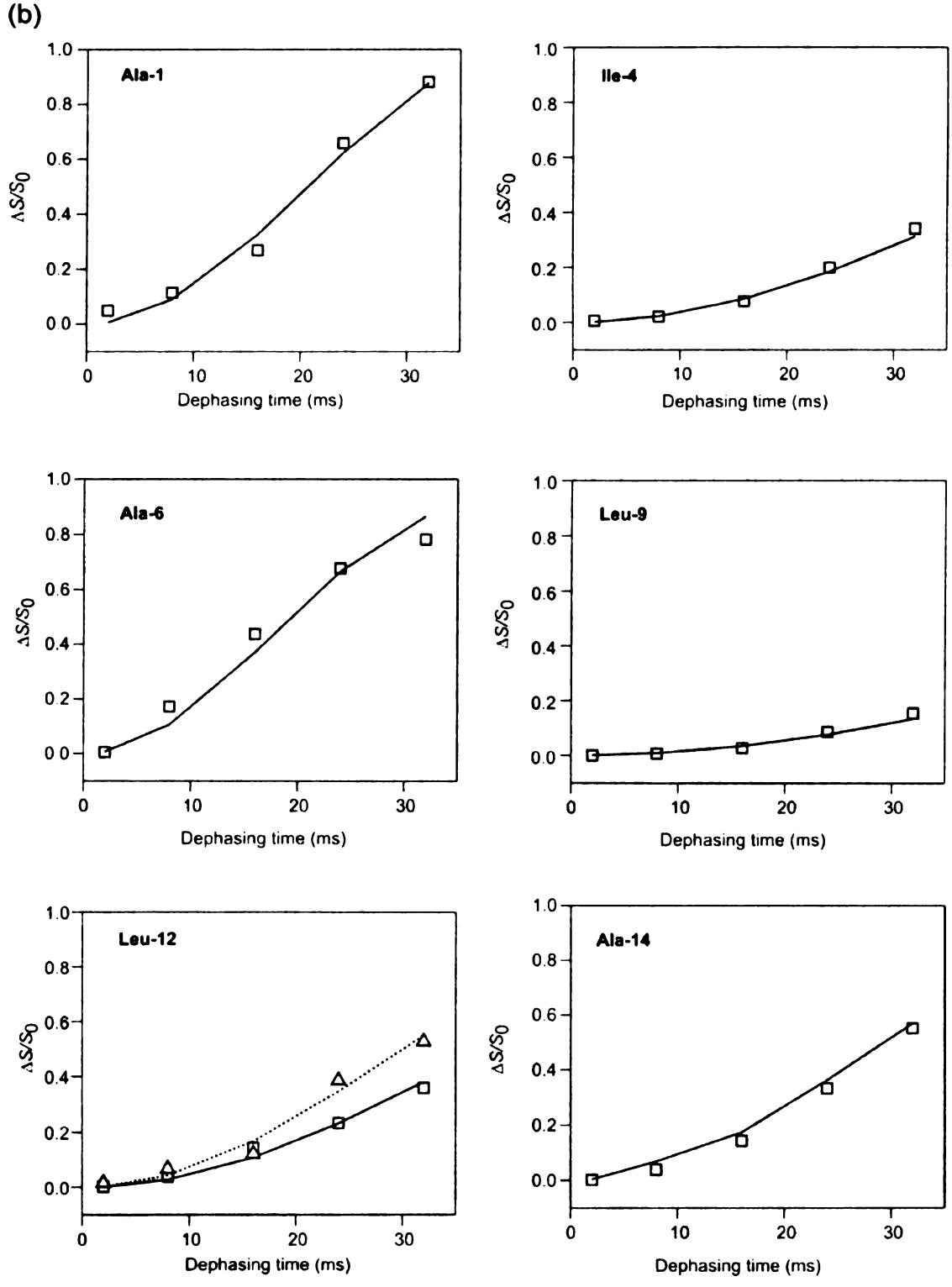

Figure 37 (b) Plots of ^{13}C-^{31}P $(\Delta S/S_0)^{lab}$ (open squares) and $(\Delta S/S_0)^{sim}$ vs. dephasing time for different residues (as labeled in the figures) of HFPmn_mut. The typical experimental uncertainties are ±0.02-0.03 and the typical corrected uncertainties are ±0.03-0.04.

provided in Figure 37b. Data fitting was not carried out for the ^{13}C-^{19}F experiments because the build-up of REDOR dephasings was not observed experimentally. Table 10 provides the best-fit distances for all the labeled residues. The labeled ^{13}COs are 6.6-10.1 Å away from the ^{31}Ps in the lipid phosphate groups. Under the experimental conditions, the temperature is below the transition temperature of the phospholipids of the lipid bilayer which means the membranes are in the gel phase. The typical membrane longitudinal distance between ^{31}P and ^{19}F(C5) is 10 Å in the gel phase lipid bilayer according to a simulated gel-phase DPPC bilayer.(*25*) This suggests the HFPmn_mut backbone is located higher than the longitude of the phosphate groups, since there is no contact between the backbone ^{13}COs and ^{19}F(C5). The simulated gel phase DPPC membrane bilayer structure indicated that there is a ~ 10 Å water layer above the bilayer surface.*(25)* Our results suggest that the HFPmn_mut may bind to the lipid bilayer surface through hydrogen bonds with the water molecules. Figure 35a showed that the ^{13}CO peaks for Ala1, Ile4 and Ala6 in the HFPmn_mut were broad. This suggested that these residues may not have a well-defined secondary structure and the carbonyl oxygens and the amide protons of these residues may not form intra-peptide hydrogen bonds. Thus there may be hydrogen bonds formed between the peptide backbone of these residues and the water molecules, or between the backbone of these residues and the lipid headgroups. All distances provided in Table 10 are greater than 6 Å, which approximately equals the sum of the length of a P=O bond (~1.8 Å), a C=O bond (~1.2 Å) and two van der Waals radius of the oxygen nuclei (~3.0 Å). This

reflects the ^{13}CO-^{31}P distance when the lipid phosphate group is in close proximity to α-helix backbone. The fitting parameters *A* in Table 10 are close to 1, which suggested that the residues Ala1 through Ala14 in almost

(a)

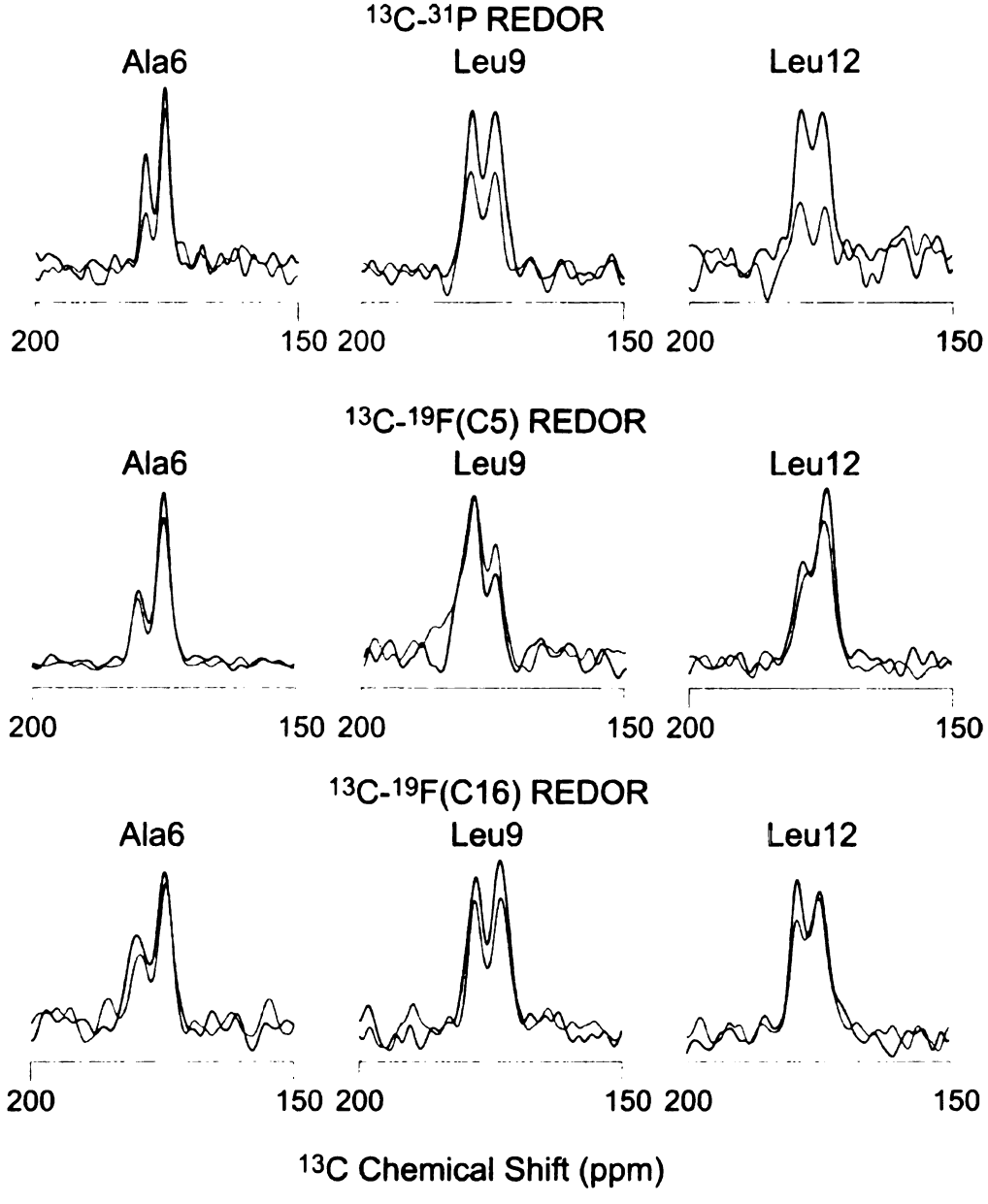

(b)

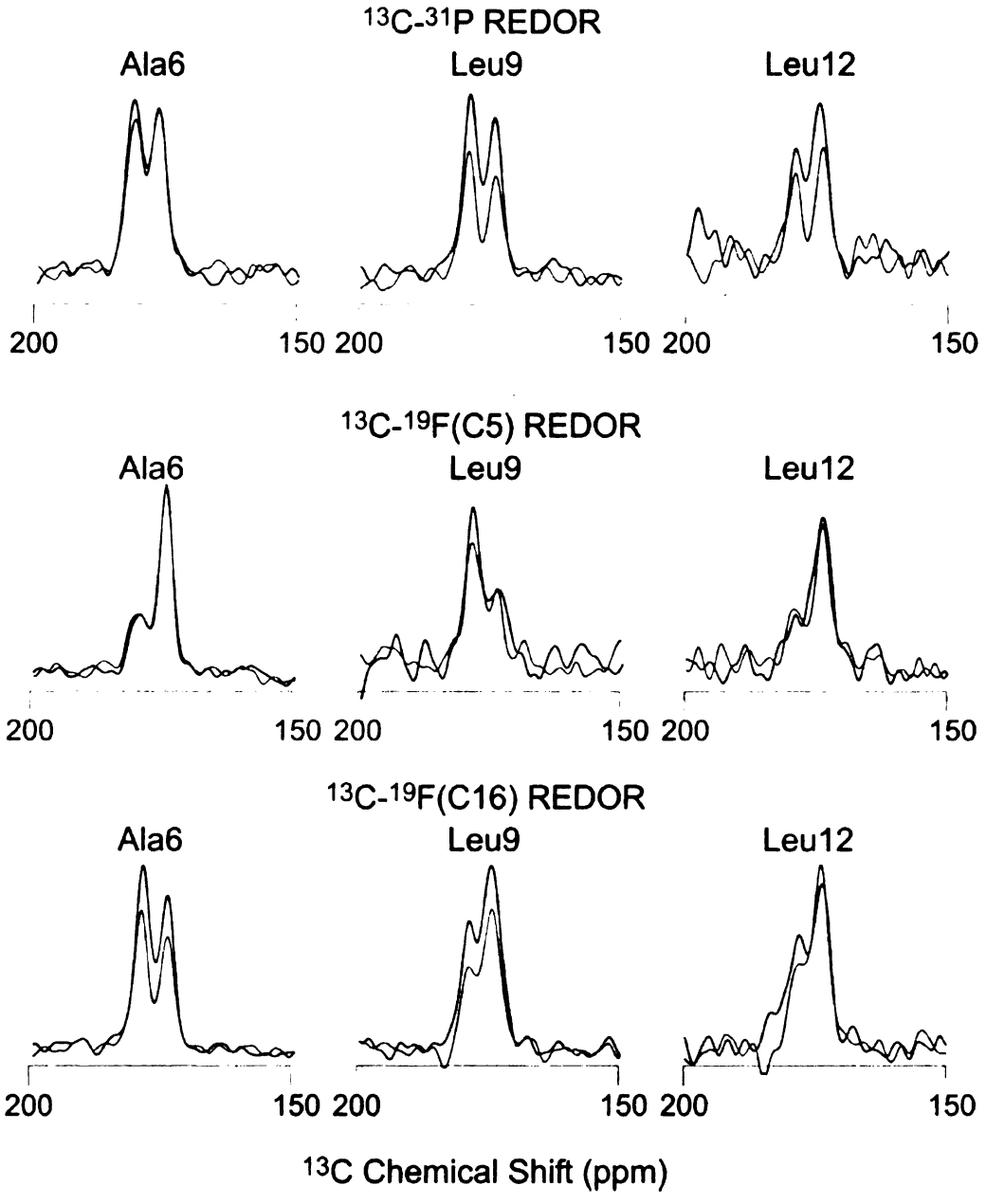

Figure 38 REDOR S_0 and S_1 spectra for (a) HFPmn and (b) HFPtr at long dephasing time (τ = 32 ms for ^{13}C-^{31}P experiments and τ = 24 ms for ^{13}C-^{19}F experiments). The S_0 and S_1 spectra were shown in black and red respectively. All spectra are processed with 200 Hz Gaussian line broadening and baseline correction. The ^{13}C-^{31}P spectra were acquired for ~ 30000 scans and the ^{13}C-^{31}P spectra were acquired for ~ 20000 scans.

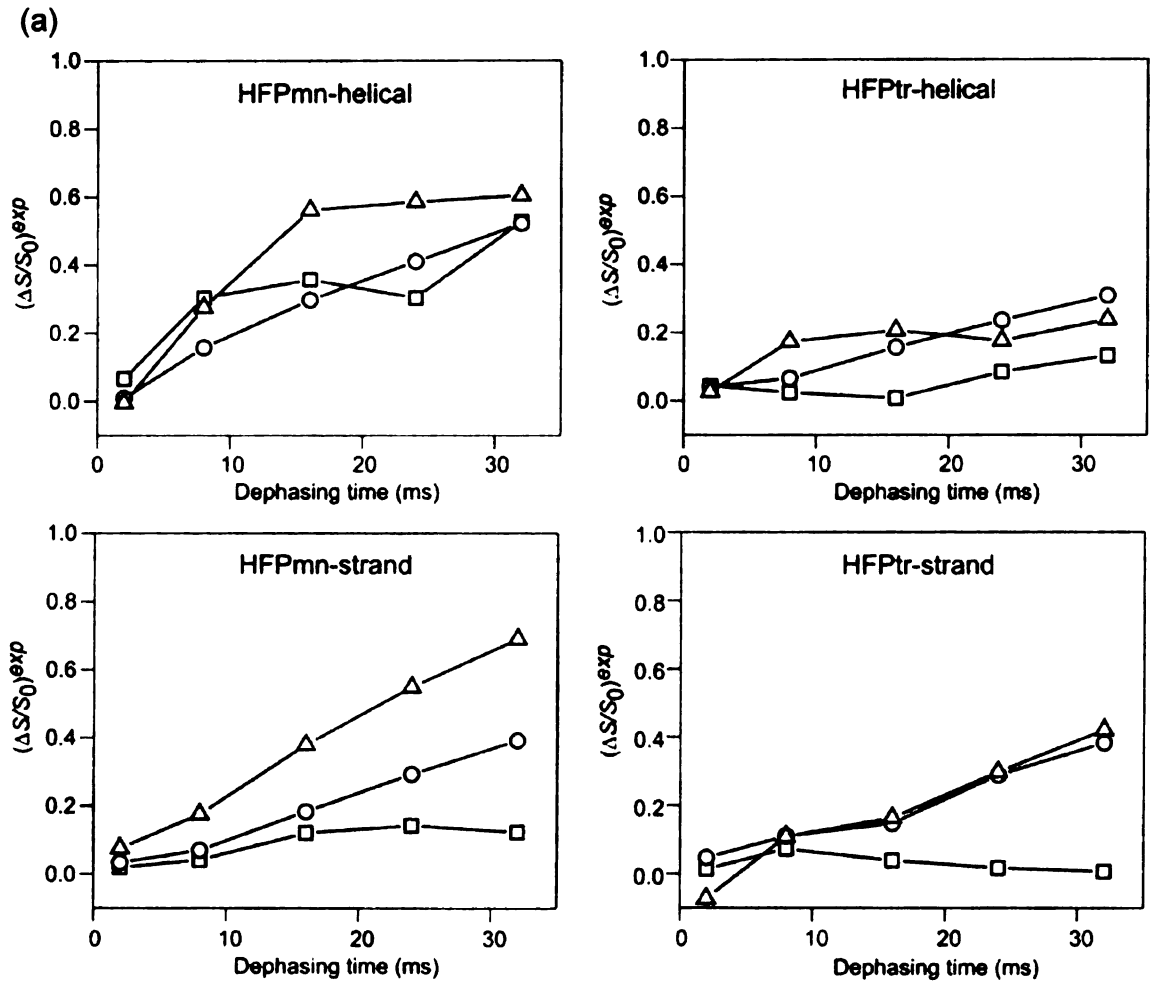

Figure 39 Plots of $(\Delta S/S_0)^{exp}$ vs. dephasing time for the ^{13}C-^{31}P experiments.

(b)

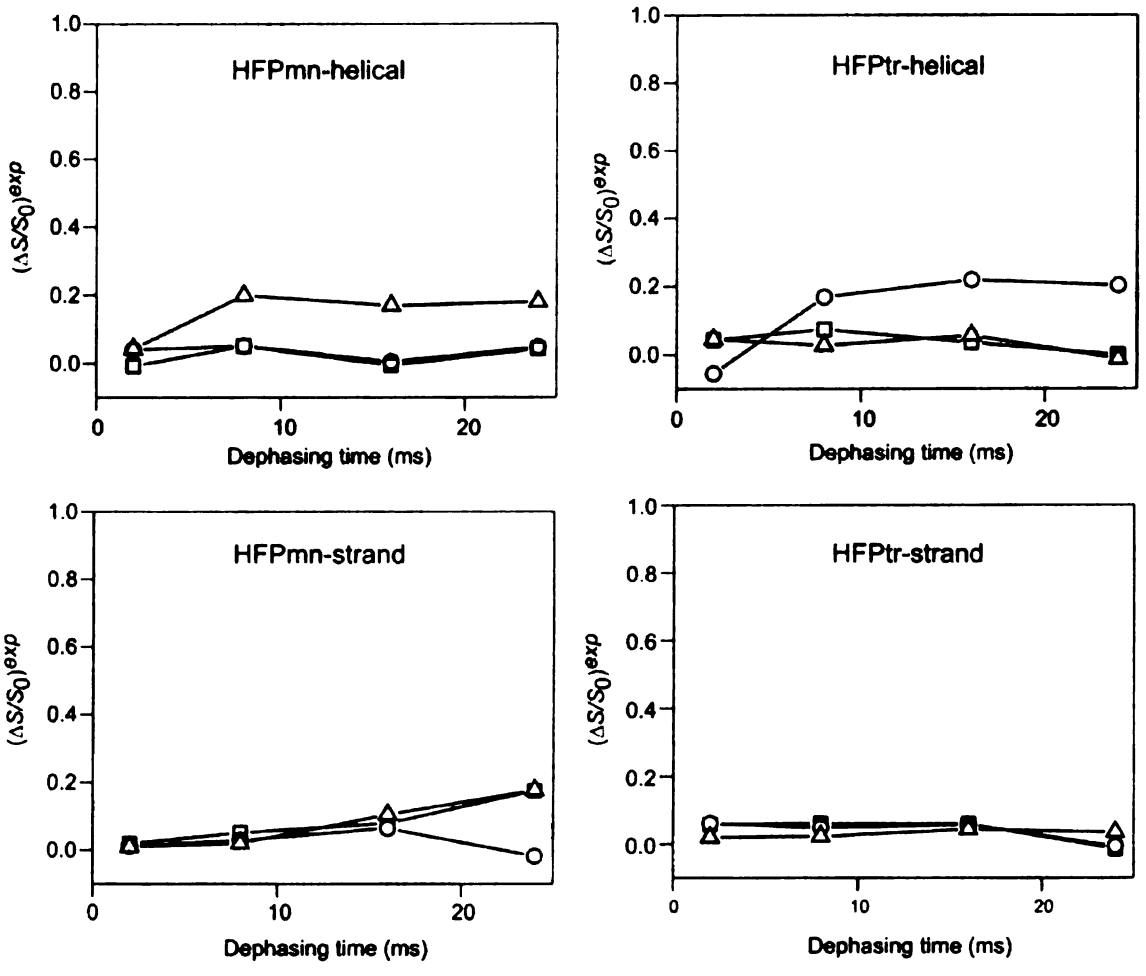

Figure 39 Plots of $(\Delta S/S_0)^{exp}$ vs. dephasing time for the ^{13}C-^{19}F(C5) experiments.

(c)

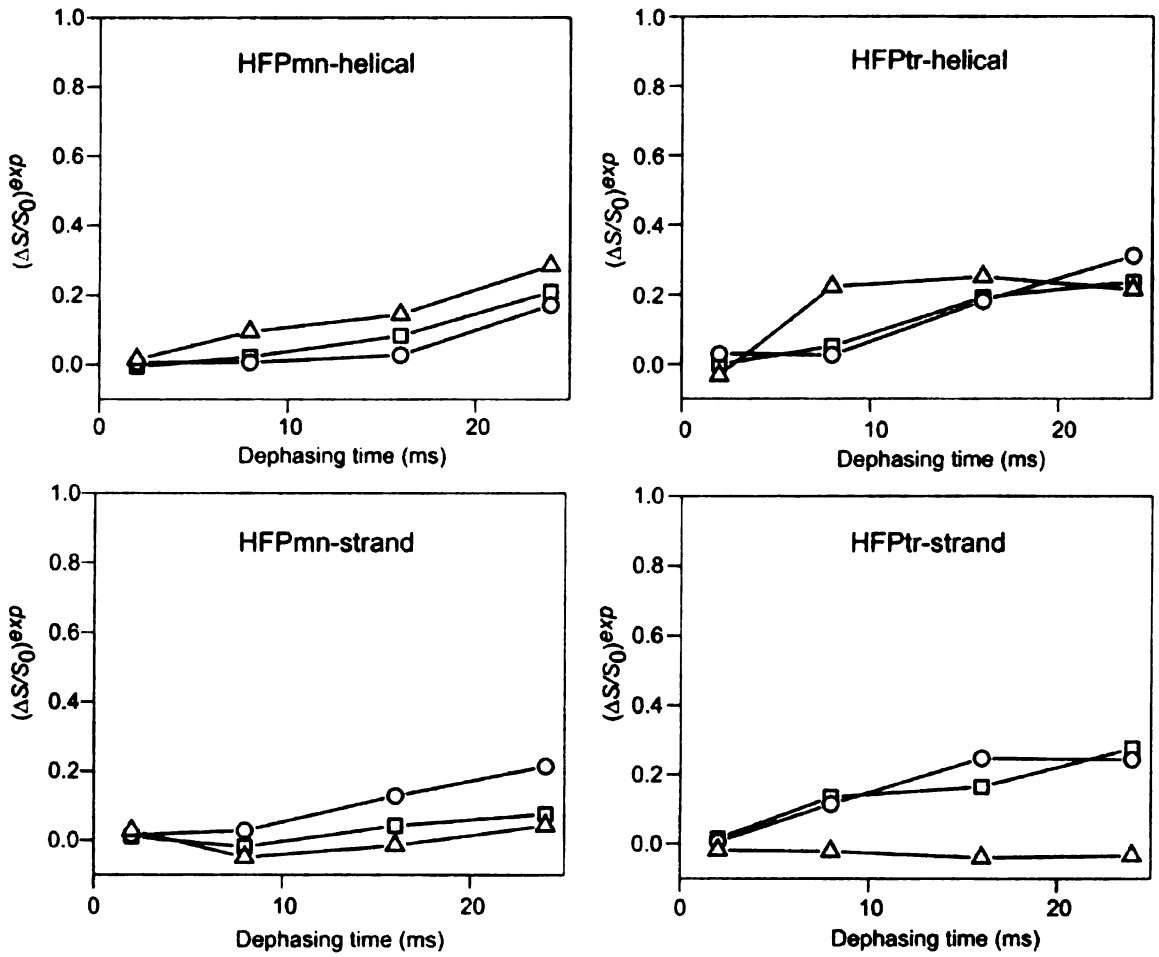

Figure 39 Plots of $(\Delta S/S_0)^{exp}$ vs. dephasing time for the (a) ^{13}C-^{31}P, (b) ^{13}C-^{19}F(C5) and (c) ^{13}C-^{19}F(C16) experiments for HFPmn and HFPtr in the α-helical and β-strand conformations. The residues Ala6, Leu9 and Leu12 are represented with the open squares, open circles and open triangles respectively. The uncertainties of $(\Delta S/S_0)^{exp}$ are typically ±0.02 ~ 0.03 and are approximately the size of the symbols. The $(\Delta S/S_0)^{exp}$ values were determined by integrating over a 1 ppm interval around the α-helical or β-strand ^{13}CO peaks in the corresponding S_0 and S_1 spectra.

all HFPmn_mut have close contact with the ^{31}Ps. Together with the fact that there is no contact with the ^{19}Fs, it suggests that the residues Ala1 through Ala14 in almost all the HFPmn_mut adopted the surface location. Furthermore, the membrane location of the α-helical HFPmn_mut in PC:PG is consistent with the observation of the surface membrane location of the β-strand HFPmn_mut in PC:PG:CHOL, which may indicate the surface location of HFPmn_mut is an intrinsic property of the peptide sequence and is independent of the membrane composition and peptide conformation.*(18)* A consequence of the surface location of HFPmn_mut is that the peptide does not penetrate the polar phospholipid headgroups and disrupt the membrane interior.

Table 10. ^{13}CO-^{31}P internuclear distances and populations for HFPmn_mut

	Ala1	Ile4	Ala6	Leu9	Leu12 [a]	Ala14
^{13}CO-^{31}P distance (Å)	6.9 (2) [b]	8.7 (2)	6.6 (1)	10.1 (3)	8.4 (2) 7.8 (2)	7.6 (2)
Population *A*	0.98 (2)	0.93 (3)	0.88 (1)	0.90 (3)	0.94 (3) 0.97 (2)	0.95 (3)
χ^2	5.1	1.7	9.7	1.3	2.0 1.8	1.4

[a] For Leu12, the first value corresponds to helical conformation and the second value corresponds to strand conformation.
[b] The uncertainties are shown in the parentheses and were determined by the $\chi^2 = \chi^2_{min}+1$ criterion.

Figure 38 displays the long time REDOR spectra for the residues Ala6, Leu9 and Leu12 for HFPmn and HFPtr. These residues were selected because (1) there is obvious non-zero ^{13}C-^{19}F dephasing in some spectra for these residues which is qualitatively different from HFPmn_mut; and (2) the α-helical and β-strand peaks are in general well-separated which facilitates quantitative analysis of the data as a function of conformation. The information obtained for

the residues Ala1, Ile4 and Ala14 will be discussed later in this section. Figure 39a and c plots the ^{13}C-^{31}P and ^{13}C-^{19}F(C16) experimental dephasing curves respectively for the α-helical and β-strand conformations for HFPmn and HFPtr. It can be qualitatively concluded that the HFPmn and HFPtr are deeply inserted into the region of phospholipid alkyl chains because both constructs show some non-zero ^{13}C-^{19}F dephasings.

A quantitative analysis was done for Ala6, Leu9 and Leu12 in the α-helical HFPmn, the α-helical HFPtr, the β-strand HFPmn and the β-strand HFPtr. The resultant membrane locations may be correlated with the different fusion activities of HFPmn and HFPtr in PC:PG bilayer. The data fitting was based on the following considerations:

(1) For each HFP in each conformation, there are two populations which differ in their membrane location. The population which is closer to the membrane surface is named "surface-located population" and the population closer to the membrane interior is named "deeply-inserted population".

(2) The typical uncertainty for the ^{13}C-^{31}P and ^{13}C-^{19}F REDOR $(\Delta S/S_0)^{exp}$ is ± 0.02-0.03. Only the ^{13}COs with $(\Delta S/S_0)^{exp} > 0.1$ at large dephasing times (τ = 32 ms for ^{13}C-^{31}P and τ = 24 ms for ^{13}C-^{19}F) are considered to have fittable dephasing relative to the uncertainties. According to the REDOR universal dephasing curve,(*32*) $\Delta S/S_0 = 0.1$ corresponds to ~ 11 Å ^{13}C-^{31}P distance at 32 ms and ~ 14 Å ^{13}C-^{19}F distance at 24 ms. Thus, we consider that the measurement limits for ^{13}C-^{31}P and ^{13}C-^{19}F REDOR experiments are 11 and 14 Å, respectively. The distance between the ^{31}P and the ^{19}F(C16) in a gel phase

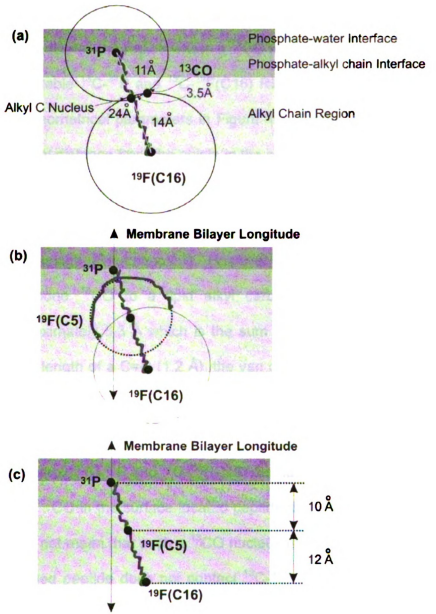

Figure 40 (a) Geometry Model for the consideration of ^{13}C-^{31}P and ^{13}C-^{19}F measurement limit. The two circles with 11 Å and 14 Å radii indicate the measurement limits of ^{13}C-^{31}P and ^{13}C-^{19}F(C16) REDOR respectively. The yellow triangle shows the geometry of the case where a ^{13}CO has the maximum vertical distance (3.5 Å) relative to the lipid alkyl chain. (b) and (c) Longitudinal positions of ^{31}P, ^{19}F(C5) and ^{19}F(C16) in the membrane bilayer. In panel (b), the dotted circle has the radius of ~ 10 Å and the solid circle has the radius of ~ 14 Å. The region marked in red indicates the possible location of the ^{13}COs of Ala6 and Leu12 in the β-strand HFPmn as described in the main text. In panel (c), the longitudinal distance between ^{31}P and ^{19}F(C5) is 10 Å and the distance between ^{19}F(C5) and ^{19}F(C16) is 12 Å.

DPPC molecule is ~ 24 Å.(*25*) The overlapped region of the two circles in Figure 40a indicates the region where a ^{13}CO nucleus in the peptide backbone can have detectable ^{13}C-^{31}P and ^{13}C-^{19}F(C16) REDOR dephasings simultaneously. Using the geometrical parameters in Figure 40a, it can be obtained that the maximum vertical distance from the points in the overlapped region to the lipid alkyl chain is 3.5 Å. This means a ^{13}CO nucleus has to be located within 3.5 Å away from a lipid alkyl carbon nucleus to have detectable ^{13}C-^{31}P and ^{13}C-^{19}F(C16) dephasings simultaneously. However, the shortest distance from a peptide backbone ^{13}CO to a lipid alkyl carbon nucleus in the lipid alkyl chain is approximately 5.3 Å which is the sum of the bond length of a C-H (1.4 Å), the bond length of a C=O (1.2 Å), the van der Waals radius of a hydrogen atom (1.2 Å) and the van der Waals radius of an oxygen atom (1.5 Å). Consequently, in the following quantitative analysis we consider that a specific ^{13}CO will not have detectable ^{13}C-^{31}P and ^{13}C-^{19}F(C16) dephasings at the same time.

(3) A ^{13}CO in the surface-located peptide does not contact ^{13}C-^{19}F(C16), and this does not mean that such a ^{13}CO nucleus must contact ^{31}P. A ^{13}CO in the deeply-inserted peptide does not contact ^{13}C-^{31}P, and this does not mean that such a ^{13}CO nucleus must contact with ^{19}F(C16).

The ^{13}C-^{31}P and ^{13}C-^{19}F(C16) $(\Delta S/S_0)^{exp}$ were first corrected using Eq. 59 to obtain $(\Delta S/S_0)^{lab}$, and then the $(\Delta S/S_0)^{lab}$ were fitted to the simulated dephasing $(\Delta S/S_0)^{sim}$ of either a ^{13}C-X two-spin system or a X-^{13}C-X three-spin system where X ≡ ^{31}P or ^{19}F(C16). The three-spin fitting was only applied to these samples with visibly large difference between their $(\Delta S/S_0)^{lab}$ and the $(\Delta S/S_0)^{sim}$ of

Table 11 The best-fit *A* and *B* population parameters for HFPmn and HFPtr in PC:PG.

	Parameter *A*				Parameter *B*			
	Ala-6	Leu-9	Leu-12	Average	Ala-6	Leu-9	Leu-12	average
HFPmn(helical)	0.62	0.62	0.65	0.63(2)[b]	0.27	----	0.31	0.29(2)
HFPtr(helical)	----[a]	0.29	0.20	0.24(4)	0.28	0.37	0.33	0.33(4)
HFPmn(strand)	----	0.61	0.66	0.64(2)	----	0.30	----	0.30[c]
HFPtr(strand)	----	0.41	0.44	0.42(2)	0.32	0.32	----	0.32[c]

[a] The dashed lines indicate that these data have $(\Delta S/S_0)^{lab} < 0.1$ at 32 ms dephasing time for ^{13}C-^{31}P data and $(\Delta S/S_0)^{lab} < 0.1$ at 24 ms dephasing time for ^{13}C-^{19}F(C16) data.
[b] The uncertainties are shown in parentheses. The uncertainties in A were determined from the difference between *A* for each residue and the average *A*. The uncertainties in *B* were similarly calculated.
[c] The uncertainties were not determined either because there is only one *A* or *B* value or because the two values are the same.

Table 12 Summary of the fitting for ^{13}C-^{31}P and ^{13}C-^{19}F(C16) experiments.[a]

		Surface-located Population			Deeply-inserted Population		
		r (Å)	θ (°)	χ^2	*r* (Å)	θ (°)	χ^2
HFPmn (helical)	A6	4.8(3)	10(2)	0.9	10.4(3)	98(3)	0.4
	L9	6.3(2)		5.1	11.8(3)	21(2)	1.5
	L12	5.2(2)		9.2	7.2(3)	24(2)	1.5
HFPtr (helical)	A6	>11			7.4(2)		0.9
	L9	6.6(3)		2.1	8.1(3)		3.6
	L12	4.6(2)		2.3	6.1(1)		9.0
HFPmn (strand)	A6	>11			>14		
	L9	7.9(2)		0.6	8.4(3)		0.4
	L12	6.2(2)		6.9	>14		
HFPtr (strand)	A6	>11			6.9(2)	21(2)	1.0
	L9	6.7(2)		6.2	6.8(2)		0.1
	L12	6.7(1)		14.8	>14		

[a] The uncertainties are provided in the parentheses and were determined by the $\chi^2 = \chi^2_{min}+1$ criterion. If the θ values were provided, the fitted values are from X-^{13}C-X simulations.

the two-spin system. The two-spin-system fitting has two variable parameters: (1) the ^{13}C-X dipolar coupling frequency *d* which depends on the ^{13}C-X internuclear distance *r* as r^{-3}; and (2) a parameter denoted *A* or *B* which respectively reflects the maximal fractional ^{13}C-^{31}P or ^{13}C-^{19}F(C16) dephasing. The logical basis of the *A* or *B* parameters includes: (1) two HFP populations; (2) some ^{13}COs may be shielded from any region of the membrane by other peptides. This is most clear for β-strand HFPs in the interior of a β-sheet; and (3) the ^{13}C-^{19}F dephasing may not reach 1 because of the 0.09 mol fraction of fluorinated lipids. The three-spin-system fitting has three variable parameters: (1) the ^{13}C-X dipolar coupling frequency *d*; (2) the angle θ between two ^{13}C-X vectors; and (3) the population parameters *A* or *B* as in the ^{13}C-X fittings. The fitting was done for every individual samples with non-zero ^{13}C-^{31}P or ^{13}C-^{19}F(C16) dephasing curves to obtain the best-fit population parameters *A* or *B*. Table 11 summarizes the best-fit *A* and *B* parameters for Ala-6, Leu-9 and Leu-12. The averaged *A* or *B* parameters were calculated for each construct and each conformation because the individual values for these residues are close to each other. This probably indicates that the fraction parameter is independent of the residues that were labeled in the region of HFP from Ala-6 to Leu-12.

The following changes can be observed by comparing the averaged *A* and *B* parameters: (1) The sum of *A* and *B* was close to 1 for HFPmn but less than 1 for HFPtr, regardless of the secondary structures. This suggests that all ^{13}COs in HFPmn are close to some regions of the membrane, but this may not

be true for HFPtr. For the helical HFPtr, the three helices may be close together

(a)

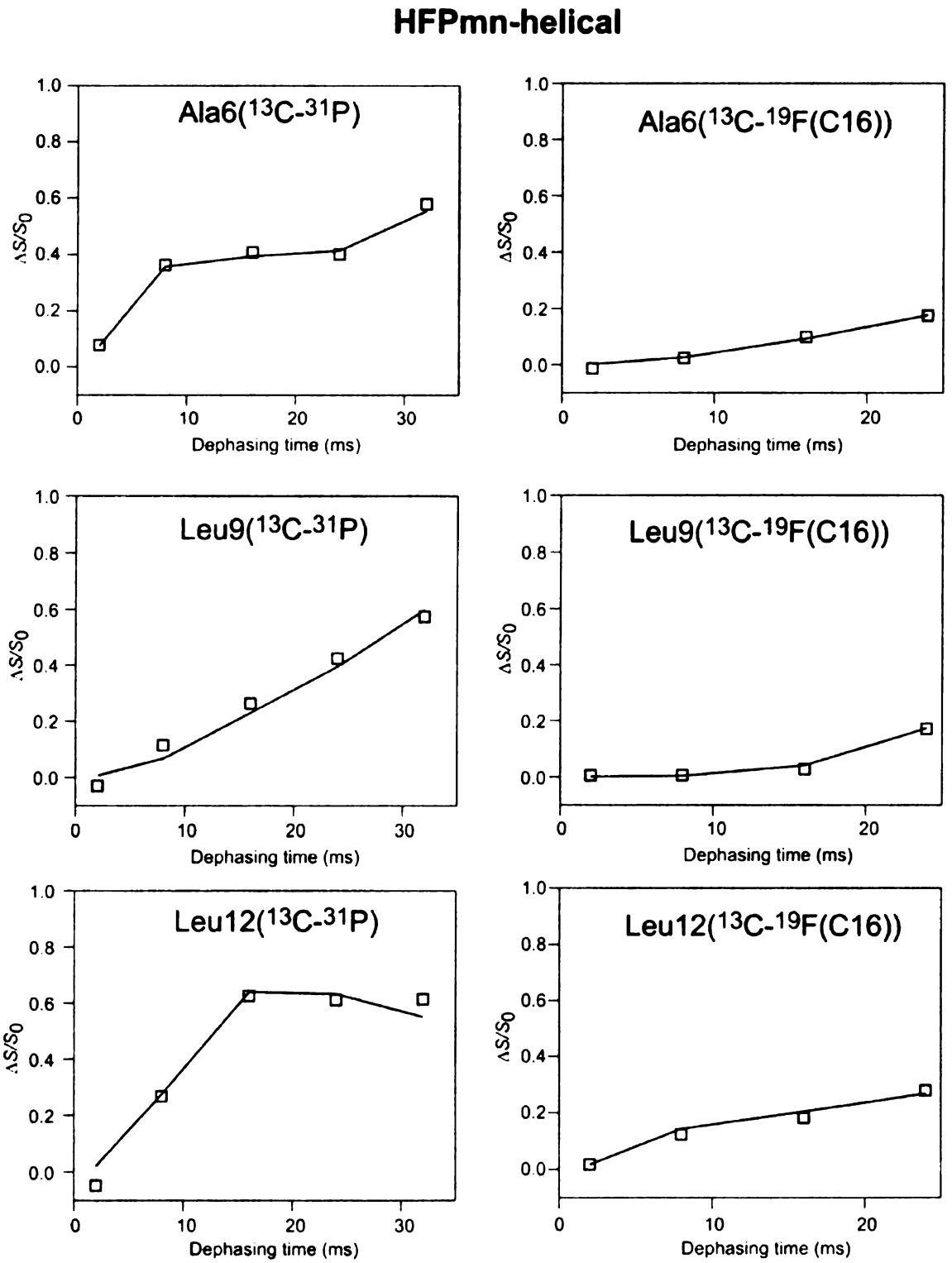

Figure 41 (a) Fitting curves for the helical HFPmn in PC:PG.

(b)

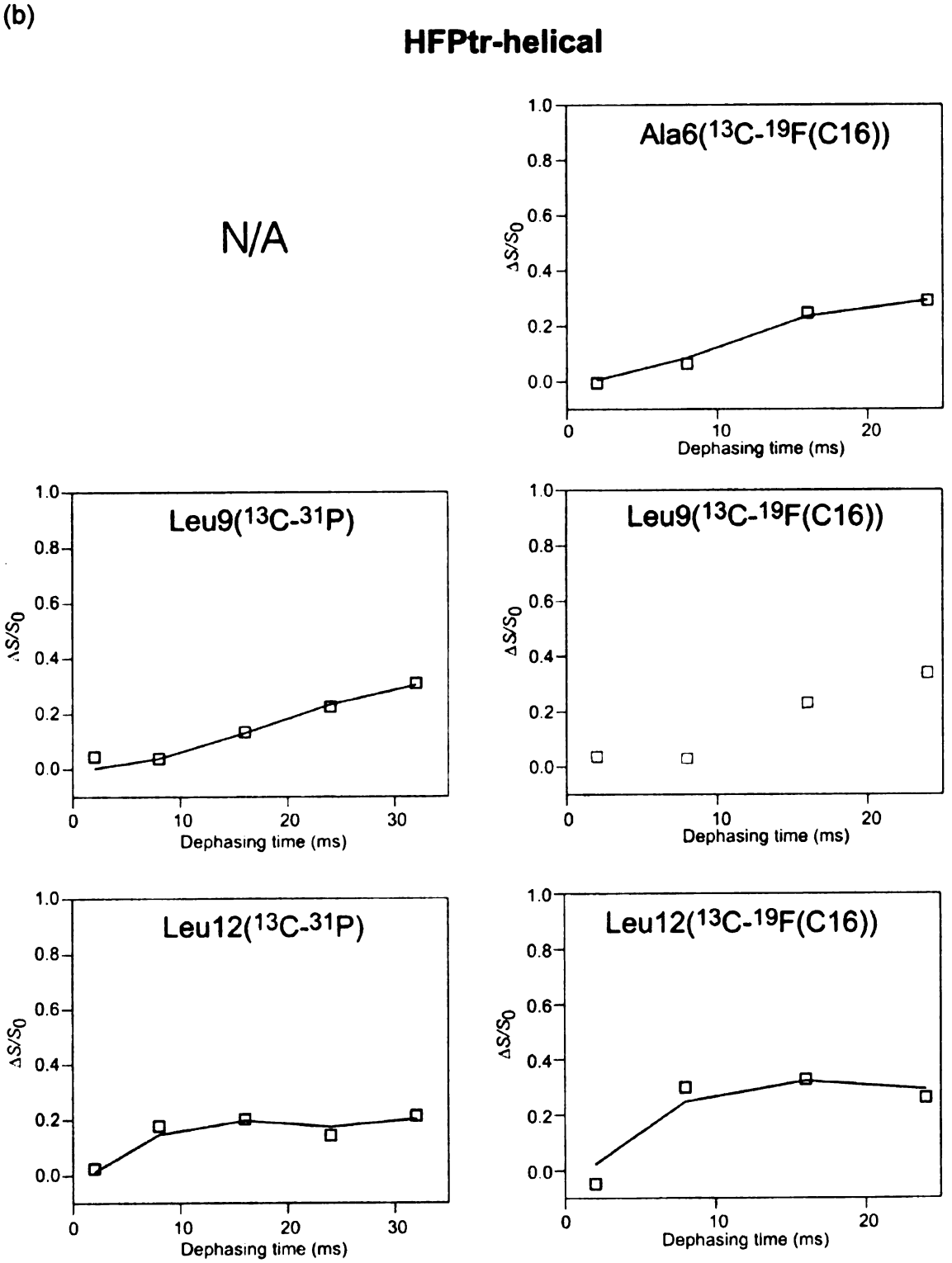

Figure 41 (b) Fitting curves for the helical HFPtr in PC:PG.

(c)

HFPmn-strand

N/A

N/A

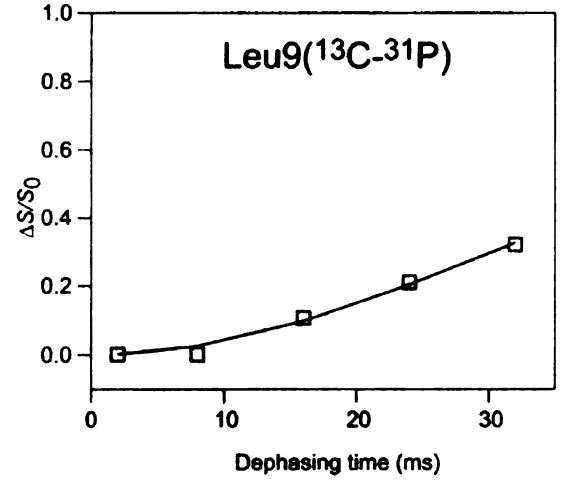

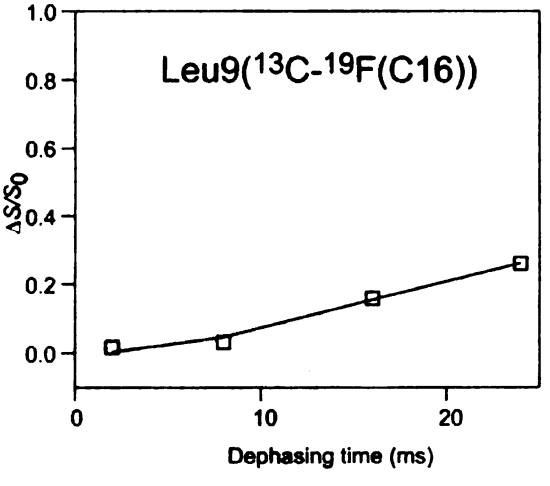

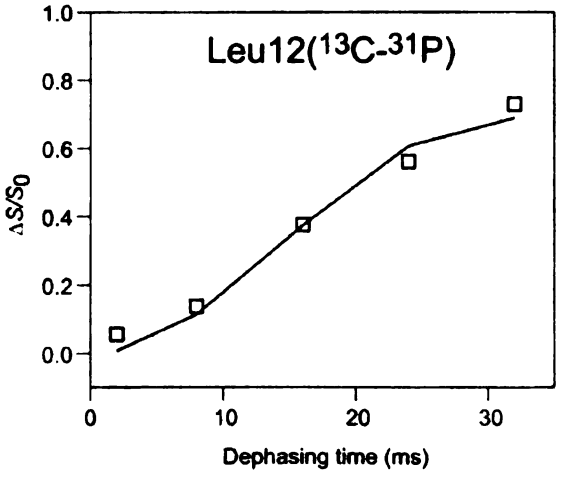

N/A

Figure 41 (c) Fitting curves for the strand HFPmn in PC:PG.

(d)

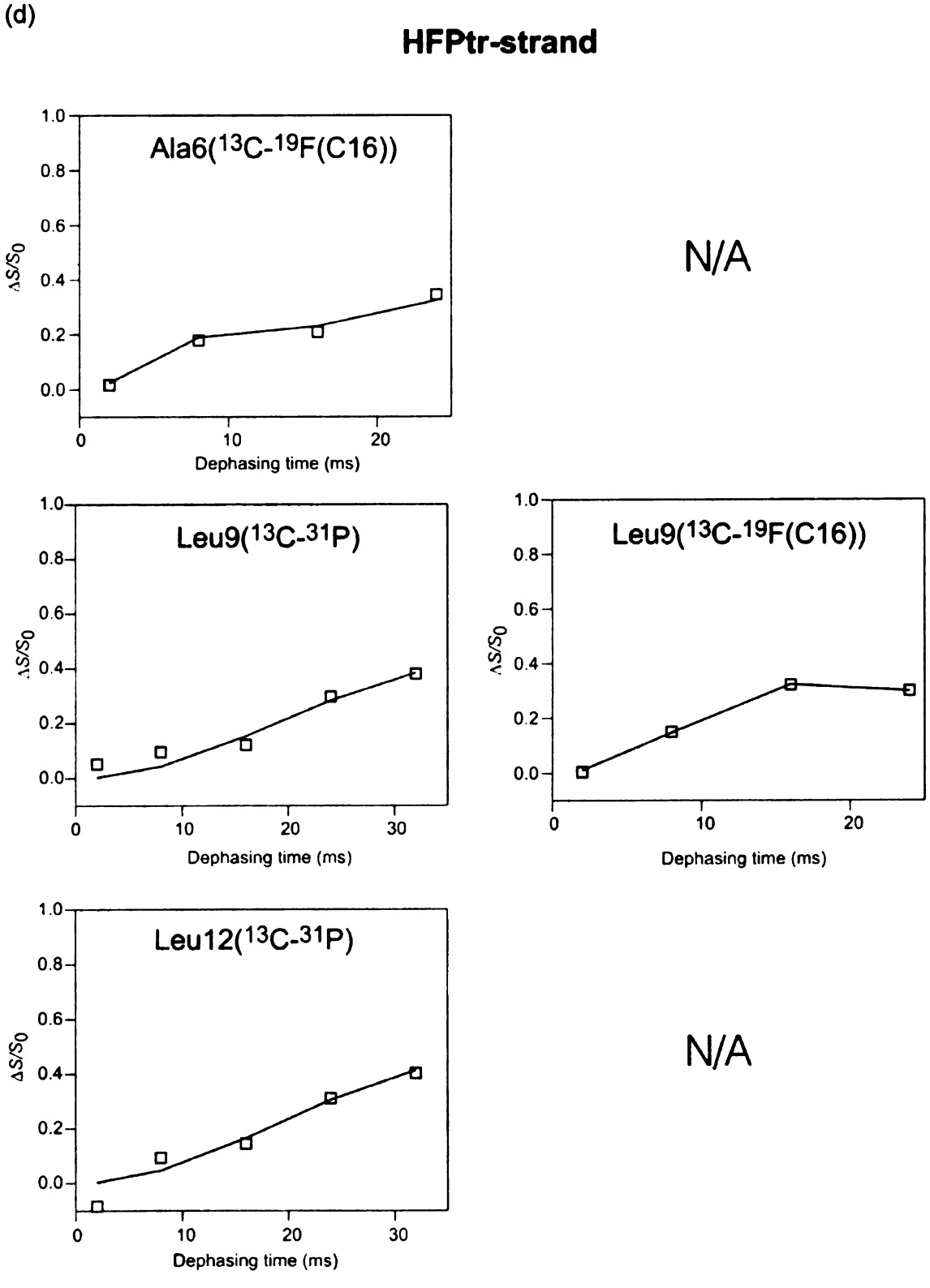

Figure 41 (d) Fitting curves for the strand HFPtr in PC:PG.

(e)

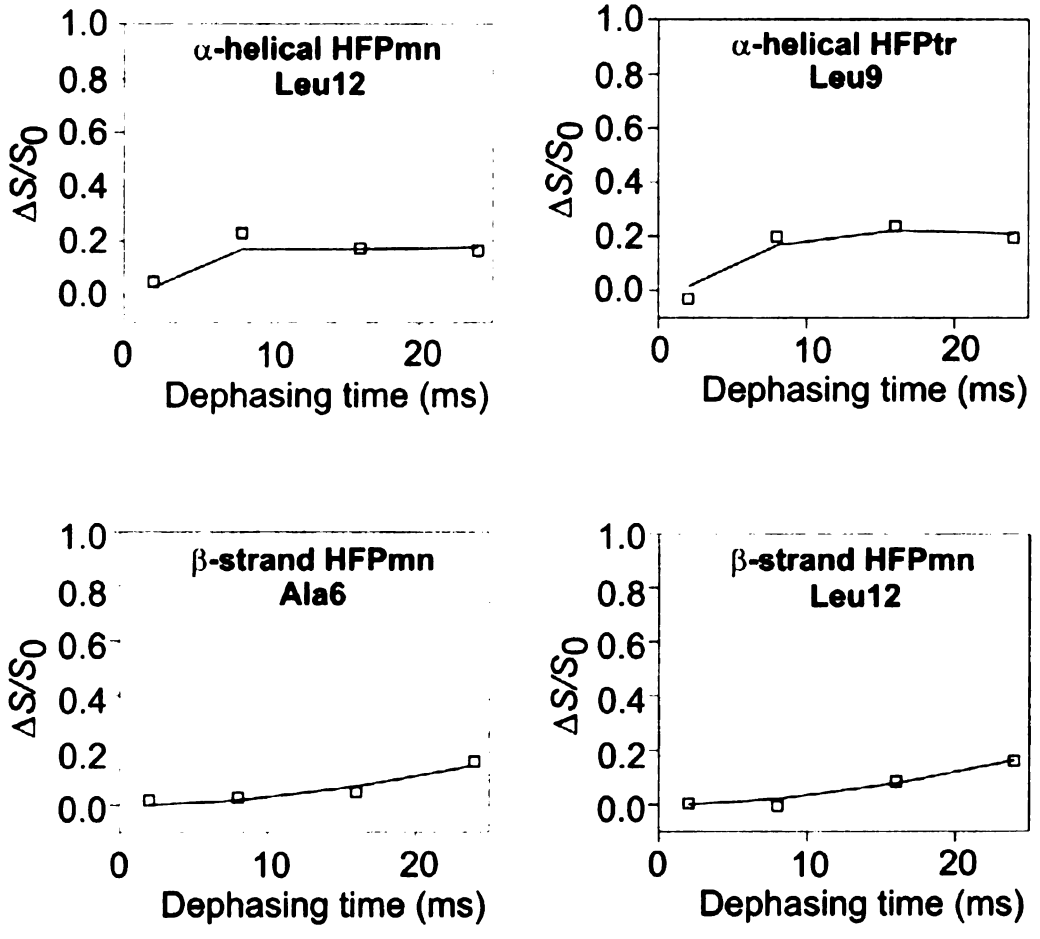

Figure 41 (e) Plots of $(\Delta S/S_0)^{lab}$ (open squares) and $(\Delta S/S_0)^{sim}$ (solid lines) vs. the dephasing time for ^{13}C-^{19}F(C5) experiments.

(f)

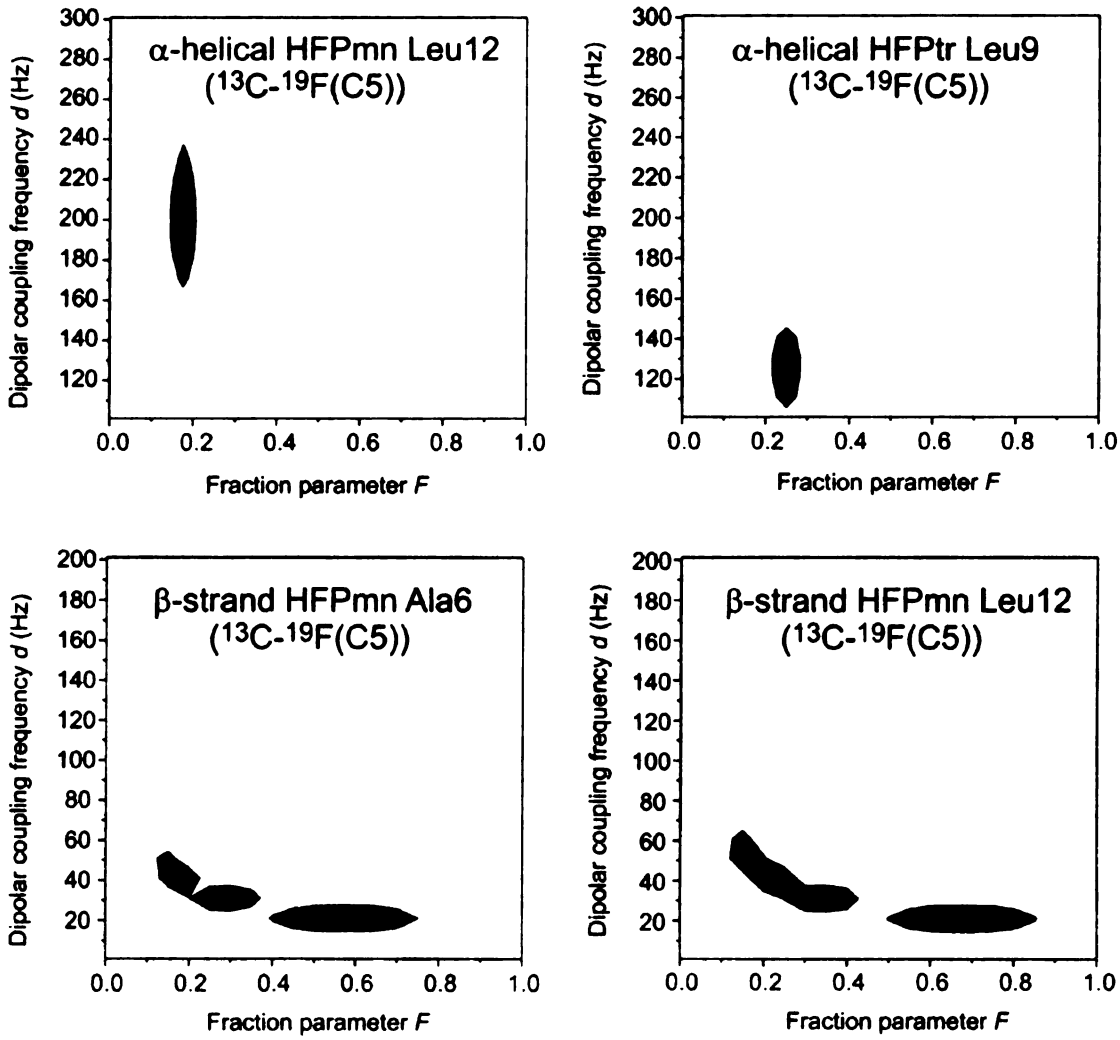

Figure 41 (a)-(d) Plot of $(\Delta S/S_0)^{lab}$ (open squares) and $(\Delta S/S_0)^{sim}$ (solid lines) vs. the dephasing time for Ala6, Leu9 and Leu12 in HFPmn and HFPtr with α-helical and β-strand conformations. The data with $(\Delta S/S_0)^{exp} < 0.1$ at 32 ms for ^{13}C-^{31}P and at 24 ms for ^{13}C-^{19}F(C16) were not fit and were labeled "N/A". (e) Plots of $(\Delta S/S_0)^{lab}$ (open squares) and $(\Delta S/S_0)^{sim}$ (solid lines) vs. the dephasing time for ^{13}C-^{19}F(C5) experiments. (f) Contour plots for the data fittings shown in (e). The regions with χ^2 values χ^2_{min} +1, χ^2_{min} +2 and χ^2_{min} +3 were shown in red, blue and green respectively, where χ^2_{min} is the best-fit root-mean-squared deviation as given in Table 13 of the main text.

and

awa

larg

far a

HFF

the

para

inse

be

effe

DPI

pop

par

pop

ind

we

wh

ar

de

in

e

n

and form a bundle. The ^{13}COs locate at the inner side of the bundle will be far away from any part of the membrane. For the strand HFPs, the HFPtr may form larger β-sheet oligomers in which more ^{13}COs are located in the inner strand and far away from the membrane. (2) The *A* parameters decrease from HFPmn to HFPtr independent of the secondary structures, while the *B* parameters remain the same. According to the logical basis to introduce the *A* and *B* parameters, the parameter *A* will be affected by (1) the change in surface-located and deeply-inserted population, and (2) the change in shielding effect. The parameter *B* will be affected by (1) the change in two populations, (2) the change in shielding effect, and (3) the dilution effect due to the utilization of 9 mol fraction of ^{19}F-DPPC. The decrease in *A* parameter indicates an increase in the deeply-inserted population, or an increase in shielding effect or both. However, since the *B* parameter remains the same, there must be an increase in the deeply-inserted population. The increase of shielding will lead to the decrease in *B* parameters, independent of the dilution effect. In other words, if there is no population change, we would expect to see a decrease in *B* parameters from HFPmn to HFPtr, which is not consistent with the data in Table 11.

The averaged fraction parameters *A* and *B* are used to refine the ^{13}C-^{31}P and ^{13}C-^{19}F(C16) distances using either a two-spin or a three-spin system as described previously. Table 12 summarizes the internuclear distances (*r*), the inter-vector angles (θ) and the best-fit χ^2 values. The θ values are in general equal or less than 90° rather than close to 180°, which means these residues are not located in the same longitudinal position as ^{19}F(C16). Figure 41a-d showed

all the fitting for the data with $(\Delta S/S_0)^{exp} > 0.1$ at long dephasing time for the residues Ala6, Leu9 and Leu12.

The $(\Delta S/S_0)^{exp}$ for the ^{13}C-^{19}F(C5) REDOR experiments are provided in Figure 39b. There are four samples which have $(\Delta S/S_0)^{exp} > 0.1$ for the ^{13}C-^{19}F(C5), α-helical HFPmn-L12, α-helical HFPtr-L9, β-strand HFPmn-A6 and β-strand HFPmn-L12. These data were fitted to ^{13}C-^{19}F two-spin systems using Eq. 59. There were two fitting parameters: the ^{13}C-^{19}F dipolar coupling frequency (*d*) which depends on the ^{13}C-^{19}F distance (*r*) and the fraction parameter (*F*) as explained previously. Table 13 summarizes these best-fit parameters and Figure 41e shows the $(\Delta S/S_0)^{lab}$ data and fitting curves. Figure 41f shows the contour plots which reflect the best-fit regions for the four samples. For the α-helical HFPmn-L12 and α-helical HFPtr-L9 samples, the best-fit regions were restricted to one single area. The best-fit *F* for α-helical HFPmn-L12 was 0.16 and it was roughly half of the parameter *B* for the α-helical HFPmn (*cf.* Table 11). The relation $F/B \approx 0.5$ may be explained by the model that the peptide inserts deeply into one leaflet of the membrane bilayer so that a ^{13}CO is in close proximity with ^{19}F(C16) in both leaflets but with ^{19}F(C5) only in a single leaflet. This model will be discussed later in the section with the data of Ile4 and Ala14. The best-fit F for α-helical HFPtr-L9 was 0.24 which was close to both *A* and *B* parameters for the α-helical HFPtr (*cf.* Table 11). Figure 41f indicated that there were multiple best-fit regions for the Ala6 and Ala12 in β-strand HFPmn. Thus it will be difficult to determine whether the dephasings for these residues were contributed by surface-located or deeply-inserted population. However, the best-fit *d* values for

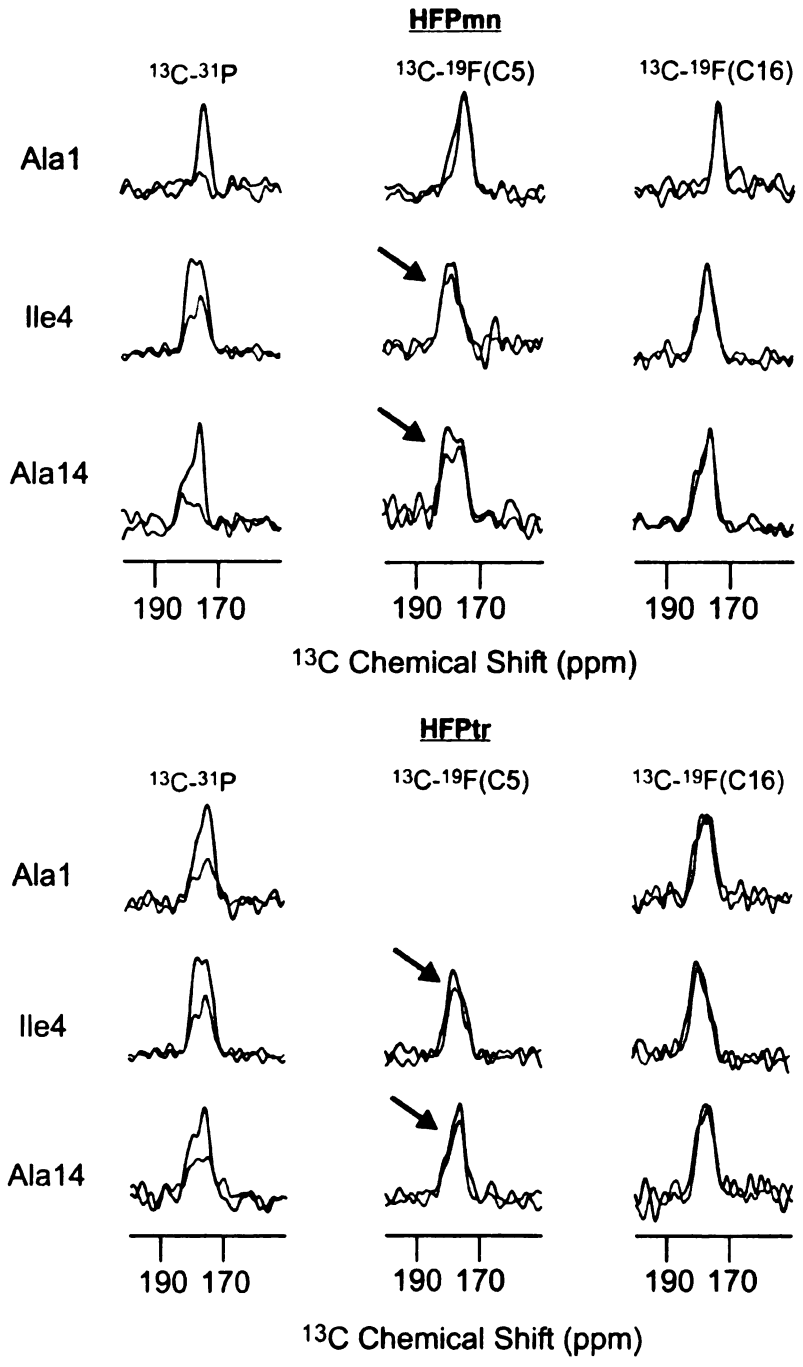

Figure 42 REDOR S_0 and S_1 spectra for Ala1, Ile4 and Ala14 in HFPmn and HFPtr at long dephasing time (τ = 32 ms for ^{13}C-^{31}P experiments and τ = 24 ms for ^{13}C-^{19}F experiments). The S_0 and S_1 spectra are shown in black and red respectively. All spectra were processed with 200 Hz Gaussian line broadening and baseline correction. The ^{13}C-^{31}P spectra were acquired for ~ 30000 scans and the ^{13}C-^{31}P spectra were acquired for ~ 20000 scans. The arrows indicate ^{13}C-^{19}F(C5) dephasing for Ile4 and Ala14.

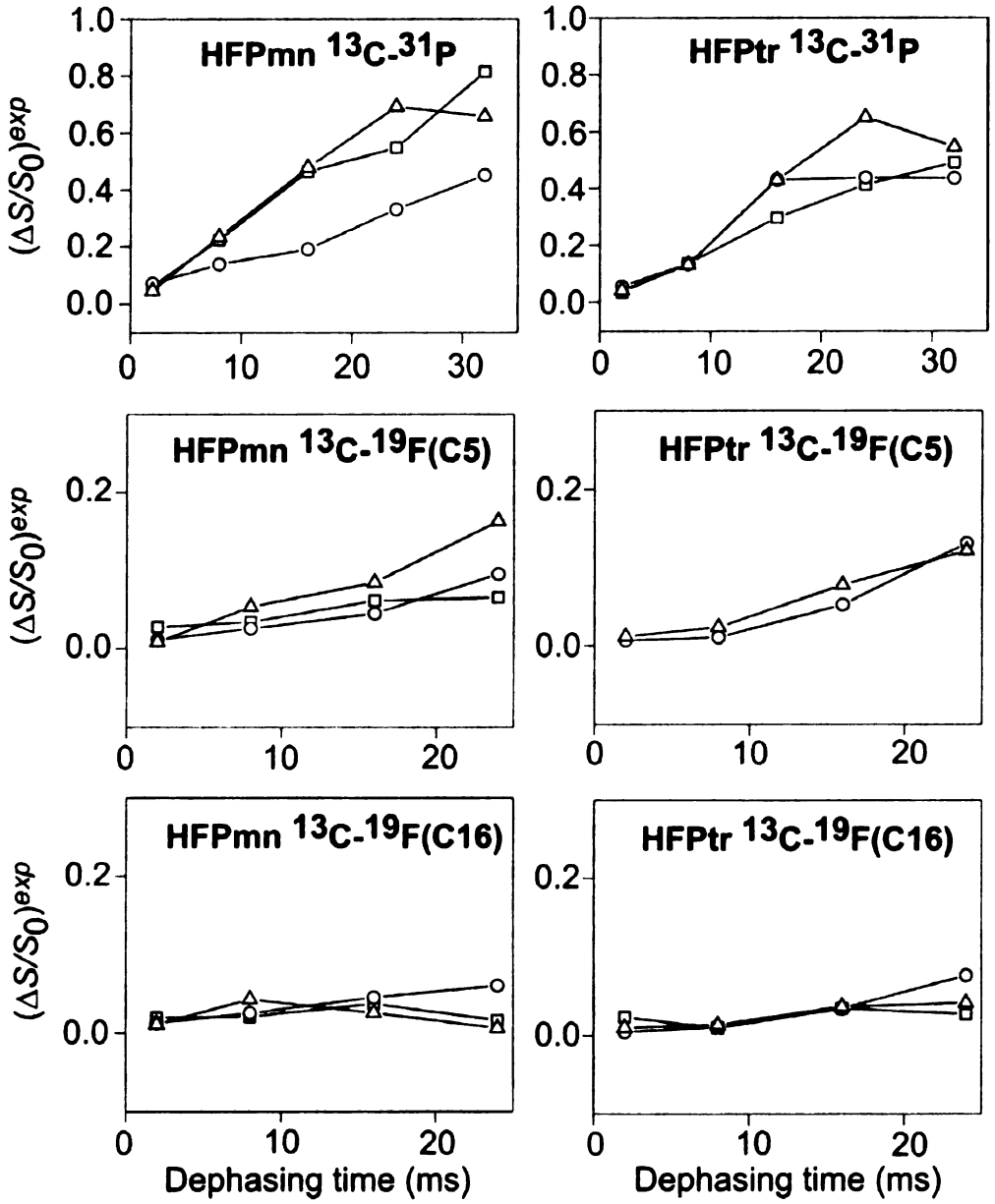

Figure 43 Plots of $(\Delta S/S_0)^{exp}$ vs. dephasing time for Ala1(open squares), Ile4 (open circles) and Ala14 (open triangles) labeled samples. The dephasing was calculated by integrating over the entire ^{13}CO peaks in the corresponding S_0 and S_1 spectra.

these two residues were 20-50 Hz which corresponded to 8.5-11.2 Å ^{13}C-^{19}F distances. Together with the results that the ^{13}C-^{19}F(C16) distances for these two residues were greater than 14 Å (*cf.* Table 12), it appears that they are located along the longitude between the ^{31}P and ^{19}F(C5) positions in the bilayer (*cf.* Figure 40b).

Table 13 Fitting results for the ^{13}C-^{19}F(C5) experiments.

	d (Hz)	*F*	*r* (Å)	χ^2
α-helical HFPmn-L12	202(16) [a]	0.16(1)	5.2(2)	1.5
α-helical HFPtr-L9	125(8)	0.24(2)	6.1(1)	1.4
β-strand HFPmn-A6	31(2)	0.27(2)	9.7(2)	0.9
β-strand HFPmn-L12	39(2)	0.22(2)	9.0(2)	1.1

[a] The uncertainties are shown in parentheses and were determined by the $\chi^2 = \chi^2_{min}+1$ criterion.

The quantitative distance fitting suggested that (1) for both HFPmn and HFPtr in both secondary structures, there is some deeply-inserted population and (2) for the deeply-inserted population, the HFPtr inserts into the region of phospholipid alkyl chains more deeply compared with the HFPmn. For the α-helical conformation, the HFPtr has a closer contact with ^{19}F(C16) compared with the HFPmn (7.4 Å vs. 10.4 Å for A6, 8.1 Å vs. 11.8 Å for L9 and 6.1 Å vs. 7.2 Å for L12). For the β-strand conformation, the ^{13}CO-^{19}F(C16) distance for Ala6 in HFPmn is greater than 14 Å, while in HFPtr it is 6.9 Å. For Leu9 the ^{13}CO-^{19}F(C16) distance is 8.4 Å for HFPmn vs. 6.8 Å for HFPtr.

Figure 42 displays the spectra at long dephasing time for Ala1, Ile4 and Ala14 of HFPmn and HFPtr, and Figure 43 displays the plots of $(\Delta S/S_0)^{exp}$ for these residues by integrating over the entire ^{13}CO peaks. The α-helical and β-

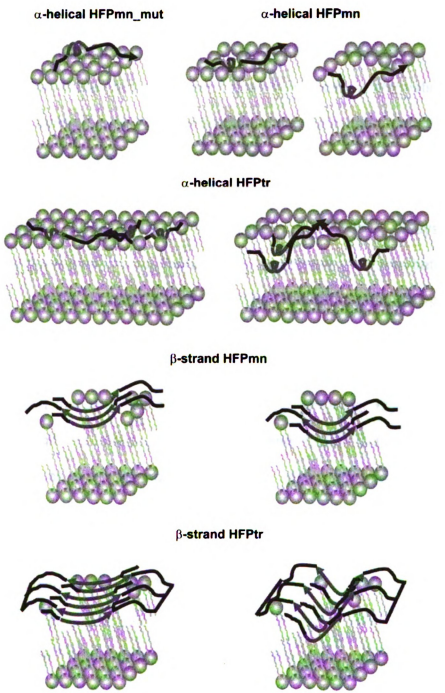

Figure 44 Insertion models for HFPmn_mut, HFPmn and HFPtr and different secondary structures. The lipid headgroups were shown in blue and the alkyl chains were displayed in gray. For the peptides, the residues from Ala6 to Leu12 were shown in red with definitive secondary structures and the other residues were displayed in black. The arrows indicated the direction from N to C terminus.

strand ^{13}CO peaks were not well-separated in the spectra for Ile4 and Ala14, thus we roughly consider that the ^{13}C-^{31}P and ^{13}C-^{19}F(C5) dephasings shown in Figure 43 for these two residues came from both conformations. The experimental build up curves provide qualitative information about whether or not there is close contact between these residues and ^{31}Ps or ^{19}Fs. In general, Ala1 has close contact with ^{31}P and has no contact with either ^{19}F(C5) or ^{19}F(C16) in both constructs, which means the N-terminus of the HFPs is always located close to the phosphate groups. There may be electrostatic attraction between the positively charged peptide N-terminus and the negatively charged lipid phosphate groups, which facilitates this close proximity. For Ile4 and Ala14, there seems to be some contact with ^{31}P and ^{19}F(C5), but not with ^{19}F(C16). These results suggest that both Ile4 and Ala14 in some HFPs are located along the membrane longitudes between positions of ^{31}P and ^{19}F(C5). This will support the model that the peptide backbone in α-helical structure is inserted into the outer leaflet rather than both leaflets. The length of a α-helix from Ile4 to Ala14 is about 16 Å. The longitudinal distance between ^{31}P and ^{19}F(C16) is ~ 22 Å, while the distance between ^{19}F(C5) and ^{19}F(C16) is ~ 13 Å (*cf.* Fig. 40c). Thus if the helix inserted into both leaflets and the ^{13}CO of Ile4 is between ^{31}P and ^{19}F(C5) of the outer leaflet, the ^{13}CO of Ala14 will be close to the ^{19}F(C16), which is inconsistent with the data in Figures 42 and 43.

Figure 44 provides semi-quantitative insertion models for the PC:PG associated HFPmn_mut, HFPmn and HFPtr in the α-helical and β-strand conformations. Comparing with the HFPmn_mut which is non-fusogenic, both the

HFPmn and HFPtr have some population of insertion into the membrane interior, and the membrane insertion is observed in both helical and strand structures. This suggests a positive between the membrane insertion and the fusion activity. The membrane insertion may be correlated with the disruption of the membrane bilayers. Our models suggested that in the hydrophobic region of HFP from Ala1 to Gly16, the N-terminal residue Ala1 and the C-terminal residue Ala14 are closer to the phosphate groups, while the residues in between such as Ala6, Leu9 and Leu12 are closer to the phospholipid alkyl chains. It is reasonable to think that such a "V-type" insertion (*cf.* Figure 44) will induce disruption to the membrane outer leaflet. Comparing with the HFPmn, the HFPtr has a closer contact with the ^{19}F(C16), and may also have a larger deeply-inserted population. Since the HFPtr was known to have a higher fusion activity than the HFPmn,(*14,15*) our results suggest that there is a positive correlation between the fusion activity and the insertion depths as well as the population of deeply inserted peptide. In the previous section focused on the PC:PG:CHOL bound HFPmn_mut, HFPmn and HFPtr, we have proposed that there was a positive correlation between the fusion activity and the membrane insertion depths for the β-strand HFPs. Thus, the fusion activity/membrane insertion depth and population correlation is independent of the membrane composition.

It is interesting to compare the present insertion models for the α-helical HFPs in PC:PG with the previous simulation works with α-helical HFPs in a similar membrane environment. In one simulation which focused on the 16-N-terminal-residue model HFP and its V2E mutant, the wild-type HFP was found to

insert obliquely into the bilayer while the mutant was located on the surface. According to their models, the residues from Ala6 to Leu12 in the wild-type HFP were located 0 – 5 Å below the longitude of the phosphate groups, while for the V2E mutant, these residues were located around the same position as the longitude of the phosphate groups.(*11*) We generally agree with the statement that the wild-type monomer inserts into the bilayer while the mutant is located on the surface. However, the best-fit distances for Ala6, Leu9 and Leu12 suggested that the HFPmn_mut is located 6 -10 Å above the phospholipid groups. The residues Ala6, Leu9 and Leu12 in the surface-located HFPmn are not likely to be below the phosphate layer because all of the three residues are > 14 Å away from the ^{19}F(C5). For the deeply-inserted population, the residues from Ala6 to Leu12 seem to be in a longitudinal position between ^{19}F(C5) and ^{19}F(C16) instead of between ^{31}P and ^{19}F(C5) because Ala6 and Leu9 have contact with ^{19}F(C16) and Leu12 has contact with both ^{19}F(C5) and ^{19}F(C16). In another simulation with the 23-residue HFPmn and its V2E mutant, it has been proposed that the wild-type HFP adopted a predominant fully inserted configuration with the residues Ala6 through Leu12 locating 10-20 Å deeper along the membrane longitude relative to the phosphate group, and the mutant had a predominant transmembrane configuration with Ala6 and Leu12 located 20-30 Å deeper longitude relative to the phosphate group.(*12*) Our results do not support the transmembrane configuration for the HFPmn_mut. A fraction of the HFPmn has a deep insertion into the region of membrane alkyl chains. However, our results seem to agree more with the insertion into the outer leaflet where the peptide

only contacts the alkyl chains in one leaflet, rather than a fully inserted model where the peptide has contact with the alkyl chains in both leaflets.

CONCLUSION

In this chapter, we described the studies of the membrane insertion of three different HFP constructs in two different biologically relevant membranes, PC:PG which reflects the relative ratio between the phospholipids with neutral and negatively charged headgroups in the host cells and PC:PG:CHOL which reflects the ratio of phospholipids:cholesterol in HIV-infected host cells. The membrane location of these constructs is correlated with their different abilities to induce vesicle fusion. These studies provide experimentally-based semi-quantitative models for the membrane locations of the HFPmn_mut, HFPmn and HFPtr in both α-helical and β-strand conformations. These models suggested that the residues from Ala6 to Leu12 had the greatest tendency to insert into the bilayer interior, regardless of the secondary structure. For the V2E-mutated HFPmn, the residues from Ala1 to Ala14 are located 6-10 Å higher relative to the longitude of the phosphate groups. Together with the stopped-flow fluorescence studies, we propose that there is a positive correlation between the fusion activity and the membrane insertion tendency and depth for the HFPs, i.e. membrane insertion is a requirement for a HFP construct to become fusogenic and a HFP construct with greater fusion activity will have greater inserted population with greater insertion depth. It is reasonable to correlate the population of insertion and the insertion depth to the membrane disruption induced by the HFP. Thus,

our results may further suggest a positive correlation between the fusion activity of HFPs and their abilities to disrupt the membrane bilayer.

REFERENCE

1. Staffs, N. a. E., New Hope in HIV Disease. *Science* **1996,** 274, 1988-1991.

2. Weissenhorn, W.; Dessen, A.; Harrison, S. C.; Skehel, J. J.; Wiley, D. C., Atomic structure of the ectodomain from HIV-1 gp41. *Nature* **1997,** 387, (6631), 426-430.

3. Jaroniec, C. P.; Kaufman, J. D.; Stahl, S. J.; Viard, M.; Blumenthal, R.; Wingfield, P. T.; Bax, A., Structure and dynamics of micelle-associated human immunodeficiency virus gp41 fusion domain. *Biochemistry* **2005,** 44, (49), 16167-16180.

4. Chang, D. K.; Cheng, S. F.; Chien, W. J., The amino-terminal fusion domain peptide of human immunodeficiency virus type 1 gp41 inserts into the sodium dodecyl sulfate micelle primarily as a helix with a conserved glycine at the micelle-water interface. *J. Virol.* **1997,** 71, (9), 6593-6602.

5. Morris, K. F.; Gao, X. F.; Wong, T. C., The interactions of the HIV gp41 fusion peptides with zwitterionic membrane mimics determined by NMR spectroscopy. *Biochim. Biophys. Acta-Biomembr.* **2004,** 1667, (1), 67-81.

6. Li, Y. L., AND Tamm, L.K., Structure and Plasticity of the Human Immunodeficiency Virus gp41 Fusion Domain in Lipid Micelles and Bilayers. *Biophys. J.* **2007,** 93, (3), 876-885.

7. Gabrys, C. M., and Weliky, D.P., Chemical Shift Assignment and Structural Plasticity of a HIV Fusion Peptide Derivative in Dodecylphosphocholine Micelles. *BBA-Biomembranes* **2007,** 1768, 3225-3234.

8. Agirre, A.; Flach, C.; Goni, F. M.; Mendelsohn, R.; Valpuesta, J. M.; Wu, F. J.; Nieva, J. L., Interactions of the HIV-1 fusion peptide with large unilamellar vesicles and monolayers. A cryo-TEM and spectroscopic study. *Biochimica Et Biophysica Acta-Biomembranes* **2000,** 1467, (1), 153-164.

9. Haque, M. E.; Koppaka, V.; Axelsen, P. H.; Lentz, B. R., Properties and structures of the influenza and HIV fusion peptides on lipid membranes: Implications for a role in fusion. *Biophys. J.* **2005,** 89, (5), 3183-3194.

10. Gordon, L. M.; Curtain, C. C.; Zhong, Y. C.; Kirkpatrick, A.; Mobley, P. W.; Waring, A. J., The amino-terminal peptide of HIV-1 glycoprotein 41 interacts with human erythrocyte membranes: peptide conformation, orientation and aggregation. *Biochim. Biophys. Acta* **1992,** 1139, (4), 257-274.

11. Kamath, S.; Wong, T. C., Membrane structure of the human immunodeficiency virus gp41 fusion domain by molecular dynamics simulation. *Biophys. J.* **2002,** 83, (1), 135-143.
12. Maddox, M. W.; Longo, M. L., Conformational partitioning of the fusion peptide of HIV-1 gp41 and its structural analogs in bilayer membranes. *Biophys. J.* **2002,** 83, (6), 3088-3096.

13. Kliger, Y.; Aharoni, A.; Rapaport, D.; Jones, P.; Blumenthal, R.; Shai, Y., Fusion peptides derived from the HIV type 1 glycoprotein 41 associate within phospholipid membranes and inhibit cell-cell Fusion. Structure- function study. *J. Biol. Chem.* **1997,** 272, (21), 13496-13505.

14. Yang, R.; Prorok, M.; Castellino, F. J.; Weliky, D. P., A trimeric HIV-1 fusion peptide construct which does not self-associate in aqueous solution and which has 15-fold higher membrane fusion rate. *J. Am. Chem. Soc.* **2004,** 126, (45), 14722-14723.

15. Qiang, W., and Weilky, D.P., HIV Fusion Peptide and Its Cross-Linked Oligomers: Efficient Syntheses, Significance of the Trimer in Fusion Activity, Correlation of β Strand Conformation with Membrane Cholesterol, and Proximity to Lipid Headgroups. *Biochemistry* **2009,** 48, (2), 289-301.

16. Caffrey, M.; Cai, M.; Kaufman, J.; Stahl, S. J.; Wingfield, P. T.; Covell, D. G.; Gronenborn, A. M.; Clore, G. M., Three-dimensional solution structure of the 44 kDa ectodomain of SIV gp41. *EMBO J.* **1998,** 17, (16), 4572-4584.

17. Qiang, W., Yang, J., and Weliky, D.P., Solid-state nuclear magnetic resonance measurements of HIV fusion peptide to lipid distances reveal the intimate contact of beta strand peptide with membranes and the proximity of the Ala-14-Gly-16 region with lipid headgroups. *Biochemistry* **2007,** 46, (17), 4997-5008.

18. Qiang, W., Sun, Y., and Weliky, D.P., A strong correlation between fusogenicity and membrane insertion depth of the HIV fusion peptide. *submitted to Proc. Natl. Acad. Sci. USA.*

19. Qiang, W., and Weilky, D.P., unpublished experiments.

20. Chan, W. C., and White, P.D., *Fmoc Solid Phase Peptide Synthesis: A Practical Approach* **2000**, 94-109.

21. Yang, R.; Yang, J.; Weliky, D. P., Synthesis, enhanced fusogenicity, and solid state NMR measurements of cross-linked HIV-1 fusion peptides. *Biochemistry* **2003,** 42, (12), 3527-3535.

22. Struck, D. K.; Hoekstra, D.; Pagano, R. E., Use of resonance energy transfer to monitor membrane fusion. *Biochemistry* **1981,** 20, (14), 4093-9.

23. Aloia, R. C.; Tian, H.; Jensen, F. C., Lipid composition and fluidity of the human immunodeficiency virus envelope and host cell plasma membranes. *Proc. Natl. Acad. Sci. U.S.A.* **1993,** 90, (11), 5181-5185.

24. Brugger, B.; Glass, B.; Haberkant, P.; Leibrecht, I.; Wieland, F. T.; Krasslich, H. G., The HIV lipidome: A raft with an unusual composition. *Proc. Natl. Acad. Sci. U.S.A.* **2006,** 103, (8), 2641-2646.

25. Venable, R. M., Brooks, B.R., and Pastor, R.W., Molecular dynamics simulations of gel ($L\beta_I$) phase lipid bilayers in constant pressure and constant surface area ensembles. *J. Chem. Phys* **2000,** 112, 4822-4832.

26. McDonough, B.; Macdonald, P. M.; Sykes, B. D.; McElhaney, R. N., F-19 Nuclear Magnetic-Resonance Studies of Lipid Fatty Acyl Chain Order and Dynamics in Acholeplasma-Laidlawii B Membranes - a Physical, Biochemical, and Biological Evaluation of Monofluoropalmitic Acids As Membrane Probes. *Biochemistry* **1983,** 22, (22), 5097-5103.

27. Birdsall, N. J., Lee, A.G., Levine, Y.K., and Metcalfe, J.C., 19F NMR of monofluorostearic acids in lecithin vesicles. *Biochim. Biophys. Acta.* **1971,** 241, 693-696.

28. Sibi, M. P., Rutherford, D., and Sharma, R., A new electrophilic alaninol synthon. A general route to oxazolidinones of D or (R)-2-amino alcohols form L-serine. *J. Chem. Soc. Perkin. Trans.* **1994,** 1, 1675-1678.

29. Jackson, R. F. W., and Perez-Gonzalez, M., Synthesis of N-(tert-butoxycarbonyl)-beta-iodoalanine methyl ester: A useful building block in the synthesis of nonnatural alpha-amino acids via palladium catalyzed cross coupling reaactions. *Org. Syntheses* **2005,** 81, 77-81.

30. Lang, L. X., Jagoda, E., Ma, Y., Sassaman, M.B., and Eckelman, W.C., Synthesis and in vivo biodistribution of F-18 labeled 3-cis-, 3-trans-, 4-cis-, and 4-trans-fluorocyclohexane derivatives of WAY 100635. *Bioorganic & Medicinal Chemistry* **2006,** 14, 3737-3748.

31. Hirsh, D. J., Lazaro, N., Wright, L.R., Boggs, J.M., McIntosh, T.J., Schaefer, J., and Blazyk, J., A new monofluorinated phosphatidylcholine forms interdigitated bilayers. *Biophys. J.* **1998,** 75, (4), 1858-1868.

32. Mueller, K. T., Analytical Solutions for the Time Evolution of Dipolar-dephasing NMR Signals. *Journal of Magnetic Resonance Series A* **1995,** 113, (1), 81-93.

33. Zhang, H. Y.; Neal, S.; Wishart, D. S., RefDB: A database of uniformly referenced protein chemical shifts. *J. Biomol. NMR* **2003,** 25, (3), 173-195.

34. Yang, J.; Gabrys, C. M.; Weliky, D. P., Solid-state nuclear magnetic resonance evidence for an extended beta strand conformation of the membrane-bound HIV-1 fusion peptide. *Biochemistry* **2001,** 40, (27), 8126-8137.

35. Bodner, M. L., *Solid state nuclear magnetic resonance of the HIV-1 and influenza fusion peptides associated with membranes.* Ph. D. thesis, Michigan State University: East Lansing, 2006; p 122.

36. Zheng, Z., Yang, R., Bodner, M.L., and Weliky, D.P., Conformational flexibility and strand arrantments of the membrane-associated HIV fusion peptide trimer probed by solid-state NMR spectroscopy. *Biochemistry* **2006,** 45, 12960-12975.

37. Yang, J.; Parkanzky, P. D.; Khunte, B. A.; Canlas, C. G.; Yang, R.; Gabrys, C. M.; Weliky, D. P., Solid state NMR measurements of conformation and conformational distributions in the membrane-bound HIV-1 fusion peptide. *J. Mol. Graph. Model.* **2001,** 19, (1), 129-135.

38. Wasniewski, C. M.; Parkanzky, P. D.; Bodner, M. L.; Weliky, D. P., Solid-state nuclear magnetic resonance studies of HIV and influenza fusion peptide orientations in membrane bilayers using stacked glass plate samples. *Chem. Phys. Lipids* **2004,** 132, (1), 89-100.

39. Yang, J.; Prorok, M.; Castellino, F. J.; Weliky, D. P., Oligomeric beta structure of the membrane-bound HIV-1 fusion peptide formed from soluble monomers. *Biophys. J.* **2004,** 87, 1951-1963.

40. Bodner, M. L.; Gabrys, C. M.; Parkanzky, P. D.; Yang, J.; Duskin, C. A.; Weliky, D. P., Temperature dependence and resonance assignment of ^{13}C NMR spectra of selectively and uniformly labeled fusion peptides associated with membranes. *Magn. Reson. Chem.* **2004,** 42, 187-194.

41. Zheng, Z., Qiang, W., and Weliky, D.P., Investigation of finite-pulse radiofrequency-driven recoupling methods for measurement of intercarbonyl distances in polycrystalline and membrane-associated HIV fusion peptide samples. *Magn. Reson. Chem.* **2007,** 245, S247-S260.

42. Bevington, P. R.; Robinson, D. K., *Data Reduction and Error Analysis for the Physical Sciences.* 2nd ed.; McGraw-Hill: Boston, 1992; p 38-52.

43. Qiang, W., Bodner, M.L., and Weilky, D.P., Solid-state NMR Spectroscopy of HIV Fusion Peptides Associated with Host-Cell-Like Membranes: 2D Correlation Spectra and Distance Measurements Support a Fully Extended

Conformation and Models for Specific Antiparallel Strand Registries. *J. Am. Chem. Soc.* **2008,** 130, 5459-5471.

44. Yang, J.; Weliky, D. P., Solid state nuclear magnetic resonance evidence for parallel and antiparallel strand arrangements in the membrane-associated HIV-1 fusion peptide. *Biochemistry* **2003,** 42, 11879-11890.

45. Gordon, L. M.; Mobley, P. W.; Pilpa, R.; Sherman, M. A.; Waring, A. J., Conformational mapping of the N-terminal peptide of HIV-1 gp41 in membrane environments using ^{13}C-enhanced Fourier transform infrared spectroscopy. *Biochim. Biophys. Acta-Biomembr.* **2002,** 1559, (2), 96-120.

46. Castano, S.; Desbat, B., Structure and orientation study of fusion peptide FP23 of gp41 from HIV-1 alone or inserted into various lipid membrane models (mono-, bi- and multibi-layers) by FT-IR spectroscopies and Brewster angle microscopy. *Biochim. Biophys. Acta-Biomembr.* **2005,** 1715, (2), 81-95.

47. Sackett, K.; Shai, Y., The HIV fusion peptide adopts intermolecular parallel β-sheet structure in membranes when stabilized by the adjacent N-terminal heptad repeat: A ^{13}C FTIR study. *J. Mol. Biol.* **2005,** 350, (4), 790-805.

48. Chan, D. C.; Fass, D.; Berger, J. M.; Kim, P. S., Core structure of gp41 from the HIV envelope glycoprotein. *Cell* **1997,** 89, (2), 263-273.

49. Tan, K.; Liu, J.; Wang, J.; Shen, S.; Lu, M., Atomic structure of a thermostable subdomain of HIV-1 gp41. *Proc. Natl. Acad. Sci. U.S.A.* **1997,** 94, (23), 12303-12308.

50. Yang, Z. N.; Mueser, T. C.; Kaufman, J.; Stahl, S. J.; Wingfield, P. T.; Hyde, C. C., The crystal structure of the SIV gp41 ectodomain at 1.47 A resolution. *J. Struct. Biol.* **1999,** 126, (2), 131-144.

51. Macosko, J. C.; Kim, C. H.; Shin, Y. K., The membrane topology of the fusion peptide region of influenza hemagglutinin determined by spin-labeling EPR. *J. Mol. Biol.* **1997,** 267, (5), 1139-1148.

52. Han, X.; Bushweller, J. H.; Cafiso, D. S.; Tamm, L. K., Membrane structure and fusion-triggering conformational change of the fusion domain from influenza hemagglutinin. *Nat. Struct. Biol.* **2001,** 8, (8), 715-720.

53. Modis, Y.; Ogata, S.; Clements, D.; Harrison, S. C., Structure of the dengue virus envelope protein after membrane fusion. *Nature* **2004,** 427, (6972), 313-319.

54. Gibbons, D. L.; Vaney, M. C.; Roussel, A.; Vigouroux, A.; Reilly, B.; Lepault, J.; Kielian, M.; Rey, F. A., Conformational change and protein protein

interactions of the fusion protein of Semliki Forest virus. *Nature* **2004,** 427, (6972), 320-325.

55. Roche, S., Bressanelli, S., Rey, F.A., and Gaudin, Y., Crystal Structure of the low-pH form of the vesicular stomatitis virus glycoprotein G. *Science* **2006,** 313, 187-191.

56. Heldwein, E. E., Lou, H., Bender, F.C., Cohen, G.H., Eisenberg, R.J., and Harrison, S.C., Crystal Structure of glycoprotein B from herpes simplex virus 1. *Science* **2006,** 313, 217-220.

57. Hessa, T., Kim, H., Bihlmaier, K., Lundin, C., Boekel, J., Andersson, H., Nilsson, I., White, S.H., and Heijne, G., Recognition of tranmembrane helices by the endoplasmic reticulum translocon. *Nature* **2005,** 433, 377-381.

58. Toke, O.; Maloy, W. L.; Kim, S. J.; Blazyk, J.; Schaefer, J., Secondary structure and lipid contact of a peptide antibiotic in phospholipid Bilayers by REDOR. *Biophys. J.* **2004,** 87, (1), 662-674.

59. Charloteaux, B., Lorin, A., Crowet, J.M., Stroobant, V., Lins, L., Thomas, A., and Brasseur, R., The N-terminal 12 residue long peptide of HIV gp41 is the minimal peptide sufficient to induce significant T-cell-like membrane destablization in vitro. *J. Mol. Biol.* **2006,** 359, 597-609.

60. Chang, D. K.; Cheng, S. F., Determination of the equilibrium micelle-inserting position of the fusion peptide of gp41 of human immunodeficiency virus type 1 at amino acid resolution by exchange broadening of amide proton resonances. *J. Biomol. NMR* **1998,** 12, (4), 549-552.

61. Langham, A.; Kaznessis, Y., Simulation of the N-terminus of HIV-1 glycoprotein 41000 fusion peptide in micelles. *J. Pept. Sci.* **2005,** 11, (4), 215-224.

62. Bloom, M.; Evans, E.; Mouritsen, O. G., Physical properties of the fluid lipid-bilayer component of cell membranes: a perspective. *Quat. Rev. Biophys.* **1991,** 24, (3), 293-397.

63. Nir, S., and Nieva, J.L., Interaction of peptides with liposomes: pore formation and fusion. *Prog. Lipid Res.* **2000,** 39, 181-206.

64. White, J. M., Delos, S.E., Brecher, M., and Schornberg, K., Structures and mechanisms of viral membrane fusion proteins: Multiple variations on a common theme. *Crit. Rev. Biochem. Mol. Biol.* **2008,** 43, 189-219.

65. Freed, E. O.; Delwart, E. L.; Buchschacher, G. L., Jr.; Panganiban, A. T., A mutation in the human immunodeficiency virus type 1 transmembrane

glycoprotein gp41 dominantly interferes with fusion and infectivity. *Proc. Natl. Acad. Sci. U.S.A.* **1992,** 89, (1), 70-74.

66. Jaroniec, C. P.; Tounge, B. A.; Herzfeld, J.; Griffin, R. G., Frequency selective heteronuclear dipolar recoupling in rotating solids: Accurate ^{13}C-^{15}N distance measurements in uniformly ^{13}C, ^{15}N-labeled peptides. *J. Am. Chem. Soc.* **2001**, 123, (15), 3507-3519.

67. Nieva, J. L.; Nir, S.; Muga, A.; Goni, F. M.; Wilschut, J., Interaction of the HIV-1 fusion peptide with phospholipid vesicles: different structural requirements for fusion and leakage. *Biochemistry* **1994,** 33, (11), 3201-3209.

68. Reichert, J., Grasnick, D., Afonin, S., Buerck, J., Wadhwani, P., and Ulrich, A.S., A critical evaluation of the conformational requirements of fusogenic peptides in membranes. *European Biophysics Journal with Biophysics Letters* **2007,** 36, (4-5), 405-413.

69. Sackett, K., and Weliky, D.P., Unpublished experiments.

CHAPTER VII

SUMMARY AND FUTURE WORK

The overall goal of this project is to understand the HIV-induced membrane fusion mechanism from the atomic-resolution structural point of view. The HIV fusion peptide was used as a model peptide for the entire fusion protein gp41 to provide insights into structure and membrane insertion. My specific goals included the measurements of structure for the membrane associated HIV fusion peptides and the detection of the HFP-membrane interaction. A summary of the conclusions for my studies: **(1)** The HFP trimer has been considered as a biologically relevant construct for HFPs based on the structure of the soluble part of gp41, and my study provided a feasible approach to chemically synthesize the HFPtr. This improved synthetic scheme utilized the cross-linking of C-terminal lysines and cysteines to buildup a trimeric scaffold. With the optimized experimental conditions described in Chapter II, the overall yield has been increased by at least a factor of three and the purity has also been greatly improved.(*1,2*) In addition, the method to buildup the trimeric scaffold should be applicable to the synthesis of other hetero- or homo-trimers. **(2)** The structures of membrane-associated HFPs have been studied using solid-state NMR methods, in particular, the secondary structures of HFPmn, HFPdm and HFPtr in both cholesterol-containing and non-cholesterol-containing membranes, and the tertiary structure of HFPmn in cholesterol-containing membrane. The population of β-strand conformations is correlated with the membrane cholesterol. There

was not an obvious dependence of secondary structure on cross-linking. Since there had been shown a positive correlation between the extent of cross-linking and the fusion activity of different HFP constructs,(*1*) it did not seem that the fusion activity can be correlated with the secondary structure. The tertiary structure of HFPmn in cholesterol-containing membrane has been studied using ^{13}C-^{15}N REDOR experiments, and the results supported two specific anti-parallel β-sheet registries. **(3)** The membrane location of HFPs has also been studied mainly with ^{13}C-^{31}P and ^{13}C-^{19}F REDOR methods. A systematic distance measurement method has been developed to detect the distances between the backbones of a series of singly-^{13}CO labeled peptides and different positions in lipid bilayers such as ^{31}P and ^{19}F in the fluorinated phospholipids 5-^{19}F-DPPC and 16-^{19}F-DPPC. The studies concluded that HFPs with both α-helical and β-strand conformations can insert into the membrane bilayer interior. The N-terminus was always located close to the lipid phosphate groups while the hydrophobic middle regions of HFP, e.g. Ala6 to Leu12 are more likely to be located close to the phospholipid alkyl chains in a single leaflet. The cross-linked HFPs such as HFPtr inserted more deeply and may have larger deeply-inserted population compared with the HFPmn.

It is important to have local membrane disruption to induce membrane fusion.(*3*) Our model proposed in chapter VI suggested that the membrane disruption can be caused by the insertion of HFPs into the phospholipid alkyl chains of the membrane outer leaflet. There is a positive correlation between the membrane insertion depth and population and the ability to fuse the vesicles for

different HFP constructs, and the correlation is independent of the secondary structure of HFPs. From the methodology point of view, the systematic measurement of membrane location of the peptide backbone ^{13}COs provides atomic resolution information about membrane insertion of the HIV fusion peptides. The method should be in principle applicable to other membrane associated peptides where commonly used structural characterization methods such as solution NMR and X-ray crystallography are not applicable. However, this method may be better applied to a small β-sheet oligomeric peptide/protein system than to a larger β-sheet oligomeric peptide/protein system because in the latter case most of the labeled ^{13}Cs will be located in the center of the β-sheet and will be far away from any region of the membrane.

The experimental results provide insights for understanding the HIV-induced membrane fusion mechanism. It has been proposed previously that both the assembly of HFPs and the membrane disruption caused by HFPs could be pre-requisites for membrane fusion.(*3*) Overall, my research contributes to the fusion mechanism by studying whether the structure and membrane insertion could potentially be important to affect the fusion activity of the HFP.

First of all, the secondary structure does not seem to be a crucial factor to affect the fusion activity because there is not an obvious correlation between the secondary structures and the fusion activities for HFPs with different extents of cross-linking.

Second, it had been proposed that the V2E mutant was non-fusogenic because the substitution of Val2 to Glu2 prevented the formation of fusion active

assembly of HFPs.(*4*) My work for the first time demonstrated that HFPmn in host-cell like membrane environments will adopt anti-parallel β-sheet structure with at least two registries. In addition, the work provided a general approach to detect the registries for β-sheet structures. The tertiary structure may be important for HFP to induce fusion. It will be interesting to investigate whether there are certain registries associated with the non-fusogenic HFPmn_mut and whether there are some other assembly patterns associated with the highly-fusogenic HFPtr.

Third, the membrane insertion studies clearly showed that there is a positive correlation between the membrane insertion depths of different HFP constructs and the fusion activities of these HFPs. There may also be a positive correlation between the deeply-inserted population and the fusion activity of these HFPs. With the reasonable hypothesis that the insertion would induce membrane disruption, our results may suggest that there is a positive correlation between the ability to disrupt the membrane and the ability of fuse the membranes for different HFP constructs. The distance measurements also demonstrated that the most hydrophobic region of HFPs insert into the membrane, i.e. starting from around Ala6 and ending at around Leu12.

The ultimate goal of the project is to understand the fusion mechanism induced by the gp41 from the structural point of view. Large proteins can be expressed with amino acid-type ^{13}CO and ^{15}N labelings.(*5*) This will bring up a problem if one would like to apply the ^{13}C-^{31}P or ^{13}C-^{19}F REDOR distance measurements to the membrane-associated protein systems. Since the isotope

labels are on all residues of a particular amino acid type rather than on a singly labeled residue, the ^{13}C signals from all labeled residues will be generated during the cross polarization (CP) period. In order to solve the problem, the regular CP has to be replaced by a double cross polarization (DCP) sequence where the ^{13}C magnetization is generated through the route $^{1}H \rightarrow {}^{15}N \rightarrow {}^{13}C$.(*6*) Consequently, the only observable ^{13}C label at the end of DCP period will be the one with an adjacent ^{15}N label. This modification will help to filter out the natural abundance ^{13}C and the other isotopically labeled residues. The DCP building block can then be incorporated into other distance measurement pulse sequences such as ^{13}C-^{31}P REDOR and the modified pulse sequence can be used for the protein samples.

Another interesting future direction will be to apply the ^{13}C-^{15}N REDOR methods to other HFP constructs such as HFPtr or HFPmn_mut to study the possible tertiary structures such as anti-parallel β-sheet registries or parallel β-sheet registries. The predominant tertiary structure for these constructs can then be compared with the predominant 16 or 17-residue-overlapped anti-parallel β-sheet for HFPmn, and the results may provide insight on whether there is a correlation between the tertiary structure and the fusion activity for different HFP constructs.

REFERENCE

1. Yang, R.; Prorok, M.; Castellino, F. J.; Weliky, D. P., A trimeric HIV-1 fusion peptide construct which does not self-associate in aqueous solution and which has 15-fold higher membrane fusion rate. *J. Am. Chem. Soc.* **2004,** 126, (45), 14722-14723.

2. Yang, R.; Yang, J.; Weliky, D. P., Synthesis, enhanced fusogenicity, and solid state NMR measurements of cross-linked HIV-1 fusion peptides. *Biochemistry* **2003,** 42, (12), 3527-3535.

3. Nir, S., and Nieva, J.L., Interaction of peptides with liposomes: pore formation and fusion. *Prog. Lipid Res.* **2000,** 39, 181-206.

4. Freed, E. O.; Delwart, E. L.; Buchschacher, G. L., Jr.; Panganiban, A. T., A mutation in the human immunodeficiency virus type 1 transmembrane glycoprotein gp41 dominantly interferes with fusion and infectivity. *Proc. Natl. Acad. Sci. U.S.A.* **1992,** 89, (1), 70-74.

5. Curtis-Fisk, J., Spencer, R.M., and Weliky, D.P., Isotopically Labeled Expression in *E. coli*, Purification, and Refolding of the Full Ectodomain of the Influenza Virus Membrane Fusion Protein. *Protein Expression and Purification*, **2008**, 61, 212-219.

6. Baldus, M.; Petkova, A. T.; Herzfeld, J.; Griffin, R. G., Cross polarization in the tilted frame: assignment and spectral simplification in heteronuclear spin systems. *Molecular Physics* **1998,** 95, (6), 1197-1207.

APPENDIX 1. NMR FILES CHECKLIST

Figure 14 2D PDSD experiments @ ../home/wei4b/data/2D-PDSD/

HFPmn in PC:PG (HFPmn-PCPG-50ms)

HFPdm in PC:PG (HFPdm-PCPG-50ms)

HFPtr in PC:PG (HFPtr-PCPG-50ms)

HFPmn in PC:PG:CHOL (HFPmn-PCPGCHOL-50ms)

HFPdm in PC:PG:CHOL (HFPdm-PCPGCHOL-50ms)

HFPtr in PC:PG:CHOL (HFPtr-PCPGCHOL-50ms)

Figure 18 1D ^{13}C-^{15}N REDOR experiments @../home/wei4b/data/13C-15N-REDOR

A14(^{13}C)-V2(^{15}N) HFPmn in PC:PG:CHOL (13C-15N-A14-V2)

A14(^{13}C)-G3(^{15}N) HFPmn in PC:PG:CHOL (13C-15N-A14-G3-new)

A14(^{13}C)-I4(^{15}N) HFPmn in PC:PG:CHOL (13C-15N-A14-I4)

A14(^{13}C)-G5(^{15}N) HFPmn in PC:PG:CHOL (13C-15N-A14-G5-new)

1D ^{13}C-^{31}P REDOR experiments @../home/wei4b/data/13C-31P

Figure 18 A1V2G3(^{13}C) HFPmn in PC:PG (FPmnK3-A1V2G3)

A1V2G3(^{13}C) HFPmn in PC:PG:CHOL (FPmnK3-A1V2G3-CHOL)

Figures 26 and 27 G5A6L7(^{13}C) HFPmn in PC:PG (FPmnK3-G5A6L7-PCPG)

G5A6L7(^{13}C) HFPmn in PC:PG:CHOL (FPmnK3-G5A6L7-chol)

F8L9G10(^{13}C) HFPmn in PC:PG (FPmn-F8L9G10-PCPG)

F8L9G10(^{13}C) HFPmn in PC:PG:CHOL (FPmn-F8L9G10-chol)

F11L12G13(^{13}C) HFPmn in PC:PG (FPmnK3-F11L12G13-PCPG)

F11L12G13(^{13}C) HFPmn in PC:PG:CHOL (FPmnK3-F11L12G13-chol)

A14A15G16(^{13}C) HFPmn in PC:PG (FPmnK3-A14A15G16-PCPG)

A14A15G16(^{13}C) HFPmn in PC:PG:CHOL (FPmnK3-A14A15G16-chol)

The following spectra were displayed in Figures 30, 33, 35, 38 and 41 with detailed

names described in the corresponding figure captions.

A1(^{13}C) HFPmn in PC:PG (HFPmn-A1-PCPG)

A1(^{13}C) HFPmn in PC:PG:CHOL (HFPmn-A1-chol)

I4(^{13}C) HFPmn in PC:PG (HFPmn-I4-PCPG)

I4(^{13}C) HFPmn in PC:PG:CHOL (HFPmn-I4-chol)

A6(^{13}C) HFPmn in PC:PG (HFPmn-A6-PCPG)

A6(^{13}C) HFPmn in PC:PG:CHOL (HFPmn-A6-chol)

L9(^{13}C) HFPmn in PC:PG (HFPmn-L9-PCPG)

L9(^{13}C) HFPmn in PC:PG:CHOL (HFPmn-L9-chol)

L12(^{13}C) HFPmn in PC:PG (HFPmn-L12-PCPG)

L12(^{13}C) HFPmn in PC:PG:CHOL (HFPmn-L12-chol)

A14(^{13}C) HFPmn in PC:PG (HFPmn-A14-PCPG)

A14(^{13}C) HFPmn in PC:PG:CHOL (HFPmn-A14-chol)

A15(^{13}C) HFPmn in PC:PG (HFPmn-A15-PCPG)

A15(^{13}C) HFPmn in PC:PG:CHOL (HFPmn-A15-chol)

A1(^{13}C) HFPmn_mut in PC:PG (HFPmnmut-A1-PCPG)

A1(^{13}C) HFPmn_mut in PC:PG:CHOL (HFPmnmut-A1-chol)

I4(^{13}C) HFPmn_mut in PC:PG (HFPmnmut-I4-PCPG)

I4(^{13}C) HFPmn_mut in PC:PG:CHOL (HFPmnmut-I4-chol)

A6(^{13}C) HFPmn_mut in PC:PG (HFPmnmut-A6-PCPG)

A6(^{13}C) HFPmn_mut in PC:PG:CHOL (HFPmnmut-A6-chol)

L9(^{13}C) HFPmn_mut in PC:PG (HFPmnmut-L9-PCPG)

L9(^{13}C) HFPmn_mut in PC:PG:CHOL (HFPmnmut-L9-chol)

L12(^{13}C) HFPmn_mut in PC:PG (HFPmnmut-L12-PCPG)

L12(^{13}C) HFPmn_mut in PC:PG:CHOL (HFPmnmut-L12-chol)

A14(^{13}C) HFPmn_mut in PC:PG (HFPmnmut-A14-PCPG)

A14(^{13}C) HFPmn_mut in PC:PG:CHOL (HFPmnmut-A14-chol)

A1(^{13}C) HFPtr in PC:PG (HFPtr-A1-PCPG)

A1(^{13}C) HFPtr in PC:PG:CHOL (HFPtr-A1-chol)

I4(^{13}C) HFPtr in PC:PG (HFPtr-I4-PCPG)

I4(^{13}C) HFPtr in PC:PG:CHOL (HFPtr-I4-chol)

A6(^{13}C) HFPtr in PC:PG (HFPtr-A6-PCPG)

A6(^{13}C) HFPtr in PC:PG:CHOL (HFPtr-A6-chol)

L9(^{13}C) HFPtr in PC:PG (HFPtr-L9-PCPG)

L9(^{13}C) HFPtr in PC:PG:CHOL (HFPtr-L9-chol)

L12(^{13}C) HFPtr in PC:PG (HFPtr-L12-PCPG)

L12(^{13}C) HFPtr in PC:PG:CHOL (HFPtr-L12-chol)

A14(^{13}C) HFPtr in PC:PG (HFPtr-A14-PCPG)

A14(^{13}C) HFPtr in PC:PG:CHOL (HFPtr-A14-chol)

1D ^{13}C-^{19}F(C16) REDOR experiments @../home/wei4b/data/13C-19F(C16)

A1(^{13}C) HFPmn in PC:PG (HFPmn-A1-PCPG)

A1(^{13}C) HFPmn in PC:PG:CHOL (HFPmn-A1-chol)

I4(^{13}C) HFPmn in PC:PG (HFPmn-I4-PCPG)

I4(^{13}C) HFPmn in PC:PG:CHOL (HFPmn-I4-chol)

A6(^{13}C) HFPmn in PC:PG (HFPmn-A6-PCPG)

A6(^{13}C) HFPmn in PC:PG:CHOL (HFPmn-A6-chol)

L9(^{13}C) HFPmn in PC:PG (HFPmn-L9-PCPG)

L9(^{13}C) HFPmn in PC:PG:CHOL (HFPmn-L9-chol)

L12(^{13}C) HFPmn in PC:PG (HFPmn-L12-PCPG)

L12(^{13}C) HFPmn in PC:PG:CHOL (HFPmn-L12-chol)

A14(^{13}C) HFPmn in PC:PG (HFPmn-A14-PCPG)

A14(^{13}C) HFPmn in PC:PG:CHOL (HFPmn-A14-chol)

A1(^{13}C) HFPmn_mut in PC:PG (HFPmnmut-A1-PCPG)

A1(^{13}C) HFPmn_mut in PC:PG:CHOL (HFPmnmut-A1-chol)

I4(^{13}C) HFPmn_mut in PC:PG (HFPmnmut-I4-PCPG)

I4(^{13}C) HFPmn_mut in PC:PG:CHOL (HFPmnmut-I4-chol)

A6(^{13}C) HFPmn_mut in PC:PG (HFPmnmut-A6-PCPG)

A6(^{13}C) HFPmn_mut in PC:PG:CHOL (HFPmnmut-A6-chol)

L9(^{13}C) HFPmn_mut in PC:PG (HFPmnmut-L9-PCPG)

L9(^{13}C) HFPmn_mut in PC:PG:CHOL (HFPmnmut-L9-chol)

L12(^{13}C) HFPmn_mut in PC:PG (HFPmnmut-L12-PCPG)

L12(^{13}C) HFPmn_mut in PC:PG:CHOL (HFPmnmut-L12-chol)

A14(^{13}C) HFPmn_mut in PC:PG (HFPmnmut-A14-PCPG)

A14(^{13}C) HFPmn_mut in PC:PG:CHOL (HFPmnmut-A14-chol)

A1(^{13}C) HFPtr in PC:PG (HFPtr-A1-PCPG)

A1(^{13}C) HFPtr in PC:PG:CHOL (HFPtr-A1-chol)

I4(^{13}C) HFPtr in PC:PG (HFPtr-I4-PCPG)

I4(^{13}C) HFPtr in PC:PG:CHOL (HFPtr-I4-chol)

A6(^{13}C) HFPtr in PC:PG (HFPtr-A6-PCPG)

A6(^{13}C) HFPtr in PC:PG:CHOL (HFPtr-A6-chol)

L9(^{13}C) HFPtr in PC:PG (HFPtr-L9-PCPG)

L9(^{13}C) HFPtr in PC:PG:CHOL (HFPtr-L9-chol)

L12(^{13}C) HFPtr in PC:PG (HFPtr-L12-PCPG)

L12(^{13}C) HFPtr in PC:PG:CHOL (HFPtr-L12-chol)

A14(^{13}C) HFPtr in PC:PG (HFPtr-A14-PCPG)

A14(^{13}C) HFPtr in PC:PG:CHOL (HFPtr-A14-chol)

1D ^{13}C-^{19}F(C5) REDOR experiments @../home/wei4b/data/13C-19F(C5)

A1(^{13}C) HFPmn in PC:PG:CHOL (HFPmn-A1-chol)

A6(^{13}C) HFPmn in PC:PG:CHOL (HFPmn-A6-chol)

L9(^{13}C) HFPmn in PC:PG:CHOL (HFPmn-L9-chol)

A6(^{13}C) HFPmn_mut in PC:PG:CHOL (HFPmnmut-A6-chol)

L9(^{13}C) HFPmn_mut in PC:PG:CHOL (HFPmnmut-L9-chol)

A6(^{13}C) HFPtr in PC:PG:CHOL (HFPtr-A6-chol)

L9(^{13}C) HFPtr in PC:PG:CHOL (HFPtr-L9-chol)

A1(^{13}C) HFPmn in PC:PG (HFPmn-A1-PCPG)

I4(^{13}C) HFPmn in PC:PG (HFPmn-I4-PCPG)

A6(^{13}C) HFPmn in PC:PG (HFPmn-A6-PCPG)

L9(^{13}C) HFPmn in PC:PG (HFPmn-L9-PCPG)

L12(^{13}C) HFPmn in PC:PG (HFPmn-L12-PCPG)

A14(^{13}C) HFPmn in PC:PG (HFPmn-A14-PCPG)

I4(^{13}C) HFPmn_mut in PC:PG (HFPmnmut-I4-PCPG)

A6(^{13}C) HFPmn_mut in PC:PG (HFPmnmut-A6-PCPG)

L9(^{13}C) HFPmn_mut in PC:PG (HFPmnmut-L9-PCPG)

L12(^{13}C) HFPmn_mut in PC:PG (HFPmnmut-L12-PCPG)

A14(^{13}C) HFPmn_mut in PC:PG (HFPmnmut-A14-PCPG)

I4(^{13}C) HFPtr in PC:PG:CHOL (HFPtr-I4-PCPG)

A6(^{13}C) HFPtr in PC:PG:CHOL (HFPtr-A6-PCPG)

L9(^{13}C) HFPtr in PC:PG:CHOL (HFPtr-L9-PCPG)

L12(^{13}C) HFPtr in PC:PG:CHOL (HFPtr-L12-PCPG)

A14(^{13}C) HFPtr in PC:PG:CHOL (HFPtr-A14-PCPG)

Figure 13 1D DCP setup experiments @../home/wei4b/data/DCP

Double ^{13}C labeled NAL DCP spectra (dcp-double13CNAL)

APPENDIX 2. TROUBLE SHOOTING FOR MAS PROBES

1. Sample spinning problems

(1) The sample is not spinning at all.

a. The alignment for the pieces in spinning module is not good enough if you can feel some difficulty when inserting the rotor;

b. The drive and bearing gas have been reversed when installing the spinning module with the end piece that is connected to the magic angle spinning adjustment, the groove on the end piece has to be placed on the drive gas side.

(2) The rotor is spinning, but the MAS controller is not reading.

a. Restart the MAS controller;

b. Cut the tip of the optical fiber;

c. The optical fiber is broken if you can see red laser all over the probe instead of just the spinning module region;

d. The two pinholes on the spinning module front panel are too far from each other. This is always because you are using a 6 mm spinning module front panel intead of a 4 mm one.

(3) The rotor is not spinning stably.

a. Remark the rotor;

b. Repack the rotor tightly;

c. Reset the bearing gas parameters in ACC panel. The typical values for a 4 mm MAS probe are: adjust 2 psi, span 100 Hz and maximum 35 psi.

2. Probe Tuning problems

When you change the configuration of a probe, follow the suggested capacitors on the manual. Check the low power tuning before inserting the probe into the magnet.

(1) There is no resonance. There is always some contacting problem. Check the connection of every capacitor and coil, especially the weak soldering spots. The following figure is for the HFXY probe. The four spots that typically have contact problems are pointed out with red arrows.

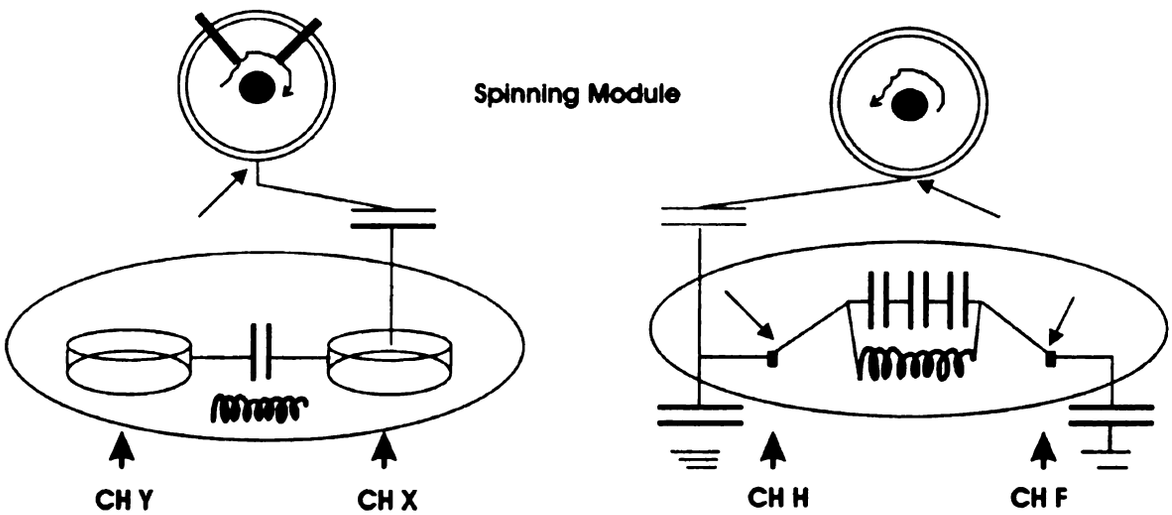

Figure A1 Schematic pictures for a quadruple HFXY 4mm MAS probe.

(2) There is resonance, but the position is not moving at all when you move the tuning rods. This is special for the ^{1}H and ^{19}F channels of the HFXY probe, and the problem is the screws on the ^{1}H and ^{19}F tuning rods are off. As shown in the pictures below, these tuning rods use the plastic screws to connect the adjustable knob outside the rod and the copper piece inside the rod. The screw will be off if it has been over adjusted.

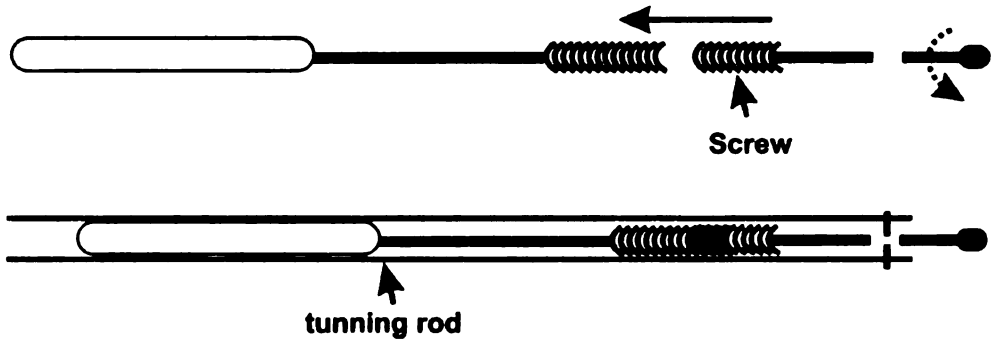

Figure A2 Schematic pictures for a ^{1}H or ^{19}F tunning rode on a quadruple HFXY 4mm MAS probe.

(3) There is resonance in the low power tuning, but it's not at the correct frequency, and you cannot get the right frequency by adjusting the tune and match knobs in the probe. In this case you may want to try different sets of capacitors. The one suggested on the manual is NOT always perfect. For the HFXY probe, the current configuration is HFPC (X ≡ ^{31}P and Y ≡ ^{13}C), and it is good for routine experiments such as ^{13}C-^{31}P REDOR, ^{13}C-^{19}F REDOR and ^{13}C-^{13}C 2D correlation. If you find the tuning for this probe is not satisfying and want to change the pieces, here are some suggestions:

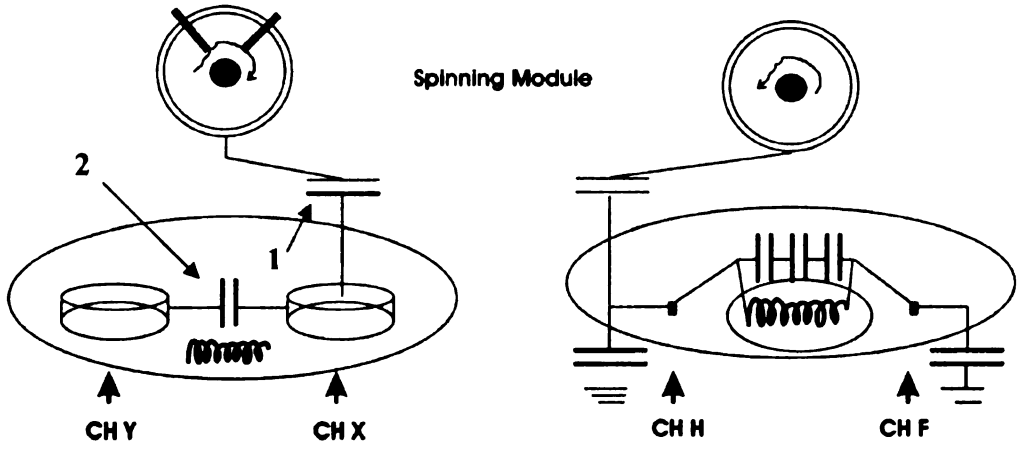

Figure A3 Schematic pictures for a quadruple HFXY 4mm MAS probe.

a. For CH X and CH Y, you can always change the capacitors 1 and 2, and you can adjust the length of the coil bridged over capacitor 2 gently.

b. For CH H and CH F, the current forward/reflection voltage ratio is 8:1 and 9:1 respectively and it works well for REDOR and PDSD experiments. It is NOT recommended to adjust any pieces connecting these two channels because they are very sensitive and the connection soldering points are weak. However, the coil in the red circle above is adjustable and is the ONLY adjustable part for the two channels. If you do readjust the coil, double check all the soldering points before assembling the probe.

APPENDIX 3 FMOC MANUAL PEPTIDE SYNTHESIS

The following solutions are commonly used in the FMOC peptide synthesis, and one can always make them before the synthesis:

Deprotection Solution: piperidine/DMF solution with 1:3 volume ratio.

Capping Solution: acetic anhydride/pyridine/DMF solution with 2:1:3 volume ratio.

Coupling Solution: 0.45M HBTU and 0.45M HOBt in DMF.

These solutions should be placed in brown bottles, sealed with parafilms, and stored in the fume hood.

The Cleavage Solution should be fresh and should be prepared right before utilization.

Cleavage Solution: TFA/thioanisole/EDT/anisole solution with 90:5:3:2 volume ratio.

Procedures for regular peptide synthesis. (The procedures were applicable for the synthesis of HFPmn, HFPmn(Cys), HFPmn_mut and HFPdm(Cys) used in this thesis):

1. We generally use the Ala or Gly-preloaded Wang Resin for the manual synthesis. A typical scale of synthesis was 0.1 mmol. For the synthesis of HIV fusion peptide monomer, we use the preloaded Wang Resins with substitution of 0.6 mmol/g, and for the synthesis of Cys-containing dimer as described in chapter II, we use preloaded Wang resins with substitution of 0.2 mmol/g. The synthesis starts from weighing the appropriate amount of Wang Resin and placing the resin into a 5 mL polypropylene column from Pierce (Rockford, IL).

2. Wash the resin with DCM, drain the DCM, and repeat these for two or three times.
3. Soak the resin in DCM for 2 hours, and then drain the DCM.
4. Wash the resin with DMF, and drain the DMF.
5. Soak the resin with 3 mL Deprotection solution, place the column on a rotation stage and mix for 5 minutes, and then drain the deprotection solution.
6. Soak the resin with 3 mL Deprotection solution, mix on a rotation stage for 20 minutes, and drain the deprotection solution.
7. At the same time with step 6, dissolve the Fmoc-protected amino acid into the coupling solution. The amino acid: resin ratio used in our lab is 5:1 for the unlabeled residues and 3:1 for the ^{13}C or ^{15}N labeled residues. The amino acid:HBTU:HOBt molar ratio should be 9:9:10. (For example, for an unlabeled residue, the amount of amino acid is 0.5 mmol if 0.1mmol resin was used, and the amino acid was dissolved into 1mL 0.45M Coupling Solution.)
8. Wash the resin with DMF, drain the DMF, and repeat these for 6 - 8 times in order to totally remove the piperidine.
9. Add DIPEA into the amino acid solution. The DIPEA:amino acid molar ratio is 2:1.
10. Add DMF into the amino acid solution until the total volume reaches ~ 4 mL, and transfer the solution into the column.
11. Place the column onto the rotating stage, and mix for 2 hours. (The coupling time may vary for different amino acids and peptide sequences as described

in chapter II, *cf.* the figure captions of Figures 3 and 5) One can check the completeness of the coupling step using the Ninhydrin test.*

12. After the coupling step, drain the coupling solution.
13. Repeat the steps 4 through 12 for the following residues.
14. After the coupling step for the last residue, repeat steps 4 though 6 to deprotect the last Fmoc group.
15. Wash the resin 3 ~ 5 times with DMF and drain, and then 2 ~ 3 times with DCM and drain.
16. Place the column into a dessicator with high vacuum pump for at least 6 hours to remove the residual DCM.
17. Soak the dry resin with 3 mL fresh cleavage solution, seal the column with parafilm, and mix it for 2 hours. (The Arg(Pbf) requires more cleavage time, and add 0.5 hour for every extra Arg(Pbf) residue.)
18. After the cleavage, remove the parafilm, then remove the cap of the column, and then collect the solution part with a 50 mL centrifuge tube and discard the residual resin.**
19. Remove the TFA from the solution using N_2 gas flow in the fume hood, and add cold methyl t-butyl ether drop wise into the residual solution (~ 1 mL). One should usually see white cotton-like precipitate while adding the ether.
20. Place the centrifuge tube into the freezer for overnight, and separate the supernatant and precipitate through centrifugation. Collect the precipitate and discard the supernatant.

21. Remove the residual ether in the precipitate using N_2 gas flow, dissolve the peptide into 5 mL D.I. water, and lyophilize to get crude product.
22. HPLC purification with a H_2O/Acetonitrile gradient and MS identification as described in chapter II.

*Ninhydrin Test:

Solution A: 5% Ninhydrin in ethanol (w/v); Solution B: 80% Phenol in ethanol (w/v); Solution C: KCN in pyridine (2 mL 0.001M KCN in 98 mL pyridine)

Sample a few resin beads and wash with DMF and DCM several times. Transfer the resin to a small glass tube and add 2 drops of the above solutions. Mix well and heat to 100 °C for 5 minutes. The presence of resin-bound free amine is indicated by blue resin beads.

**Cleavage

The reagents thioanisole, EDT and TFA have pungent odor. There will be pressure during cleavage, thus please remove the parafilm and cap very carefully before collecting the cleavage solution.

Procedures for the Cys crosslinking between HFPmn(Cys) to form HFPdm.

1. Dissolve the purified HFPmn(Cys) into D.I. H_2O in a 1.5 mL eppendorf tube to reach the peptide concentration ~ 5 mM.

2. Add DMAP powder into the peptide solution to reach the concentration of 10 mM, and adjust the pH of the solution to ~ 8 using 1M NaOH.

3. Gently vortex the eppendorf tube for 2 hours with the solution exposed to the air.

4. Dilute the peptide solution with 10-time volume of D.I.water, freeze the diluted solution and lyophilize it for overnight to obtain the crude product.

5. HPLC purification with a H_2O/Acetonitrile gradient as described in chapter II.

Procedures for the Cys crosslinking between HFPmn(Cys) and HFPdm(Cys) to form HFPtr.

1. Dissolve the purified HFPmn(Cys) and HFPdm(Cys) into D.I. H_2O in an 1.5 mL eppendorf tube to reach the concentrations of 5 mM and 7.5 mM respectively.

2. Add DMAP powder into the peptide solution to reach the concentration of 10 mM, and adjust the pH of the solution to ~ 8 using 1M NaOH.

3. Gently vortex the eppendorf tube for 2.5 hours with the solution exposed to the air.

4. Dilute the peptide solution with 10-time volume of D.I.water, freeze the diluted solution and lyophilize it for overnight to obtain the crude product.

5. HPLC purification with a H_2O/Acetonitrile gradient as described in chapter II.

Procedures for the Cys crosslinking between HFPmn(Cys) to form HFPte

1. Dissolve the purified HFPdm(Cys) into D.I. H_2O in an 1.5 mL eppendorf tube to reach the concentration of 5 mM.

2. Add DMAP powder into the peptide solution to reach the concentration of 10 mM, and adjust the pH of the solution to ~ 8 using 1M NaOH.

3. Gently vortex the eppendorf tube overnight with the solution exposed to the air.

4. Dilute the peptide solution with 10-time volume of D.I.water, freeze the diluted solution and lyophilize it for overnight to obtain the crude product.

5. HPLC purification with a H_2O/Acetonitrile gradient as described in chapter II.

APPENDIX 4 INTRODUCTION TO NMR

This appendix helps to explain the description of Average Hamiltonian Theory in chapter III.

Spin Behavior in a magnetic field. Nuclei with spin of 1/2 such as ^{1}H, ^{13}C, ^{15}N, ^{31}P and ^{19}F have two possible spin states with magnetic quantum number m = 1/2 or -1/2. If the nucleus is placed in a magnetic field, there will be an interaction between the nuclear magnetic moment $\vec{\mu}$ and the external magnetic field $\overrightarrow{B_0} = B_0\hat{z}$. The energy associated with $\vec{\mu}$ in $\overrightarrow{B_0}$ is given by

$$E = -\vec{\mu} \cdot \vec{B}_0 = -\mu_z B_0 = -m\gamma\hbar B_0 \quad \text{(A1)}$$

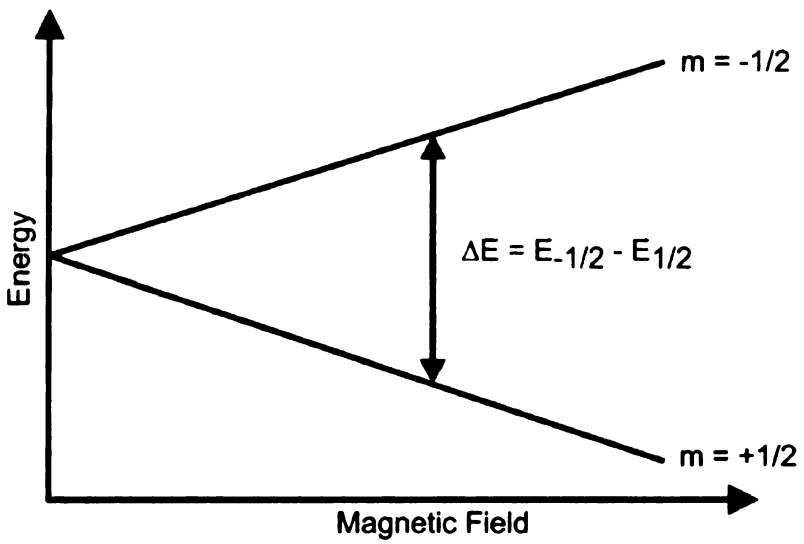

Figure A4 Energy Splitting for a spin 1/2 nucleus in the external magnetic field.

In Eq. A1 the term μ_z represents the z component of the nuclear magnetic moment because the external magnetic field is always defined as being along the z direction in the laboratory frame. γ is the gyromagnetic ratio and $\hbar$ is Planck's

constant divided by 2π. Thus, the splitting between the two energy levels with m = 1/2 and -1/2 is shown in Figure A4 for a nucleus with spin 1/2, and the energy difference between the two levels are

$$\Delta E = \gamma \hbar B_0 = h \cdot \upsilon_0 \quad \text{(A2)}$$

where v_0 is also known as the Larmor frequency.

Magnetization and time evolution of magnetization. The concept of magnetization in the field of NMR was defined as the vector sum of individual magnetic moments $\vec{\mu}$. It is usually convenient to describe the system using magnetization because it provides a macroscopic picture for the spin system.

$$\vec{M} = \sum \vec{\mu} \quad \text{(A3)}$$

The direction of the magnetization for an equilibrium spin system is along the z axis because the Boltzmann population of individual $\vec{\mu}$ that are aligned along the z axis is larger than the Boltzmann population of the $\vec{\mu}$ aligned along the -z axis. To understand the time evolution of magnetization, it will be helpful to first consider the time evolution of an individual magnetic moment. An individual magnetic moment $\vec{\mu}$ in a field $\vec{B}$ is subject to a torque $\vec{N}$, which is defined as

$$\vec{N} = \vec{\mu} \times \vec{B} \quad \text{(A4)}$$

Analogous to the Newton's Law where force is the time derivative of momentum, in the rotational motion, torque is the time derivative of angular momentum $\vec{L}$.

$$\vec{N} = \frac{d}{dt}\vec{L} \quad \text{(A5)}$$

In the quantum mechanics, the angular momentum and magnetic moment are correlated through the constant of gyromagnetic ratio.

$$\vec{\mu} = \gamma \vec{L} \quad \text{(A6)}$$

The combination of Eqs. A4, A5 and A6 gives the time evolution of an individual magnetic moment.

$$\frac{d}{dt}\vec{\mu} = \gamma \vec{\mu} \times \vec{B} = \vec{\mu} \times \gamma \vec{B} \quad \text{(A7)}$$

The discussion for an individual magnetic moment can be extended to the macroscopic magnetization, thus

$$\frac{d}{dt}\vec{M} = \vec{M} \times \gamma \vec{B} \quad \text{(A8)}$$

Time evolution of the spin system. In quantum mechanics, a spin system can be expressed as the linear combination of time-independent eigenfunctions and their corresponding time-dependent coefficients.

$$\Psi = \sum_m c_m \psi_m = \sum_m c_m |m\rangle \quad \text{(A9)}$$

The ensemble average of these coefficients forms a matrix which is generally named density matrix. The density matrix is the matrix representation of an operator known as density operator σ.

$$\overline{c_n c_m^*} = \langle n|\sigma|m\rangle = \sigma_{nm} \quad \text{(A10)}$$

The system can be represented as the density matrix and density operator. The time evolution of the density operator reflects the time evolution of a spin system.

According to the Eq. A9, the time-dependent Schrodinger Equation can be written as

$$i\sum_n \frac{dc_n(t)}{dt}|n\rangle = \sum_n c_n(t)H|n\rangle \quad \text{(A11)}$$

Using the orthogonal condition between different eigenfunctions and some algebra, the time evolution of the coefficient c_k(t) is

$$i\frac{dc_k(t)}{dt} = \sum_n c_n(t)\langle k|H|n\rangle \quad \text{(A12)}$$

Thus, the time evolution of an arbitrary element in the density matrix under the Hamiltonian is given by

$$\begin{aligned}\frac{d\langle k|\sigma|m\rangle}{dt} &= \frac{d\overline{c_k c_m^*}}{dt} = \overline{c_k \frac{dc_m^*}{dt}} + \overline{\frac{dc_k}{dt}c_m^*} = i\sum_n \overline{c_k c_n^*}\langle n|H|m\rangle - i\sum_n \overline{c_n c_m^*}\langle k|H|n\rangle \\ &= i\sum_n \langle k|\sigma|n\rangle\langle n|H|m\rangle - i\sum_n \langle k|H|n\rangle\langle n|\sigma|m\rangle = i\langle k|[\sigma,H]|m\rangle\end{aligned} \quad \text{(A13)}$$

In the operator form, or for the entire density matrix, the time evolution can be expressed as

$$\frac{d\sigma(t)}{dt} = -i[H,\sigma(t)] \quad \text{(A14a)}$$

This differential equation has a solution when the Hamiltonian is time-independent.

$$\sigma(t) = \exp[-iHt]\cdot\sigma(0)\cdot\exp[iHt] \quad \text{(A14b)}$$

Spin interaction Hamiltonians. In quantum mechanics, the Hamiltonian operator is associated with the total energy of the system. In NMR, the nuclear spin Hamiltonians are associated with the energies of different types of couplings

between the nuclear spins with different types of magnetic fields. For example, the Zeeman Hamiltonian (H_Z) corresponds to the coupling of nuclear spins with the external static magnetic field. The chemical shift Hamiltonian (H_{CS}) corresponds to the coupling with the induced magnetic fields originating from orbital motions of electrons. The dipolar coupling Hamiltonian (H_D) corresponds to the coupling with the magnetic field from the magnetic dipole moment of another spin. The expression for H_Z can be derived from Eq. A1 and the relation $\vec{\mu} = \gamma\hbar\vec{I}$, where $\vec{I} \equiv I_x\vec{x} + I_y\vec{y} + I_z\vec{z}$.

$$E_{Zeeman} = -\vec{\mu}\cdot\vec{B}_0 \Rightarrow H_Z = -\gamma\hbar\vec{I}\cdot\vec{B}_0 \quad \text{(A15)}$$

In the lab frame where the z-axis is set along the direction of the external magnetic field, we have $\vec{B}_0 = B_0\vec{z}$.

$$H_Z = -\gamma\hbar B_0 I_Z \quad \text{(A16)}$$

For H_{CS} and H_D, it is always convenient to first express the Hamiltonian in the principal axis system, and then to transform them into the lab frame through Wigner Rotation introduced in Chapter III of the main text.

For H_{CS} , we could write an analogous expression as Eq. A15.

$$E_{CS} = -\vec{\mu}\cdot\vec{B}_S \Rightarrow H_{CS} = -\gamma\hbar\vec{I}\cdot\vec{B}_S = (-\gamma\hbar)\vec{I}\cdot\overline{\overline{S}}\cdot\vec{B}_0 \quad \text{(A17)}$$

In Eq. A17, the term $\vec{B}_S$ represents the induced magnetic field due to the motion of electrons and the term $\overline{\overline{S}}$ is a tensor which reflects the shielding effect. As shown in Fig. A5, the fact that $\overline{\overline{S}}$ is a tensor rather than a numerical value

indicates that the induced field and the original field can be along different directions, and the effective field is the vector sum of $\vec{B}_0$ and $\vec{B}_S$.

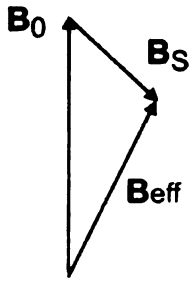

Figure A5. The vector representation of the fact that the induced shielding field is not necessarily parallel to the original field.

To evaluate H_{CS} in the principal axis system, one always expresses the Hamiltonian as the product of the elements of two second-rank Cartesian tensors or spherical tensors.

$$\vec{I}\cdot\overline{\overline{S}}\cdot\vec{B}_0=\sum_{i,j}\overline{\overline{S}}_{ij}(\vec{B}_0\otimes\vec{I})_{ij} \quad \text{(A18)}$$

In Eq. 18, the term $\vec{B}_0\otimes\vec{I}$ is a dyadic product of vectors $\vec{B}_0$ and $\vec{I}$ which forms a tensor.

For H_D, the field produced by a magnetic dipole $\overrightarrow{\mu_I}$ at the origin of the coordinate system can be expressed as

$$\vec{B}_I=\frac{[3(\vec{\mu}_I\cdot\vec{r})\vec{r}-\vec{\mu}_I]}{r^3} \quad \text{(A19a)}$$

in which $\vec{r}=\frac{x\vec{i}+y\vec{j}+z\vec{k}}{r}$ and $r=\sqrt{x^2+y^2+z^2}$ (A19b)

The vector $\vec{r}$ is the internuclear vector between the two coupled dipoles. The expression of the dipole-dipole interaction and the associated Hamiltonian thus can be written analogous to Eqs. A15 and A17 as

$$E_D = -\vec{\mu}_S \cdot \vec{B}_I = -\frac{[3(\vec{\mu}_I \cdot \vec{r})(\vec{\mu}_S \cdot \vec{r}) - \vec{\mu}_I \cdot \vec{\mu}_S]}{r^3}$$
$$\Rightarrow H_D = -\frac{\hbar^2 \gamma_I \gamma_S}{r^3}[3(I \cdot \vec{r})(S \cdot \vec{r}) - I \cdot S] \quad \text{(A20)}$$

In most cases, the magnitude of Zeeman Hamiltonian is much larger than the magnitude of chemical shift and dipolar coupling Hamiltonians. Therefore, there is always a truncation effect for the H_{CS} and H_D, and the terms containing spin operators which do not commute with H_Z (or I_Z according to Eq. A16) will be averaged to zero. Thus, the truncated H_{CS} is proportional to I_Z, the truncated heteronuclear H_D is proportional to $I_Z S_Z$, and the truncated homonuclear H_D is proportional to $I_Z S_Z + \frac{1}{4}(I_+ S_- + I_- S_+)$ where $I_\pm = I_x \pm i I_y$ and $S_\pm = S_x \pm i S_y$.

Rotating frame. Another type of important nuclear spin interaction is the interaction between spins and the external *rf* magnetic field because the *rf* pulses are widely utilized in NMR. In the case of magic angle spinning probes with solenoid coils, the *rf* field is oscillating with the carrier frequency ω_{rf} along the MAS rotor axis which is tilted by θ relative to the external magnetic field. Thus, the *rf* field can be decomposed into two parts that are either parallel or perpendicular to the external magnetic field.

$$\vec{B}_{rf} = B_1 \cos\theta \cos[\omega_{rf} t + \varphi]\vec{z} + B_1 \sin\theta \cos[\omega_{rf} t + \varphi]\vec{z} \quad \text{(A21)}$$

In Eq. A21, B_1 and φ are the amplitude and phase of the *rf* field, and can be time-dependent.

The *z* component in Eq. A21 is an oscillating field with frequency ω_{rf}. However, this field can be neglected because the time scale of the oscillation (*nanosec*) is much shorter than the experimental time scales such as dwell time and *rf* pulses (*microsec*), and the time average of the oscillations field is zero.

The *x* component in Eq. A21 can be decomposed as two rotating fields with angular frequencies ω_{rf} and $-\omega_{rf}$ since

$$\cos[\omega_{rf}t+\varphi]=\frac{1}{2}\exp[i(\omega_{rf}t+\varphi)]+\frac{1}{2}\exp[-i(\omega_{rf}t+\varphi)] \quad \text{(A22)}$$

With the condition $\omega_{rf}\approx\omega_L$, the rotating field with frequency $-\omega_{rf}$ can be neglected. In a classical picture, the nucleus spin μ is rotating around the *z*-axis in the lab frame under the effect of B_0 with angular frequency ω_L. The rotating field with frequency $\omega_{rf}\approx\omega_L$ will provide efficient torque to the nucleus spin which will induce the transition of magnetization over time.

$$\vec{N}=\frac{d}{dt}\vec{\mu}=\gamma\vec{\mu}\times\vec{B}_{rf,x}=\gamma\mu B_{rf,x}\sin<\vec{\mu},\vec{B}_{rf,x}> \quad \text{(A23)}$$

As shown in Eq. A23, an efficienct torque requires an approximately time-independent angle $<\vec{\mu},\vec{B}_{rf,x}>$ which can be satisfied by the rotating field with frequency ω_{rf}. The field with frequency $-\omega_{rf}$ will have a time-dependent angle $<\vec{\mu},\vec{B}_{rf,x}>$ and the interaction according to Eq. A23 will be reduced over time.

It is usually more convenient to make the *rf* field appear static by transforming the system to a rotating frame with angular frequency ω_{rf}. In the rotating frame, for the simplest case that $\omega_{rf} = \omega_L$, the field acting on the magnetization is just the static B_1 field along the x axis. If the initial magnetization is along the z axis, e.g. equilibrium state, the effect of applying a *rf* field is to tilt the magnetization into the xy plane (also known as the transverse plane) according to Eq. A8.

Magic Angle Spinning (MAS) and spinning sidebands. Manipulation of the spin interaction such as chemical shift and dipolar coupling can be achieved by rotating the sample about an axis which is tilted by an angle θ with respect to the external magnetic field B_0. The angle θ, known as magic angle, satisfies the condition $3\cos^2\theta - 1 = 0$ and θ = 54.7°. Here we will analyze the effect of the MAS on the chemical shift Hamiltonian.

According to Eq. 5 in chapter III, a general expression to the chemical shift is

$$H_{CS} = C_{CS} \cdot \sum_{l} \sum_{m=-l}^{l} (-1)^m \cdot R^{CS}_{l,-m} \cdot T^{CS}_{l,m} \quad \text{(A24)}$$

where the values of *l* are 0, 1 or 2. In the condition of high field where $H_z >> H^{int}$, the non-secular terms (*l* = 1 and 2) in Eq. A24 will become time-dependent due to the manipulation of Zeeman Hamiltonian, and their time averages will be zero. Thus, eq. A24 can be simplified as

$$H_{CS} = C_{CS}(R_{00}T_{00} + R_{10}T_{10} + R_{20}T_{20}) \quad \text{(A25)}$$

On the right side of Eq. A25, the middle term represents the anti-symmetric part of the Hamiltonians. This part is not detectable for chemical shift and therefore

can be neglected. The last term on the right side of Eq. A25 represents the anisotropic part of the chemical shift Hamiltonian (or H_{CSA}) in the principal axis system. When transforming into the lab frame, this term will the periodic with the period $\frac{1}{\omega_R}$ where ω_R is the sample spinning frequency. The rotational angular frequency of the transverse magnetization under the periodical H_{CSA} will also be periodical and will have the form

$$\omega(t) = A + B\xi(t) \quad \text{(A26)}$$

The terms *A* and *B* are time-independent and are related to the Euler angle set (α, β, γ) which correlates the principal axis system and the rotor frame, and the magic angle θ. The term $\xi(t)$ is periodic and related to the sample spinning frequency. The FID due to this precession can be expressed as

$$S(t) \propto \exp[i\omega(t)] = \exp(iAt)\exp[iB\int_0^t \xi(t')dt'] \quad \text{(A27)}$$

The second term on the right side of Eq. 27 will be unity for multiples of the sample spinning period. The FID will consequently contain a sequence of echoes separated by $1/\omega_R$. Fourier Tansformation of the FID with echoes provides spinning sidebands at multiples of ω_R away from the isotropic chemical shift in the frequency domain.

Evolution of transverse magnetization and its Fourier relationship to the NMR spectrum. Consider a simple NMR experiments where a 90° pulse was applied followed by detection. Initially the magnetization is along z axis and the 90° pulse

will flip the magnetization to the xy plane. Consider the situation that at the beginning of the acquisition period, the magnetization is along the x axis. During the acquisition period, the spin system is subject to only the Zeeman Hamiltonian. The time evolution of the magnetization is controlled by Eq. A14a with the density operator $\sigma(0) \propto I_x$ and $H_z \propto \omega_0 I_z$, where I_x and I_z are the x and z components of the spin operator and $\omega_0 = \gamma B_0$. Since the Zeeman Hamiltonian is time-independent, according to Eq. A14b, the density operator at time *t* is

$$\sigma(t) \propto \exp[-i\omega_0 I_z t] I_x \exp[i\omega_0 I_z t] = I_x \cos(\omega_0 t) + I_y \sin(\omega_0 t) \quad \text{(A28)}$$

This means the magnetization will rotate in the transverse plane. The detected time-domain signal is the transverse magnetization. It is convenient to write the transverse magnetization in its complex form $\mu_+ = \mu_x + i\mu_y \propto I_+$. Without considering relaxation, the expectation value will be

$$S(t) \equiv \left\langle I^+ \right\rangle \propto Tr\{\sigma(t) I^+\} = Tr\{[I_x \cos(\omega_0 t) + I_y \sin(\omega_0 t)] \cdot [I_x + iI_y]\} \quad \text{(A29)}$$

It is easier to evaluate the time-domain signal in the matrix form where

$$I_x = \frac{1}{2}\begin{bmatrix} 0 & 1 \\ 1 & 0 \end{bmatrix} \text{ and } I_y = \frac{1}{2}\begin{bmatrix} 0 & -i \\ i & 0 \end{bmatrix} \quad \text{(A30)}$$

Using Eq. A30, one can evaluate the time-domain signal in Eq. A29 as

$$S(t) \propto \exp[i\omega_0 t] \quad \text{(A31)}$$

Eq. A31 indicates an oscillation in the time-domain signal, and after the Fourier transformation the frequency-domain spectrum showed a single resonance line at frequency ω_0. Considering relaxation which makes the tranverse

magnetization return to its thermoequilibrium state, e.g. zero, there will be a exponential decay term adding to the time-domain signal expressed in Eq. A31.

$$S(t) \propto \exp[i\omega_0 t - \lambda t] \quad \text{(A32)}$$

The parameter λ is the decay constant. The Fourier transformation of Eq. 32 results in a Lorentzian lineshape in the frequency domain, and linewidth is proportional to the decay constant λ.

Effect of the powder average on evolution of the transverse magnetization. This part provides a qualitative picture about how the recovered heteronuclear dipolar coupling affects the ^{13}C signal in the REDOR S_1 spectrum. Considering that the zero-order average heteronuclear dipolar coupling Hamiltonian under Magic Angle Spinning is the only interaction in the S_1 spectrum.

$$< H_{D,hetero} >_0 \propto \omega_{IS} \sin(2\beta)\sin\gamma \cdot I_z S_z \quad \text{(A33)}$$

In Eq. 33 the ω_{IS} represents the magnitude of the dipolar coupling frequency which is related to the gyromagnetic ratios and the internuclear distance. The angles β and γ are Euler angles between the principal axis system of the dipolar coupling frame and the lab frame at a single time in the rotor cycle. For an individual I-S internuclear vector, the value of these angles is related to the orientation of the I-S vector relative to external magnetic field. The time evolution of initial density operator, which is proportional to I_x can be expressed as

$$\sigma(t) = I_x \cos(\tilde{\omega}t) + 2I_y S_z \sin(\tilde{\omega}t) \text{ and } \tilde{\omega} \propto \omega_{IS} \sin(2\beta)\sin\gamma \quad \text{(A34)}$$

The term with the spin operator $I_y S_z$ is undetectable based on Eq. 22 in the main text. Thus, the detected time-domain signal is

$$S(t) \propto Tr\{\sigma(t) I^+\} = Tr\{I_x \cos(\tilde{\omega} t) \cdot (I_x + iI_y)\} \propto \cos(\tilde{\omega} t)[1 + iTr\{I_x I_y\}] \quad \text{(A35)}$$

With the matrix form of the spin operators I_x and I_y

$$I_x \propto \begin{bmatrix} 0 & 0 & 1 & 0 \\ 0 & 0 & 0 & 1 \\ 1 & 0 & 0 & 0 \\ 0 & 1 & 0 & 0 \end{bmatrix} \text{ and } I_y \propto \begin{bmatrix} 0 & 0 & -i & 0 \\ 0 & 0 & 0 & -i \\ i & 0 & 0 & 0 \\ 0 & i & 0 & 0 \end{bmatrix}$$

, one can obtain from Eq. A35 that

$Tr\{I_x I_y\} = 0$ and

$$S(t) \propto \cos(\tilde{\omega} t) \quad \text{(A36)}$$

Eq. A36 indicates that the time-domain signal of spin I due to the I-S dipolar coupling with a particular orientation relative to the magnetic field is a cosine oscillation with its own frequency $\tilde{\omega}$. In a powder sample where an individual I-S spin pair can adopt any orientation relative to the external field, the net transverse magnetization will decay since it will be the sum of the time-domain signals of individual spin pairs with same initial phase but different oscillation frequencies (Figure A6). Thus, it can be qualitatively understood that in the REDOR S_1 spectrum there is an attenuation in the detected signal relative to the S_0 spectrum. In REDOR experiments, one acquires S_1 spectra with different dephasing times, which correspond to different evolution times of the transverse magnetization under the heteronuclear dipolar coupling. Thus, it is understandable that there will be a buildup curve because the transverse magnetization is not entirely reduced at short dephasing times.

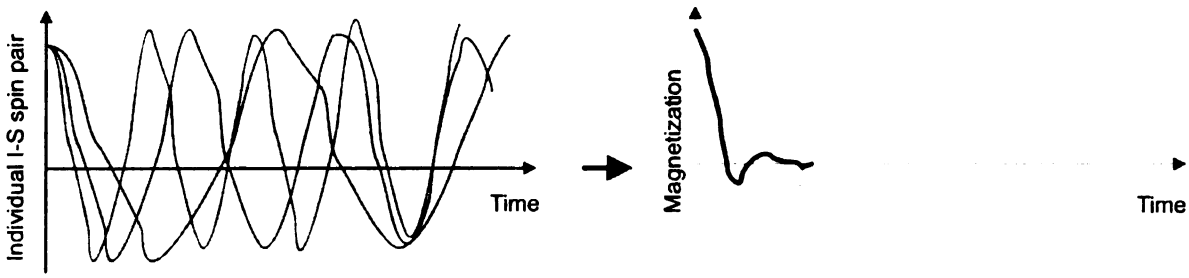

Figure A6 Decay of the transverse magnetization due to the powder averaging.

Bibliography

1. Cavanagh, C., Fairbrother, W.J., Palmer, A.R., and Skelton, N.J. (1996). Protein NMR Spectroscopy: Principles and Practice. San Diego: Academic Press.

2. Schmidt-Rohr, K., and Spiess, H.W. (1996). Multidimentional Solid-state NMR and Polymers. London: Academic Press.

3. Stejskal, E.O., and Memory, J.D. (1994). High Resolution NMR in the Solid State. New York: Oxford University Press.

4. Tycko, R. (1994). Nuclear Magnetic Resonance Probes of Molecular Dynamics. Dordrecht: Kluwer Academic Publishers.

5. Haeberlen, U. (1976). High Resolution NMR in Solids Selective Averaging. New York: Academic Press.

6. Mehring M. (1983). Principles of High Resolution NMR in Solids. New York: Springer-Verlag.

7. Jaroniec C.M. (2008). "Heteronuclear Decoupling and Recoupling" in U.S.-Canada Winter School on Biomolecular Solid State NMR. Stowe, Vermont, January 20-25, 2008.